

**Development of Functional Organic Materials Using
Oxygen-Bridged Triarylamine Skeleton as Quasiplanar Structure**

Hidetaka Nishimura

2016

Table of Contents

General Introduction	1
Chapter 1 On-top π -Stacking of Quasiplanar Molecules in Hole-Transporting Materials: Inducing Anisotropic Carrier Mobility in Amorphous Films	27
Chapter 2 The Influence of Quasiplanar Structures of Partially Oxygen-Bridged Triphenylamine Dimers on the Properties of their Bulk Films	57
Chapter 3 Development of Transparent Organic Hole-Transporting Materials Using Partially Oxygen-Bridged Triphenylamine Skeletons	71
Chapter 4 Hole-Transporting Materials with a Two-Dimensionally Expanded π -System around an Azulene Core for Efficient Perovskite Solar Cells	89
Chapter 5 Oxygen-Bridged Diphenylnaphthylamine as a Scaffold for Full-Color Circularly Polarized Luminescent Materials	125
List of Publications	157
Acknowledgment	159

General Introduction

In a last few decades, the researches in the field of organic electronics, such as organic field effect transistors (OFETs),¹ organic light-emitting diodes (OLEDs),² and organic photovoltaics (OPVs),³ have been actively conducted toward their applications in our daily life (Figure 1). As compared with these electronics devices based on inorganic materials such as silicon, the devices consisted of organic materials can offer advantages in terms of lightweight, flexibility, and possible low cost fabrication by printing methods, as well as the structural diversity of the organic materials that allows fine-tuning of their properties.



Figure 1. Representative applications in the field of organic electronics.

The progress in the organic electronics was attributed in large part to the development of excellent organic semiconductors. Organic compounds had been believed to be insulators until a finding in the middle of 20th century. In 1954, Akamatsu and Inokuchi found that charge-transfer complex composed of perylene and bromine shows electrical conductivity in the same level with inorganic semiconductors (Figure 2).⁴ In 1973, Ferraris and Heeger then reported that TTF-TCNQ complex exhibits significantly high conductivity, which is comparable with that of metal materials.⁵ In 1977, Shirakawa and coworkers found high conductivity in polyacetylene upon doping with iodine.⁶

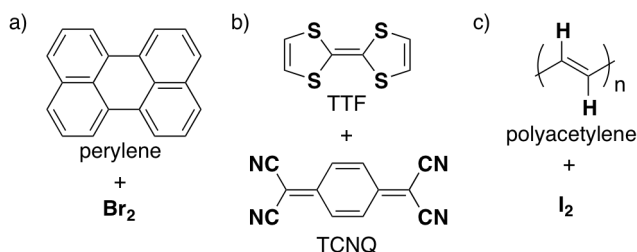


Figure 2. Examples of charge transfer complexes.

Mechanisms of Charge Transport in Organic Molecules

Inorganic materials, especially in silicon single crystals widely used as a typical semiconducting material, usually exhibit isotropic charge transport because of their intrinsic 3D network structure (Figure 3a). In contrast, organic materials consist of anisotropic molecules, in which charge carriers transport, therefore, arises between the molecules through the intermolecularly overlapped π -orbitals (Figure 3b).

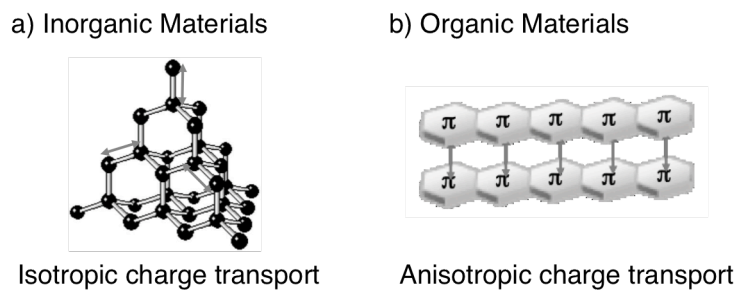


Figure 3. Charge transport directions in (a) silicon as atypical example for inorganic materials and (b) organic materials.

The mechanism of charge carrier transport can be classified into band mechanism and hopping mechanism as shown in Figure 4. In the case that molecules are densely packed by π - π interaction in the crystals, the electronic band structures consisting of valence and conduction bands form, where charge carriers can transfer through this band (band mechanism, Figure 4a). The charge carrier mobility based on the band mechanism is expressed in the following equation:

$$\mu = \frac{e\tau}{m}$$

where e is the elementary charge, τ is the relaxation time and m is the effective mass, respectively.

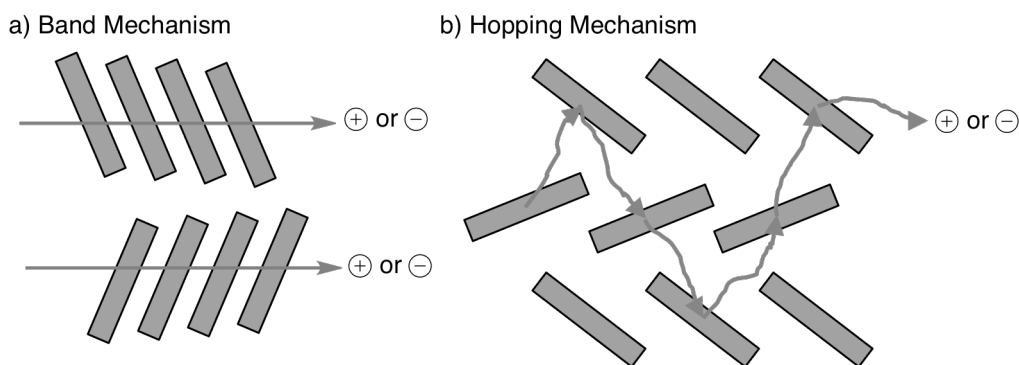


Figure 4. Schematic illustrations of (a) band mechanism and (b) hopping mechanism for charge carrier transport.

Only a few examples of organic molecules have been reported to exhibit band conduction so far.⁷ Instead, in many case of organic materials, molecules can not construct the electronic band structures, and thus show the carrier transport through hopping mechanism as shown in Figure 4b. The holes and electrons transport between the HOMOs and LUMOs that located on individual molecules, respectively (Figure 4b).

The hopping mobility follows the Marcus equation⁸:

$$\mu = \frac{er^2V^2}{6k_B\hbar T} \left(\frac{\pi}{\lambda k_B T} \right)^{1/2} \exp \left(-\frac{\lambda}{4k_B T} \right)$$

where r is the distance between neighboring molecules, V is the electronic coupling, k_B is the Boltzmann constant, \hbar is the reduced Plank constant, T is the temperature, and λ is the reorganization energy. In this equation, V and λ are the molecule-specific parameters, thus being the key parameters in the hopping transport.

In this charge transporting mechanism, neutral molecule changes to charged states that returns to the original neutral state by subsequent charge carrier transport to the neighbor molecules. The reorganization energy λ is defined as the energy changes resulting from the charge transfer. That is, if the reorganization energy λ is small enough, the organic molecule can easily accept a transfer of a charge carrier, which would be related to small conformational changes in the solid state. The author calculated the reorganization energies of various organic materials at B3LYP/6-31G(d) level of theory (Figure 5). For example, planar hole-transporting (p-type) materials, such as tetracene ($\lambda_h = 0.11$ meV) and pentacene ($\lambda_h = 0.09$ meV) with delocalized π -orbitals in the rigidly fused carbon skeleton, show particularly small reorganization energies. As a typical planar electron-transporting (n-type) material, perylene bisimide derivative that has strong electron withdrawing groups on the planar perylene skeleton also show small reorganization energy ($\lambda_h = 0.16$ meV). π -Delocalization in the skeleton seems to be effective in decreasing the reorganization energy, since fullerene C₆₀ with I_h symmetry shows 0.085 meV for hole mobility and 0.16 meV for electron mobility, respectively. In the case of non-planar materials, such as triphenylamine-based hole-transporting materials, large values of the reorganization energies are shown due to less π -conjugation compared to the planar materials. For example, N,N'-diphenyl-N,N'-di(*m*-tolyl)benzidine (TPD) with a twisted propeller-like structure shows the larger reorganization energy ($\lambda_h = 0.28$ meV). These reorganization energies for the novel skeleton can be estimated by DFT calculations in the molecular design, which would provide useful information on the molecules in advance.

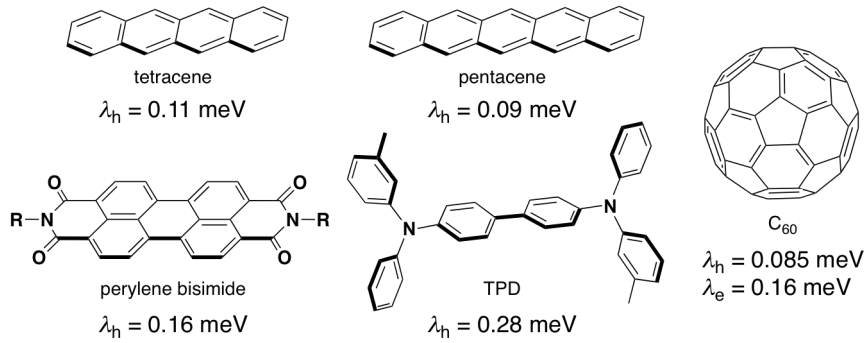


Figure 5. Reorganization energies (λ) of organic molecules calculated at B3LYP/6-31G(d) level.

Electronic coupling V represents the strengths in the interactions of π -orbitals between the neighboring molecules, which is rather difficult to be predicted in molecular design. Brédas *et al.* analyzed the electronic couplings for a dimer of tetracene by theoretical calculations.⁹ The electronic couplings between the HOMOs and the LUMOs increase as the intermolecular distance d between the two tetracene skeletons decreases (Figure 6a), although such perfectly cofacial contact cannot be observed in most organic molecules. They also examined the effect of the slipping degree between the two molecules on electronic coupling V (Figure 6b): One tetracene molecule is slipped along the horizontal direction with keeping the π -stacked distance. The maximum values for both of the electronic couplings between the HOMOs and the LUMOs are obtained in fully overlapped structure, the local maximum for the electronic couplings appear in the different structures, which depends on the distribution of the HOMOs and the LUMOs, respectively. These results suggest that not only the π -stacked distance but also the degree of slipping provide a strong impact on the charge transport properties of organic materials.

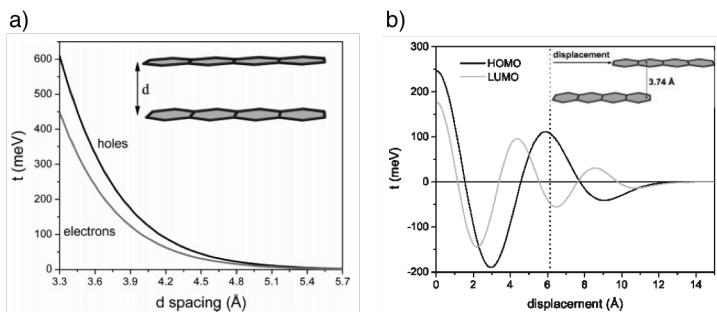


Figure 6. Theoretical electronic couplings (V) using two tetracene molecules.

Crystalline Organic Semiconductors

As crystalline organic semiconductors, acenes, such as tetracene and pentacene, are the typical compounds. π -Orbitals of acenes are delocalized over the entire skeleton (Figure 7a). In the crystalline state, they have two main intermolecular interactions between the neighboring molecules, i.e., π - π (face-to-face) interaction and CH- π (edge-to-face) interaction. These interactions resulted in the formation of inclined arrangement of molecules, so-called “herringbone stacking” (Figure 7b). This stacking structure shows two-dimensional charge transport properties.

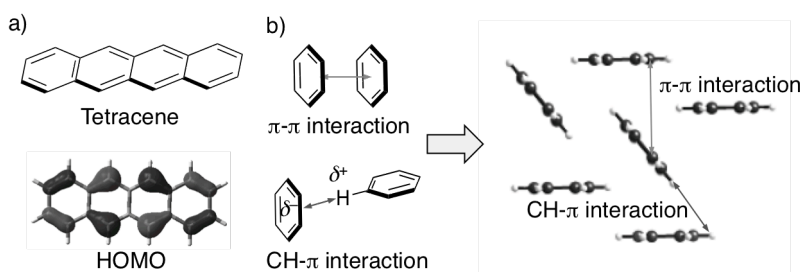
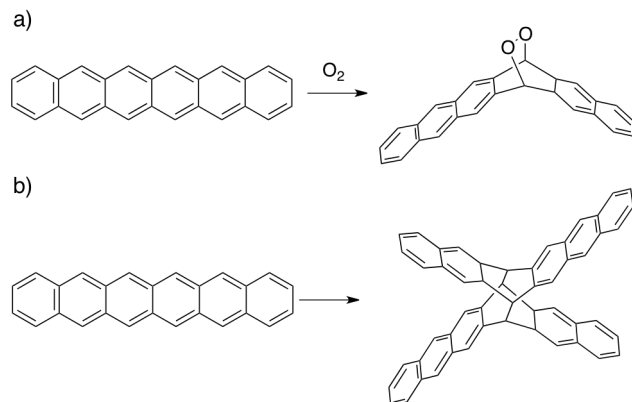


Figure 7. (a) Molecular structure and the HOMO of tetracene. (b) Intermolecular interactions between benzene rings and herringbone structure.

Hole Mobilities of Non-Substituted Acenes

With increasing the number of fused rings in acenes, the reorganization energies become smaller and the electronic couplings become larger. Therefore, hole mobilities of acenes increase as the number of fused rings increases.¹⁰ Although the π -extension of acenes is effective for improving hole mobility, the stability of acenes severely decreases with introducing fused rings. For example, hexacene easily reacts with oxygen in solution (Scheme 1a).¹¹ Furthermore, hexacene also undergoes dimerization (Scheme 1b). This instability currently makes it difficult to synthesize non-substituted acenes with more fused rings than hexacene.¹²



Scheme 1. Reactivity of hexacene.

Approach to Control of Molecular Orientation in the Crystalline States

In order to obtain high hole mobility, we need another approaches other than π -extension of molecules. As mentioned above, charge transport property depends on π -extension of molecules and degree of π -overlap between the neighboring molecules. Therefore it is important to control molecular orientation in the solid state.

A primary approach would be introduction of substituents to the acene skeletons. The substituent effects can be classified into three types. One is inhibition of CH- π interactions by increasing of C/H ratio. In addition to this effect, another is using electronic effect of substituents. The other is steric effect of substituents. In the following section, some reported strategies toward the control of molecular orientation in the single crystals are summarized.

Increasing of C/H Ratio

As the substituents to increase C/H ratio, halogen substituents or phenyl rings are often used.

- **Introduction of Halogen Substituents**

It is known that halogenated benzene molecules stack vertically with π - π interaction in the crystal.¹³

Bao *et al.* developed 5,11-dichlorotetracene (**DCT**).¹⁴ In the crystalline state, this compound forms dense π -stacking with the distance of 3.49 Å and the large π -overlap area was observed as compared to that of tetracene (Figure 8a). A single crystal of **DCT** prepared by sublimation exhibited slightly higher hole mobility of 1.6 cm²/Vs than that of tetracene (1.3 cm²/Vs).

Chi and Chen *et al.* reported 5,6,11,12-tetrachlorotetracene (**TCT**).¹⁵ By the steric

hindrances between the chlorine atoms, the tetracene skeleton of **TCT** was slightly distorted from a planer structure. In a similar fashion to **DCT**, **TCT** forms π -stacking in the crystalline state (Figure 8b), whereas the stacking distance in **TCT** is slightly longer than **DCT**. **TCT** exhibited hole mobility of $1.7 \text{ cm}^2/\text{Vs}$, which is comparable to that of **DCT** ($1.6 \text{ cm}^2/\text{Vs}$) and higher than that of tetracene ($1.3 \text{ cm}^2/\text{Vs}$). This result would be due to effective π -overlap in the crystal of **TCT**. It is notably that the packing structure of **DCT** and **TCT** is not herringbone stacking but columnar stacking, indicating that the CH- π interactions are weakened by the substitutions with chlorine atoms.

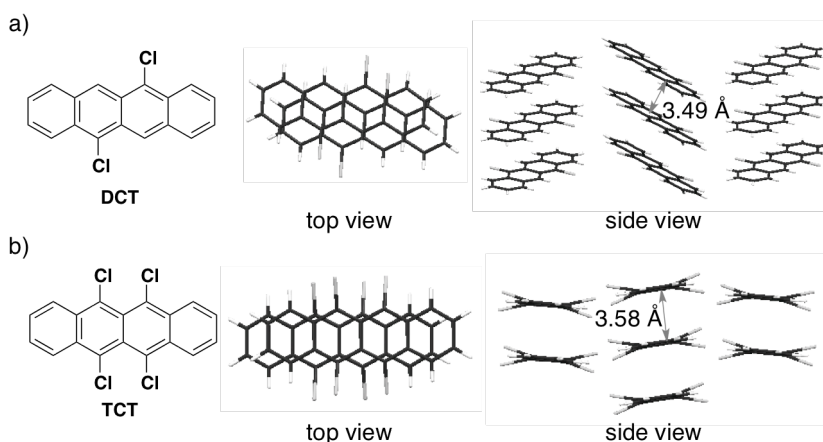


Figure 8. Molecular structures and packing structures of (a) **DCT** and (b) **TCT**. π - π distances between neighbouring molecules are also shown.

• Introduction of Phenyl Rings

Among the organic semiconductors, rubrene (*5,6,11,12-tetraphenyltetracene*) shows the highest hole mobility of $40 \text{ cm}^2/\text{Vs}$ in the single crystal.¹⁶ Such a high mobility arises from its molecular orientation. Rubrene is known to form unique herringbone stacking in the crystalline state (Figure 9). Two neighboring rubrene molecules show almost no slipping in the short axis of the π -skeleton. With respect to the high hole mobility, Brédas and coworkers carried out theoretical calculations.⁹ In their calculations, the dimeric structure of rubrene was reproduced well and shown to possess high electronic couplings for hole transport. It has been demonstrated that rubrene could construct the electronic bands in crystal and exhibits charge transport by the band mechanism.

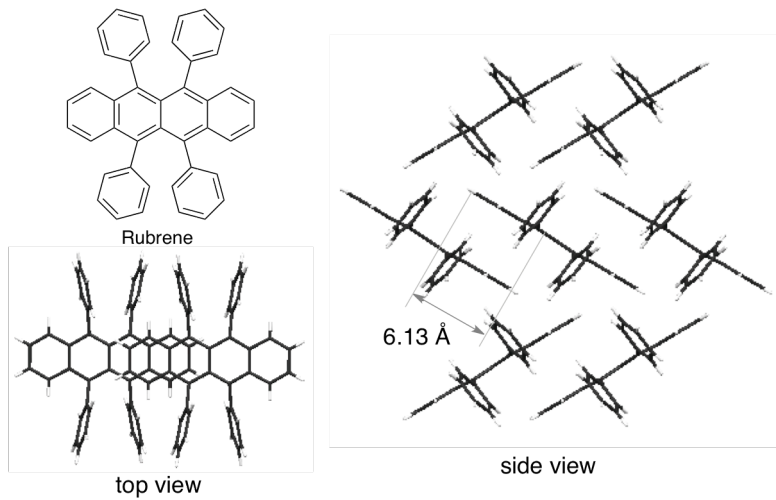


Figure 9. Molecular structure and packing structure of rubrene. Slipping distance is also shown.

Electronic Effect

As the examples of using electronic effects, fluorine or sulfur groups are introduced as substituents.

• Introduction of Fluorine Atoms

Fluorine has the largest electronegativity among all elements. Therefore, the carbon atoms in fluorobenzene are positively charged due to the strong electron withdrawing effects of fluorine atoms. Because the π -system in pristine benzene is negatively charged, hexafluorobenzene and benzene molecules alternatively stack to form π -stacked columns in their co-crystals.¹⁷

Swager *et al.* reported tetracene derivatives **FTETa-d** in which a part of peripheral hydrogen atoms are replaced by fluorine atoms (Figure 10).¹⁸ All of **FTETa-d** formed π -stacked columnar structures in the crystalline states.

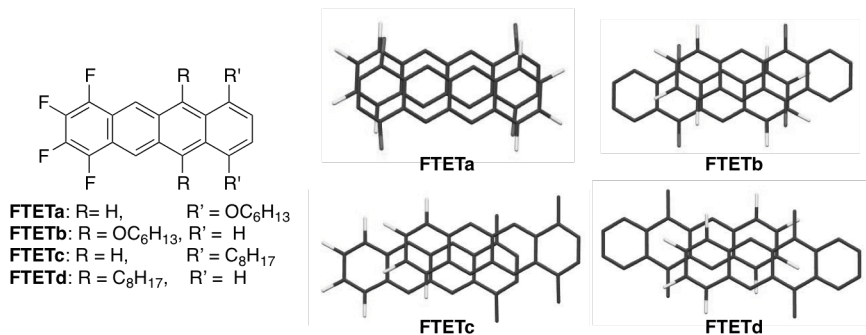


Figure 10. Molecular structures and packing structures of **FTETa-d**. Alkyl chains were omitted for clarity.

Okamoto and Matsuo developed the tetracene derivative (**FPPT**) in which the 5-position of a tetracene was substituted by a phenyl ring (Ph) and the 11-position was substituted by a perfluorophenyl ring (FPh) (Figure 11a).¹⁹ They expected two type of intermolecular interactions for this compound. One is the π - π interaction between the Ph and FPh moieties in the lateral direction. Another is CH–F interaction between the neighboring molecules in the vertical direction that is, π -stacked direction. In the crystalline state, the Ph and FPh moieties show π - π contact with the distance of 3.37 Å as well as CH–F interactions with the shortest distance of 2.40 Å (Figure 11b). As a result of these intermolecular interactions, tetracene skeletons form dense π -stacking with the distance of 3.30 to 3.35 Å (Figure 11c). Even though the hole mobility in the film of **FPPT** (4.2×10^{-2} cm²/Vs)²⁰ is not high, presumably due to the small π -overlapping, this report can be regarded as one of the successful examples for the control of molecular orientation by the intermolecular interactions.

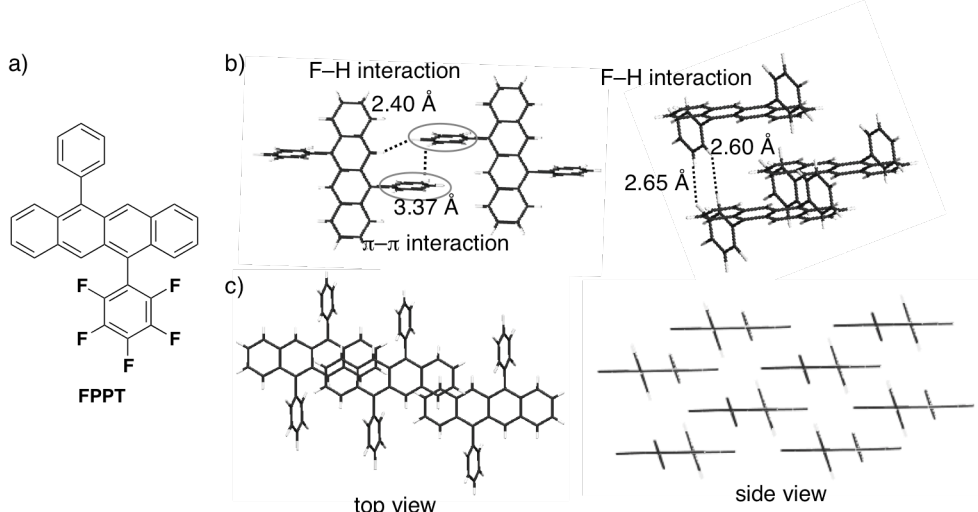


Figure 11. (a) Molecular structure, (b) intermolecular interactions between the neighboring molecules and (c) packing structures of **FPPT**.

• Introduction of Sulfur Containing Groups

Sulfur containing functional groups could be also used for the control of molecular orientation.

Kobayashi *et al.* reported methylthio substituted acene derivatives (Figure 12).²¹ In the crystalline state, these compounds form face-to-face π -stacking with intermolecular S–S interactions in the lateral directions or intermolecular S– π interactions along the π -stacked direction. They measured hole mobilities of tetracene derivatives (**STET**) and pentacene derivative (**SPNT**). Spin-coated films of **STET** and **SPNT** showed low hole

mobility of $4.0 \times 10^{-2} \text{ cm}^2/\text{Vs}$ and $1.3 \times 10^{-2} \text{ cm}^2/\text{Vs}$, respectively.

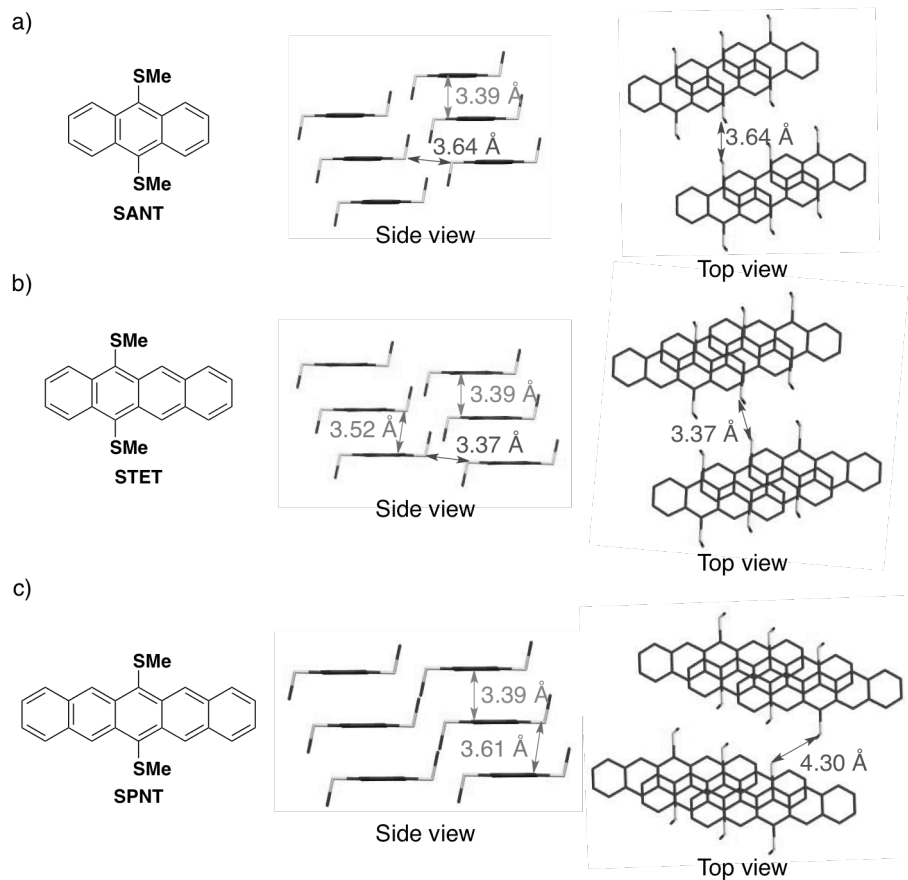


Figure 12. Molecular structures and packing structures of (a) **SANT**, (b) **STET**, and (c) **SPNT**, respectively.

Bao *et al.* developed hexathiapentacene (**HTPcr**) (Figure 13).²² This compound forms π -stacking by the suppression of CH- π interactions by the peripheral sulfur atoms. In addition, S-S interactions are shown between the neighboring molecules with S-S distances of 3.37–3.41 Å. These short S-S distances would be due to the positive charges on the outer S atoms and negative charges on the central S atoms. Hole mobility of this compound in the thin film was not high ($4.0 \times 10^{-2} \text{ cm}^2/\text{Vs}$), that might be explained by the charge trapping in the dipolar field between the zwitterions.

Whereas hole mobilities of sulfur-substituted derivatives are not high, sulfur or other calcogen atoms would be effective for the control of molecular orientation.

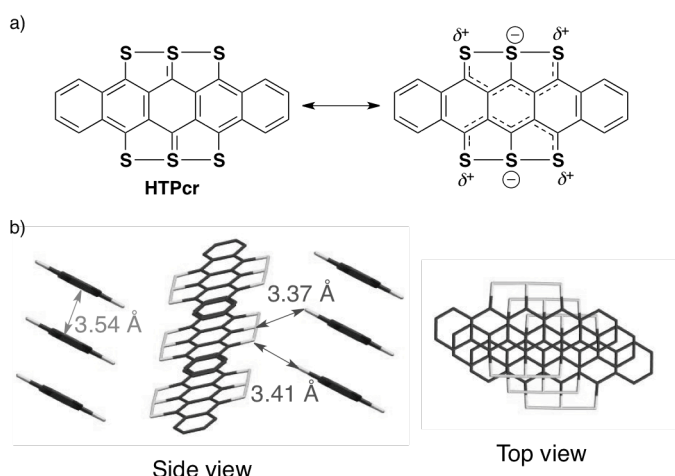


Figure 13. (a) Molecular structure and electronic state of **HTPcr**. (b) Packing structure of **HTPcr**.

Steric Effect

As another approach, Anthony *et al.* focused on the shape of substituents.

- **Control of Molecular Orientation by the Shape of Substituents**

They developed 6,13-bis(triisopropylsilyl)pentacene (**TIPS-PNT**) (Figure 14).²³ They envisioned in this compound that bulky substituents could suppress CH- π interaction between the neighboring molecules and the alkyne spacers would prevent to disrupt π -stacking of pentacene skeletons by the bulky substituents. In the crystalline state, **TIPS-PNT** forms two-dimensional columnar stacking, which is slipped to the longer axis of the skeletons. Arising from such molecular orientation, **TIPS-PNT** showed high hole mobility of $0.4 \text{ cm}^2/\text{Vs}$, which is comparable with non-substituted pentacene.²⁴

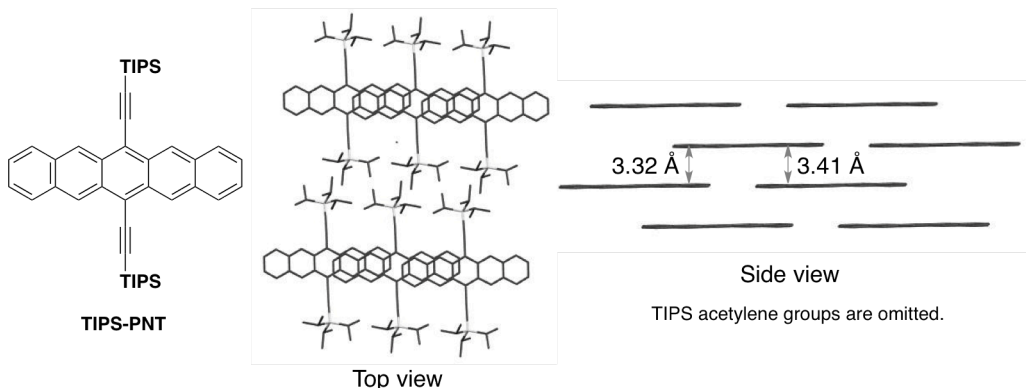


Figure 14. Molecular structures and packing structures of **TIPS-PNT**.

Based on these results, they examined size effects of the substituents in 6,13-substituted compounds.²⁵ Desired packing structure for effective overlapping of the π -skeletons is shown in Figure 15a. Considering the length for the longer axis of pentacene skeleton ($\sim 14 \text{ \AA}$), size of the substituents should be smaller than 7 \AA . Because the size of TIPS group is 7.5 \AA , they developed derivatives with smaller substituents than TIPS, such as *t*-Bu (***t*-Bu-PNT**) or trimethylsilyl (**TMS-PNT**). ***t*-Bu-PNT** forms not the desired packing structure but one-dimensional slipped stacking. By increasing the size of substituents to TMS, desired stacking structure was obtained.

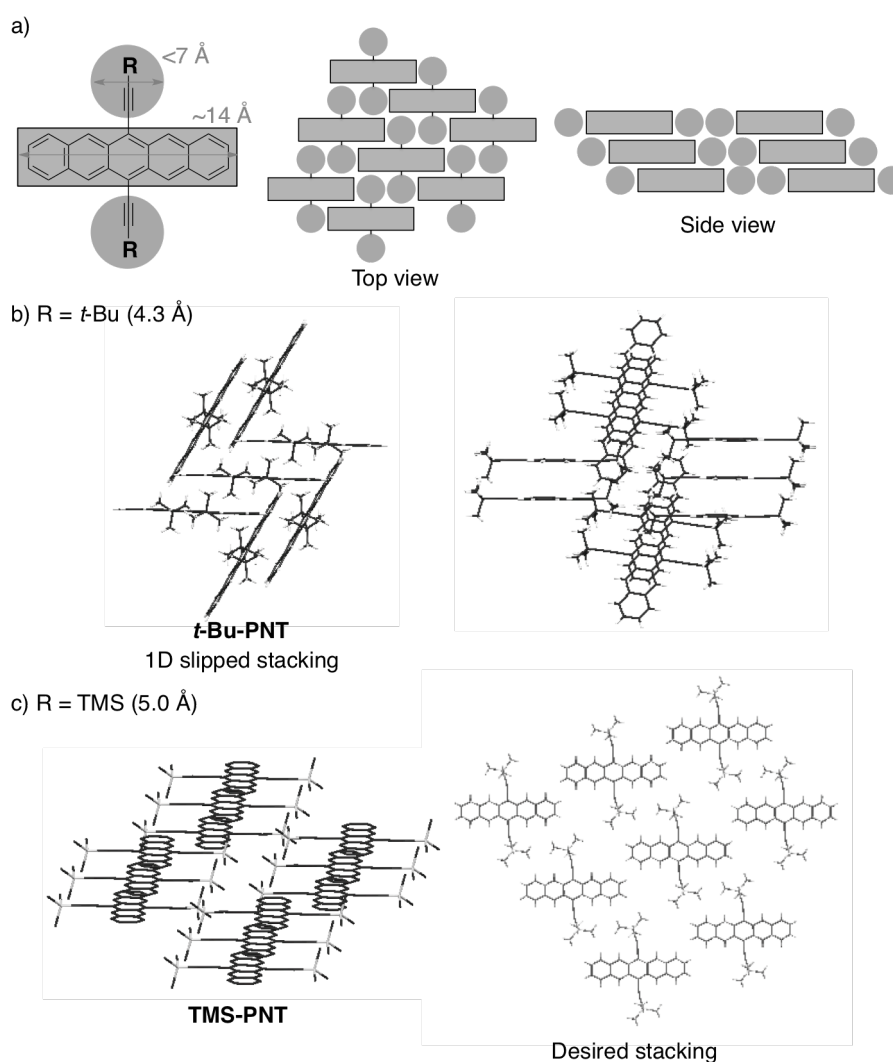


Figure 15. (a) Illustrations of desired packing structure. Packing structures of (b) ***t*-Bu-PNT** and (c) **TMS-PNT**.

Thus far, the attempts of controlling the molecular orientation in crystals are shown. In order to improve the performances in the organic devices, the direction of molecular orientation to the substrate is also important.

Direction of Charge Transport in the Organic Device

The directions of charge transport depend on the structures of each organic device. For example, OFETs require charge transport in the parallel direction to the substrates, whereas OLEDs and OPVs need that in the perpendicular direction (Figure 16). Therefore, the device performances can be improved by controlling the arrangement of molecules so as to show higher carrier mobility in the desired directions.

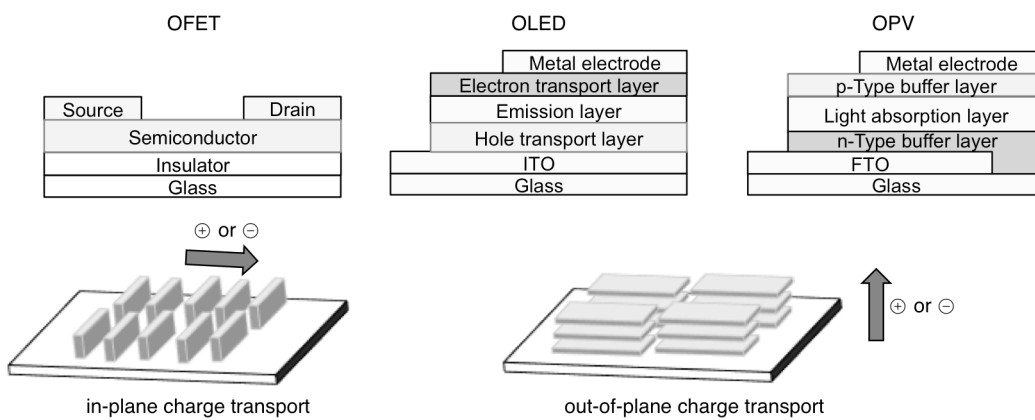


Figure 16. Device structures and directions for charge transport.

Control for the Direction of Molecular Orientation to the Substrate

Takimiya *et al.* succeeded in achieving the high hole mobility in parallel direction to the substrate by the control of molecular orientation. They developed dinaphtho[2,3-*b*:2',3'-*f*]thieno[3',2'-*b*]thiophene (**DNTT**) (Figure 17).²⁶ This compound forms herringbone stacking in the crystalline state. The maximum hole mobility of **DNTT** in the vacuum-deposited film on the Si/SiO₂ substrate measured by FET technique was 2.9 cm²/Vs.

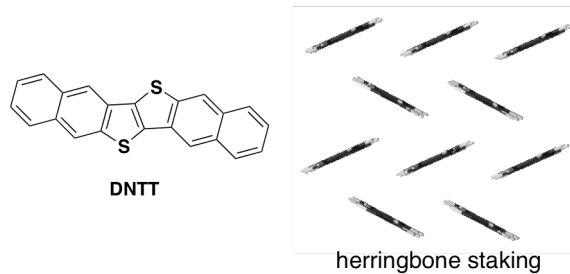


Figure 17. Molecular structure and packing structure of **DNTT**.

They also developed alkyl-substituted **DNTTs**. Alkyl chains show van der Waals interactions, especially, attractive interaction between the alkyl chains.²⁷ Therefore, alkyl-substituted compounds have a potential to form dense π -stacking. As long alkyl chains, hexyl, octyl, decyl or dodecyl chains were introduced into 2- and 9-position of **DNTT** (Figure 18).²⁸ Due to the stronger intermolecular interactions in alkyl-substituted **DNTTs**, all derivatives show bathochromic shifts of absorption from non-substituted **DNTT** in the vacuum-deposited films. The largest red-shifted absorption of **C₁₀-DNTT** suggests its strongest intermolecular interactions. The X-ray diffraction patterns indicated crystalline order of the molecules in the films and the molecules were found to be aligned perpendicular to the substrate.

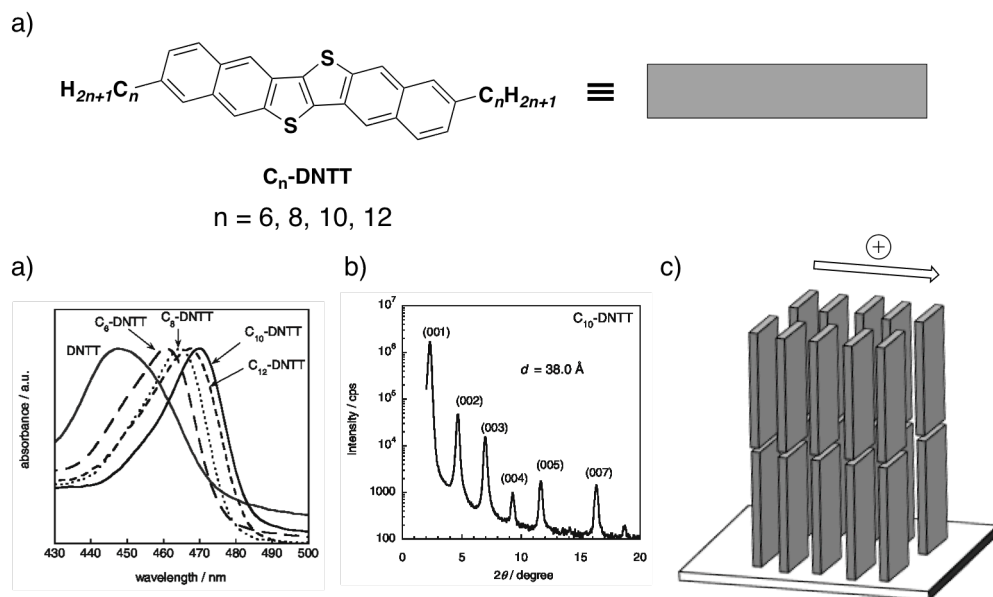


Figure 18. (a) Molecular structure of **C_n-DNTT**. (b) UV-vis absorption spectra for the vacuum-deposited films of **DNTT** and **C_n-DNTT**. (c) Out-of-plane XRD pattern of the vacuum-deposited film of **C₁₀-DNTT**. (d) Illustration of molecular orientation to the substrate estimated from XRD pattern.

As suggested from absorption spectra, C₁₀-DNTT exhibited the highest hole mobility of 3.7 cm²/Vs under the same condition. By treatment of the substrate, hole mobility of C₁₀-DNTT were improved to 7.9 cm²/Vs. Furthermore, C₁₀-DNTT exhibited the further higher mobility of 11 cm²/Vs by using a method of oriented growth to provide single crystalline film.²⁹

Molecular Orientation in the Amorphous Films

In the OPV and OLED devices, charge transport in the perpendicular direction is required. Organic semiconductors are generally used as the amorphous states in these devices. These molecules are assumed to form random orientation in the amorphous films. The examples of the studies on the molecular orientation in the amorphous states are still limited³⁰ because molecular orientations are usually not determined unambiguously.

Recently, some groups found the presence of ordered molecular orientation in the amorphous film to some extent even in the amorphous films. They reported the study on the influence of the molecular orientation on device performance.

Molecular Orientation in the Blend Films for Organic Photovoltaics

Osaka *et al.* studied the relationship between molecular orientation of p-type polymers and device performance of organic bulk-hetero junction solar cells using these polymers.³¹ They developed p-type polymers **PTzBT-14HD**, which are composed of alkylthiophene and thiazolothiazole as donor and as acceptor units, respectively (Figure 19). Two-dimensional grazing incidence X-ray diffraction (2D-GIXD) measurements revealed that different molecular orientations are observed in the polymer-only films and in the blend films with n-type material PC₆₁BM. In the polymer-only films, polymer forms edge-on orientations to the substrates. In contrast, the molecular orientations are changed to the face-on orientations in the blend films. The population of the face-on orientation is also affected by molecular weight of polymer. The maximum population of the face-on orientation is exhibited with a molecular weight of $M_n = 33$ kDa. By the formation of out-of-plane stacking of **PTzBT-14HD** with $M_n = 33$ kDa in the blend film, charge trapping or recombination before reaching the electrode would be prevented effectively and the highest solar cell power conversion efficiency (PCE) of 5.7% is exhibited.

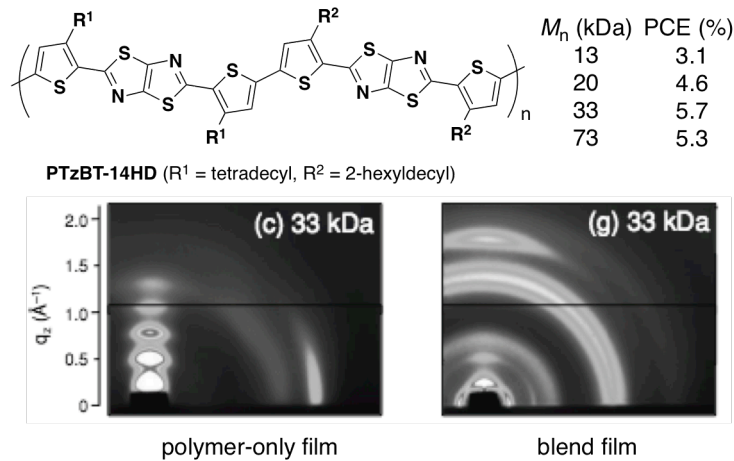


Figure 19. (a) Molecular structures of PTzBT-14HD. Molecular weights and power conversion efficiencies (PCEs) of solar cells were also shown. (b) Two-dimensional grazing incidence X-ray diffraction image of PTzBT-14HD with $M_n = 33$ kDa in the polymer-only film and the blend film.

Molecular Orientations in the Vacuum-Deposited Amorphous Films

In the OLED devices, triarylamine derivatives with a propeller-like structure, such as **TPD** and *N,N'*-di(1-naphthyl)-*N,N'*-diphenylbenzidine (**α-NPD**), are used as representative molecules.³²

In order to elucidate molecular orientation in the amorphous films, Yokoyama *et al.* conducted variable angle spectroscopic ellipsometry (VASE) measurements. Ellipsometry is an analytical method to examine the refractive indices (n) and the extinction coefficients (k), which depend on polarizability and transition dipole moment, respectively, from reflected elliptically polarized light (Figure 20). Because these parameters are influenced along with the longer molecular axis, if molecules are stacked in the perpendicular direction to the substrates, n and k of parallel direction become lower than those of perpendicular direction. They found that some compounds retains molecular orientation to some extent even in the amorphous films.³³

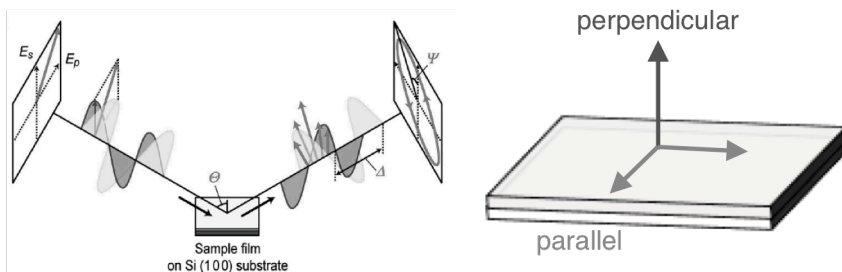


Figure 20. Schematic representation of variable angle spectroscopic ellipsometry measurement.

In vacuum-deposited films of **TPD** and **α -NPD**, the differences of n or k are small, suggesting random orientation of the molecules (Figure 21). In contrast, larger molecules (**TPD15** and **BSB-Cz**) show clear differences of these values between the directions to the substrates. The values of parallel direction are higher than those of perpendicular direction, suggesting horizontal molecular orientation of these molecules.

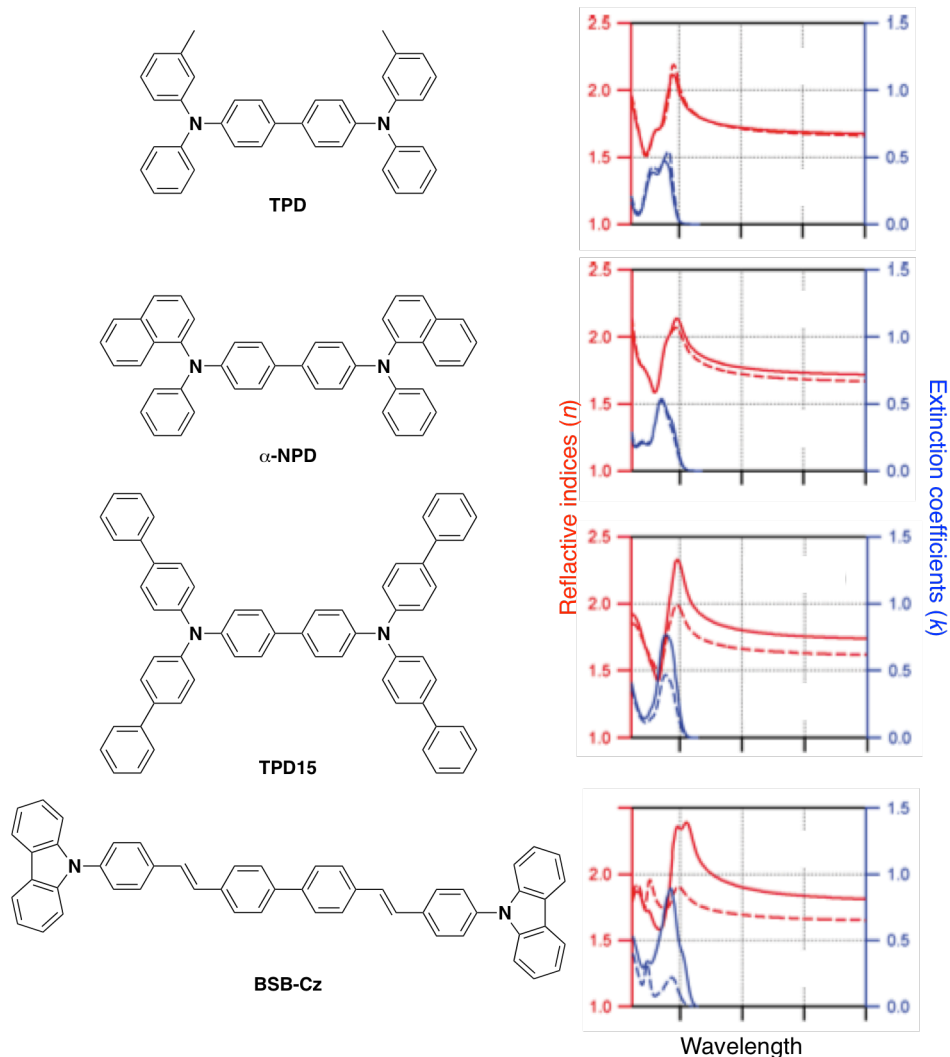


Figure 21. Molecular structures and anisotropies in the refractive indices (red) and the extinction coefficients (blue) of the vacuum-deposited films. The solid and dashed lines indicate the perpendicular and parallel components, respectively.

Further studies were conducted using **BSB-Cz** (Figure 22).³⁴ The vacuum-deposited films of **BSB-Cz** were prepared at the different substrate temperature of 25 °C and 90 °C. XRD measurements showed that both of these films retain amorphous states. On the other hand, the anisotropy of molecular orientation was found to become small in higher temperature. When the film was prepared at 90 °C, almost random orientation is observed. Arising from these differences of orientation, hole mobility measured by time-of-flight technique³⁵ for the film with horizontal orientation became 2.5 times higher than that with random orientation.

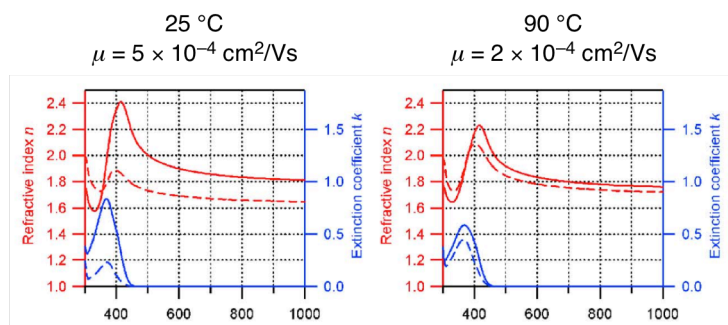


Figure 22. Anisotropies in the refractive indices (red) and the extinction coefficients (blue) of BSB-Cz in the vacuum-deposited films prepared at 25 °C and 90 °C. The hole mobilities are also shown.

As has been described above, many studies for control of molecular orientation to obtain high hole mobilities were conducted. However, the studies in the crystalline states were limited in functionalization of planar acene skeletons. In addition, the molecular design strategies to control molecular orientations in amorphous states do not exist. To develop excellent hole-transporting materials with high hole mobilities, development of the molecular design strategies is important.

Survey of This Thesis

As the π-conjugated skeletons for the charge-transporting materials to control molecular orientation in the solid states, the author focused on quasiplanar structure, which is slightly twisted from planar structure.³⁶ As a model compound for quasiplanar skeleton, partially oxygen-bridged triarylamine, in which three phenyl groups are constrained in a quasiplanar fashion by two oxygen-tethers, was designed and synthesized (Figure 23).

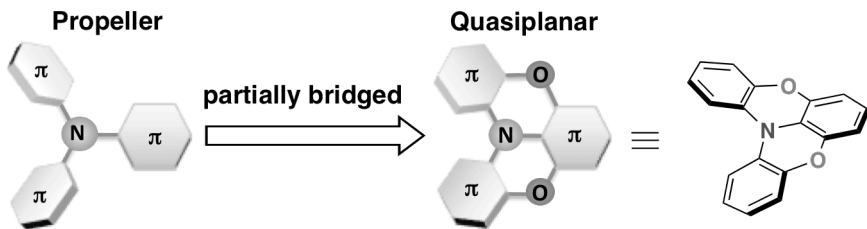


Figure 23. Molecular design aspects for quasiplanar structure.

The author envisioned that the use of quasiplanar scaffolds should be beneficial to provide: a) delocalized π -conjugation by enhanced planarity, and b) dense π -stacking in the solid state, arising from slightly twisted molecular structures. In addition, the dispersion in the direction of the C–H bonds in the lateral position of the quasiplanar molecules should decrease the contribution of the CH– π interactions between the neighboring molecules. Furthermore the inversion energy for the flipping of the two phenyl rings calculated at the B3LYP/6-31G(d) level was 9.1 kcal/mol, which indicates the easy flipping in solution or under sublimation conditions. These characters would facilitate the formation of on-top π -stacking in the solid state. In this thesis, the author developed new materials containing partially oxygen-bridged triarylamine skeletons and investigated their properties both in solution and in the solid states.

In Chapter 1, in order to investigate the relationship between quasiplanar skeleton and molecular orientation in the solid states, a series of partially oxygen bridged triarylamine dimers **1–4** were developed (Figure 24). In crystalline states, these dimers show a tendency to form one-dimensional on-top π -stacking. Furthermore, **1** and **2** retain the face-on π -stacking to some extent in the vacuum-deposited films, facilitating out-of-plane charge transport.

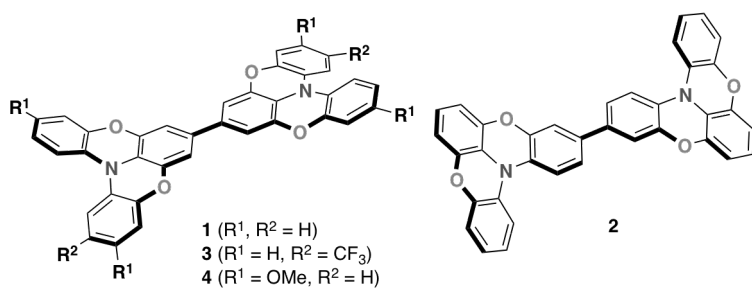


Figure 24. Molecular structures of oxygen-bridged triarylamine dimers.

Chapter 2 describes the investigation for influence of quasiplanar structures on the molecular orientation in the amorphous film prepared with oxygen-bridged triphenylamine dimers (Figure 25). Fluorescence spectroscopy revealed that these dimers retain two different states in the bulk films, that is, the monomer-like random orientation and crystalline-like π -stacking orientation. Arising from such orientations, these dimers exhibited bulk charge mobility derived from crystalline-like π -stacking structure in the amorphous films. When these dimers were used as a hole injection layer in OLED devices, the external quantum efficiencies were found to be superior to that of the standard device.

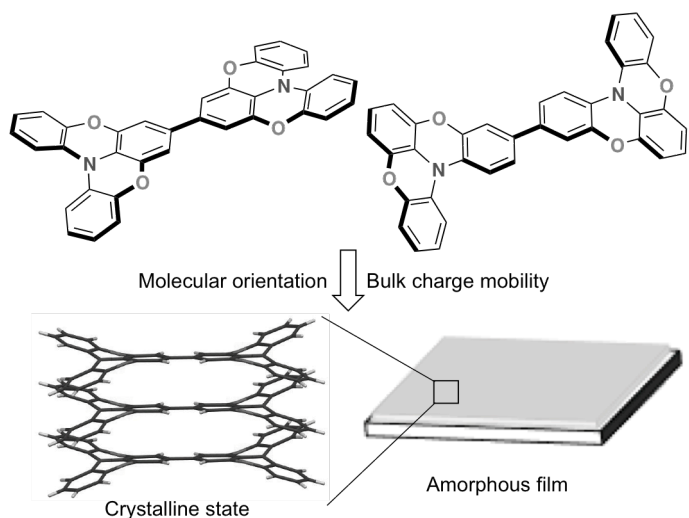


Figure 25. The influence of quasiplanar skeleton on the molecular orientation and the properties in the bulk film.

Chapter 3 describes the synthesis and properties of transparent hole-transporting materials using quasiplanar skeletons. In these compounds, oxygen-bridged triphenylamine skeletons are introduced into *meta*-positions of benzene rings (Figure 26). These compounds show absorption bands only in the UV region. In addition, these compounds exhibit excellent thermal stability for the amorphous films over 160 °C. Furthermore, these compounds exhibited comparable hole mobilities with oxygen-bridged triphenylamine dimer, studied in Chapter 2, for the vacuum-deposited films.

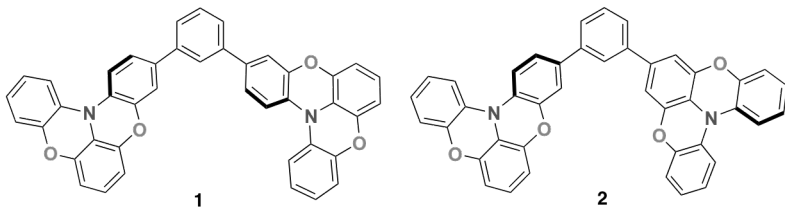


Figure 26. Molecular structures of *meta*-benzene linked oxygen-bridged triphenylamine derivatives.

In recent years, perovskite solar cells have been developed as new generation printable photovoltaics.³⁷ In these solar cells, organic hole-transporting materials (HTMs) are used in p-type buffer layer. Although many examples of HTMs were reported, 2,2',7,7'-tetrakis(*N,N*-di-*p*-methoxyphenylamine)-9,9'-spirobifluorene (Spiro-OMeTAD) is still used as standard hole-transporting material.

Chapter 4 describes the synthesis and properties of two-dimensionally expanded molecules, in which partially oxygen-bridged triarylamine skeletons are attached to a core skeleton, such as azulene or biphenyl (Figure 27). It is demonstrated that perovskite solar cells using new HTM **1** exhibited higher PCEs than those using conventional HTM. Furthermore, the key factors to exhibit high device performance were elucidated.

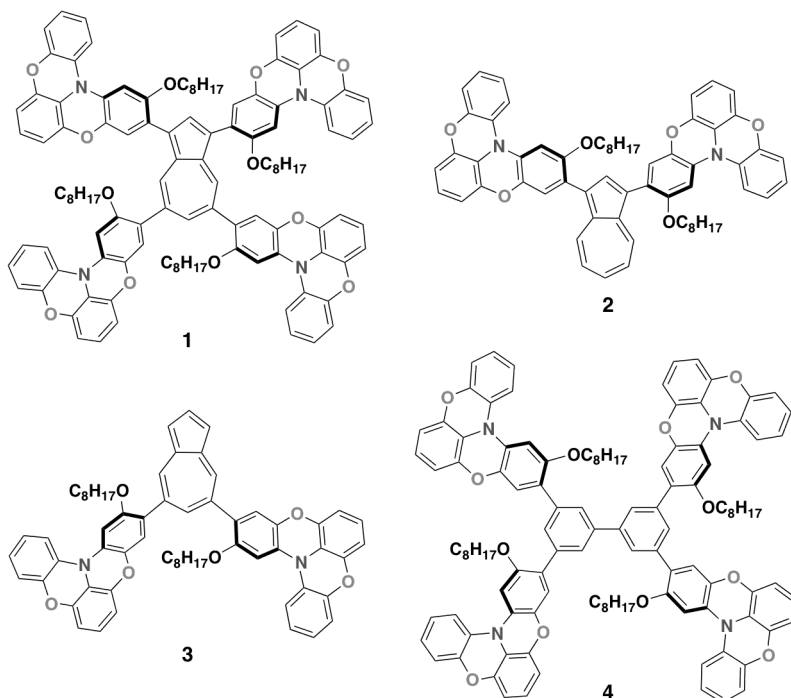


Figure 27. Molecular structures of hole-transporting materials for perovskite solar cells.

In Chapters 1–4, the author focused on the flexibility of non-bridged rings in partially oxygen-bridged triarylamine skeletons to control molecular orientation and developed charge-transporting materials. From a different point of view, the author focused on helical structure that can be formed by the replacement of one phenyl ring to a naphthyl ring in oxygen-bridged triarylamine skeleton (Figure 28).

In Chapter 5, oxygen-bridged diphenylnaphthylamine derivatives were developed as CPL materials.³⁸ These compounds exhibit CPL signals with dissymmetry factor (*g* value) of $\sim 10^{-3}$ both in solution and the solid states. Furthermore, the author demonstrated the utility of oxygen-bridged diphenylnaphthylamine as a scaffold for emission-color-tunable CPL materials. In this system, the deflection in the frontier orbitals induces intramolecular charge transfer characters, which enables tuning of the emission colors from blue to deep-red by substituent effects or the solvent effects.

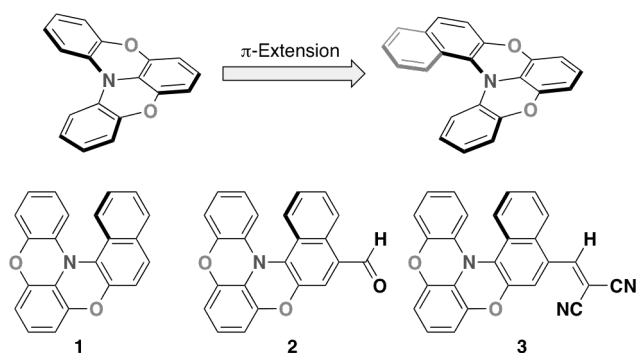


Figure 28. Molecular design for the color tunable CPL materials.

Reference

1. (a) Facchetti, A. *Mater. Today* **2007**, *10*, 28. (b) Anthony, J. E. *Angew. Chem., Int. Ed.* **2008**, *47*, 452. (c) Klauk, H. *Chem. Soc. Rev.* **2010**, *39*, 2643. (d) Wang, C.; Dong, H.; Hu, W.; Liu, Y.; Zhu, D. *Chem. Rev.* **2012**, *112*, 2208. (e) Torsi, L.; Magliulo, M.; Manoli, K.; Palazzo, G. **2013**, *42*, 8612. (f) Sirringhaus, H. *Adv. Mater.* **2014**, *26*, 1319.
2. (a) Shirota, Y. *J. Mater. Chem.* **2000**, *10*, 1. (b) Shirota, Y.; Kageyama, H. *Chem. Rev.* **2007**, *107*, 953. (c) Xiao, L.; Chen, Z.; Qu, B.; Luo, J.; Kong, S.; Gong, Q.; Kido, J. *Adv. Mater.* **2011**, *23*, 926. (d) Chen, Y.; Ma, D. *J. Mater. Chem.* **2012**, *22*, 18718. (e) Jou, J.-H.; Kumar, S.; Agrawal, A.; Li, T.-H.; Sahoo, S. *J. Mater. Chem.*

C **2015**, *3*, 2974.

3. (a) Hoppe, H.; Sariciftci, N. S. *J. Mater. Res.* **2004**, *19*, 1924. (b) Walker, B.; Kim, C.; Nguyen, T.-Q. *Chem. Mater.* **2011**, *23*, 470. (c) Facchetti, A. *Chem. Mater.* **2011**, *23*, 733. (d) Mishra, A.; Bäuerle, P. *Angew. Chem., Int. Ed.* **2012**, *51*, 2020. (e) Kularatne, R. S.; Magurudeniya, H. D.; Sista, P.; Biewer, M. C.; Stefan, M. C. *J. Polym. Sci., Part A: Polym. Chem.* **2013**, *51*, 743. (f) Cao, W.; Xue, J. *Energy Environ. Sci.* **2014**, *7*, 2123.
4. Akamatsu, H.; Inokuchi, H.; Matsunaga, Y. *Nature* **1954**, *173*, 168.
5. (a) Ferraris, J.; Cowan, D. O.; Walatka, V.; Perlstein, J. H. *J. Am. Chem. Soc.* **1973**, *95*, 948. (b) Coleman, L. B.; Cohen, M. J.; Sandman, D. J.; Yamaguchi, F. G.; Garito, A. F.; Heeger, A. J. *Solid State Commun.* **1973**, *12*, 1125.
6. Shirakawa, H.; Louis, E. J.; MacDiomid, A. G.; Chiang, C. K.; Heeger, A. J. *J. Chem. Soc., Chem. Commun.* **1977**, 578.
7. (a) Machida, S.; Nakayama, Y.; Duhm, S.; Xin, Q.; Funakoshi, A.; Ogawa, N.; Kera, S.; Ueno, N.; Ishii, H. *Phys. Rev. Lett.* **2010**, *104*, 156401. (b) Yamagishi, M.; Soeda, J.; Uemura, T.; Okada, Y.; Takatsuki, Y.; Nishikawa, T.; Nakazawa, T.; Nakazawa, Y.; Doi, I.; Takimiya, K.; Takeya, J. *Phys. Rev. B* **2010**, *81*, 161306. (c) Okada, Y.; Sakai, K.; Uemura, T.; Nakazawa, Y.; Takeya, J. *Phys. Rev. B* **2011**, *84*, 245308. (d) Kobayashi, H.; Kobayashi, N.; Hosoi, S.; Koshitani, N.; Murakami, D.; Shirasawa, R.; Kudo, Y.; Hobara, D.; Tokita, Y.; Itabashi, M. *J. Chem. Phys.* **2013**, *139*, 014707. (e) Mitsui, C.; Okamoto, T.; Yamagishi, M.; Tsurumi, J.; Yoshimoto, K.; Nakahara, K.; Soeda, J.; Hirose, Y.; Sato, H.; Yamano, A.; Uemura, T.; Takeya, J. *Adv. Mater.* **2014**, *26*, 4546.
8. (a) Marcus, R. A. *J. Chem. Phys.* **1956**, *24*, 966. (b) Marcus, R. A.; Sutin, N. *Biochem. Biophys. Acta.* **1985**, *811*, 265.
9. (a) da Silva Filho, D. A.; Kim, E.-G.; Bredas, J.-L. *Adv. Mater.* **2005**, *17*, 1072. (b) Coropceanu, V.; Cornil, J.; da Silva Filho, D. A.; Olivier, Y.; Silbey, R.; Bredas, J.-L. *Chem. Rev.* **2007**, *107*, 926.
10. (a) Goldmann, C.; Haas, S.; Krellner, C.; Pernstich, K. P.; Gundlach D. J.; Batlogg, B. *J. Appl. Phys.* **2004**, *96*, 2080. (b) Ciciora, F.; Santato, C.; Dinelli, F.; Murgia, M.; Loi, M. A.; Biscarini, F.; Zamboni, R.; Heremans, P.; Muccini, *Adv. Funct. Mater.* **2005**, *15*, 375. (c) Jurchescu, O. D.; Popinciuc, M.; van Wees, B. J.; Palstra, T. T. M. *Adv. Mater.* **2007**, *19*, 688. (d) Yang, H.; Shin, T. J.; Ling, M.-M.; Cho, K.; Ryu, C. Y.; Bao, Z. *J. Am. Chem. Soc.* **2005**, *127*, 11542.
11. Mondal, R.; Adhikari, R. M.; Shah, B. K.; Neckers, D. C. *Org. Lett.* **2007**, *9*, 2505.

12. Watanabe, M.; Chang, Y. J.; Liu, S.-W.; Chao, T.-H.; Goto, K.; Islam, M. M.; Yuan, C.-H.; Tao, Y.-T.; Shimmyozu, T.; Chow, T. J. *Nat. Chem.* **2012**, *4*, 574.
13. Sarma, J. A. R. P.; Desiraju, G. R. *Acc. Chem. Res.* **1986**, *19*, 222.
14. Moon, H.; Zeis, R.; Borkent, E.-J.; Besnard, C.; Lovinger, A. J.; Siegrist, T.; Kloc, C.; Bao, Z. *J. Am. Chem. Soc.* **2004**, *126*, 15322.
15. Chi, X.; Li, D.; Zhang, H.; Chen, Y.; Garcia, V.; Garcia, C.; Siegrist, T. *Org. Electron.* **2008**, *9*, 234.
16. Takeya, J.; Yamagishi, M.; Tominari, Y.; Hirahara, R.; Nakazawa, Y.; Nishkawa, T.; Kawase, T.; Shimoda, T.; Ogawa, S. *Appl. Phys. Lett.* **2007**, *90*, 102120.
17. Williams, J. H. *Acc. Chem. Res.* **1993**, *26*, 593.
18. Chen, Z.; Müller, P.; Swager, T. M. *Org. Lett.* **2006**, *8*, 273.
19. Okamoto, T.; Nakahara, K.; Saeki, A.; Seki, S.; Oh, J. H.; Akkerman, H. B.; Bao, Z.; Matsuo, Y. *Chem. Mater.* **2011**, *23*, 1646.
20. Zhang, B.; Kan, Y.-H.; Geng, Y.; Duan, Y.-A.; Li, H.-B.; Hua, J.; Su, Z.-M. *Org. Electron.* **2013**, *14*, 1359.
21. (a) Kobayashi, K.; Masu, H.; Shuto, A.; Yamaguchi, K. *Chem. Mater.* **2005**, *17*, 6666. (b) Kobayashi, K.; Shimaoka, R.; Kawahata, M.; Yamanaka, M.; Yamaguchi, K. *Org. Lett.* **2006**, *8*, 2385. (c) Kimoto, T.; Tanaka, K.; Kawahara, M.; Yamaguchi, K.; Otsubo, S.; Sakai, Y.; Ono, Y.; Ohno, A.; Kobayashi, K. *J. Org. Chem.* **2011**, *76*, 5018.
22. Briseno, A. L.; Miao, Q.; Ling, M.-M.; Reese, C.; Meng, H.; Bao, Z.; Wudl, F. *J. Am. Chem. Soc.* **2006**, *128*, 15576.
23. Anthony, J. E.; Brooks, J. S.; Eaton, D. L.; Parkin, S. R. *J. Am. Chem. Soc.* **2001**, *123*, 9482.
24. Sheraw, C. D.; Jackson, T. N.; Eaton, D. L.; Anthony, J. E. *Adv. Mater.* **2003**, *15*, 2009.
25. Anthony, J. E.; Eaton, D. L.; Parkin, S. R. *Org. Lett.* **2002**, *4*, 15.
26. Yamamoto, T.; Takimiya, K. *J. Am. Chem. Soc.* **2007**, *129*, 2224.
27. Inokuchi, H.; Saito, G.; Wu, P.; Seki, K.; Tang, T. B.; Mori, T.; Imaeda, K.; Enoki, T.; Higuchi, Y.; Inaka, K.; Yasuoka, N. *Chem. Lett.* **1986**, *8*, 1263.
28. Kang, M. J.; Doi, I.; Mori, H.; Miyazaki, E.; Takimiya, K.; Ikeda, M.; Kuwabara, H. *Adv. Mater.* **2011**, *23*, 1222.
29. Nakamura, K.; Hirome, Y.; Soeda, J.; Yoshiwumi, M.; Uemura, T.; Uno, M.; Li, W.; Kang, M. J.; Yamagishi, M.; Okada, Y.; Miyazaki, E.; Nakazawa, Y.; Nakao, A.; Takimiya, K.; Takeya, J. *Adv. Mater.* **2011**, *23*, 1626.

30. (a) Gao, H. *Theor. Chem. Acc.* **2010**, *127*, 759. (b) Yamada, T.; Sato, T.; Tanaka, K.; Kaji, H. *Org. Electron.* **2010**, *11*, 255. (c) Kaji, H.; Yamada, T.; Tsukamoto, N.; Horii, F. *Chem. Phys. Lett.* **2005**, *401*, 246. (d) Yamada, T.; Kaji, H. *J. Mol. Struc.* **2009**, *927*, 82. (e) Sugiyama, T.; Furukawa, Y.; Fujimura, H. *Chem. Phys. Lett.* **2005**, *405*, 330.
31. Osaka, I.; Saito, M.; Mori, H.; Koganezawa, T.; Takimiya, K. *Adv. Mater.* **2012**, *24*, 425.
32. Shirota, Y.; Kageyama, H. *Chem. Rev.* **2007**, *107*, 953.
33. (a) Yokoyama, D.; Sakaguchi, A.; Suzuki, M. Adachi, C. *Appl. Phys. Lett.* **2008**, *93*, 173302. (b) Yokoyama, D.; Sakaguchi, A.; Suzuki, M. Adachi, C. *Org. Electron.* **2009**, *10*, 127.
34. (a) Yokoyama, D.; Adachi, C. *J. Appl. Phys.* **2010**, *107*, 123512. (b) Yokoyama, D.; Setoguchi, Y.; Sakaguchi, A.; Suzuki, M. Adachi, C. *Adv. Funct. Mater.* **2010**, *20*, 386.
35. (a) Kepler, R. G. *Phys. Rev.* **1960**, *119*, 1226. (b) Leblanc, O. H. *J. Chem. Phys.* **1960**, *33*, 626. (c) Gill, W. D. *J. Appl. Phys.* **1972**, *43*, 5033.
36. Kuratsu, M.; Kozaki, M.; Okada, K. *Chem. Lett.* **2004**, *33*, 1174.
37. (a) Kim, H. S.; Lee, C. R.; Im, J. H.; Lee, K. B.; Moehl, T.; Marchioro, A.; Moon, S. J.; Humphry-Baker, R.; Yum, J. H.; Moser, J. E.; Grätzel, M.; Park, N.-G. *Sci. Rep.* **2012**, *2*, 591. (b) Stranks, S. D.; Eperon, G. E.; Grancini, G.; Menelaou, C.; Alcocer, M. J. P.; Leijtens, T.; Herz, L. M.; Petrozza, A.; Snaith, H. J. *Science* **2013**, *342*, 341. (c) Xing, G.; Mathews, N.; Sun, S.; Lim, S. S.; Lam, Y. M.; Grätzel, M.; Mhaisalkar, S.; Sum, T. C. *Science* **2013**, *342*, 344. (d) Gao, P.; Grätzel, M.; Nazeeruddin, M. K. *Energy Environ. Sci.* **2014**, *7*, 2448. (e) Miyasaka, T. *Chem. Lett.* **2015**, *44*, 720. (f) Jung, H. S.; Park, N.-G. *Small* **2015**, *11*, 10. (g) Luo, S.; Daoud, W. A. *J. Mater. Chem. A* **2015**, *3*, 8992. (h) Yu, Z.; Sun, L. *Adv. Energy Mater.* **2015**, *5*, 1500213.
38. (a) Riehl, J. P.; Richardson, F. S. *J. Chem. Phys.* **1976**, *65*, 1011. (b) Richardson, F. S.; Riehl, J. P. *Chem. Rev.* **1977**, *77*, 773. (c) Riehl, J. P. *Chem. Rev.* **1986**, *86*, 1. (d) Carr, R.; Evans, N. H.; Parker, D. **2012**, *41*, 7673. (e) Watanabe, K.; Akagi, K. *Sci. Technol. Adv. Mater.* **2014**, *15*, 044203. (f) Sánchez-Carnerero, E. M.; Agarrabeitia, A. R.; Moreno, F.; Maroto, B. L.; Muller, G.; Ortiz, M. J.; de la Moya, S. *Chem. Eur. J.* **2015**, *21*, 13488.

Chapter 1

On-top π -Stacking of Quasiplanar Molecules in Hole-Transporting Materials: Inducing Anisotropic Carrier Mobility in Amorphous Films

Abstract: As hole-transporting materials, dimers of partially oxygen-bridged triarylaminies were designed and synthesized. X-ray structural analyses revealed that these compounds form on-top π -stacking aggregates in the crystalline state. TRMC measurements exhibited that anisotropic charge-transporting properties were induced in direction of the π -stacking. Interestingly, these compounds retained some of the face-on π -stacking even in the vacuum-deposited amorphous films, thus facilitating an out-of-plane carrier mobility.

Introduction

As mentioned in General Introduction, it is important to develop excellent charge transporting materials with high charge mobility for the achievement of high performance organic devices, e.g., organic field-effect transistors (OFETs),¹ organic light-emitting diodes (OLEDs),² and organic photovoltaics (OPVs).³ In the charge transport of the organic compounds in the bulk, the interaction between neighbor molecules should be crucial because of the limited size of the molecules.⁴ In the molecular design of these materials, it is therefore important not only to control the π -electronic structure for tuning the HOMO and LUMO levels and lowering of the reorganization energy (λ), but also to control the packing structure in the solid state to facilitate large electronic coupling (V).

Acenes, such as pentacene or tetracene, are widely used in OFETs as typical charge-transporting materials, because of their rigid π -conjugated skeletons with high planarity. In the solid state, pentacene adopts a herringbone structure with a tilted molecular arrangement, which is derived from not only π - π interactions but also the presence of CH- π interactions (electrostatic interaction).⁵ For a molecular design to prevent CH- π interactions, introducing substituents in the peri-position of acenes or increasing the C/H ratio in the ring-fused aromatic compounds can be an effective strategy, which would lead to the formation of a better packing motif for charge mobility.^{2,6} However, molecular design approaches that allow effective control over the molecular orientation in the solid state remain limited.

Representative examples for hole-transporting materials used in OLEDs are triarylamines with propeller-like structures, such as *N,N'*-di(1-naphthyl)-*N,N'*-diphenylbenzidine (α -NPD)^{7a} and *N,N'*-diphenyl-*N,N'*-di(*m*-tolyl)benzidine (TPD) (Figure 1).^{7b} These materials are used as amorphous films. Therefore, the conformations of individual molecules as well as of their aggregates have not been determined unambiguously, thus rendering precise molecular design difficult.⁸ Accordingly, the elucidation of the exact relationship between the molecular orientation in the crystalline and amorphous state remains a key challenge to be addressed in the development of advanced charge transporting materials.

In this chapter, the author examines the effects of partially bridged triarylamine skeletons for charge transporting materials. As the model compounds, a series of partially oxygen-bridged triarylamine dimers **1–4** (Figure 1) was designed and synthesized. The properties of **1–4** were examined both in solution and the solid state. In addition, the relationship between the packing structures and charge transport properties of **1** and **2** were investigated in detail. The author demonstrates that **1** and **2**

exhibit anisotropic charge transport properties both in the crystalline and vacuum-deposited film.

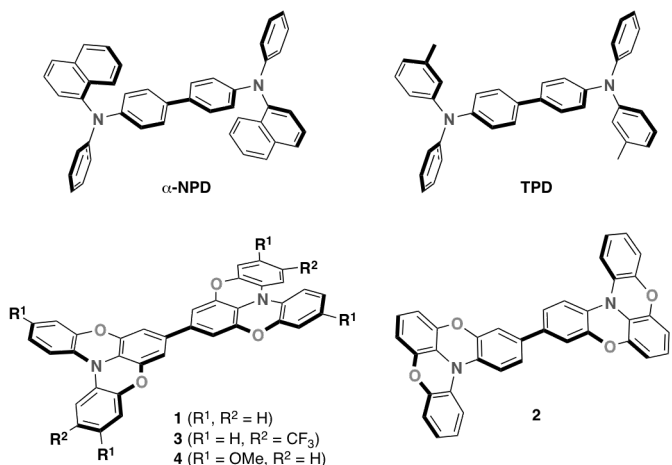
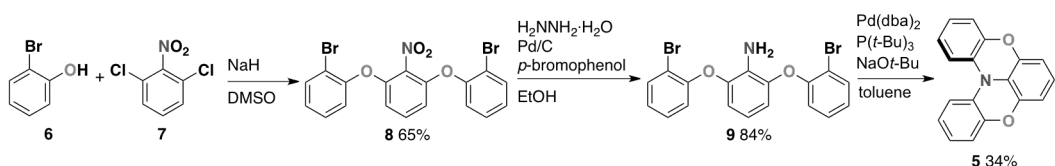


Figure 1. Molecular structures of α -NPD, TPD, and partially oxygen-bridged triarylamine dimers **1–4**.

Results and Discussion

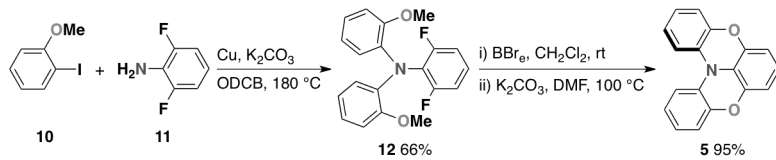
Synthesis

Regarding the construction of oxygen-bridged triarylamine skeleton, Okada *et al.* had reported the synthesis of partially oxygen-bridged **5** by intermolecular nucleophilic aromatic substitution followed by intramolecular arylation to nitrogen center, as shown in Scheme 1.⁹



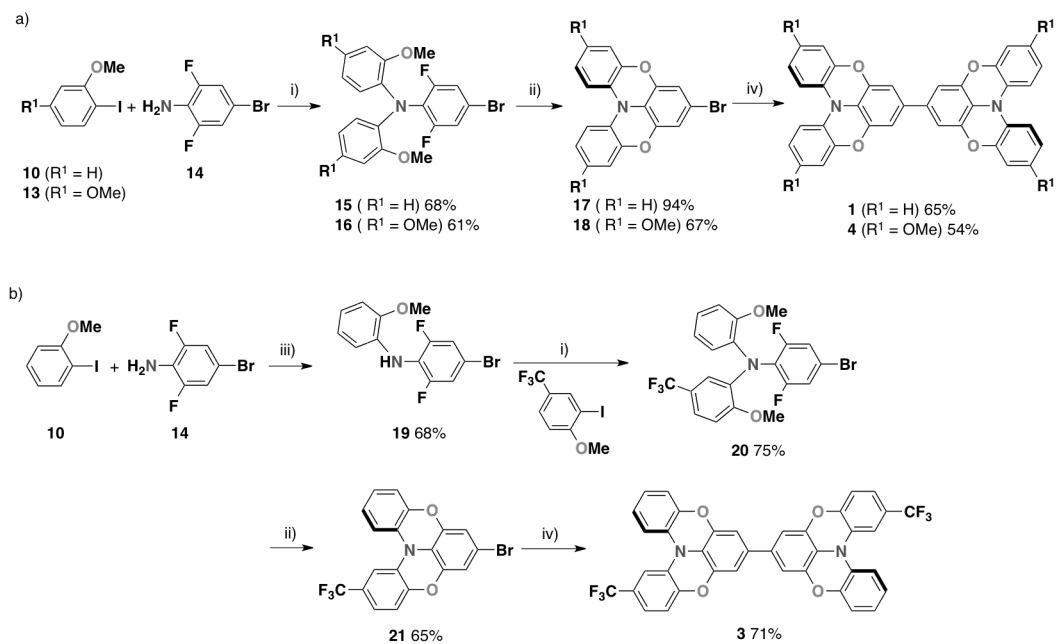
Scheme 1.

The author's synthetic strategy for this skeleton was to use intramolecular nucleophilic aromatic substitution as the key reaction as shown in Scheme 2. Ullmann reactions of **10** with **11** gave compound **12** in 66% yield.¹⁰ After removal of the protecting methyl groups in **12** by treatment with BBr_3 , subsequent treatment with K_2CO_3 in DMF at 100 °C afforded the cyclized product **5** in 95% yield. This synthetic route is straightforward, based on commercially available starting materials, and can be easily scaled up.



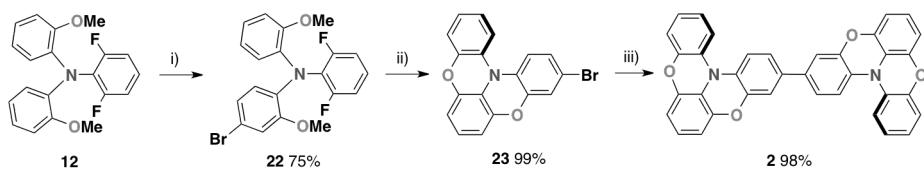
Scheme 2.

This reaction can be applied to the synthesis of the other derivatives using adequate starting materials. Thus, the use of 4-bromo-2,6-difluoroaniline **14** instead of **11** gave the substituted derivative **17**. In a similar manner, the use of 1-iodo-2,4-dimethoxybenzene **13** gave the methoxy derivative **18** (Scheme 3a). Our synthetic route also enables the synthesis of asymmetric derivative **21** by the combination of two successive coupling reactions of **14** with different aryl rings. Thus, Pd⁰-catalyzed arylation of **14** with **10** gave selectively the monoarylated derivative **19** in 68% yield (Scheme 3b). Subsequently, Ullmann arylation of **19** with 1-iodo-2-methoxy-4-(trifluoromethyl)biphenyl afforded **20** in 75 % yield. The double cyclization of compound **20** gave the asymmetric derivative **21** in 65% yield. Homocoupling¹¹ of the obtained bromo-derivatives of **17**, **18**, and **21** yielded dimers **1**, **3**, and **4** (54–71%) as pale yellow solids, respectively.



Scheme 3. Reagents/conditions: i) Cu, K₂CO₃, *o*-dichlorobenzene, 180 °C; ii) 1. BBr₃, CH₂Cl₂, 2. K₂CO₃, DMF, 100 °C, (then CH₃I, 60 °C for **18**); iii) Pd₂(dba)₃·CHCl₃, P(*t*-Bu)₃, NaOt-Bu, toluene, 100 °C; iv) Ni(cod)₂, bipyridine, COD, THF, 60 °C.

Dimer **2**, in which the partially oxygen-bridged triphenylamine unit connected at the different position from that of **1**, was also prepared by this method (Scheme 4). Bromination of non-cyclized triarylamine **12** with 1 equiv NBS was found to give monobrominated derivative **22**, selectively. Subsequently, two-fold cyclization of **22** afforded monobrominated quasiplanar derivative **23** in almost quantitative yield. Finally, homocoupling reaction of **23** yielded dimer **2** as pale yellow solids in 98% yield. The obtained dimers **1–4** were characterized by NMR, HRMS, and elemental analysis.



Scheme 4. Reagents/conditions: i) NBS (1 equiv), $\text{CHCl}_3/\text{AcOH}$, ii) 1. BBr_3 , CH_2Cl_2 , 2. K_2CO_3 , DMF , 100°C ; iii) $\text{Ni}(\text{cod})_2$, bipyridine, COD , THF , 60°C .

Thermal Property

The thermal stability is one of the important properties for organic semiconductors. Thermogravimetric analysis (TGA) showed that **1–4** have high decomposition temperatures (T_{d5}) between 408 and 449°C , indicating their considerable thermal stability (Figure 2).

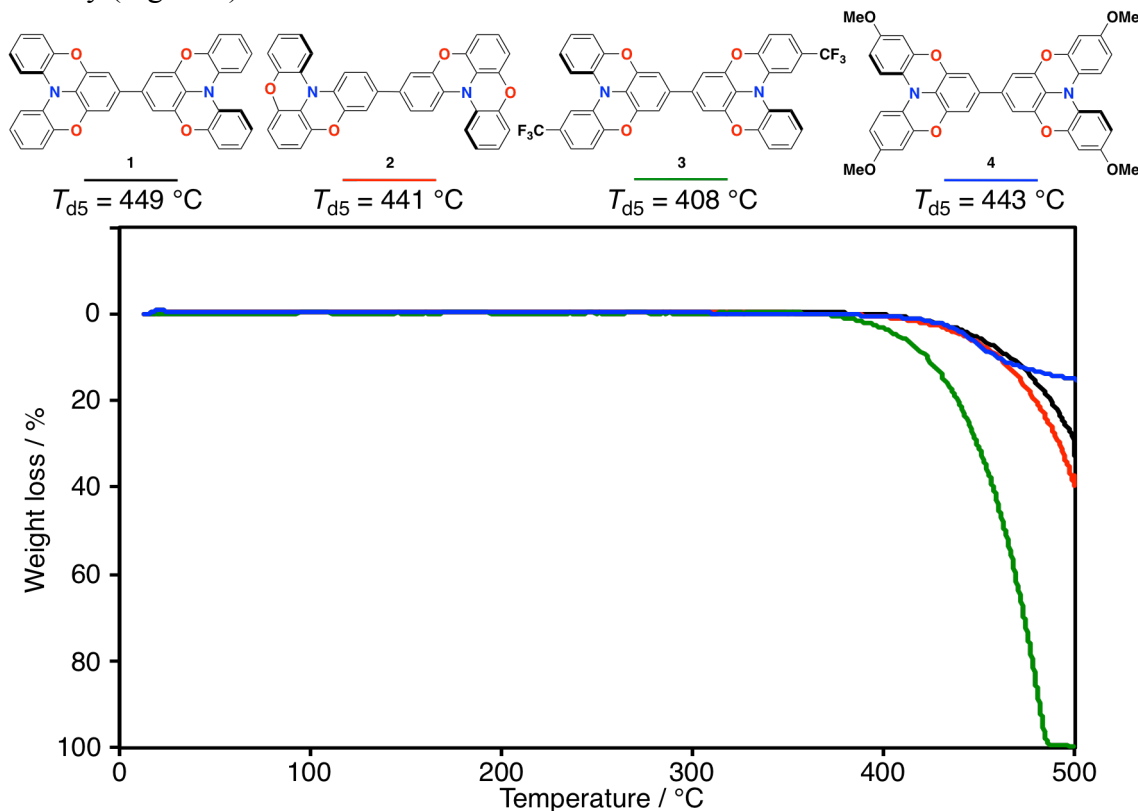


Figure 2. Thermogravimetric analysis of **1–4** heating at $15^\circ\text{C}/\text{min}$ under N_2 .

Since the organic compounds are used as amorphous states in OLED devices, their amorphous stability is also important property. Differential scanning calorimetry (DSC) measurement was conducted on dimers **1–4**. While dimers **1**, **3** and **4** show moderate glass transition temperatures ($T_g = 34\text{--}64\text{ }^\circ\text{C}$), dimer **2** exhibits a significant high T_g ($123\text{ }^\circ\text{C}$), which reflects the lower symmetry resulting from the different connection motif between the triarylamine moieties in **2** relative to **1** (Figure 3). The T_g of **2** is also higher than those of conventional amorphous hole-transporting materials, TPD ($65\text{ }^\circ\text{C}$) and α -NPD ($96\text{ }^\circ\text{C}$),¹² suggesting an excellent stability in amorphous state of **2**.

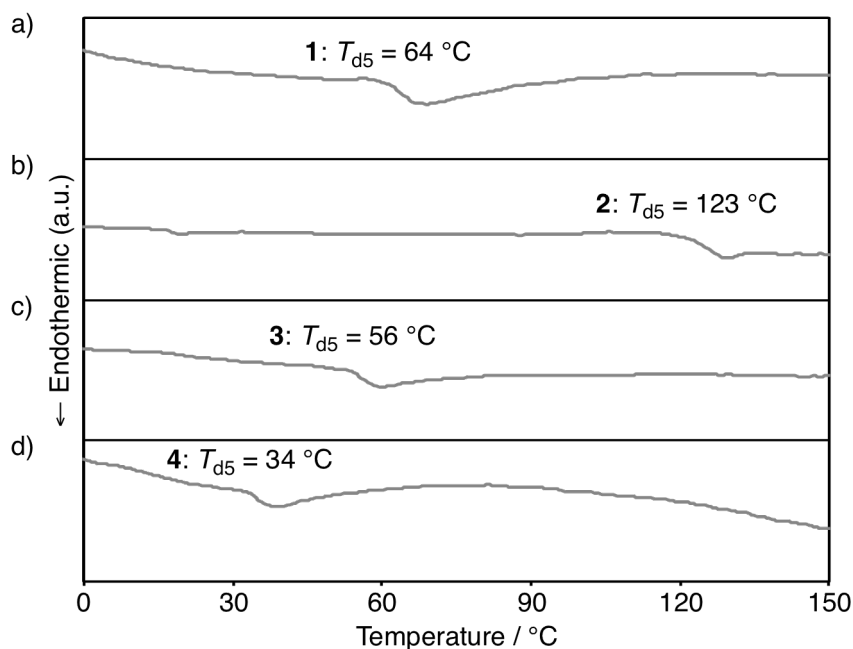


Figure 3. Differential scanning calorimetry of a) **1**, b) **2**, c) **3**, and d) **4**, heating at $10\text{ }^\circ\text{C}/\text{min}$ under N_2 .

Electrochemical Property

To examine the electrochemical properties, cyclic voltammetry (CV) was conducted on **1–4** in CH_2Cl_2 . Cyclic voltammograms for **1–4** show reversible multi-step oxidation waves as shown in Figure 4, suggesting the formation of stable cationic species under the conditions applied. The difference in connecting position does not affect the first oxidation potential (**1**, $+0.25\text{ V}$ (vs Fc/Fc^+); **2**, $+0.23\text{ V}$) significantly, whereas the introduction of electron-withdrawing group (CF_3), or electron-donating group (OMe) shifts the first oxidation potentials in positive (**3**, $+0.41\text{ V}$) or negative (**4**, $+0.02\text{ V}$) direction. According to the equation $\text{HOMO} = -(E_{\text{onset}} + 5.10\text{ eV})^{13}$, the HOMO levels of **1–4** were estimated to be -5.26 eV , -5.25 eV , -5.44 eV , and -5.04 eV ,

respectively. These results indicate that the HOMO levels should be tunable by the peripheral substituents on the outer phenyl rings. From a practical perspective, this is a highly important aspect in the molecular design of charge-transporting materials, since the efficiency of the charge injection from the electrode in the devices is very sensitive towards the energy level of the HOMO.

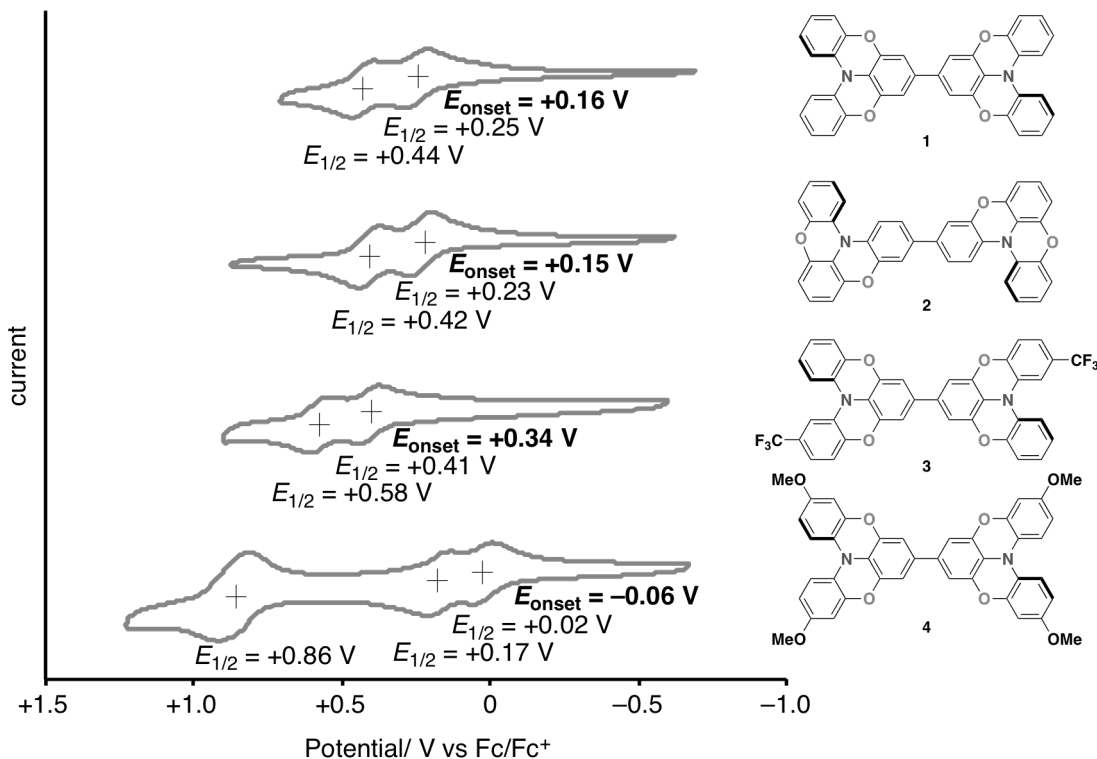


Figure 4. Cyclic voltammograms of **1–4** in CH_2Cl_2 (0.3 mM), measured with $(n\text{-Bu})_4\text{N}^+\text{PF}_6^-$ as a supporting electrolyte at a scan rate of 100 mVs⁻¹.

Photophysical Property

The photophysical properties of **1–4** were measured in CH_2Cl_2 (Figure 5). In the UV-vis absorption spectra, **1–4** show absorption maxima at 387 nm, 397 nm, 385 nm and 405 nm, respectively. In the fluorescence spectroscopies, **1–3** show blue emission (**1**, $\lambda_{\text{em}} = 451 \text{ nm}$, $\Phi = 0.51$; **2**, $\lambda_{\text{em}} = 449 \text{ nm}$, $\Phi = 0.69$; **3**, $\lambda_{\text{em}} = 439 \text{ nm}$, $\Phi = 0.45$) and **4** shows green emission (**4**, $\lambda_{\text{em}} = 489 \text{ nm}$, $\Phi = 0.77$) with moderate to good quantum yields.

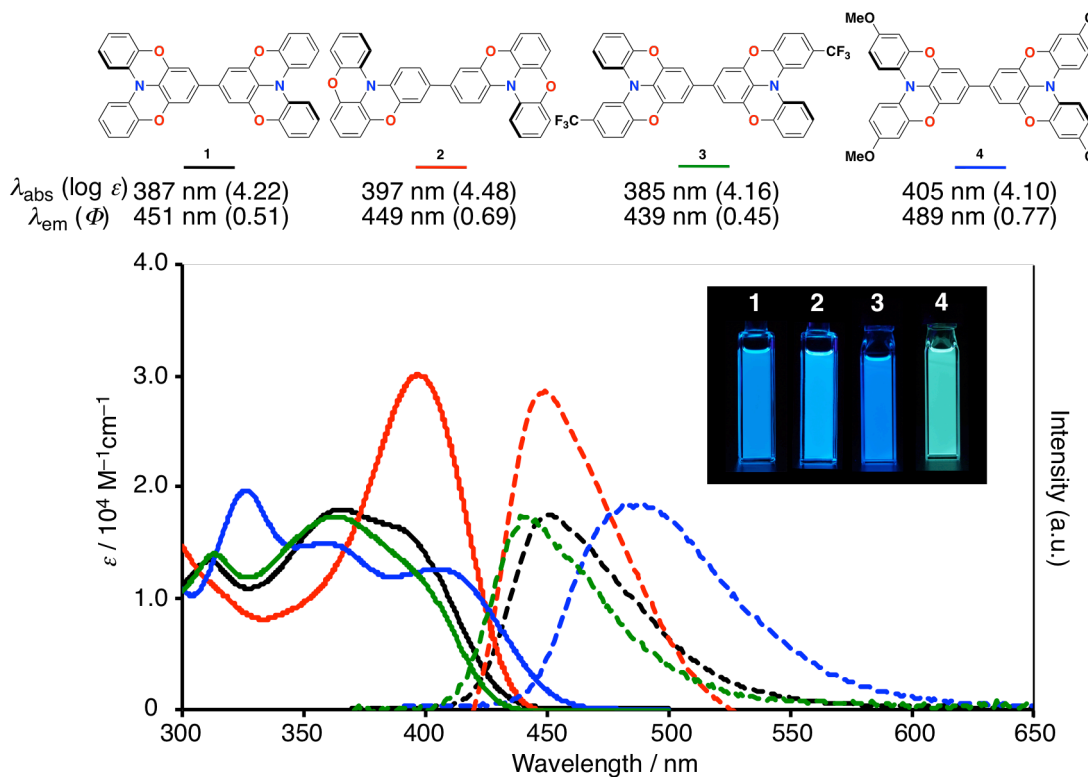


Figure 5. UV-vis absorption spectra (solid line) and fluorescence spectra (dash line) of **1–4** in CH₂Cl₂.

DFT Calculations

To gain insights into the geometry and electronic structure for these dimers, DFT calculations were conducted on **1–4** at the B3LYP/6-31G(d) level of theory. The optimized structures of **1–4** confirmed to have the expected quasiplanar geometry in the partially oxygen-bridged triarylamine moieties (Figure 6a). The Kohn-Sham (KS)-HOMOs of **1–4** are highly delocalized over the whole π-skeleton, which allows effective tuning of the HOMO levels through the peripheral substituents on the outer phenyl rings (Figure 6b). Fully delocalized HOMOs should also lower the reorganization energies for the hole transfer. The reorganization energies for **1–4** were estimated to be $\lambda^+ = 0.15$ eV, 0.15 eV, 0.18 eV, and 0.17 eV, which are lower than those for TPD ($\lambda^+ = 0.26$ eV) or α-NPD ($\lambda^+ = 0.28$ eV). These results suggest that the dimers **1–4** have significant potential as hole-transporting materials in terms of electronic structure.

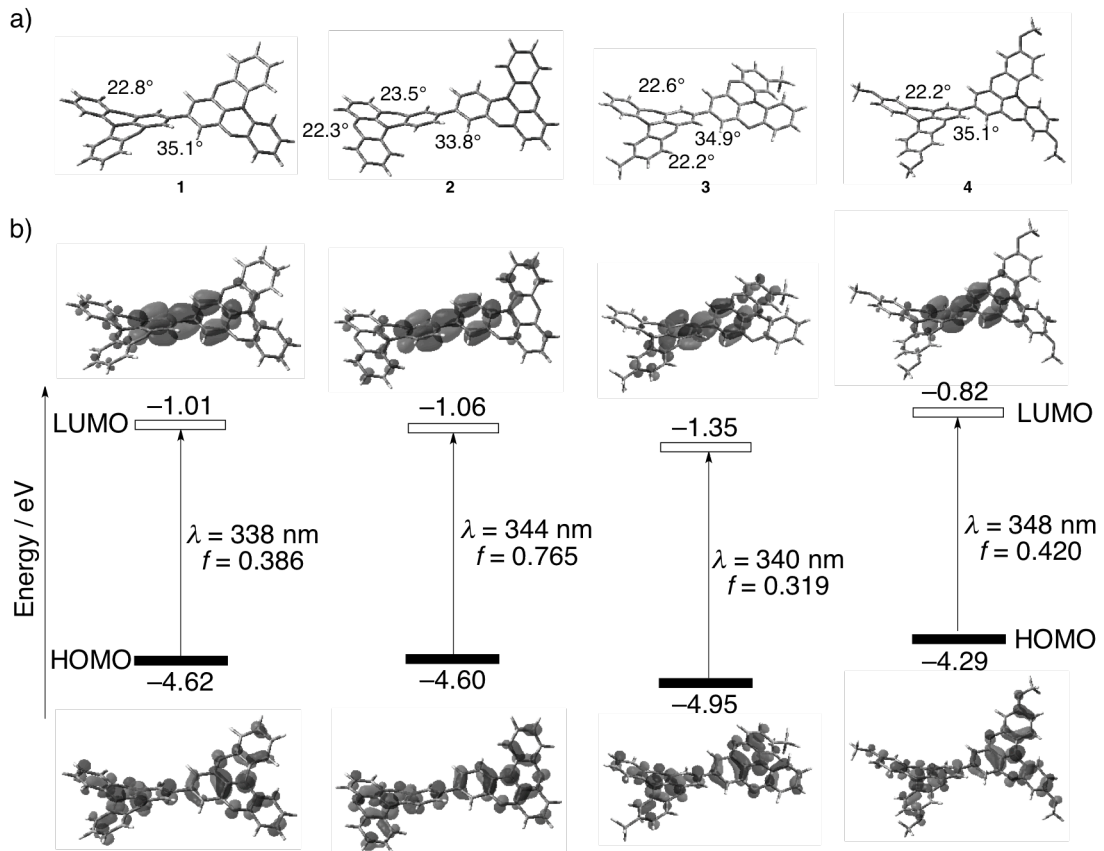


Figure 6. a) Optimized structures and the dihedral angles between phenyl rings for **1–4** (B3LYP/6-31G(d)) and b) Pictorial presentation of the frontier orbitals, a plot of the Kohn-Sham HOMO and LUMO energy levels for **1–4** (B3LYP/6-31G(d)), and optical transition with oscillator strength (CAM-B3LYP/6-31G(d) // B3LYP/6-31G(d)).

X-ray Crystal Structure

Single crystals of **1–4** suitable for X-ray diffraction analysis were obtained by sublimation or recrystallization. The X-ray crystal structural analysis confirmed that dimers **1–4** have quasiplanar structure even in the crystalline state (Figure 7), similar to the optimized structure in the gas phase. For example, the dihedral angles between the outer and inner phenyl rings in **1** ($18.6^\circ/23.0^\circ$; see Figure 7a) are in good agreement with that of the optimized structure (22.8°). On the other hand, the dihedral angles between the inner phenyl rings in the crystal structures for **1** (0.0°) and **4** (49.7°) are not consistent with those of the optimized structures of **1–4** ($33.8\text{--}35.1^\circ$) in the gas phase. This discrepancy is most likely due to the packing forces in the crystal structure, which flattens the biphenyl moiety.

In the packing structures, all of the dimers **1–4** were found to form one-dimensional on-top π -stacks with intermolecular distances of $3.72\text{--}3.79$ Å (Figures

7). This result indicates that the compounds with this quasiplanar structural motif share a general tendency for the observed packing mode. According to the DFT calculations (B3LYP/6-31G(d)), the inversion barrier for the flipping of the two non-tethered phenyl rings was estimated to be 9.1 kcal/mol, indicating free flipping of quasiplanar moiety in solution or under sublimation conditions. This flexibility of quasiplanar skeleton would facilitate to form the observed dense π -stacking in the on-top mode.

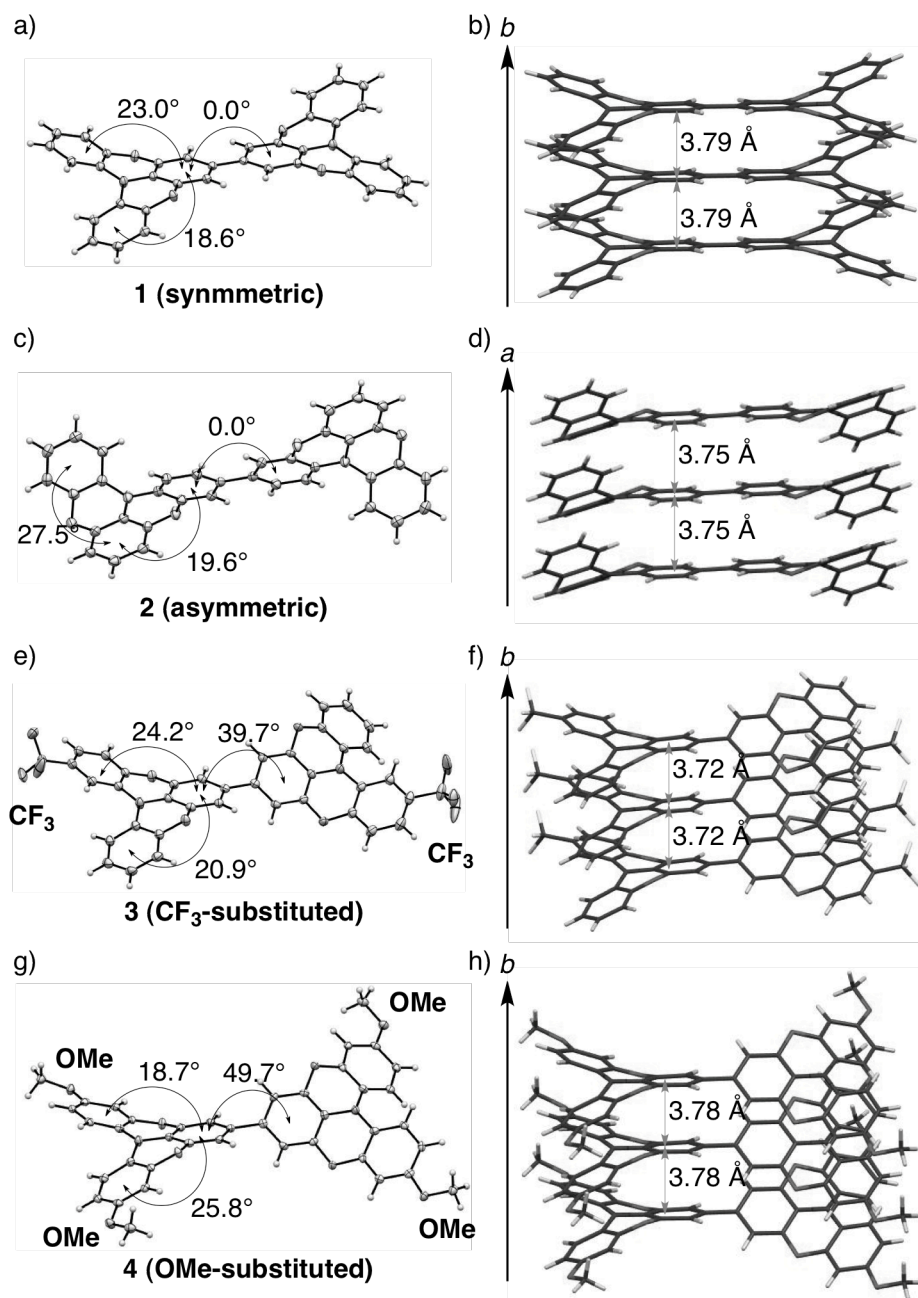


Figure 7. X-ray crystal structures: ORTEP drawings (50% probability for thermal ellipsoids) and packing structures for (a, b) **1**, (c, d) **2**, (e, f) **3**, and (g, h) **4**.

Among the dimers, **2** was found to have crystalline polymorphism. Thus, while recrystallization of **2** from toluene (110–120 °C) afforded needle-like crystals (*P*–1), containing one-dimensional on-top π -stacks of **2** along the short *a*-axis (Figure 7d), similar to the other dimers **1**, **3**, and **4**, recrystallization from *o*-dichlorobenzene (ODCB) at higher temperature (140–160 °C) or sublimation (265 °C, 0.1 mmHg) provided plate-like crystals (*P*₂₁/a), in which **2** formed two-dimensional π -stacks with a slipped arrangement (Figure 8). Since neither a phase transition between these two crystals, nor a difference in the melting point could be observed, the plate-like crystals most likely form by entropy-driven processes at higher temperature.

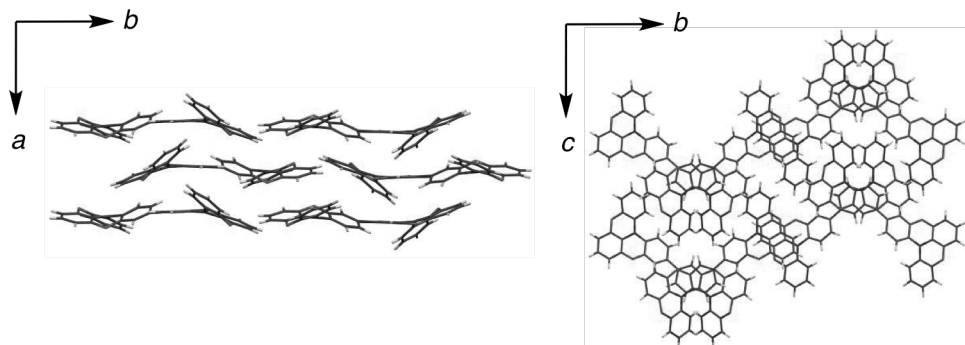


Figure 8. Packing structures for crystal of **2** (*P*₂₁/a) obtained from ODCB solution at higher temperature (140–160 °C).

Theoretical Calculations of Charge Transport Property

To gain insight into the relationship between packing structures and charge transport properties, electronic couplings (*V*) between HOMOs were evaluated by theoretical calculations at the PW91/DZP level.¹⁴ As shown in Figure 9a,b, in the one-dimensional π -stacked needle-like crystals of **1** and **2** (*P*–1), anisotropic charge transport properties were confirmed. One-dimensional on-top π -stacks show larger *V* values (**1**: 82.6 meV, **2** (*P*–1): 98.2 meV) in the direction of the π -stacking (Figure 9a,b), than that in the other directions (**1**: 0.31–1.48 meV, **2** (*P*–1): 0.22–6.94 meV). In contrast, two-dimensional stacked crystal of **2** (*P*₂₁/a) shows isotropic *V* values (1.75–12.8 meV) as shown in Figure 9c.

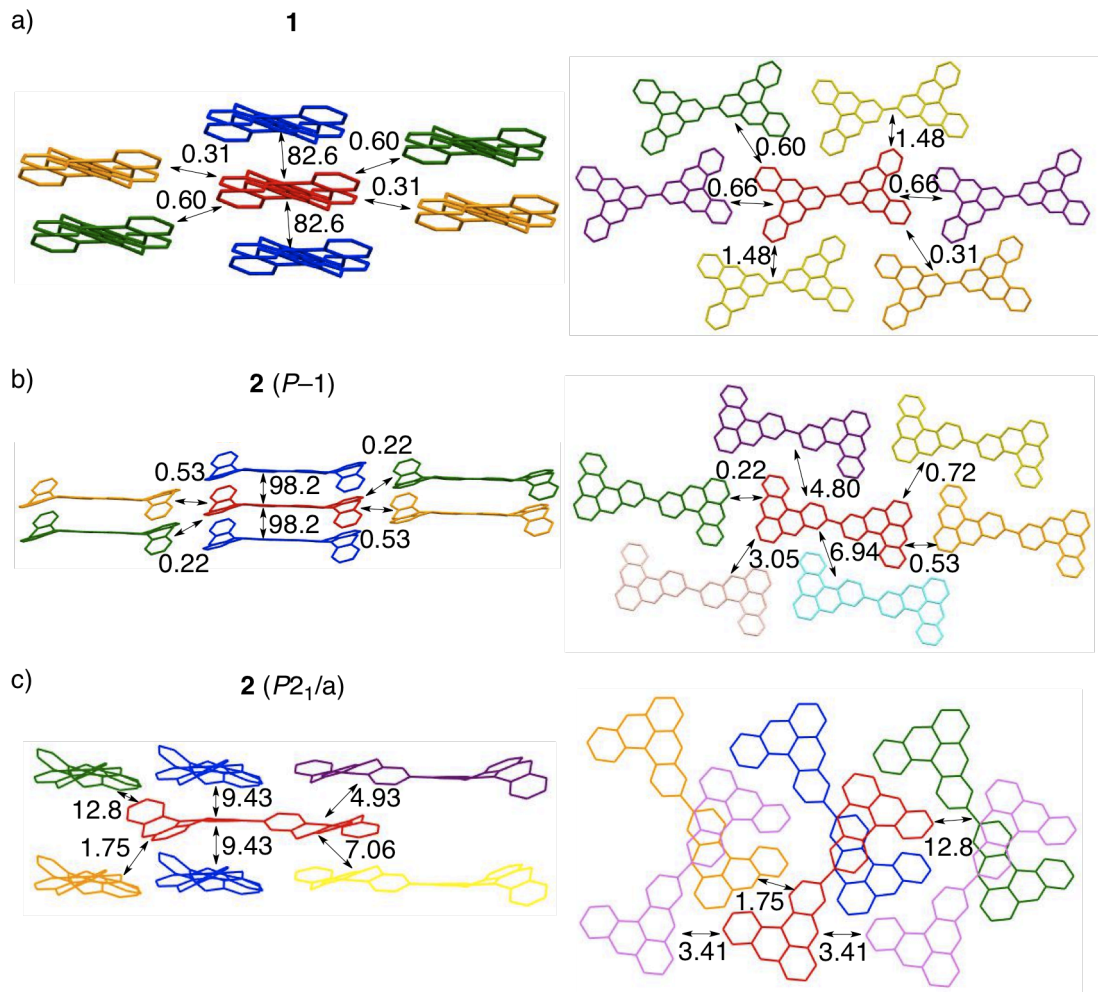
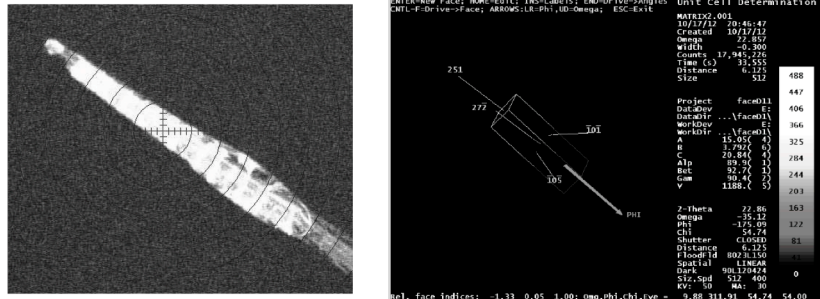


Figure 9. Electronic couplings (meV) between HOMOs of neighbor molecules in the X-ray crystal structures calculated at the PW91/DZP level: (a) One-dimensional packing structure for needle-like crystals of **1**, (b) one-dimensional packing structure for needle-like crystal of **2** (*P*-1), and (c) two-dimensional packing structure for plate-like crystal of **2** (*P*₂₁/a).

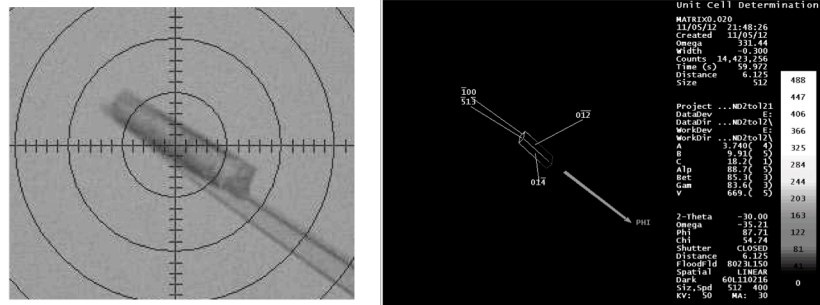
Direction of Stacking in the Crystals

To examine the relationship between packing structure and charge mobility, the directions of π -stacking in the crystals were determined by face index measurement on the crystals. As shown in Figure 10, face index confirmed that the longest axis in the needle-like crystal of **1** (*P*₂₁/c) and **2** (*P*-1) and plate-like crystal of **2** (*P*₂₁/a) corresponds to the π -stacking direction (Figure 10).

a) **1** (Monoclinic $P2_1/c$)



b) **2** (Triclinic $P\bar{1}$)



c) **2** (Monoclinic $P2_1/a$)

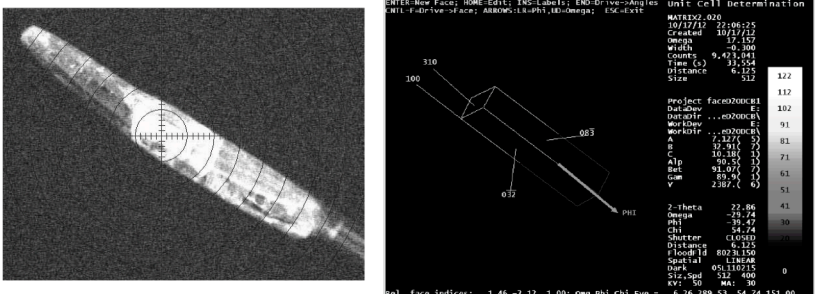


Figure 10. Face index determination for the needle-like crystals of (a) **1** ($P2_1/c$) and (b) **2** ($P\bar{1}$), and (c) plate-like crystal of **2** ($P2_1/a$).

TRMC Measurement

On the basis of the correspondence between the crystal axis and the π -stacking direction, charge mobilities in the crystalline states were conducted by time-resolved microwave conductivity (TRMC) measurements.¹⁵ TRMC measures the local mobility of charge carriers ($\phi\Sigma\mu$) under an oscillating microwave electric field in the absence of contact between the semiconductors and the metal of electrodes, where ϕ is defined as the charge carrier generation efficiency. It should be noted that the local mobility ($\Sigma\mu$)

obtained by TRMC is different from the bulk mobility in time-of-flight (TOF), space-charge-limited current (SCLC), and organic field-effect transistor (OFET) measurements, as the absence of the contact between the semiconductors and the electrode in TRMC measurements allows the evaluation of the intrinsic charge carrier mobility and its anisotropy.¹⁵ As the sample for TRMC measurement, several dozens of crystals were aligned on a quartz substrate (Figure 11a–c), in which the longest axis correspond to the π -stacking direction. The charge carrier generation efficiency (ϕ) was measured for the vacuum-deposited film and was subsequently used to estimate the local mobility $\Sigma\mu$ in the crystals. As estimated by the calculations, the one-dimensional π -stacked needle-like crystals of **1** and **2** showed significant anisotropy of charge mobility. It was substantially higher in the direction of the on-top π -stacking (**1**: $\Sigma\mu = 0.31 \text{ cm}^2 \text{ V}^{-1} \text{ s}^{-1}$, **2**: $\Sigma\mu = 0.34 \text{ cm}^2 \text{ V}^{-1} \text{ s}^{-1}$) compared to the other directions (**1**: $\Sigma\mu = 0.07\text{--}0.09 \text{ cm}^2 \text{ V}^{-1} \text{ s}^{-1}$, **2**: $\Sigma\mu = 0.09\text{--}0.10 \text{ cm}^2 \text{ V}^{-1} \text{ s}^{-1}$). No such anisotropy was observed in the two-dimensional π -stacking in the plate-like crystals of **2** ($\Sigma\mu = 0.09\text{--}0.10 \text{ cm}^2 \text{ V}^{-1} \text{ s}^{-1}$). These results are in qualitative agreement with the electronic couplings estimated by DFT calculations as mentioned above.

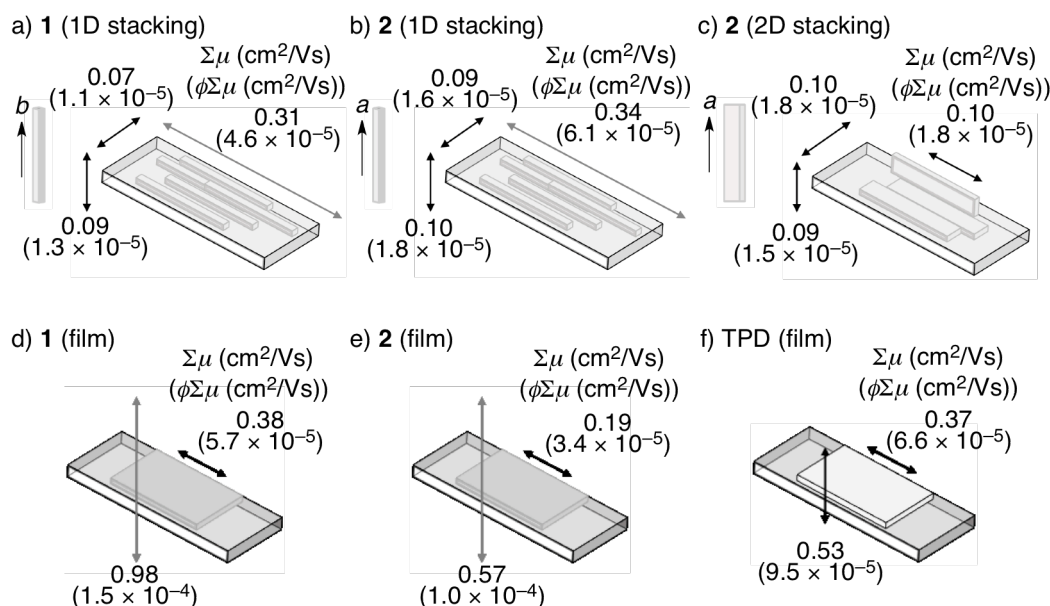


Figure 11. Anisotropy in the carrier mobility measured by TRMC method under excitation at 355 nm for (a) needle-like crystals of **1** (b) needle-like crystals of **2**, and (c) plate-like crystals of **2**, and the vacuum-deposited film of (d) **1**, (e) **2**, and (f) TPD. The charge carrier generation efficiencies (ϕ , **1**: 1.48×10^{-4} , **2**: 1.76×10^{-4} , TPD: 1.80×10^{-4}) were measured for the vacuum-deposited film and were subsequently used to estimate the local mobility $\Sigma\mu$ both in the crystals and film.

In the organic electronic devices such as OLEDs and OPVs, the charge-transporting materials are generally used as films. Therefore, the author also conducted TRMC measurements on the vacuum-deposited films of **1** and **2** (Figure 11d, e). Interestingly, significant anisotropies of the carrier mobility were observed even in the vacuum-deposited films. The mobility in the perpendicular direction ($\Sigma\mu_{\text{per}}$) to the quartz substrate (**1**: $0.98 \text{ cm}^2 \text{ V}^{-1} \text{ s}^{-1}$; **2**: $0.57 \text{ cm}^2 \text{ V}^{-1} \text{ s}^{-1}$) was approximately three times higher than that in the parallel direction ($\Sigma\mu_{\text{par}}$) to the substrate (**1**: $0.38 \text{ cm}^2 \text{ V}^{-1} \text{ s}^{-1}$; **2**: $0.19 \text{ cm}^2 \text{ V}^{-1} \text{ s}^{-1}$). In order to validate that the quasiplanar structure of **1** and **2** is responsible for this anisotropy, TRMC control measurements were conducted on the vacuum-deposited film of TPD as a typical amorphous hole-transporting material (Figure 11f). In the film of TPD, a minimal anisotropy of the carrier mobility was observed as $\Sigma\mu_{\text{per}}/\Sigma\mu_{\text{par}} = 1.4$ ($\Sigma\mu_{\text{per}} = 0.53 \text{ cm}^2 \text{ V}^{-1} \text{ s}^{-1}$; $\Sigma\mu_{\text{par}} = 0.37 \text{ cm}^2 \text{ V}^{-1} \text{ s}^{-1}$), which was significantly less prominent than those in films of **1** ($\Sigma\mu_{\text{per}}/\Sigma\mu_{\text{par}} = 2.6$) and **2** ($\Sigma\mu_{\text{per}}/\Sigma\mu_{\text{par}} = 3.0$).

Molecular Orientations in the Vacuum-Deposited Films

To confirm the origin of the observed anisotropic charge mobility in the film, the ordering structures of **1** and **2** in the vacuum-deposited films were investigated by X-ray diffraction studies. The vacuum-deposited films of **1** and **2** did not exhibit any distinct diffraction peaks in measurements using a laboratory X-ray diffractometer with a sealed-tube X-ray generator (RIGAKU Ultima IV; Figure 12a–d), which suggests that these films are essentially amorphous.

However, in the two-dimensional grazing-incidence X-ray diffraction (2D-GIXD), and using a synchrotron radiation source,^{3e} a diffraction halo corresponding to the π -stacking along the q_z -axis (out-of-plane; $q = 1.69\text{--}1.74 \text{ \AA}^{-1}$, Figure 12e) was observed in the vacuum-deposited films of **2**, whereas no distinct diffraction was observed in the direction of the q_{xy} -axis (in-plane). The determined π -stacking distance (d_{π}) of $3.6\text{--}3.7 \text{ \AA}$ is in good agreement with the results obtained from the crystal structures. This finding suggests a horizontal molecular orientation (face-on), in which the π -stacking structure was retained to some extent, even in the amorphous state (Figure 12f).¹⁶ These results accordingly support the anisotropy of the charge mobility observed by TRMC. In contrast, on the basis of variable angle spectroscopic ellipsometry measurements, nonplanar TPD was reported to be randomly oriented in the vacuum-deposited films under similar conditions.^{16b} It is therefore feasible to conclude that the anisotropy of the carrier mobility is most likely enhanced by the quasiplanar structural motif of oxygen-bridged triarylamines **1** and **2**.

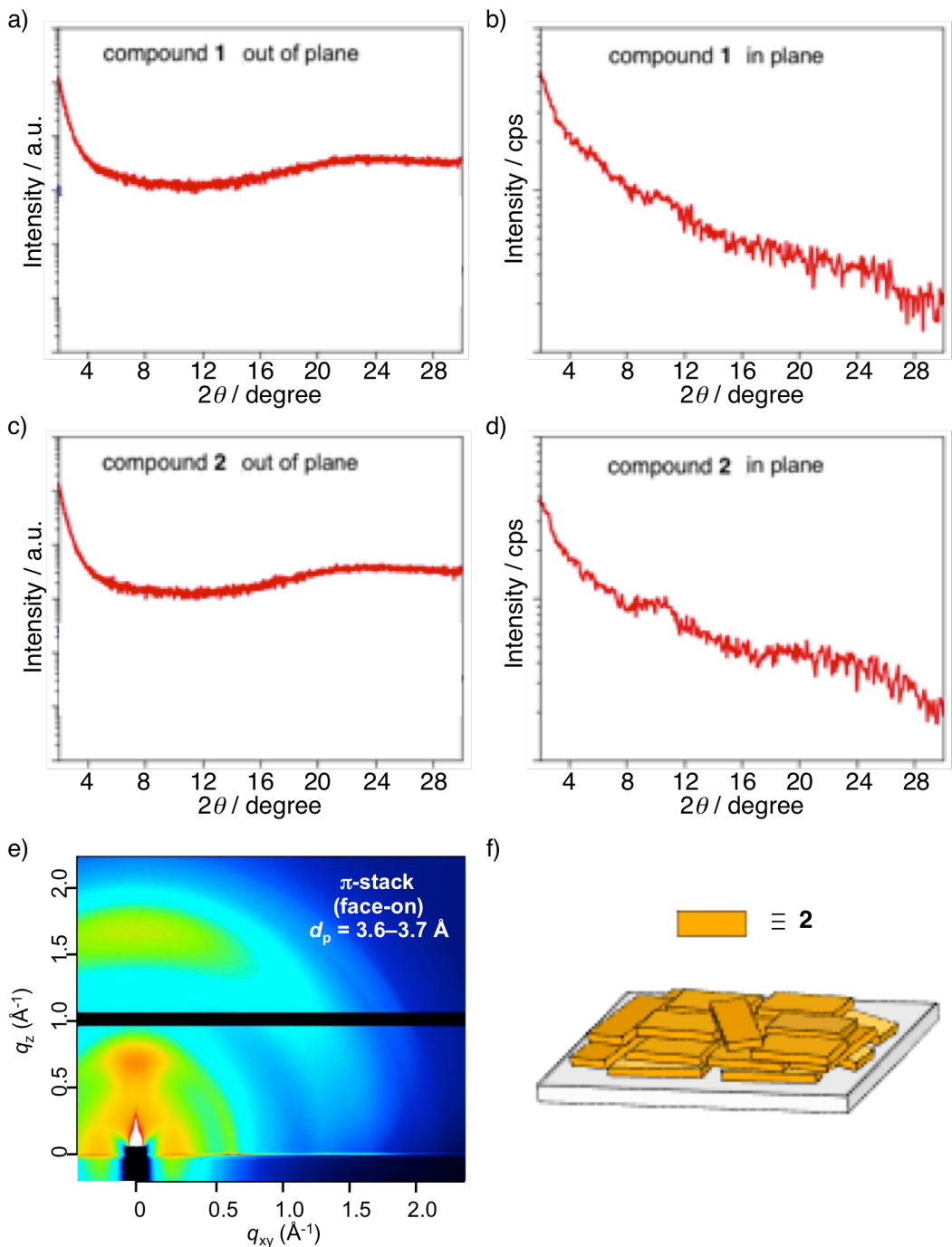


Figure 12. (a-d) XRD diffractions of vacuum deposited films (100 nm thickness) using a laboratory X-ray diffractometer with a sealed-tube X-ray generator (RIGAKU Ultima); (a) out of plane and (b) in plane for **1**, and (c) out of plane and (d) in plane for **2**. (e) 2D-GIXD image of a vacuum deposited film of **2**. (f) Image of molecular orientation of **2** in vacuum deposited film.

Conclusion

In conclusion, the author demonstrated that quasiplanar structures can be used as the key feature in the molecular design of triarylamines to obtain delocalized HOMOs and on-top π -stacks in the crystalline state, which leads to the observed high and anisotropic carrier mobilities in the π -stacking direction. The author also found that these compounds retain some degree of the face-on π -stacking in amorphous films, thus facilitating out-of-plane charge transport. These characteristics would be extraordinarily beneficial for charge-transporting materials in OLEDs, OPVs, and perovskite-sensitized solar cells,¹⁷ all of which require high levels of out-of-plane charge transport.

Experimental Section

General.

All reactions were carried out under an argon atmosphere. Thin layer chromatography (TLC) was performed on plates coated with 0.25 mm thick silica gel 60F-254 (Merck). Column chromatography was performed using PSQ 60B (Fuji Silyria). Melting points (mp) were measured on a Yanaco Micro Melting Point Apparatus. ^1H and ^{13}C NMR spectra were recorded with a Varian Mercury 300 (300 MHz for ^1H and 75 MHz for ^{13}C) or Bruker Avance III 600US (600 MHz for ^1H and 150 MHz for ^{13}C) spectrometer. The NMR chemical shifts are reported in ppm with reference to residual protons and carbons of CDCl_3 (δ 7.26 ppm in ^1H NMR, δ 77.0 ppm in ^{13}C NMR) and CD_2Cl_2 (δ 5.32 ppm in ^1H NMR, δ 53.8 ppm in ^{13}C NMR). Thermogravimetric analysis (TGA) was performed on a Shimadzu TGA-50 apparatus (Shimadzu Co.,). The values are given for a weight-loss of 5% (T_{d5}). Different scanning calorimetry (DSC) was performed on a Shimadzu DSC-60 apparatus (Shimadzu Co.,). Cyclic voltammetry (CV) was performed on an ALS/chi-620C electrochemical analyzer. The CV cell consisted of a glassy carbon electrode, a Pt wire counter electrode, and an Ag/AgNO_3 reference electrode. The measurement was carried out under an argon atmosphere using CH_2Cl_2 solutions of samples (0.3 mM) with 0.1 M tetrabutylammonium hexafluorophosphate ($\text{Bu}_4\text{N}^+\text{PF}_6^-$) as a supporting electrolyte. The redox potentials were calibrated with ferrocene as an internal standard. UV-vis absorption measurement was performed with a Shimadzu UV-3150 spectrometer (Shimadzu Co.), in degassed spectral grade solvents. Fluorescence measurement was performed with a HORIBA FluoroMax 4P-NIR. Quantum yields were determined with a Hamamatsu Photonics Quantaurus QY C11347 with calibrated integrating sphere system.

Synthesis.

2,6-Difluoro-N,N-bis(2-methoxyphenyl)aniline (12).

o-Iodoanisole **10** (18.0 g, 77.0 mmol), 2,6-difluoroaniline **11** (4.80 g, 37.2 mmol), K₂CO₃ (19.4 g, 140 mmol) and copper powder (6.66 g, 105 mmol) were mixed in dry *o*-dichlorobenzene (ODCB) (100 mL) and stirred at 180 °C for 110 h. The insoluble materials were filtered off and washed with CH₂Cl₂ (120 mL). The combined filtrate was washed with water and extracted with CH₂Cl₂ (40 mL × 3). The organic phase was dried over MgSO₄, filtered off, and concentrated under reduced pressure. The obtained crude product was washed with hexane to give 8.34 g (24.5 mmol) of **12** as white solids in 66% yield.

mp 178.7–179.6 °C; ¹H NMR (300 MHz, CDCl₃): δ 7.10–6.94 (m, 3H), 6.94–6.76 (m, 8H), 3.58 (s, 6H); ¹³C NMR (75 MHz, CDCl₃): δ 159.0 (dd, ¹J(C,F) = 249 Hz, ³J(C,F) = 6.3 Hz), 153.2, 136.7, 125.0 (t, ²J(C,F) = 15.0 Hz), 124.4, 124.2, 123.8 (t, ³J(C,F) = 9.8 Hz), 121.1, 113.2, 111.5 (dd, ²J(C,F) = 16.6 Hz, ⁴J(C,F) = 7.2 Hz), 56.1; HRMS (FAB) (*m/z*): [M]⁺ calcd. for C₂₀H₁₇F₂NO, 341.1227; found, 341.1227; Elemental analysis calcd (%) for C₂₀H₁₇F₂NO₂: C 70.37, H 5.02, N 4.10; found: C 70.22, H 5.21, N 3.98.

Benzo[5,6][1,4]oxazino[2,3,4-*k*]phenoxazine (5).

12 (5.80 g, 17.0 mmol) was dissolved in dry CH₂Cl₂ (340 mL). The solution was cooled to –78 °C, then BBr₃ (3.20 mL, 33.8 mmol) was added and the mixture was slowly warmed up to room temperature and stirred for 3 h. The reaction mixture was poured into water and extracted with CH₂Cl₂ (100 mL × 3). The organic phase was dried over Na₂SO₄, filtered off, and concentrated under reduced pressure to give 5.18 g (16.6 mmol) of crude product as brown solids in 97% yield.

90% of this solid (4.70 g, 15.0 mmol) was dissolved in DMF (140 mL). K₂CO₃ (6.22 g, 45.0 mmol) was added and the mixture was stirred at 100 °C for 19 h. After addition of 1 M HCl aq. (100 mL), the products were extracted with CH₂Cl₂ (90 mL × 3). The organic phase was dried over Na₂SO₄, filtered off, and concentrated under reduced pressure. The obtained crude product was purified by silica gel short column chromatography (CH₂Cl₂, *R*_f = 0.85) to give 4.06 g (14.9 mmol) of **5** in 95% yield as white solids.

¹H NMR (300 MHz, CDCl₃): δ 7.33 (d, ³J(H,H) = 7.5 Hz, 2H), 6.98–6.87 (m, 6H), 6.75 (t, ³J(H,H) = 8.1 Hz, 1H), 6.50 (d, ³J(H,H) = 8.1 Hz, 2H).

4-Bromo-2,6-difluoro-N,N-bis(2-methoxyphenyl)aniline (15).

o-Iodoanisole **10** (19.8 g, 84.6 mmol), 4-bromo-2,6-difluoroaniline **14** (7.74 g, 37.2 mmol), K₂CO₃ (21.5 g, 156 mmol), and copper powder (7.82 g, 123 mmol) were mixed in dry ODCB (100 mL) and stirred at 180 °C for 110 h. The insoluble materials were filtered off and washed with CH₂Cl₂ (100 mL × 3). The combined filtrate was washed with water. The organic phase was dried over MgSO₄, filtered off, and concentrated under reduced pressure. The obtained crude product was washed with hexane to give 10.6 g (25.4 mmol) of **15** as white solids in 68% yield.

mp: 157.5–158.5 °C; ¹H NMR (300 MHz, CDCl₃): δ 7.10–6.94 (m, 4H), 6.94–6.81 (m, 6H), 3.60 (s, 6H); ¹³C NMR (75 MHz, CDCl₃): δ 158.2 (dd, ¹J(C,F) = 252.4 Hz, ³J(C,F) = 6.9 Hz), 153.3, 136.11, 124.66 (t, ²J(C,F) = 12.9 Hz), 124.62, 124.61, 121.1, 115.3 (dd, ²J(C,F) = 17.8 Hz, ⁴J(C,F) = 9.2 Hz), 114.7 (t, ³J(C,F) = 12.0 Hz), 113.0, 56.0; HRMS (FAB) (*m/z*): [M]⁺ calcd. for C₂₀H₁₆BrF₂NO₂, 419.0332; found, 419.0325; Elemental analysis calcd (%) for C₂₀H₁₆BrF₂NO₂: C 57.16, H 3.84, N 3.33; found: C 57.16, H 3.90, N 3.40.

7-Bromobenzo[5,6][1,4]oxazino[2,3,4-*k*]phenoxazine (17).

15 (2.09 g, 5.00 mmol) was dissolved in dry CH₂Cl₂ (100 mL). The solution was cooled to –78 °C, then BBr₃ (1.00 mL, 10.6 mmol) was added and the mixture was slowly warmed up to room temperature and stirred for 3 h. The reaction mixture was poured into water (200 mL) and extracted with CH₂Cl₂ (30 mL × 3). The organic phase was dried over Na₂SO₄, filtered off, and concentrated under reduced pressure to give 2.02 g of crude product as white solids.

This solid was dissolved in DMF (60 mL). K₂CO₃ (2.07 g, 15.0 mmol) was added and the mixture was stirred at 100 °C for 12 h. After cooling, white solids were precipitated. The solids were filtered and washed with water to give 1.06 g (3.00 mmol) of **17** in 60% yield as white solids. The filtrate was concentrated under reduced pressure. The obtained solids were added to water and extracted with CH₂Cl₂ (30 mL × 3). The organic phase was dried over Na₂SO₄, filtered off, and concentrated under reduced pressure. The obtained solids were purified by silica gel short column chromatography (CH₂Cl₂, *R*_f = 0.78) to give 0.591 g (1.68 mmol) of **17** in 34% yield as white solids. In total, 1.65 g (4.68 mmol) of **17** was obtained in 94% yield.

mp: 215.5–216.3 °C; ¹H NMR (300 MHz, C₆D₆): δ 6.93–6.88 (m, 2H), 6.70–6.63 (m, 2H), 6.60–6.52 (m, 4H), 6.50 (s, 2H); ¹³C NMR (75 MHz, CDCl₃): δ 146.7, 145.7, 128.7, 123.9, 123.6, 120.4, 117.5, 115.2, 114.7, 114.5; HRMS (FAB) (*m/z*): [M]⁺ calcd. for C₁₈H₁₀BrNO₂, 350.9895; found, 350.9880; Elemental analysis calcd (%) for C₁₈H₁₀BrNO₂: C 61.39, H 2.86, N 3.98; found: C 61.01, H 3.00, N 4.02.

7,7'-Dibenzo[5,6][1,4]oxazino[2,3,4-*k*l]phenoxazine (1).

17 (4.20 g, 12.0 mmol), Ni(cod)₂ (3.96 g, 14.4 mmol), 1,5-cyclooctadiene (1.77 g, 16.4 mmol), and 2,2'-bipyridine (2.25 g, 14.4 mmol) were dissolved in dry THF (360 mL) and the resulting mixture was stirred at 60 °C for 24 h. The reaction mixture was absorbed on silica gel. The mixture was eluted by CS₂ (*R*_f = 0.40) followed by Soxhlet extraction with toluene. The resulting solution was concentrated to give 2.11 g (3.88 mmol) of **1** in 65% yield as yellow solids.

mp: 375.2–376.1 °C; ¹H NMR (300 MHz, CD₂Cl₂): δ 7.36 (d, ³J(H,H) = 6.9 Hz, 4H), 7.05–6.90 (m, 12H), 6.69 (s, 4H); ¹³C NMR (150 MHz, CD₂Cl₂-CS₂ = 1 : 4): δ 147.2, 145.8, 136.0, 129.1, 124.2, 124.0, 120.5, 117.9, 115.0, 109.5; HRMS (FAB) (*m/z*): [M]⁺ calcd. for C₃₆H₂₀N₂O₄, 544.1423; found, 544.1429; Elemental analysis calcd (%) for C₃₆H₂₀N₂O₄: C 79.40, H 3.70, N 5.14; found: C 79.57, H 3.88, N 5.13.

4-Bromo-N-(2,6-difluorophenyl)-2-methoxy-N-(2-methoxyphenyl)aniline (22).

12 (2.57 g, 7.53 mmol) and *N*-bromosuccinimide (1.33 g, 7.48 mmol) were dissolved in CHCl₃ (60 mL) and acetic acid (60 mL). The mixture was stirred at room temperature for 12 h. The reaction mixture was neutralized with saturated NaHCO₃ aq. and extracted with CHCl₃ (90 mL × 3). The organic phase was dried over Na₂SO₄, filtered off, and concentrated under reduced pressure. The obtained crude product was purified by silica gel column chromatography (CH₂Cl₂ : hexane = 2 : 3, *R*_f = 0.50) to give 2.36 g (5.63 mmol) of **22** as white solids in 75% yield.

mp: 119.1–120.1 °C; ¹H NMR (300 MHz, CDCl₃): δ 7.11–6.97 (m, 3H), 6.95 (dd, ³J(H,H) = 8.4 Hz, ⁴J(H,H) = 2.1 Hz, 1H), 6.93–6.76 (m, 5H), 6.74 (d, ³J(H,H) = 8.4 Hz, 1H), 3.59 (s, 3H), 3.56 (s, 3H); ¹³C NMR (75 MHz, CDCl₃): δ 159.0 (dd, ¹J(C,F) = 249.5 Hz, ³J(C,F) = 5.7 Hz), 153.5, 153.3, 136.1, 125.0, 124.8, 124.7, 124.4 (t, ³J(C,F) = 6.9 Hz), 124.3, 124.1, 123.9, 121.1, 116.3, 116.1, 113.2, 111.5 (dd, ²J(C,F) = 16.0 Hz, ⁴J(C,F) = 6.8 Hz), 56.2, 56.1; HRMS (FAB) (*m/z*): [M]⁺ calcd. for C₂₀H₁₆BrF₂NO₂, 419.0332; found, 419.0332; Elemental analysis calcd (%) for C₂₀H₁₆BrF₂NO₂: C 57.16, H 3.84, N 3.33; found: C 57.26, H 3.88, N 3.38.

3-Bromobenzo[5,6][1,4]oxazino[2,3,4-*k*l]phenoxazine (23).

22 (1.82 g, 4.33 mmol) was dissolved in dry CH₂Cl₂ (90 mL). The solusion was cooled to –78 °C, then BBr₃ (1.00 mL, 10.6 mmol) was added. The mixture was slowly warmed up to room temperature and stirred for 4 h. The reaction mixture was poured into water and extracted with CH₂Cl₂ (50 mL × 3). The organic phase was dried over

Na_2SO_4 , filtered off, and concentrated under reduced pressure to give 1.74 g of the product containing CH_2Cl_2 as white solids.

These solids were dissolved in DMF (60 mL). K_2CO_3 (1.84 g, 13.3 mmol) was added and the mixture was stirred at 100 °C for 15.5 h. The reaction mixture was concentrated under reduced pressure. After addition of water, the product was extracted with CH_2Cl_2 (50 mL × 3). The organic phase was dried over Na_2SO_4 , filtered off, and concentrated under reduced pressure. The obtained crude product was purified by silica gel short column chromatography (CH_2Cl_2 , $R_f = 0.95$) to give 1.51 g (4.28 mmol) of **23** in 99% yield as white solids.

mp: 145.3–146.3 °C; ^1H NMR (300 MHz, CDCl_3): δ 7.25 (d, $^3J(\text{H},\text{H}) = 6.9$ Hz, 1H), 7.19 (dd, $^3J(\text{H},\text{H}) = 6.9$ Hz, $^4J(\text{H},\text{H}) = 2.4$ Hz, 1H), 7.07–7.02 (m, 2H), 6.98–6.88 (m, 3H), 6.76 (t, $^3J(\text{C},\text{H}) = 8.4$ Hz, 1H), 6.51 (dd, $^3J(\text{H},\text{H}) = 8.4$ Hz, $^4J(\text{H},\text{H}) = 1.2$ Hz, 1H), 6.49 (dd, $^3J(\text{H},\text{H}) = 8.4$ Hz, $^4J(\text{H},\text{H}) = 1.2$ Hz, 1H); ^{13}C NMR (75 MHz, CDCl_3): δ 147.6, 146.9, 145.3, 144.9, 128.6, 128.4, 126.3, 123.9, 123.73, 123.65, 120.6, 120.4, 117.6, 115.5, 114.49, 114.47, 111.5, 111.1; HRMS (FAB) (m/z): $[\text{M}]^+$ calcd. for $\text{C}_{18}\text{H}_{10}\text{BrNO}_2$, 350.9895; found, 350.9897; Elemental analysis calcd (%) for $\text{C}_{18}\text{H}_{10}\text{BrNO}_2$: C 61.39, H 2.86, N 3.98; found: C 61.53, H 2.79, N 4.00.

3,3'-Dibenzo[5,6][1,4]oxazino[2,3,4-*k*l]phenoxazine (2).

23 (0.351 g, 1.00 mmol), $\text{Ni}(\text{cod})_2$ (0.329 g, 1.20 mmol), 1,5-cyclooctadiene (0.14 mL, 1.14 mmol) and 2,2'-bipyridine (0.189 g, 1.21 mmol) were dissolved in dry THF (30 mL) and the resulting mixture was stirred at 60 °C for 18 h. The reaction mixture was concentrated under reduced pressure and absorbed on silica gel. The mixture was extracted with toluene ($R_f = 0.95$) by using Soxhlet extractor and the resulting solution was concentrated under reduced pressure. The solid was washed with hexane to give 0.268 g (0.491 mmol) of **2** in 98% yield as yellow solid.

mp: 337.6–338.6 °C; ^1H NMR (300 MHz, $\text{CD}_2\text{Cl}_2\text{-CS}_2 = 1 : 1$): δ 7.38 (d, $^3J(\text{H},\text{H}) = 8.4$ Hz, 2H), 7.36 (dd, $^3J(\text{H},\text{H}) = 8.1$ Hz, $^4J(\text{H},\text{H}) = 1.5$ Hz, 2H), 7.16 (dd, $^3J(\text{H},\text{H}) = 8.4$ Hz, $^4J(\text{H},\text{H}) = 2.1$ Hz, 2H), 7.10 (d, $^4J(\text{H},\text{H}) = 2.1$ Hz, 2H), 7.02–6.88 (m, 6H), 6.79 (t, $^3J(\text{H},\text{H}) = 8.1$ Hz, 2H), 6.53 (dd, $^3J(\text{H},\text{H}) = 8.4$ Hz, $^4J(\text{H},\text{H}) = 1.2$ Hz, 2H), 6.51 (dd, $^3J(\text{H},\text{H}) = 8.4$ Hz, $^4J(\text{H},\text{H}) = 1.2$ Hz, 2H); ^{13}C NMR spectrum was not able to be recorded due to its poor solubility. HRMS (FAB) (m/z): $[\text{M}]^+$ calcd. for $\text{C}_{36}\text{H}_{20}\text{N}_2\text{O}_4$, 544.1423; found, 544.1426; Elemental analysis calcd (%) for $\text{C}_{36}\text{H}_{20}\text{N}_2\text{O}_4$: C 79.40, H 3.70, N 5.14; found: C 79.22, H 3.59, N 5.17.

4-Bromo-N-(2,4-dimethoxyphenyl)-2,6-difluoroaniline (19).

o-Iodoanisole **10** (6.55 g, 28.0 mmol), 4-bromo-2,6-difluoroaniline **14** (5.20 g, 25.0 mmol), Pd₂(dba)₃·CHCl₃ (0.417 g, 0.402 mmol), sodium *tert*-butoxide (2.89 g, 30.0 mmol), and tri-*tert*-butylphosphine (0.608 g, 3.01 mmol) were dissolved in dry toluene (70 mL) and the mixture was stirred at 100 °C for 24 h. The insoluble materials were filtered off and extracted with toluene (50 mL). After addition of water to filtrate, the products were extracted with toluene (30 mL × 3). The organic phase was dried over Na₂SO₄, filtered off, and concentrated under reduced pressure. The obtained crude product was purified by silica gel column chromatography (CH₂Cl₂ : hexane = 1 : 5, *R*_f = 0.26) to give 5.33 g (17.0 mmol) of **19** as white solids in 68% yield.

mp: 71.2–72.2 °C; ¹H NMR (300 MHz, CDCl₃): δ 7.20–7.11 (m, 2H), 6.91–6.80 (m, 3H), 6.57 (td, ³J(H,H) = 8.7 Hz, ⁴J(H,H) = 2.7 Hz, 1H), 5.83 (br, 1H), 3.93 (s, 3H); ¹³C NMR (75 MHz, CDCl₃): δ 156.7 (dd, ¹J(C,F) = 250.1 Hz, ³J(C,F) = 6.3 Hz), 147.7, 132.5, 120.7, 120.2, 118.7 (t, ³J(C,F) = 14.9 Hz), 115.8 (dd, ²J(C,F) = 18.3 Hz, ⁴J(C,F) = 8.6 Hz), 114.6 (t, ³J(C,F) = 11.7 Hz), 113.2 (t, ⁴J(C,F) = 2.9 Hz) 110.1, 55.6; HRMS (FAB) (*m/z*): [M]⁺ calcd. for C₁₃H₁₀BrF₂NO, 312.9914; found, 312.9923; Elemental analysis calcd (%) for C₁₃H₁₀BrF₂NO: C 49.71, H 3.21, N 4.46; found: C 49.79, H 3.17, N 4.52.

4-Bromo-2,6-difluoro-N-(2-methoxy-5-(trifluoromethyl)phenyl)-N-(2-methoxyphenyl)aniline (20).

19 (0.862 g, 2.75 mmol), 2-iodo-4-trifluoromethylanisole (0.990 g, 3.28 mmol), K₂CO₃ (0.857 g, 6.20 mmol), and copper powder (0.317 g, 4.99 mmol) were dissolved in dry ODCB (20 mL) and the mixture was stirred at 180 °C for 65 h. The insoluble materials were filtered off, and the solid was washed with CH₂Cl₂ (50 mL). After addition of water to filtrate, the products were extracted with CH₂Cl₂ (10 mL × 3). The organic phase was dried over Na₂SO₄, filtered off, and concentrated under reduced pressure. The obtained crude product was purified by silica gel column chromatography (CH₂Cl₂ : hexane = 1 : 3, *R*_f = 0.31) to give 1.00 g (2.05 mmol) of **20** as white solids in 75% yield.

mp: 98.4–99.4 °C; ¹H NMR (300 MHz, CDCl₃): δ 7.29 (d, ³J(H,H) = 9.0 Hz, 1H), 7.12 (ddd, ³J(H,H) = 7.2 Hz, ³J(H,H) = 6.9 Hz, ⁴J(H,H) = 2.1 Hz, 1H), 7.07 (d, ⁴J(H,H) = 1.8 Hz, 1H), 7.02 (d, ³J(H,H) = 8.1 Hz, 2H), 6.95–6.88 (m, 4H), 3.64 (s, 3H), 3.59 (s, 3H); ¹³C NMR (75 MHz, CDCl₃): δ 158.5 (dd, ¹J(C,F) = 253 Hz, ³J(C,F) = 6.9 Hz), 155.0, 153.4, 136.3, 135.1, 125.6, 125.1, 124.2 (q, ¹J(C,F) = 270 Hz), 123.2 (q, ²J(C,F) = 32.6 Hz), 121.2, 121.0, 120.5 (q, ³J(C,F) = 3.45 Hz), 115.8, 115.48, 115.47 (dd, ²J(C,F) = 18.1, ⁴J(C,F) = 8.9 Hz), 113.0, 112.1, 56.0, 55.9; HRMS (FAB) (*m/z*): [M]⁺ calcd. for

$C_{21}H_{15}BrF_5NO_2$, 487.0206; found, 487.0206; Elemental analysis calcd (%) for $C_{21}H_{15}BrF_5NO_2$: C 51.66, H 3.10, N 2.87; found: C 51.89, H 3.09, N 2.92.

7-Bromo-2-(trifluoromethyl)benzo[5,6][1,4]oxazino[2,3,4-*k*]phenoxazine (21).

20 (3.113 g, 6.38 mmol) was dissolved in dry CH_2Cl_2 (200 mL). The solution was cooled to $-78^\circ C$, then BBr_3 (1.25 mL, 13.2 mmol) was added. The mixture was slowly warmed up to room temperature and stirred for 3 h. The reaction mixture was poured into water (100 mL) and extracted with CH_2Cl_2 (50 mL \times 3). The organic phase was dried over Na_2SO_4 , filtered off, and concentrated under reduced pressure to give 3.063 g of the crude product containing CH_2Cl_2 as white solids.

These solids were dissolved in DMF (130 mL). K_2CO_3 (2.642 g, 19.1 mmol) was added and the mixture was stirred at $100^\circ C$ for 12 h. The reaction mixture was concentrated under reduced pressure. After addition of 1M NH_4Cl aq. (100 mL), the product was extracted with CH_2Cl_2 (80 mL \times 3). The organic phase was dried over Na_2SO_4 , filtered off, and concentrated under reduced pressure. The obtained crude product was purified by silica gel short column chromatography (CH_2Cl_2 , R_f = 0.95) and then purified by silica gel column chromatography (CH_2Cl_2 : hexane = 1 : 5, R_f = 0.66) to give 1.741 g (4.14 mmol) of **21** in 65% yield as white solids.

mp: 146.1–147.0 $^\circ C$; 1H NMR (300 MHz, $CDCl_3$): δ 7.53 (d, $^4J(H,H)$ = 2.1 Hz, 1H), 7.28 (dd, $^3J(H,H)$ = 6.6 Hz, $^4J(H,H)$ = 1.2 Hz, 1H), 7.16 (d, $^3J(H,H)$ = 8.4 Hz, 1H), 7.04–6.88 (m, 4H), 6.69 (dd, $^3J(H,H)$ = 7.8 Hz, $^4J(H,H)$ = 2.1 Hz, 2H); ^{13}C NMR (75 MHz, $CDCl_3$): δ 149.2, 146.6, 145.6, 145.2, 129.5, 126.7, 125.5, 124.5, 124.3, 121.9, 120.7 (q, $^3J(C,F)$ = 4.0 Hz), 119.7, 117.9, 117.7, 115.9, 115.2, 114.6, 114.4, 111.6 (q, $^3J(C,F)$ = 4.1 Hz); HRMS (FAB) (m/z): $[M]^+$ calcd. for $C_{19}H_9BrF_3NO_2$, 418.9769; found, 418.9783; Elemental analysis calcd (%) for $C_{19}H_9BrF_3NO_2$: C 54.31, H 2.16, N 3.33; found: C 54.43, H 2.42, N 3.53.

2,2'-Bis(trifluoromethyl)-7,7'-bibenzo[5,6][1,4]oxazino[2,3,4-*k*]phenoxazine (3).

21 (0.964 g, 2.29 mmol), $Ni(cod)_2$ (0.379 g, 1.38 mmol), 1,5-cyclooctadiene (0.35 mL, 2.85 mmol), and 2,2'-bipyridine (0.432 g, 2.77 mmol) were dissolved in dry THF (60 mL) and the mixture was stirred at $60^\circ C$ for 14.5 h. The reaction mixture was concentrated under reduced pressure and absorbed on silica gel. The mixture was extracted with toluene (R_f = 0.96) by using Soxhlet extractor and the resulting solution was concentrated under reduced pressure. The solid was washed with hexane to give 553.3 mg (0.813 mmol) of **3** in 71% yield as yellow solids.

mp: 363.2–364.2 °C; ^1H NMR (300 MHz, CD_2Cl_2): δ 7.60 (d, $^4J(\text{H},\text{H}) = 1.2$ Hz, 2H), 7.34 (dd, $^3J(\text{H},\text{H}) = 7.8$, $^4J(\text{H},\text{H}) = 2.1$ Hz, 2H), 7.20 (d, $^3J(\text{H},\text{H}) = 9.0$ Hz, 2H), 7.07–6.95 (m, 8H), 6.73 (dd, $^3J(\text{H},\text{H}) = 6.3$ Hz, $^4J(\text{H},\text{H}) = 1.8$ Hz, 4H); ^{13}C NMR spectrum was not able to be recorded due to its poor solubility. HRMS (FAB) (m/z): $[\text{M}]^+$ calcd. for $\text{C}_{38}\text{H}_{18}\text{F}_6\text{N}_2\text{O}_4$, 680.1171; found, 680.1169; Elemental analysis calcd (%) for $\text{C}_{38}\text{H}_{18}\text{F}_6\text{N}_2\text{O}_4$: C 67.06, H 2.67, N 4.12; found: C 67.20, H 2.61, N 4.25.

4-Bromo-N,N-bis(2,4-dimethoxyphenyl)-2,6-difluoroaniline (16).

2,4-Dimethoxyiodobenzene **13** (20.4 g, 77.2 mmol), 4-bromo-2,6-difluoroaniline **14** (6.86 g, 33.0 mmol), K_2CO_3 (18.2 g, 132 mmol), and copper powder (6.80 g, 107 mmol) were dissolved in dry ODCB (90 mL) and stirred at 180 °C for 150 h. The insoluble materials were filtered off, and extracted with CH_2Cl_2 (100 mL × 3). The combined organic solution was washed with water. The organic phase was dried over MgSO_4 , filtered off, and concentrated under reduced pressure. The obtained crude product was purified by silica gel column chromatography (CH_2Cl_2 : hexane = 3 : 1, $R_f = 0.56$) to give 9.63 g (20.1 mmol) of **16** in 61% yield as white solids.

mp: 119.2–120.1 °C; ^1H NMR (300 MHz, CDCl_3): δ 6.97–6.86 (m, 2H), 6.82 (d, $^3J(\text{H},\text{H}) = 8.4$ Hz, 2H), 6.45 (d, $^4J(\text{H},\text{H}) = 2.7$ Hz, 2H), 6.38 (dd, $^3J(\text{H},\text{H}) = 8.4$ Hz, $^4J(\text{H},\text{H}) = 2.7$ Hz, 2H), 3.78 (s, 6H), 3.59 (s, 6H); ^{13}C NMR (75 MHz, CDCl_3): δ 159.0 (dd, $^1J(\text{C},\text{F}) = 248.4$ Hz, $^3J(\text{C},\text{F}) = 6.3$ Hz), 157.0, 154.6, 131.0, 125.7 (t, $^3J(\text{C},\text{F}) = 12.5$ Hz), 125.3, 123.0 (t, $^3J(\text{C},\text{F}) = 9.8$ Hz), 111.7 (dd, $^2J(\text{C},\text{F}) = 16.0$ Hz, $^4J(\text{C},\text{F}) = 8.0$ Hz), 104.8, 100.9, 56.4, 55.6; HRMS (FAB) (m/z): $[\text{M}]^+$ calcd. for $\text{C}_{22}\text{H}_{20}\text{BrF}_2\text{NO}_4$, 479.0544; found, 479.0544; Elemental analysis calcd (%) for $\text{C}_{22}\text{H}_{20}\text{BrF}_2\text{NO}_4$: C 55.01, H 4.20, N 2.92; found: C 54.99, H 4.18, N 2.99.

7-Bromo-3,11-dimethoxybenzo[5,6][1,4]oxazino[2,3,4-*k*]phenoxazine (18).

16 (4.68 g, 9.77 mmol) was dissolved in dry CH_2Cl_2 (190 mL). The solution was cooled to –78 °C, then BBr_3 (6.50 mL, 68.6 mmol) was added. The mixture was slowly warmed up to room temperature and stirred for 3 h. The reaction mixture was poured into 1M HCl aq. (100 mL) and the products were extracted with ethyl acetate (50 mL × 3). The organic phase was dried over Na_2SO_4 , filtered off, and concentrated under reduced pressure to give 4.08 g (9.61 mmol) of the crude product as brown solids in 98% yield.

86% of this solid (3.50 g, 8.26 mmol) was dissolved in DMF (200 mL). K_2CO_3 (6.85 g, 49.6 mmol) was added and the mixture was stirred at 100 °C for 14 h. After the solution was cooled to room temperature, iodomethane (2.00 mL, 32.1 mmol) was added. The

solution was further stirred at 60 °C for 5 h. After addition of 1M HCl aq. (100 mL), the product was extracted with ethyl acetate (100 mL × 3). The organic phase was dried over Na₂SO₄, filtered off, and concentrated under reduced pressure. The obtained crude product was purified by silica gel short column chromatography (CH₂Cl₂, *R*_f = 0.85) to give 2.29 g (5.56 mmol) of **18** in 67% yield as white solids.

¹H NMR (300 MHz, C₆D₆): δ 6.89 (d, ³J(H,H) = 9.7 Hz, 2H), 6.56 (s, 2H), 6.46 (d, ⁴J(H,H) = 2.7 Hz, 2H), 6.28 (dd, ³J(H,H) = 9.7 Hz, ⁴J(H,H) = 2.7 Hz, 2H), 3.21 (s, 6H; OMe); ¹³C NMR (75 MHz, C₆D₆): δ 156.3, 147.7, 145.6, 122.5, 121.2, 115.0, 114.77, 114.74, 108.9, 104.2, 55.1; HRMS (FAB) (*m/z*): [M]⁺ calcd. for C₂₀H₁₄BrNO₄, 411.0106; found, 411.0087; Elemental analysis calcd (%) for C₂₀H₁₄BrNO₄: C 58.27, H 3.42, N 3.40; found: C 58.35, H 3.44, N 3.39.

3,3',11,11'-Tetramethoxy-7,7'-dibenzo[5,6][1,4]oxazino[2,3,4-*k*l]phenoxazine (4)

18 (1.85 g, 4.50 mmol), Ni(cod)₂ (1.49 g, 5.41 mmol), 1,5-cyclooctadiene (0.586 g, 5.42 mmol), and 2,2'-bipyridine (0.843 g, 5.40 mmol) were dissolved in dry THF (130 mL) and the mixture was stirred at 60 °C for 12 h. The reaction mixture was absorbed on silica gel. The mixture was extracted with toluene (*R*_f = 0.95) by using Soxhlet extractor and the resulting solution was concentrated under reduced pressure. The solid was washed with hexane to give 0.810 g (1.22 mmol) of **4** in 54% yield as yellow solids.

mp: 351.8–353.8 °C; ¹H NMR (300 MHz, CD₂Cl₂-CS₂ = 1 : 1): δ 6.99 (d, ³J(H,H) = 8.7 Hz, 4H), 6.44 (s, 4H), 6.34 (d, ⁴J(H,H) = 2.7 Hz, 4H), 6.27 (dd, ³J(H,H) = 8.7 Hz, ⁴J(H,H) = 2.7 Hz, 4H), 3.52 (s, 12H); ¹³C NMR spectrum was not able to be recorded due to its poor solubility. HRMS (FAB) (*m/z*): [M]⁺ calcd. for C₄₀H₂₈N₂O₈, 664.1846; found, 664.1818; Elemental analysis calcd (%) for C₄₀H₂₈N₂O₈: C 72.28, H 4.25, N 4.21; found: C 72.33, H 4.28, N 4.25.

Computation method.

DFT calculations for optimization, reorganization energies, and inversion barrier were conducted using the Gaussian 09 program.¹⁸ Calculations of electronic couplings for crystal structures were conducted using ADF program.¹⁴

X-Ray crystal structure analysis.

Crystallographic data have been deposited with the Cambridge Crystallographic Data Center as supplementary publication no. CCDC-978719 (**1**), CCDC-978720 (**2** (needle)), CCDC-978721 (**2** (plate)), CCDC-978722 (**3**), and CCDC-978723 (**4**). These data can be obtained free of charge from The Cambridge Crystallographic Data Centre

via www.ccdc.cam.ac.uk/data_request/cif.

Compound 1. Single crystals suitable for X-ray analysis were obtained by sublimation (320 °C, 1 mmHg). Intensity data were collected at 100 K on a Rigaku Single Crystal CCD X-ray Diffractometer (Saturn 70 with MicroMax-007) with Mo K α radiation ($\lambda = 0.71070 \text{ \AA}$) and graphite monochromater. The collected diffraction data were processed with the HKL2000 software program. A total of 10621 reflections were measured with a maximum 2 θ angle of 53.0°, of which 2412 were independent reflections ($R_{\text{int}} = 0.0344$). The structure was solved by direct methods (SHELXS-97¹⁹) and refined by the full-matrix least-squares on F^2 (SHELXL-97¹⁹). All non-hydrogen atoms were refined anisotropically. All hydrogen atoms were placed using AFIX instructions. The crystal data are as follows: C₃₆H₂₀N₂O₄; FW = 544.54, crystal size 0.20 × 0.05 × 0.01 mm³, Monoclinic, P2₁/c, $a = 15.0313(3) \text{ \AA}$, $b = 3.78850(10) \text{ \AA}$, $c = 20.8910(4) \text{ \AA}$, $\beta = 92.7778(10)^\circ$, $V = 1188.26(5) \text{ \AA}^3$, $Z = 2$, $D_c = 1.522 \text{ g cm}^{-3}$. The refinement converged to $R_1 = 0.0378$, wR₂ = 0.0997 ($I > 2\sigma(I)$), GOF = 1.024.

Compound 2 (needle-like crystal). Single crystal suitable for X-ray crystal structure analysis were obtained by recrystallization from a toluene solution at 110–120 °C. Single-crystal X-ray data were collected at 153 K on a on a Rigaku Single Crystal CCD X-ray Diffractometer (Saturn 70 with MicroMax-007) with Mo K α radiation ($\lambda = 0.71075 \text{ \AA}$) and graphite monochromater. The collected diffraction data were processed with the HKL2000 software program. A total of 6127 reflections were measured at the maximum 2 θ angle of 51.0°, of which 2195 were independent reflections ($R_{\text{int}} = 0.0314$). The structure was solved by direct methods (SHELXS-97¹⁹) and refined by the full-matrix least-squares on F^2 (SHELXL-97¹⁹). All non-hydrogen atoms were refined anisotropically. All hydrogen atoms were placed using AFIX instructions. The crystal data are as follows: C₃₆H₂₀N₂O₄; FW = 544.54, crystal size 0.15 × 0.10 × 0.02 mm³, Triclinic, P-1, $a = 3.7530(2) \text{ \AA}$, $b = 9.9323(4) \text{ \AA}$, $c = 16.1659(8) \text{ \AA}$, $\alpha = 86.2985(19)^\circ$, $\beta = 84.906(2)^\circ$, $\gamma = 83.653(4)^\circ$, $V = 595.63(5) \text{ \AA}^3$, $Z = 1$, $D_c = 1.518 \text{ g cm}^{-3}$. The refinement converged to $R_1 = 0.0353$, wR₂ = 0.0914 ($I > 2\sigma(I)$), GOF = 1.033.

Compound 2 (plate-like crystal). Single crystal suitable for X-ray analysis were obtained by recrystallization from an *o*-dichlorobenzene solution at 140–160 °C. Intensity data were collected at 100 K on a Bruker Single Crystal CCD X-ray Diffractometer (SMART APEX) with Mo K α radiation ($\lambda = 0.71070 \text{ \AA}$) and graphite monochromater. A total of 12321 reflections were measured with a maximum 2 θ angle

of 51.0° , of which 4426 were independent reflections ($R_{\text{int}} = 0.0321$). The structure was solved by direct methods (SHELXS-97¹⁹) and refined by the full-matrix least-squares on F^2 (SHELXL-97¹⁹). All non-hydrogen atoms were refined anisotropically. All hydrogen atoms were placed using AFIX instructions. The crystal data are as follows: $\text{C}_{36}\text{H}_{20}\text{N}_2\text{O}_4$; FW = 544.54, crystal size $0.25 \times 0.20 \times 0.05 \text{ mm}^3$, Monoclinic, $P2_1/a$, $a = 7.1216(6) \text{ \AA}$, $b = 32.802(3) \text{ \AA}$, $c = 10.2152(9) \text{ \AA}$, $\beta = 91.043(2)^\circ$, $V = 2385.9(4) \text{ \AA}^3$, $Z = 4$, $D_c = 1.516 \text{ g cm}^{-3}$. The refinement converged to $R_1 = 0.0442$, $wR_2 = 0.0880$ ($I > 2\sigma(I)$), GOF = 1.030.

Compound 3. Single crystals suitable for X-ray analysis were obtained by sublimation (260–290 °C, 0.06 mmHg). Intensity data were collected at 103 K using a diffractometer equipped with an ADSC Quantun315 CCD detector with synchrotron radiation at a wavelength of 0.75 Å at the SPring-8 beamline BL38B1. A total of 7967 reflections were measured with a maximum 2θ angle of 51.0° , of which 1921 were independent reflections ($R_{\text{int}} = 0.0635$). The collected diffraction data were processed with the HKL2000 software program. The structure was solved by direct methods (SHELXS-97¹⁹) and refined by the full-matrix least-squares on F^2 (SHELXL-97¹⁹). The molecule sits on symmetric axis. The CF_3 moieties were disordered and were solved using an appropriate disordered model with the occupancies of C19A, F1A–F3A and C19B, F1B–F3B as 0.5 and 0.5, respectively. Since the molecule exhibits pseudo- C_i symmetry due to inevitable severe disorder of the CF_3 moieties, the number of the parameters gets larger with anisotropic temperature factors. Therefore, it is necessary to collect reflections in the wide range of θ_{max} in order to get the numbers of reflections over 10-times of the parameters. In these reasons, the completeness of data to the range of $\theta_{\text{max}} = 28^\circ$ seems to be somewhat insufficient as pointed out with Alert A. However, the author believes the enough data necessary for the high-resolution analysis could be collected sufficiently, and the analysis has been well done with sufficient accuracy. All non-hydrogen atoms were refined anisotropically. All hydrogen atoms were placed using AFIX instructions. The crystal data are as follows: $\text{C}_{38}\text{H}_{18}\text{F}_6\text{N}_2\text{O}_4$; FW = 680.54, crystal size $0.10 \times 0.10 \times 0.02 \text{ mm}^3$, Monoclinic, $C2/c$, $a = 22.1065(3) \text{ \AA}$, $b = 3.7146(1) \text{ \AA}$, $c = 33.3362(3) \text{ \AA}$, $\beta = 92.0252(5)^\circ$, $V = 2735.75(9) \text{ \AA}^3$, $Z = 4$, $D_c = 1.652 \text{ g cm}^{-3}$. The refinement converged to $R_1 = 0.0595$, $wR_2 = 0.1440$ ($I > 2\sigma(I)$), GOF = 1.052.

Compound 4. Single crystals suitable for X-ray analysis were obtained by sublimation (270–300 °C, 0.06 mmHg). Intensity data were collected at 100 K on a Bruker Single Crystal CCD X-ray Diffractometer (SMART APEX) with Mo K α radiation ($\lambda =$

0.71070 Å) and graphite monochromater. A total of 6902 reflections were measured with a maximum 2θ angle of 51.0°, of which 2665 were independent reflections ($R_{\text{int}} = 0.0310$). The structure was solved by direct methods (SHELXS-97¹⁹) and refined by the full-matrix least-squares on F^2 (SHELXL-97¹⁹). All non-hydrogen atoms were refined anisotropically. All hydrogen atoms were placed using AFIX instructions. The crystal data are as follows: C₄₀H₂₀N₂O₈; FW = 664.64, crystal size 0.20 × 0.08 × 0.05 mm³, Monoclinic, C2/c, $a = 28.226(4)$ Å, $b = 3.7761(5)$ Å, $c = 27.100(3)$ Å, $\beta = 97.531(2)$ °, $V = 2863.5(6)$ Å³, $Z = 4$, $D_c = 1.542$ g cm⁻³. The refinement converged to $R_1 = 0.0415$, $wR_2 = 0.0933$ ($I > 2\sigma(I)$), GOF = 1.031.

Time-resolved microwave conductivity (TRMC) method.¹⁵

Transient photoconductivity was measured by flash-photolysis time-resolved microwave conductivity (FP-TRMC). A resonant cavity was used to obtain a high degree of sensitivity in the measurement of conductivity. The resonant frequency and the microwave power were set at ~9.1 GHz and 3 mW, respectively, so that the electric field of the microwave was sufficiently small not to disturb the motion of charge carriers. The value of conductivity is converted to the product of the quantum yield ϕ and the sum of charge carrier mobilities $\Sigma\mu$, by $\phi\Sigma\mu = \Delta\sigma(eI_0F_{\text{light}})^{-1}$, where e , I_0 , F_{light} , and $\Delta\sigma$ are the unit charge of a single electron, incident photon density of excitation laser (photons/m²), a correction (or filling) factor (/m), and a transient photoconductivity, respectively. The change of conductivity is equivalent with $\Delta P_r/(AP_r)$, where ΔP_r , P_r , and A are change of reflected microwave power, a power of reflected microwave, and a sensitivity factor [(S/m)⁻¹], respectively. Third harmonic generation (THG, 355 nm) of a Nd:YAG laser (Spectra Physics Inc. INDI, 5–8 ns pulse duration) was used as an excitation source. The incident photon density was set at 9.1×10^{15} photons cm⁻². The sample was set at the highest electric field in a resonant cavity. FP-TRMC experiments were performed at room temperature.

The values of ϕ in the compounds were determined by conventional photo-current measurement in a vacuum chamber (10^{-4} Pa) using an inter-digitated Au electrodes on a glass substrate with 5 μm gap under excitation at 355 nm with the photon density of 9.1×10^{15} photons/cm². Crystal samples were prepared by alignment of several dozens of crystals on a quartz substrate. In addition to crystal samples, film samples were prepared by vapor deposition onto a quartz substrate in a vacuum chamber (10^{-4} Pa) at a 100 nm thick. Transient current was predominantly observed on the film sample under the applied bias of 0–10 V ($0–2.0 \times 10^4$ Vcm⁻¹), and monitored by a Tektronix TDS3032B digital oscilloscope.

Two-dimentional grazing-incidence X-ray diffraction (2D-GIXD) measurements.

Grazing incidence X-ray diffraction (GIXD) measurements were conducted at the SPring-8 on beamline BL19B2. The sample was irradiated at a fixed incident angle on the order of 0.12° through a Huber diffractometer with an X-ray energy of 12.39 keV ($\lambda = 1 \text{ \AA}$). The GIXD patterns were recorded with a 2D image detector (Pilatus 300K). Samples for the X-ray measurements were prepared by vapor deposition onto a quartz substrate in a vacuum chamber (10^{-4} Pa) at a 100 nm thick.

Reference

1. (a) Anthony, J. E. *Angew. Chem., Int. Ed.* **2008**, *47*, 452. (b) Klauk, H. *Chem. Soc. Rev.* **2010**, *39*, 2643. (c) Wang, C.; Dong, H.; Hu, W.; Liu, Y.; Zhu, D. *Chem. Rev.* **2012**, *112*, 2208.
2. (a) Shirota, Y.; Kageyama, H. *Chem. Rev.* **2007**, *107*, 953. (b) Xiao, L.; Chen, Z.; Qu, B.; Luo, J.; Kong, S.; Gong, Q.; Kido, J. *Adv. Mater.* **2011**, *23*, 926.
3. (a) Walker, B.; Kim, C.; Nguyen, T.-Q. *Chem. Mater.* **2011**, *23*, 470. (b) Facchetti, A. *Chem. Mater.* **2011**, *23*, 733. (c) Mishra, A.; Bäuerle, P. *Angew. Chem., Int. Ed.* **2012**, *51*, 2020. (d) Kularatne, R. S.; Magurudeniya, H. D.; Sista, P.; Biewer, M. C.; Stefan, M. C. *J. Polym. Sci., Part A: Polym. Chem.* **2013**, *51*, 743. (e) Osaka, I.; Kakara, T.; Takemura, N.; Koganezawa, T.; Takimiya, K. *J. Am. Chem. Soc.* **2013**, *135*, 8834.
4. Coropceanu, V.; Cornil, J.; Filho, D. A. S.; Olivier, Y.; Silbey, R.; Brédas, J.-L. *Chem. Rev.* **2007**, *107*, 926.
5. Holmes, D.; Kumaraswamy, S.; Matzger, A. J.; Vollhardt, K. P. C. *Chem.–Eur. J.* **1999**, *5*, 3399.
6. (a) Anthony, J. E.; Brooks, J. S.; Eaton, D. L.; Parkin, S. R. *J. Am. Chem. Soc.* **2001**, *123*, 9482. (b) Zhang, X.; Coté, A. P.; Matzger, A. J. *J. Am. Chem. Soc.* **2005**, *127*, 10502. (c) Miao, Q.; Chi, X.; Xiao, S.; Zeis, R.; Lefenfeld, M.; Siegrist, T.; Steigerwald, M. L.; Nuckolls, C. *J. Am. Chem. Soc.* **2006**, *128*, 1340.
7. (a) Huang, L.-Q.; Cao, Q.-Y.; Yi, C. Yang, C.-J.; Gao, X.-C. *Acta Crystallogr., Sect. E: Struct Rep. Online* **2006**, *62*, o2075. (b) Zhang, Z.; Burkholder, E.; Zubietta, J. *Acta Crystallogr., Sect. C: Crys. Struct. Commun.* **2004**, *60*, o452.
8. Yamada, T.; Sato, T.; Tanaka, K.; Kaji, H. *Org. Electron.* **2010**, *11*, 255.
9. Kuratsu, M.; Kozaki, M.; Okada, K. *Chem. Lett.* **2004**, *33*, 1174.
10. Bushby, R. J.; Kilner, C. A.; Taylor, N.; Vale, M. E. *Tetrahedron* **2007**, *63*, 11458.
11. Yamamoto, T.; Morita, A.; Miyazaki, Y.; Maruyama, T.; Wakayama, H.; Zhou,

- Z.-h.; Nakamura, Y.; Kanbara, T. *Macromolecules* **1992**, *25*, 1214.
- 12. Pommerehne, J.; Vestweber, H.; Guss, W.; Mahrt, R. F.; Bässler, H.; Porsch, M.; Daub, J. *Adv. Mater.* **1995**, *7*, 551.
 - 13. Cardona, C. M.; Li, W.; Kaifer, A. E.; Stockdale, D.; Bazan, G. C. *Adv. Mater.* **2011**, *23*, 2367.
 - 14. ADF2012.01, SCM, Theoretical Chemistry, Vrije Universiteit, Amsterdam, The Netherlands, <http://www.scm.com>.
 - 15. (a) Saeki, A.; Koizumi, Y.; Aida, T.; Seki, S. *Acc. Chem. Res.* **2012**, *45*, 1193. (b) Saeki, A.; Seki, S.; Takenobu, T.; Iwasa, Y.; Tagawa, S. *Adv. Mater.* **2008**, *20*, 920. (c) Yasutani, Y.; Saeki, A.; Fukumatsu, T.; Koizumi, Y.; Seki, S. *Chem. Lett.* **2013**, *42*, 19.
 - 16. (a) Yokoyama, D.; *J. Mater. Chem.* **2011**, *21*, 19187–19202 and references cited therein; b) Yokoyama, D.; Sakaguchi, A.; Suzuki, M.; Adachi, C. *Appl. Phys. Lett.* **2008**, *93*, 173302.
 - 17. (a) Kojima, A.; Teshima, K.; Shirai, Y.; Miyasaka, T. *J. Am. Chem. Soc.* **2009**, *131*, 6050. (b) Lee, M. M.; Teuscher, J.; Miyasaka, T.; Murakami, T. N.; Snaith, H. J. *Science* **2012**, *338*, 643. (c) Heo, J. H.; Im, S. H.; Noh, J. H.; Mandal, T. N.; Lim, C.-S.; Chang, J. A.; Lee, Y. H.; Kim, H.; Sarkar, A.; Nazeeruddin, M. K.; Grätzel, M.; Seok, S. I. *Nat. Photon.* **2013**, *7*, 486.
 - 18. Gaussian 09 (Revision A.02), Frisch, M. J.; Trucks, G. W.; Schlegel, H. B.; Scuseria, G. E.; Robb, M. A.; Cheeseman, J. R.; Scalmani, G.; Barone, V.; Mennucci, B.; Petersson, G. A.; Nakatsuji, H.; Caricato, M.; Li, X.; Hratchian, H. P.; Izmaylov, A. F.; Bloino, J.; Zheng, G.; Sonnenberg, J. L.; Hada, M.; Ehara, M.; Toyota, K.; Fukuda, R.; Hasegawa, J.; Ishida, M.; Nakajima, T.; Honda, Y.; Kitao, O.; Nakai, H.; Vreven, T.; Montgomery, Jr., J. A.; Peralta, J. E.; Ogliaro, F.; Bearpark, M.; Heyd, J. J.; Brothers, E.; Kudin, K. N.; Staroverov, V. N.; Keith, T.; Kobayashi, R.; Normand, J.; Raghavachari, K.; Rendell, A.; Burant, J. C.; Iyengar, S. S.; Tomasi, J.; Cossi, M.; Rega, N.; Millam, J. M.; Klene, M.; Knox, J. E.; Cross, J. B.; Bakken, V.; Adamo, C.; Jaramillo, J.; Gomperts, R.; Stratmann, R. E.; Yazyev, O.; Austin, A. J.; Cammi, R.; Pomelli, C.; Ochterski, J. W.; Martin, R. L.; Morokuma, K.; Zakrzewski, V. G.; Voth, G. A.; Salvador, P.; Dannenberg, J. J.; Dapprich, S.; Daniels, A. D.; Farkas, O.; Foresman, J. B.; Ortiz, J. V.; Cioslowski, J.; Fox, D. J., Gaussian, Inc., Wallingford CT, 2009.
 - 19. Sheldrick, G. M. SHELX-97, Program for the Refinement of Crystal Structures; University of Göttingen: Göttingen, Germany, 1997.

Chapter 2

The Influence of Quasiplanar Structures of Partially Oxygen-Bridged Triphenylamine Dimers on the Properties of their Bulk Films

Abstract: The molecular orientations in the amorphous films of doubly oxygen-bridged triphenylamine dimers **1** and **2** with quasiplanar structure were examined by fluorescence spectroscopy. Fluorescence spectroscopy revealed that **1** and **2** retain two different states in the bulk amorphous films, i.e., the monomer-like random orientation and the crystalline-like π -stacking orientation. Regarding the crystalline-like π -stacking orientation, **1** forms one-dimensional π -stacking structure whereas **2** forms two-dimensional π -stacking structure, reflecting the difference in molecular structure. Arising from the retained π -stacking, **1** showed strong electric field dependency of charge mobilities in the bulk film. On the other hand, **2** exhibited higher electron mobility as well as high hole mobility, exhibiting ambipolar properties. When these dimers were used as hole-injection layer in the organic light-emitting diode (OLED) devices, the external quantum efficiencies became superior to that of the standard device.

Introduction

In Chapter 1, the synthesis and fundamental properties of a series of doubly oxygen-bridged triarylamine dimers were described.¹ In the crystalline states, these dimers were found to have a tendency to form one-dimensional on-top π -stacking providing dense molecular packing owing to their quasiplanar skeleton. Since these dimers are stable at high temperature, preparations of the vacuum-deposited films are possible. Two-dimensional grazing-incidence X-ray diffraction (2D-GIXD)² and time-resolved microwave conductivity (TRMC)³ measurements revealed that these dimers retained some degree of the face-on π -stacking crystal structures even in the amorphous films, thus facilitating an out-of-plane charge mobility. Although TRMC measurements allow the evaluation of the intrinsic charge mobility and its anisotropy if present, this method measures the local mobility of charge carriers in the small area (~ 20 nm) without any contact to metal electrodes, which is different from the bulk mobility that should be crucial in the device application.

In this Chapter, the author focused his attention on the properties of the bulk material, especially of the vacuum-deposited films of dimers **1** and **2** with quasiplanar structures, in which doubly oxygen-bridged triphenylamine skeletons are connected at the different positions (Figure 1a,b). Firstly, the molecular orientations of these molecules in the vacuum-deposited films were examined by fluorescence spectroscopy to study the intermolecular interaction. Secondly, the author evaluated the bulk charge mobility for the amorphous films by time-of-flight (TOF)⁴ measurement and discussed them based on their packing modes of quasiplanar structures. Thirdly, the author demonstrated that these compounds could be applied as the materials for hole-injection layer in the organic light-emitting diode (OLED) devices,⁵ which increased external quantum efficiencies compared to the standard device.

Results and Discussion

Crystal Structures

As mentioned in Chapter 1, both dimers **1** and **2** form one-dimensional on-top π -stacking (1D-stacking) structures in their needle-like crystals (Figure 1c,d), whereas dimer **2**, with a different connection motif compared with **1**, has crystalline polymorphisms; needle-like crystals obtained from toluene (110–120 °C) have 1D-stacking structure (Figure 1d), while plate-like crystals prepared from *o*-dichlorobenzene at higher temperature (140–160 °C) or sublimation (265 °C, 0.1 mmHg) exhibit two-dimensional slipped π -stacking (2D-stacking) structure (Figure 1e). The author examined how these differences in packing structures in the single crystals

affect the molecular orientation and charge mobility in the amorphous films prepared by vacuum-deposition in detail.

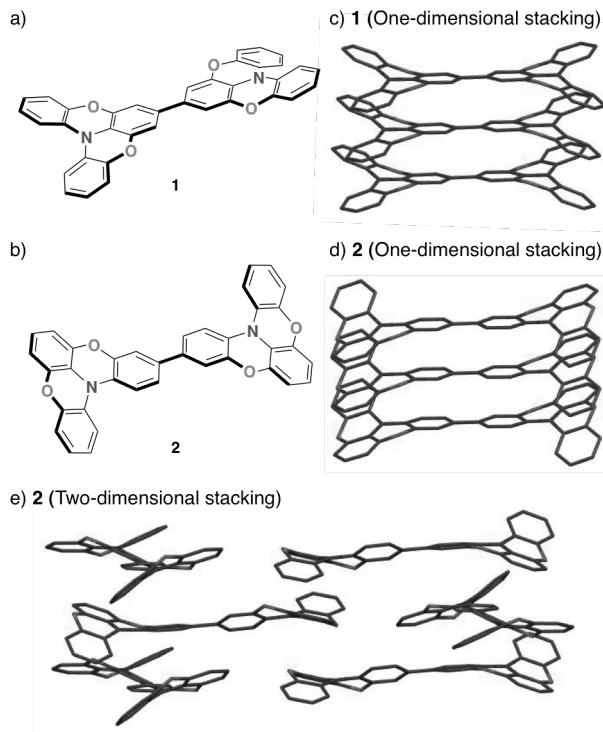


Figure 1. Molecular structures of dimers (a) **1** and (b) **2**. Packing structures determined for the single crystals of (c) **1**, (d) **2** with one-dimensional π -stacking, and (e) **2** with two-dimensional π -stacking.

Photophysical Property

As mentioned in Chapter 1, the films of **1** and **2** were prepared by vacuum deposition. Both films exhibit no distinct diffraction peaks in wide-angle X-ray scattering measurements using a laboratory X-ray diffractometer equipped with a sealed-tube X-ray generator (RIGAKU Ultima IV), suggesting that these films are essentially amorphous. In order to examine the molecular orientation of these dimers in the bulk films, i.e., completely random orientation of the molecules with small intermolecular interaction and/or partial crystalline state being kept with strong intermolecular interaction, UV-vis absorption and fluorescence spectroscopies were conducted on the single crystals, the amorphous films, and their CH_2Cl_2 solutions (Figure 2). The thicknesses of amorphous films of **1** and **2** are 120 nm and 130 nm,

respectively. In UV-vis absorption spectra, the amorphous films of **1** and **2** show absorption bands at 400 nm and 405 nm, respectively. These are slightly red-shifted compared with those for CH_2Cl_2 solutions (**1**: 387 nm, **2**: 397 nm), suggesting that intermolecular interaction exists in some extent in the amorphous films.

Upon fluorescence measurements, which would give further information, crystalline **1** shows an emission band at 491 nm ($\Phi = 0.40$), which is significantly red-shifted compared to that in CH_2Cl_2 solution (451 nm, $\Phi = 0.51$), with slight decrease in quantum yield as shown in Figure 2a. This should be attributed to strong intermolecular interaction at the excited state arising from the on-top π -stacking structure. Similarly, crystalline **2** with 1D-stacking and 2D-stacking structures show emission bands at 511 nm ($\Phi = 0.55$) and 474 nm ($\Phi = 0.17$), respectively, both of which are red-shifted compared to that in CH_2Cl_2 solution (449 nm, $\Phi = 0.69$). In comparison between these two crystals, i.e., 1D- and 2D-stackings, the red-shift observed for the 2D-stacking is smaller than that for the 1D-stacking, indicating that intermolecular interaction in the 2D-stacking crystals is weaker likely due to the slipped stacking motif of the molecules. Based on the observed difference in fluorescence spectra of the crystalline states of **1** and **2**, the molecular orientation of **1** and **2** in the amorphous films was examined.

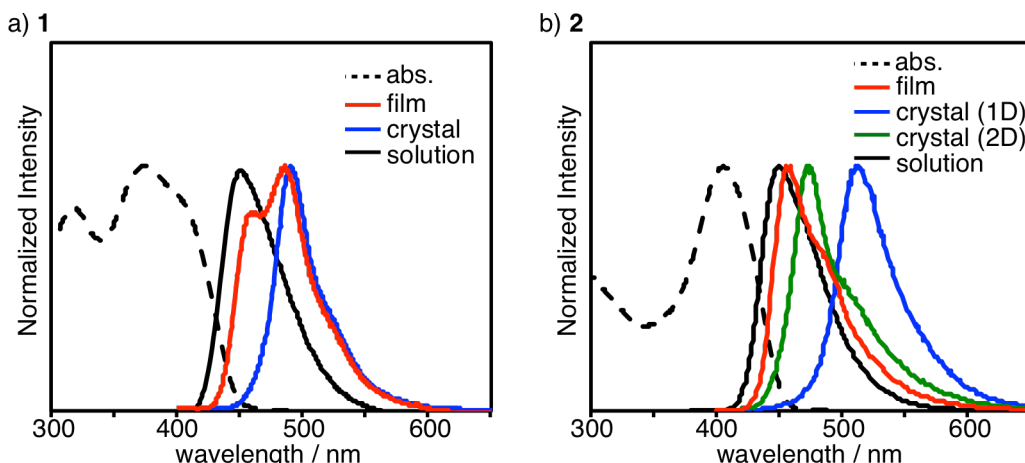


Figure 2. UV-vis absorption spectra in the amorphous films (dashed line in black) and fluorescence spectra (solid lines) of (a) **1** and (b) **2**; amorphous films on a quartz (red), grinded 1D-stacking crystals (blue), grinded 2D-stacking crystals (green), and CH_2Cl_2 solution (black) as a reference.

The amorphous film of **1** exhibits two emission bands at 456 nm and 487 nm. The emission at 487 nm corresponds to that observed for the 1D-stacking crystals (491 nm), showing that the amorphous film has a similar molecular orientation with the 1D-stacking with intermolecular interaction. In contrast, the emission at 456 nm is similar to that in CH₂Cl₂ solution (451 nm), suggesting that situation of the molecules in the amorphous film are similar to that of the solution, i.e., single molecule surrounded by another molecules without considerable intermolecular interaction between the neighbor molecules. Appearance of these two bands indicates that two different states of molecular orientation coexist in the amorphous film of **1** at the same time and probably by fine phase separation, i.e., the crystalline-like on-top π -stacking orientation with strong intermolecular interaction between the neighbor molecules and the monomer-like random orientation with less intermolecular interaction.

The amorphous film of **2** also exhibits two fluorescence bands at 456 nm and 480 nm, indicating coexistence of the monomer-like random orientation and π -stacking orientation in the same manner observed for the amorphous film of **1**. The emission band at 480 nm is very similar to the emission from the 2D-stacking crystals (474 nm), rather than that from the 1D-stacking crystals (511 nm), demonstrating that the major packing mode observed in the amorphous film should correspond to the 2D-stacking. This is rationalized by considering that the plate-like single crystals with 2D-stacking are obtained by sublimation (265 °C, 0.1 mmHg) under the similar conditions to prepare the vacuum-deposited amorphous film.

Charge Mobility in the Amorphous Film

Bulk hole mobilities in the amorphous films of **1** and **2**, with a thickness of 4.9 μm and 3.7 μm , respectively, were measured using time-of-flight (TOF) technique. Figure 3a shows the electric field dependence of the logarithmic hole mobilities (μ_h) for the films of **1**, **2**, and *N,N'*-di(1-naphthyl)-*N,N'*-diphenylbenzidine (α -NPD), traditionally used for OLED as a hole-transporting material.⁶ It was shown that the hole mobility μ_h of **2** was in the range of 2.9×10^{-4} to $1.7 \times 10^{-3} \text{ cm}^2/\text{Vs}$, which is comparable with that of α -NPD ($\mu_h = 6.1 \times 10^{-4}$ to $1.5 \times 10^{-3} \text{ cm}^2/\text{Vs}$), with moderate electric field dependency in both cases. However, for the hole mobility of **1**, a significant electric field dependency was observed. Thus, the lower hole mobility of $7.5 \times 10^{-5} \text{ cm}^2/\text{Vs}$ than that of α -NPD was determined for the film of **1** under the low electric field ($E^{1/2} = 400 \text{ V}^{1/2}/\text{cm}^{1/2}$), whereas the value significantly increases as the stronger electric field is applied. Under the high electric field ($E^{1/2} > 600 \text{ V}^{1/2}/\text{cm}^{1/2}$), that is general value applied in OLED devices, the comparable hole mobility of $8.1 \times 10^{-4} \text{ cm}^2/\text{Vs}$ was

observed. Accordingly, the hole mobility of **1** was found to increase by 11 times at the maximum within the applied conditions.

Although these compounds were designed for hole-transporting materials, electron mobility (μ_e) of **1** and **2** were also measured by TOF technique (Figure 3b). While electron mobility of **1** also showed strong electric field dependency, moderate electron mobility ($\mu_e = 1.2 \times 10^{-5}$ to $1.2 \times 10^{-4} \text{ cm}^2/\text{Vs}$) was obtained, which is one-order lower than its hole mobility. In contrast to **1**, surprisingly, high electron mobility of $\mu_e = 1.2 \times 10^{-3}$ to $2.8 \times 10^{-3} \text{ cm}^2/\text{Vs}$ was observed for the film of **2**, which is in the same order with its hole mobility. This result indicates potential use of **2** as ambipolar charge-transporting materials.

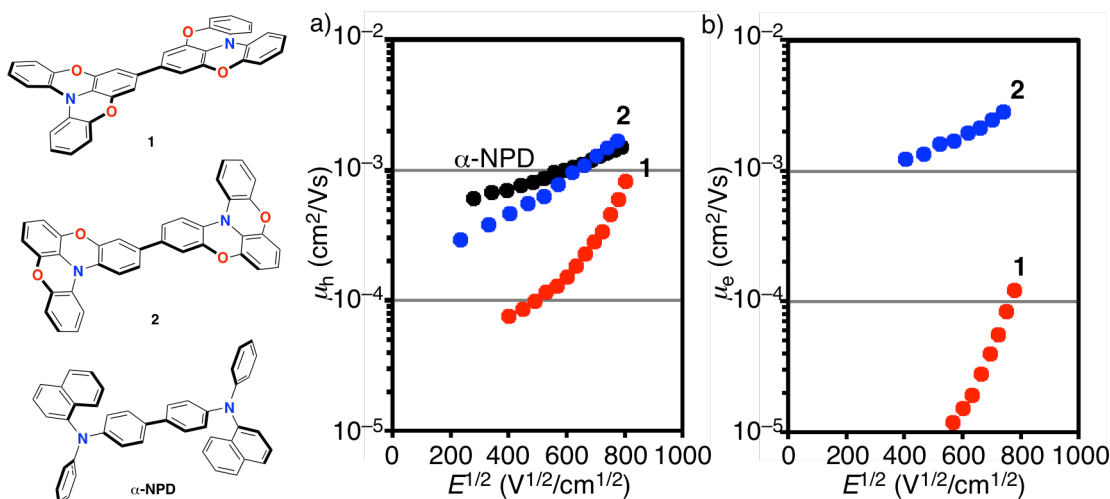


Figure 3. (a) Hole and (b) electron mobilities of **1** (red), **2** (blue) and α -NPD (black) in the amorphous films measured by TOF technique. Molecular structures of **1**, **2**, and α -NPD are also shown.

Theoretical Calculations of Charge Transport Properties

In order to elucidate the factors for the difference in charge transport properties between **1** and **2**, theoretical calculations would afford useful information. According to the Marcus theory, low reorganization energy and large electronic coupling should be important to exhibit high charge carrier mobilities.⁷ Firstly, reorganization energies for the both cationic (hole mobility) and anionic (electron mobility) species of **1** and **2** in a gas-phase were calculated by the DFT method at the B3LYP/6-31G(d) level of theory. Whereas the same values of reorganization energy were obtained for hole mobilities of

1 (0.15 eV) and **2** (0.15 eV), the value of reorganization energy for electron mobility of **2** (0.41 eV) was found to be slightly smaller than that of **1** (0.47 eV).

Secondly, electronic couplings were evaluated for the packing structures in the single crystals using the fragment analysis method embedded in the Amsterdam Differential Functional (ADF) program with PW91/DZP level of theory (Figure 4, Table 1).⁸ As mentioned in Chapter 1, the 1D-stacking crystals of **1** show anisotropy of the hole mobilities. The electronic couplings (V_{HOMO}) for **1** between the HOMOs of the two molecules along the stacking directions (82.6 meV) are significantly higher than those along side-by-side directions (0.31–1.48 meV). In contrast, V_{HOMO} for the 2D-stacking crystals of **2** (3.41–12.8 meV) are moderate in all directions with small anisotropy, due to their slipped stacking without a dominant π -stacking along specific directions.

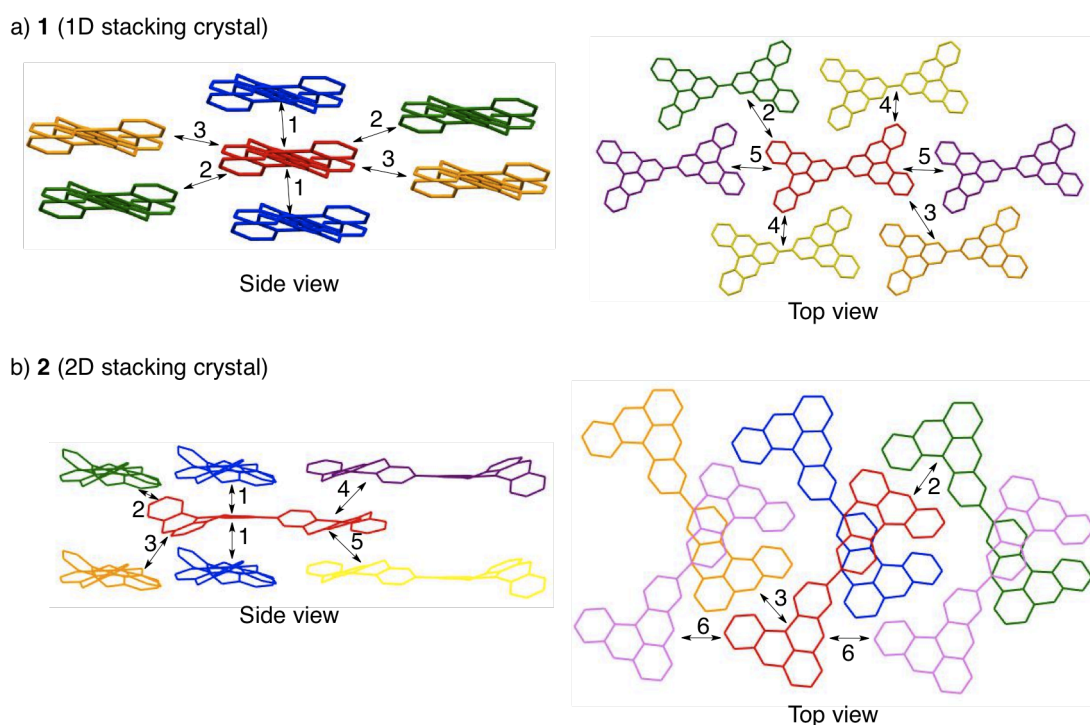


Figure 4. Packing structure and possible pairs with the neighbour molecules for (a) **1** with 1D-stacking and (b) **2** with 2D-stacking.

Table 1. Summary of Electronic Couplings between Neighbor Molecules for Crystals of **1 (1D-stacking) and **2** (2D-stacking)^a**

Pair	1 (1D-stacking)		2 (2D-stacking)	
	V_{HOMO} (meV)	V_{LUMO} (meV)	V_{HOMO} (meV)	V_{LUMO} (meV)
1	82.6	24.4	9.43	40.9
2	0.60	3.12	12.8	20.7
3	0.31	0.96	6.16	6.15
4	1.48	6.75	4.93	8.83
5	0.66	0.68	7.06	3.86
6	—	—	3.41	3.34

^aCalculated at the PW91/DZP level.

Similar to the discussion on the hole mobility, the difference in the electron mobilities between **1** and **2** is also explained by the electronic couplings between the LUMOs (V_{LUMO}) of the neighbor molecules in the packing structures (Table 1). The 1D-stacking crystals of **1** also show strong anisotropy of the electronic couplings. The V_{LUMO} along the π -stacking directions (24.4 meV) are larger than those along side-by-side directions (0.68–6.75 meV). When the values of V_{HOMO} and V_{LUMO} along the stacking direction in the crystal of **1** are compared, the V_{LUMO} is smaller than the V_{HOMO} , which can explain the lower electron mobility observed for the amorphous film of **1** (Figure 3b). In contrast, 2D-stacking structure of **2** was found to give rather large V_{LUMO} values in some charge transport pathways (3.34–40.9 meV). These large V_{LUMO} values as well as smaller reorganization energy for electron mobility (0.41 eV) would be responsible for good electron mobility in the amorphous film of **2**.

As discussed with fluorescence spectroscopy, the amorphous film of **1** partially retains crystalline-like on-top π -stacking orientation. The strong electric field dependency of charge mobilities, either holes and electrons, observed for the amorphous film of **1** could be explained by the one-dimensional π -stacking structure existing in the film (Figure 5). In the 1D-stacking crystal, there is only one major pathway available for charge transport along the π -stacking column (Table 1). Therefore, the charge mobility of **1** would most likely be affected by the structural defects in the bulk film. In the case of high electronic fields being applied, carriers could jump such structural

defects between the 1D-stacking column, and thus, the charge transport ability is significantly increased under such conditions.

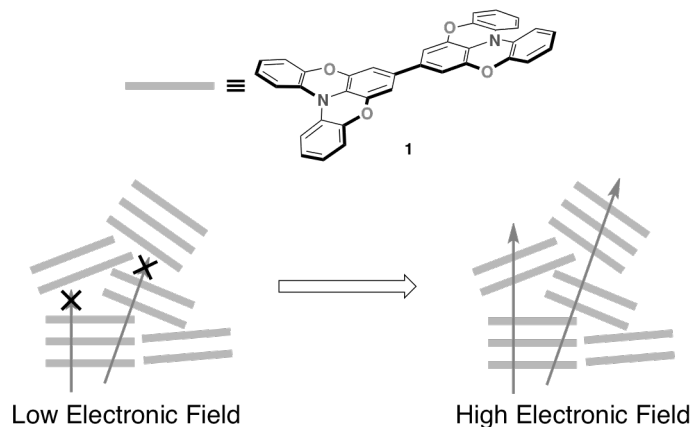


Figure 5. Schematic representation of charge transport in the amorphous film of **1**.

OLED Device Performance

Based on the hole-transporting characteristics of dimers **1** and **2** in this study, the author demonstrated the application of these materials to OLED devices. Figure 6 shows the five device structures fabricated in this study and the molecular structure of tris(8-hydroxyquinoline)aluminum(III) (Alq_3).⁹ In these devices, indium tin oxide (ITO), Alq_3 , LiF, and Al were used as anode electrode, emitting and electron-transporting layer, electron-injection layer, and cathode electrode, respectively.

Each organic layer should have appropriate energy levels of the HOMO as well as the LUMO for the effective usage as charge injection and/or transportation. The HOMO energy levels of **1**, **2**, and α -NPD in the amorphous films were directly determined by photoelectron spectroscopy. The HOMO energy levels of **1** (-5.15 eV) and **2** (-4.97 eV) thus determined are slightly higher than that of α -NPD (-5.42 eV). The LUMO energy levels were evaluated from the HOMO energy levels and the optical bandgap estimated from the absorption edge in the UV-vis spectra. The LUMO energy levels of **1** (-2.32 eV) and **2** (-2.32 eV) are high enough to block electron injection from Alq_3 (-3.25 eV).¹⁰ These results suggested the possible use of **1** and **2** as hole-transporting layer (HTL) and/or hole-injection layer (HIL) in the devices.

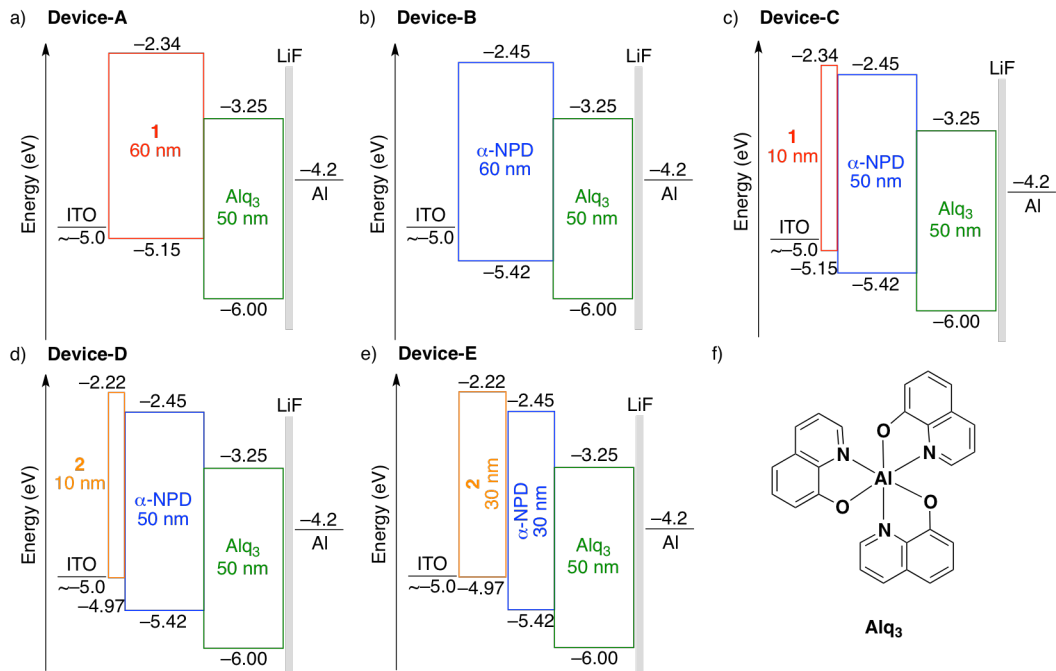


Figure 6. (a–e) Device structures and energy levels of the compounds. (f) Molecular structure of Alq₃.

Firstly, the OLED devices using **1** as HTL with a thickness of 60 nm were fabricated (**device-A**), and their performances were compared with standard OLED devices using α -NPD as a conventional HTL with the same thickness (**device-B**). As shown in Figure 7, the external quantum efficiency of **device-A** (0.32%) was apparently lower than that of **device-B** (1.03%). The low performance in **device-A** using **1** as HTL was considered to be due to the difficulty in hole injection from **1** to Alq₃ (emission layer), arising from the large difference in the HOMO levels between **1** (−5.15 eV) and Alq₃ (−6.00 eV). Taking the rather high-lying HOMO levels of **1** and **2** into consideration, these compounds should be used as HIL, rather than HTL, in the OLED device. Thus, the devices using **1** and **2** as HIL with a thickness of 10 nm in combination with α -NPD (50 nm) as HTL were fabricated (**device-C** and -**D**). The external quantum efficiency of **device-C** and -**D** were found to be 1.23% and 1.11%, respectively. These efficiencies are higher than that of the standard **device-B** (1.03%) without using **1** nor **2** as HIL. In the case of the **device-E** using **2** as HIL, the external quantum efficiency was slightly increased (1.16%) by the optimization of the thickness of the layer of **2** from 10 to 30 nm with keeping the total thickness (60 nm) of HIL and

HTL. These results demonstrate the utility of the present compounds **1** and **2** with quasiplanar skeleton in the application of OLED devices. Furthermore, the studies in this chapter clearly demonstrate that molecular design is very important to create new molecule-based materials with specific functions. Especially for the HTL and HIL materials, high charge mobility owing to dense packing and appropriate energy levels of the HOMO and LUMO, both in the solid state, as well as stability and accessibility should be controlled by molecular design.

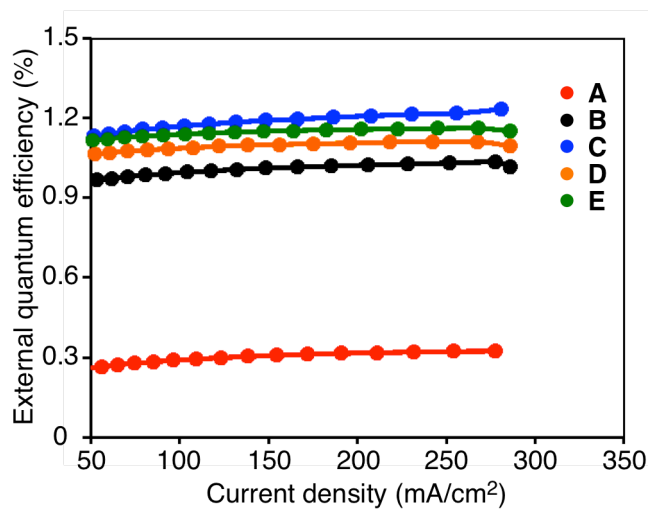


Figure 7. External quantum efficiency of OLEDs for **device-A** (red), **B** (black), **C** (blue), **D** (orange), and **E** (green).

Conclusion

In conclusion, the author evaluated the influences of quasiplanar skeleton on the molecular orientation and the properties of oxygen-bridged triphenylamine dimers **1** and **2** in the amorphous films. According to the fluorescence spectroscopies, both **1** and **2** retain two different states of the monomer-like random orientation and the crystalline-like π -stacking orientation in the bulk amorphous films. In the crystalline-like π -stacking orientation, **1** and **2** form 1D-stacking structure and 2D-stacking structure, respectively. Reflecting the retained π -stacking structures, **1** showed strong field dependency of bulk charge mobilities in the amorphous film. On the other hand, **2** exhibited not only high hole mobility but also high electron mobility (10^{-3} cm²/Vs). When **1** and **2** were used as hole-injection layer (HIL) in OLED devices, higher external quantum efficiencies were exhibited compared to standard devices without HIL.

Experimental Section

General.

Oxygen-bridged triphenylamine dimers **1** and **2** were purified by sublimation (260–320 °C, 13.3–133 Pa) before using measurement. UV-vis absorption measurement was performed with a Shimadzu UV-3150 spectrometer (Shimadzu Co.). Fluorescence measurement was performed with a HORIBA FluoroMax 4P-NIR. Quantum yields were determined with a Hamamatsu Photonics Quantaurus QY C11347 with calibrated integrating sphere system.

Computation method.

DFT calculations for reorganization energies were conducted using the Gaussian 09 program.¹¹ Calculations of electronic couplings for crystal structures were conducted using ADF program.⁸

Time-of-flight measurement.

The devices using for the time-of-flight measurement had the following structures: ITO (50 nm) / charge-transporting materials (3.7–5.1 μm) / Al (20 nm).

The indium-tin-oxide (ITO) coated glasses were used as substrate. Charge-transporting materials were vacuum deposited onto the surface of ITO-glass. The pressure of the vacuum system was 10⁻⁴ Pa during deposition of charge-transporting layers. The deposition rate of charge-transporting layers were 0.6–1.2 nm/s. The thicknesses of the charge-transporting layer of **1**, **2**, and α-NPD were 4.9 μm, 3.7 μm, and 5.1 μm, respectively. These thicknesses were determined by a stylus surface profiler (ULVAC Dektak 6M). The device was once exposed to the atmosphere, and the aluminum electrode was prepared by vapor deposition at a rate of 0.2–0.3 nm/s under the pressure of 10⁻⁵ Pa. The thickness of the aluminum electrode was estimated to be 20 nm.

Time-of-flight measurements on hole and electron mobility were carried out at room temperature using on a Sumitomo Heavy Industries Advanced Machinery (Optel) TOF-401 equipment. Selected carriers (hole or electron) drifted across the sample upon switching the direction of the applied bias. The charge mobilities (μ) were calculated as following equation:

$$\mu = \frac{d^2}{Vt}$$

where, d is the sample thickness, V is the applied voltage, and t is the transient time, respectively.

Fabrication and characteristics of OLED devices.

The OLED devices studied in this chapter had the following structures:

Device-A: ITO (50 nm) / **1** (60 nm) / Alq₃ (50 nm) / LiF (0.5 nm) / Al (100 nm)

Device-B: ITO (50 nm) / α -NPD (60 nm) / Alq₃ (50 nm) / LiF (0.5 nm) / Al (100 nm)

Device-C: ITO (50 nm) / **1** (10 nm) / α -NPD (50 nm) / Alq₃ (50 nm) / LiF (0.5 nm) / Al (100 nm)

Device-D: ITO (50 nm) / **2** (10 nm) / α -NPD (50 nm) / Alq₃ (50 nm) / LiF (0.5 nm) / Al (100 nm)

Device-E: ITO (50 nm) / **2** (30 nm) / α -NPD (30 nm) / Alq₃ (50 nm) / LiF (0.5 nm) / Al (100 nm)

OLED devices were fabricated on glass substrates coated with an indium tin oxide (ITO) conductive layer by successive vapor deposition of organic layers, followed by the deposition of LiF and Al. The deposition was carried out under 10⁻⁵ Pa. The deposition rates were 0.3 nm/s for compound **1**, **2**, α -NPD and Alq₃, 0.01 nm/s for LiF, and 0.2 nm/s for aluminum electrode, respectively. The devices thus fabricated have four active areas with 4 mm². After the deposition of all layers, the OLED devices were encapsulated with a glass cap using epoxy glue in a N₂-filled glove box. Current density–voltage–luminance (*J*–*V*–*L*) characterization was performed using a computer-controlled source meter (Source Meter 2400, Keithley Instruments Inc.) equipped with a spectroradiometer (SR-3, TOPCON Co.). The characterization was carried out on all of the four active areas. Top data among the four devices was used for discussion in this study.

Reference

1. Wakamiya, A.; Nishimura, H.; Fukushima, T.; Suzuki, F.; Saeki, A.; Seki, S.; Osaka, I.; Sasamori, T.; Murata, M.; Murata, Y.; Kaji, H. *Angew. Chem., Int. Ed.* **2014**, *53*, 5800.
2. (a) Osaka, I.; Shimawaki, M.; Mori, H.; Doi, I.; Miyazaki, E.; Koganezawa, T.; Takimiya, K. *J. Am. Chem. Soc.* **2012**, *134*, 3498. (b) Osaka, I.; Kakara, T.; Takemura, N.; Koganezawa, T.; Takimiya, K. *J. Am. Chem. Soc.* **2013**, *135*, 8834.
3. (a) Saeki, A.; Koizumi, Y.; Aida, T.; Seki, S. *Acc. Chem. Res.* **2012**, *45*, 1193. (b) Saeki, A.; Seki, S.; Takenobu, T.; Iwasa, Y.; Tagawa, S. *Adv. Mater.* **2008**, *20*, 920. (c) Yasutani, Y.; Saeki, A.; Fukumatsu, T.; Koizumi, Y.; Seki, S. *Chem. Lett.* **2013**, *42*, 19.
4. (a) Kepler, R. G. *Phys. Rev.* **1960**, *119*, 1226. (b) Leblanc, O. H. *J. Chem. Phys.*

- 1960**, **33**, 626. (c) Gill, W. D. *J. Appl. Phys.* **1972**, **43**, 5033.
- 5. (a) Shirota, Y.; Kageyama, H. *Chem. Rev.* **2007**, **107**, 953. (b) Xiao, L.; Chen, Z.; Qu, B.; Luo, J.; Kong, S.; Gong, Q.; Kido, J. *Adv. Mater.* **2011**, **23**, 926.
 - 6. Van Slyke, S. A.; Chen, C. H.; Tang, C. W. *Appl. Phys. Lett.* **1996**, **69**, 2160.
 - 7. (a) Marcus, R. A. *J. Chem. Phys.* **1956**, **24**, 966. (b) Marcus, R. A.; Sutin, N. *Biochem. Biophys. Acta* **1985**, **811**, 265. (c) Coropceanu, V.; Cornil, J.; da Silva Filho, D. A.; Olivier, Y.; Silbey, R.; Brédas, J.-L. *Chem. Rev.* **2007**, **107**, 926.
 - 8. (a) ADF2012.01, SCM, Theoretical Chemistry, Vrije Universiteit, Amsterdam, The Netherlands, <http://www.scm.com>. (b) Kim, E.-G.; Coropceanu, V.; Gruhn, N. E.; Sánchez-Carrera, R. S.; Snoeberger, R.; Matzger, A. J.; Brédas, J.-L. *J. Am. Chem. Soc.* **2007**, **129**, 13072. (c) Yamamoto, T.; Shinamura, S.; Miyazaki, E.; Takimiya, K. *Bull. Chem. Soc. Jpn.* **2010**, **83**, 120.
 - 9. Tang, C. W.; Van Slyke, S. A. *Appl. Phys. Lett.* **1987**, **51**, 913.
 - 10. Determined based on ionization potential measured by photoelectron spectroscopy and band-gap energies determined from the absorption spectrum reported as follow: Djurišić, A. B.; Lau, T. W.; Lam, L. S. M.; Chan, W. K. *Appl. Phys. A* **2004**, **78**, 375.
 - 11. Gaussian 09 (Revision A.02), Frisch, M. J.; Trucks, G. W.; Schlegel, H. B.; Scuseria, G. E.; Robb, M. A.; Cheeseman, J. R.; Scalmani, G.; Barone, V.; Mennucci, B.; Petersson, G. A.; Nakatsuji, H.; Caricato, M.; Li, X.; Hratchian, H. P.; Izmaylov, A. F.; Bloino, J.; Zheng, G.; Sonnenberg, J. L.; Hada, M.; Ehara, M.; Toyota, K.; Fukuda, R.; Hasegawa, J.; Ishida, M.; Nakajima, T.; Honda, Y.; Kitao, O.; Nakai, H.; Vreven, T.; Montgomery, Jr., J. A.; Peralta, J. E.; Ogliaro, F.; Bearpark, M.; Heyd, J. J.; Brothers, E.; Kudin, K. N.; Staroverov, V. N.; Keith, T.; Kobayashi, R.; Normand, J.; Raghavachari, K.; Rendell, A.; Burant, J. C.; Iyengar, S. S.; Tomasi, J.; Cossi, M.; Rega, N.; Millam, J. M.; Klene, M.; Knox, J. E.; Cross, J. B.; Bakken, V.; Adamo, C.; Jaramillo, J.; Gomperts, R.; Stratmann, R. E.; Yazyev, O.; Austin, A. J.; Cammi, R.; Pomelli, C.; Ochterski, J. W.; Martin, R. L.; Morokuma, K.; Zakrzewski, V. G.; Voth, G. A.; Salvador, P.; Dannenberg, J. J.; Dapprich, S.; Daniels, A. D.; Farkas, O.; Foresman, J. B.; Ortiz, J. V.; Cioslowski, J.; Fox, D. J., Gaussian, Inc., Wallingford CT, 2009.

Chapter 3

Development of Transparent Organic Hole-Transporting Materials Using Partially Oxygen-Bridged Triphenylamine Skeletons

Abstract: *m*-Benzene linked partially oxygen-bridged triphenylamine derivatives were designed and synthesized as transparent hole-transporting materials. The connection of quasiplanar triarylamine skeleton through the *meta*-position of a benzene linker effectively suppresses the π -conjugation to make the derivatives almost transparent materials having the absorption band only in the UV region. DSC and X-ray diffraction measurements revealed that these compounds have high thermal stability so as to retain amorphous states in the vacuum-deposited films even after heating at 160 °C. SCLC measurements revealed that these compounds exhibited good hole mobility in the same order to that of oxygen-bridged triphenylamine dimer, despite their less π -conjugation.

Introduction

As mentioned in the previous chapters, the development of excellent organic semiconductors with high charge mobilities and high thermal stabilities is crucial, in order to improve the device performance in the field of organic electronics, such as organic light-emitting diodes (OLEDs),¹ organic field effect transistors (OFETs),² or organic photovoltaics (OPVs).³ In addition to these two properties, transparency of the materials in the visible light region is also important characteristics for OLEDs and OFETs, in order to inhibit the decreasing of light extraction in the applications for display, lighting, light detector and so on. Even in photovoltaics, transparency of the materials is crucial in terms of light insertion, since charge-transporting materials are used between transparent electrode and light absorber. Recently, the development of transparent semiconductors attracts increasing attention particularly in tandem solar cells, such as the combination of perovskite and silicon solar cells.⁴ In this type of tandem structure, perovskite solar cells⁵ containing semiconductor layer are assumed to be deposited as top cells on silicon solar cells.

Regarding transparent hole-transporting materials (HTMs), many kinds of inorganic materials, such as CuSCN,⁶ CuGaO₂,⁷ Sr₃Cu₂Sc₂O₅S₂,⁸ MoO_x,⁹ and NiO_x,¹⁰ have been reported so far, whereas the examples of organic transparent HTMs are still limited.¹¹ In a molecular design of organic semiconductors, extension of π -conjugation in the skeletons is a general strategy so as to minimize reorganization energy (λ) as well as to gain larger electron couplings (V) between neighbor molecules in the packing structure. The extension of π -conjugation, however, would induce bathochromic shift in the light absorption of the organic molecules at the same time. Therefore, this discrepancy in the molecular design currently makes it challenging issue to develop transparent organic semiconductor.

As mentioned in previous chapters, the author showed that the molecules with quasiplanar structure have a tendency to form dense π -stacking structures, exhibiting good carrier mobility.¹² Based on these unique characteristics of quasiplanar skeletons, the author designed and synthesized oxygen-bridged triphenylamine derivatives **1** and **2** as transparent hole-transporting materials, in which two of partially oxygen-bridged triphenylamine skeleton were connected through *meta*-position of a benzene ring (Figure 1a). The properties of **1** and **2** were investigated in terms of how the disconnection of π -conjugation via *meta*-benzene-linking affects light absorption properties and thermal properties as well as hole mobilities compared with reference compounds **3** and **4** (Figure 1b).

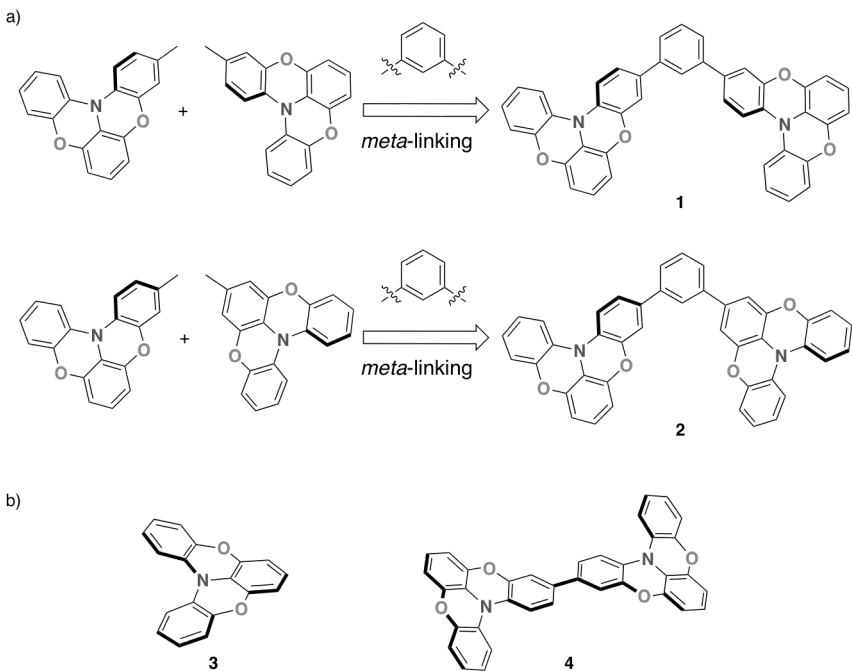
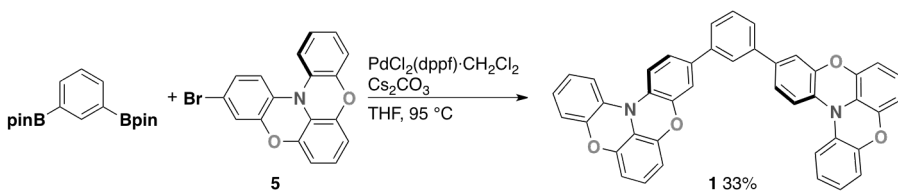


Figure 1. a) Molecular design aspects for *m*-benzene linked oxygen-bridged triphenylamine derivatives **1** and **2**. b) Reference compounds **3** and **4**

Results and Discussion

Synthesis

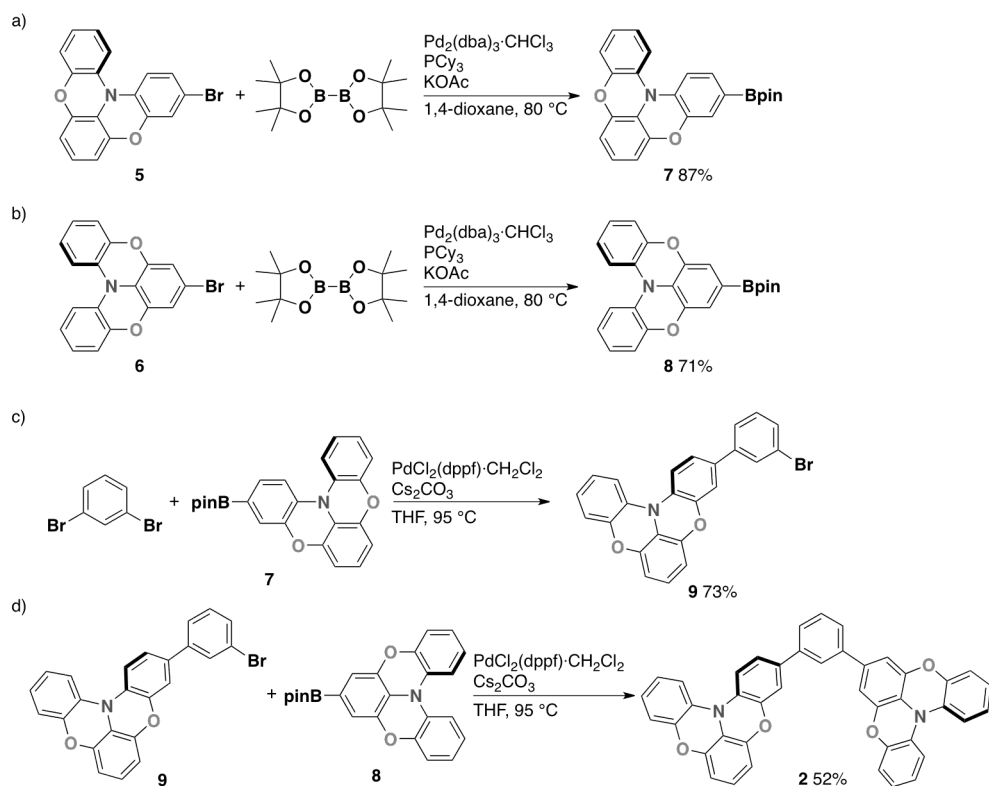
The monobrominated oxygen-bridged triphenylamine **5** was prepared according to the synthetic method as shown in Chapter 1. Suzuki-Miyaura cross-coupling of monobrominated derivative **5** and *m*-di(Bpin)benzene afforded symmetric compound **1** in 33% yield as white solids (Scheme 1).



Scheme 1.

In a similar manner, the author tried to synthesize asymmetric compound **2**, in which oxygen-bridged triphenylamine skeletons are connected at the different position via *meta*-benzene linkage, by stepwise coupling reaction. However, the coupling

reaction using 1:1 mixture of **5** and *m*-di(Bpin)benzene resulted to give two-fold coupling product **1** as the major product. Then, asymmetric compound **2** was synthesized by stepwise Suzuki-Miyaura cross-coupling reaction using opposite combination, such as *m*-dibromobenzene and borylated triphenylamine derivatives as shown in Scheme 2. Firstly, monoborylated **7** and **8** were prepared by Miyaura borylation of **5** and **6**, respectively (Scheme 2a,b). The first coupling reaction of *m*-dibromobenzene and monoborylated **7** in a 1:1 molar ratio successfully afforded mono-substituted **9** in 73% yield (Scheme 2c). Subsequently, the second cross-coupling reaction between mono-substituted **9** with monoborylated **8** afforded desired asymmetric compound **2** in 52% yield as white solids (Scheme 2d).



Scheme 2.

Electrochemical Property

The electrochemical properties were examined by cyclic voltammetry (CV) in CH_2Cl_2 (Figure 2). Both **1** and **2** show one reversible oxidation waves at $+0.31$ V (vs. Fc/Fc^+), corresponding to two-electron oxidation, suggesting electrochemically less communication between the two oxygen-bridged triphenylamine skeletons. The

oxidation potentials of **1** and **2** are similar to that of oxygen-bridged triphenylamine **3** (+0.32 V), a monomer unit, and higher than that of the direct connected dimer **4** (+0.23 V), indicating that the π -conjugation is effectively suppressed in these *meta*-benzene-linking dimers.

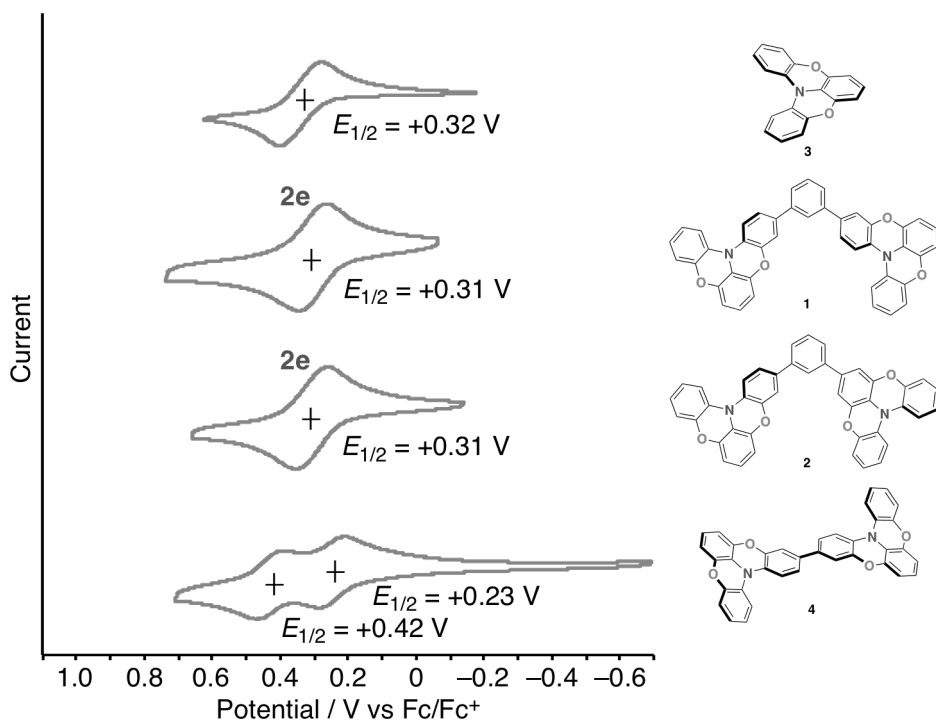


Figure 2. Cyclic voltammograms of **1–4** in CH_2Cl_2 (0.3 mM), measured with $(n\text{-Bu})_4\text{N}^+\text{PF}_6^-$ as a supporting electrolyte at a scan rate of 100 mVs⁻¹.

Photophysical Property

In UV-vis absorption spectra in CH_2Cl_2 (Figure 3), **1** and **2** exhibit absorption bands at 380 nm and 374 nm, respectively. These absorption bands in **1** and **2** are blue-shifted compared to directly connected dimer **4** (397 nm), which is attributed to the suppression of the π -conjugation through *meta*-benzene connection.

Even in UV-vis absorption spectra for the vacuum-deposited films (Figure 4), compounds **1** and **2** were found to maintain their absorption in the UV region. Although absorption peaks of **1** (388 nm) and **2** (382 nm) are slightly red-shifted from those in CH_2Cl_2 , these peaks are still remained in the UV region with their absorption edges at 426 nm for **1** and 425 nm for **2**, respectively. These results suggest potential use of **1** and **2** as transparent materials. Indeed, the vacuum-deposited films of **1** and **2** show

good transparency, which are different from direct connected dimer **4** that shows pale yellow in a form of the film, as shown in Figure 4.

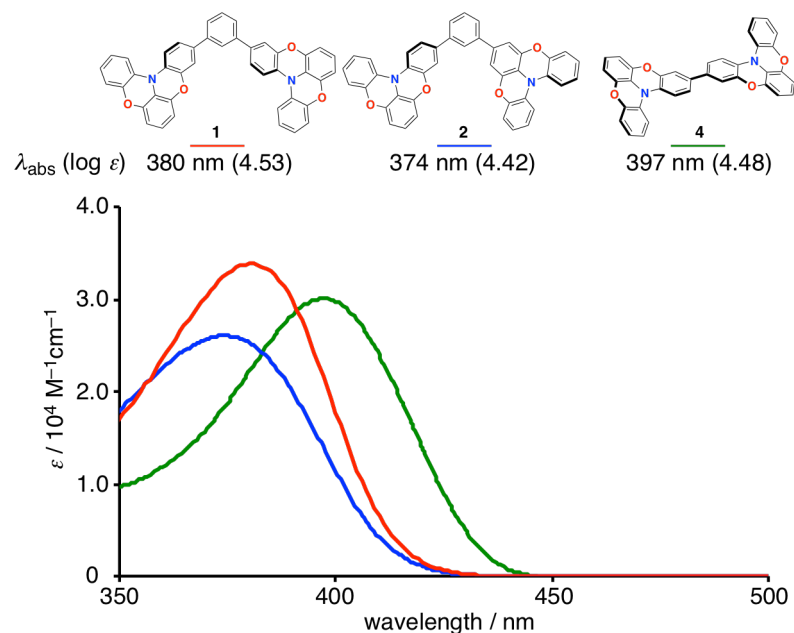


Figure 3. UV-vis absorption spectra of **1**, **2** and **4** in CH_2Cl_2 .

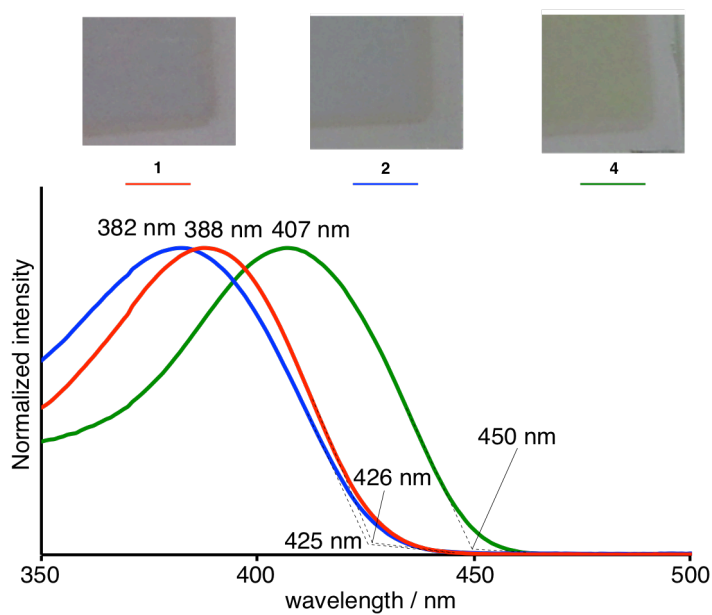


Figure 4. Photographs and UV-vis absorption spectra of **1**, **2** and **4** in the vacuum-deposited films.

Theoretical Calculations

To gain deep insights into the effects of *meta*-benzene linkage on electrochemical and photophysical properties, DFT (B3LYP/6-31G(d)) and TD-DFT (CAM-B3LYP/6-31G(d)) calculations were conducted on **1** and **2** as well as monomer **3** and directly connected dimer **4** for comparison. The *meta*-benzene linking **1** and **2** were found to have almost degenerated occupied frontier orbitals (Figure 5). These orbitals (the Kohn-Sham (KS)-HOMO and KS-HOMO-1) are delocalized over the two triphenylamine skeletons. These energy levels for **1** (-4.73 and -4.76 V) and **2** (-4.73 and -4.76 V) are almost similar to that of monomer **3** (-4.74 eV) and lower than that of dimer **4** (-4.60 eV), which is in good agreement with the oxidation potentials observed in CV measurements.

In contrast to the KS-HOMOs, the KS-LUMOs of **1** and **2** are not degenerated and locate on the central part of the molecules. The KS-LUMO levels of **1** and **2** are -1.04 eV and -1.03 eV, respectively, which are comparable with that of dimer **4** (-1.06 eV).

TD-DFT calculations showed shorter absorption wavelengths with smaller oscillator strengths for **1** and **2** than those for **4**, which are qualitatively in good agreement with the experimental results observed in UV-vis spectra. These results indicate that the degenerated KS-HOMOs with retaining lower energy levels in **1** and **2** mainly attribute to the effective inhibition of bathochromic shift in their light absorption.

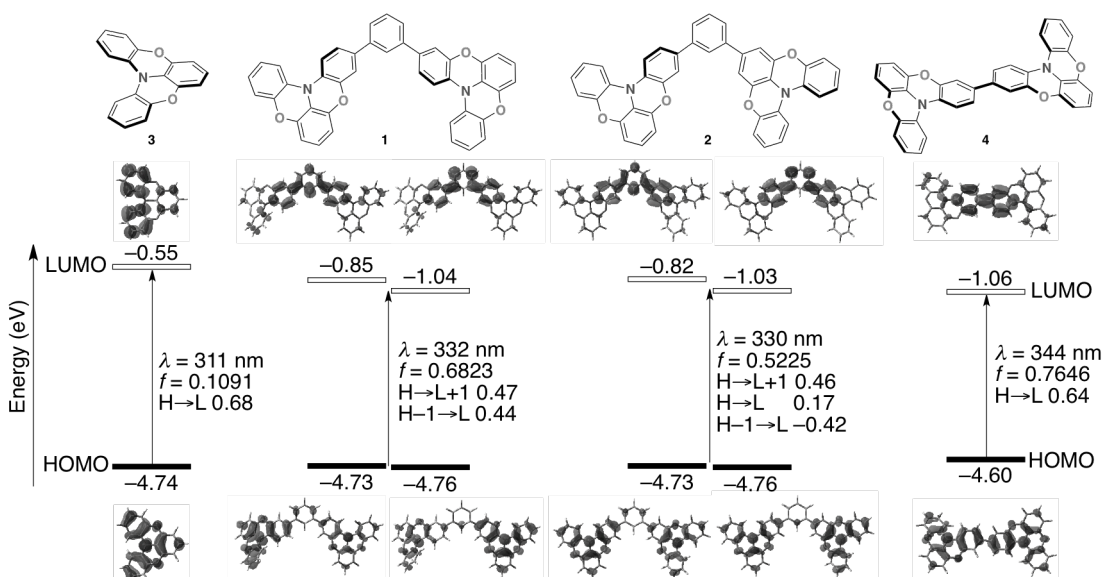


Figure 5. Pictorial presentation of the frontier orbitals, a plot of the Kohn-Sham HOMO and LUMO energy levels for **1–4** (B3LYP/6-31G(d)), and optical transition with oscillator strength (CAM-B3LYP/6-31G(d) // B3LYP/6-31G(d)).

Thermal Stability

In the application of these materials as films, thermal stability as well as amorphous stability are important. Thus the author examined thermal stability of compound **1** and **2** in detail. Thermogravimetric analysis (TGA) on **1** and **2** confirmed their high thermal stability with decomposition temperature (T_{d5}) of **1** (489 °C) and **2** (479 °C) as shown in Figure 6. These temperatures are much higher even compared to that of directly connecting dimer **4** (441 °C), indicating superior utility of **1** and **2** as materials.

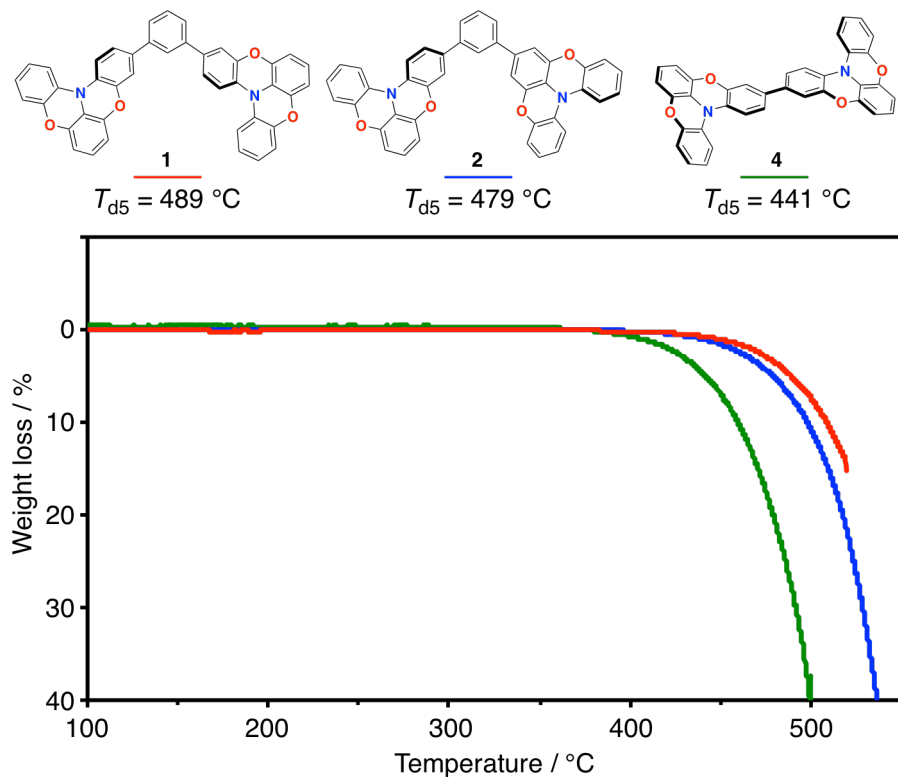


Figure 6. Thermogravimetric analysis of **1**, **2**, and **4** heating at 10 °C/min under N₂.

The amorphous stabilities of **1** and **2** were also examined by differential scanning calorimetry (DSC). As shown in Figure 7, compound **1** showed higher glass transition temperature (T_g) of 130 °C than dimer **4** (123 °C), reflecting the lower symmetry resulting from the introduction of the triphenylamines in *meta*-position of the benzene ring. The glass transition temperature of compound **2** with less symmetry further increases to 136 °C (Figure 7b), indicating their good amorphous stability.

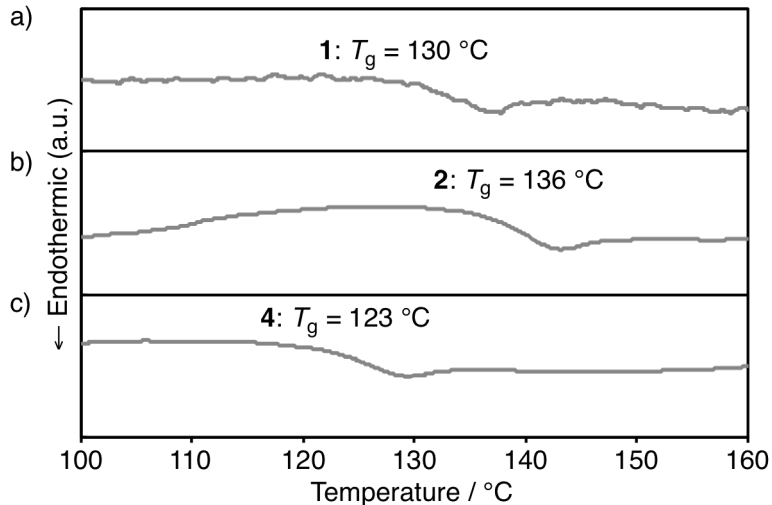


Figure 7. Differential scanning calorimetry of a) **1**, b) **2**, and c) **4** heating at 10 °C/min under N₂.

Encouraged by these results, the author also examined thermal stabilities for the films of **1** and **2** in detail. Assuming a typical device structure, the vacuum-deposited films of **1**, **2**, and **4** (50 nm) were sealed with ITO (50 nm), respectively. After annealing at 160 °C, the surfaces of these films were monitored by optical microscopy. Before annealing, all of the films were confirmed to show no aggregation (Figure 8 inset). The vacuum-deposited film of **4** exhibited aggregation to some extent after annealing for 210 min, while the films of **1** and **2** did not show any change even after annealing at 160 °C for 210 min, suggesting good film stabilities for *meta*-benzene linking compounds.

The morphologies of these films were also examined by out-of-plane X-ray diffraction (XRD) measurements (Figure 8). Before annealing, only broad diffraction peaks were detected in these films, suggesting the formation of amorphous states. The domain sizes were estimated by Scherrer equation:¹³

$$\tau = K\lambda/B\cos\theta$$

where *K* is a shape factor (0.9), λ is the wavelength of the X-ray (1.5418 Å), *B* is the full width at half maximum (FWHM, in radians), and θ is the Bragg angle of peak, respectively. Based on the analysis for the broad peak around $2\theta = 24^\circ$, the domain sizes in these films were estimated about 1.5 nm.

In the film of dimer **4**, intense peak at $2\theta = 11.2^\circ$ and weak peak at 23.9° appeared

after annealing at 160 °C for 210 min. The estimation for the peaks at 11.2° and 23.9° corresponds to the domain sizes of 21 nm and 7 nm, respectively, which suggest crystallization in the film.

In the case of **1** and **2**, the vacuum-deposited films only shifted their broad peaks from 24° to 21° even after annealing at 160 °C for 210 min. These results suggested that whereas the molecular orientations in the vacuum-deposited films of **1** and **2** might be slightly changed, these films still retained the amorphous states after annealing at 160 °C.

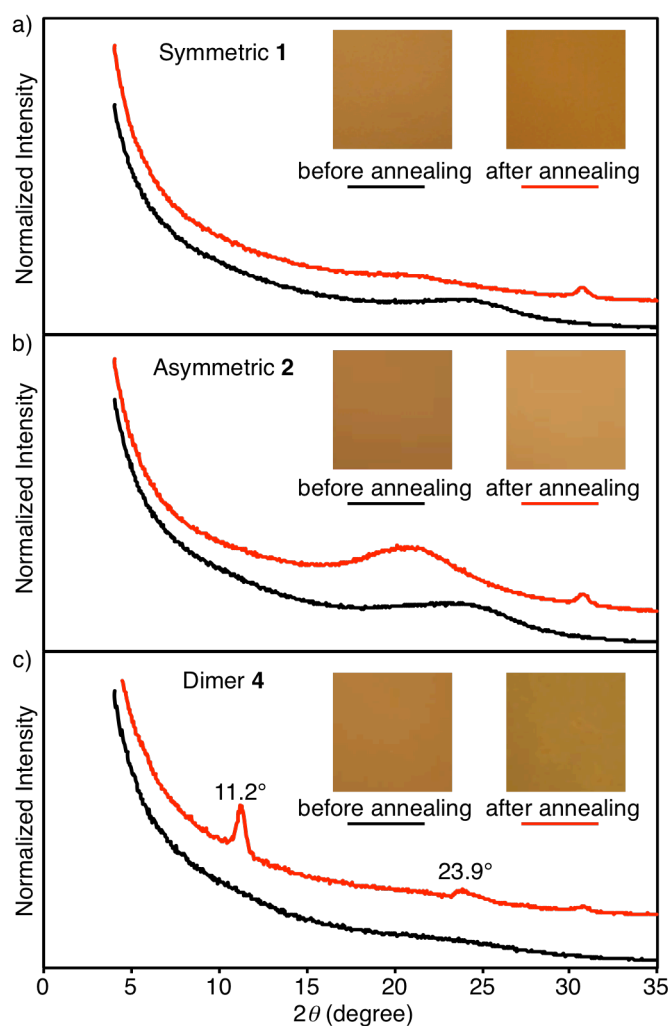


Figure 8. XRD patterns of a) **1**, b) **2**, and c) **4** in the vacuum-deposited films before (black) and after (red) thermal annealing at 160 °C for 210 min. Insets show the photographs of films before and after annealing.

Hole Mobility

The hole mobilities in the vacuum-deposited films of **1**, **2** and **4** were examined by the space-charge-limited current (SCLC) method (Figure 9).¹⁴ SCLC measurements on the vacuum-deposited films with a thickness of 65–100 nm showed that the hole mobilities at $316 \text{ (V/cm)}^{1/2}$ of **1**, **2**, and **4** were 2.2×10^{-5} , 1.6×10^{-5} and $6.5 \times 10^{-5} \text{ cm}^2/\text{Vs}$, respectively. In spite of less π -conjugation via the *meta*-position of the benzene linker, **1** and **2** exhibited good hole mobilities in the same order with that of directly connected dimer **4**. According to the Marcus theory,¹⁵ reorganization energy is one of the important parameter for the charge transport property. The reorganization energies calculated by the DFT method (B3LYP/6-31G(d)) for the hole transfer in **1** and **2** are 0.091 eV and 0.094 eV, respectively, which are much lower than that of **4** (0.15 eV). The observed good hole mobilities would most likely be attribute to these small reorganization energies induced by degeneration of the KS-HOMOs.

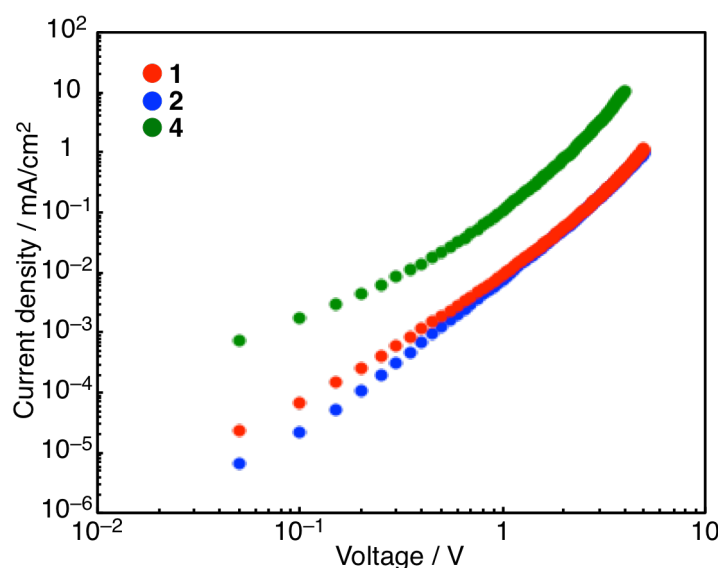


Figure 9. J – V characteristics of space-charge-limited current of a) **1**, b) **2**, and c) **4** in the vacuum-deposited films.

Conclusion

In conclusion, transparent hole-transporting materials **1** and **2**, in which two oxygen-bridged triphenylamine skeletons are connected via *meta*-position of a benzene ring, were designed and synthesized. The author demonstrated that these compounds showed excellent amorphous stability so that no crystallization was observed even after annealing at 160 °C. Furthermore, **1** and **2** were found to have both transparency and

good hole mobility in the vacuum-deposited films. These results indicate the potential use of the *meta*-benzene linked oxygen-bridged triarylamine derivatives as transparent hole-transporting materials in organic electronics devices, such as OLED, OFET, and OPV, etc.

Experimental Section

General.

All reactions were carried out under an argon atmosphere. Thin layer chromatography (TLC) was performed on plates coated with 0.25 mm thick silica gel 60F-254 (Merck). Column chromatography was performed using PSQ 60B (Fuji Silysia). Preparative gel permeation chromatography (GPC) was performed with a JAI LC-918 system equipped with RI-50 detector, JAIGEL-2H column (20 mm ID × 600 mm) and 1H column (20 mm ID × 600 mm) using toluene as eluent (flow rate: 3.8 mL/min). Melting points (mp) were measured on a Yanaco Micro Melting Point Apparatus. ¹H and ¹³C NMR spectra were recorded with a JEOL ECA 500 (500 MHz for ¹H and 125 MHz for ¹³C) spectrometers. The NMR chemical shifts are reported in ppm with reference to residual protons and carbons of CD₂Cl₂ (δ 5.32 ppm in ¹H NMR, δ 53.8 ppm in ¹³C NMR). Cyclic voltammetry (CV) was performed on an ALS/chi-620C electrochemical analyzer with the CV cell consisting of a glassy carbon electrode, a Pt wire counter electrode, and an Ag/AgNO₃ reference electrode. The measurement was carried out under an argon atmosphere using CH₂Cl₂ solutions of samples (0.3 mM) with 0.1 M tetrabutylammonium hexafluorophosphate (Bu₄N⁺PF₆⁻) as a supporting electrolyte. The redox potentials were calibrated with ferrocene as an internal standard. UV-vis absorption measurement for CH₂Cl₂ solution was performed with a Shimadzu UV-3150 spectrometer (Shimadzu Co.), in degassed spectral grade solvents. UV-vis absorption measurement for the vacuum-deposited films was performed with a JASCO V-570 UV/VIS/NIR spectrophotometer equipped with ARM-500N (JASCO Co.). Thermogravimetric analysis (TGA) was performed on a Shimadzu TGA-50 apparatus (Shimadzu Co.). The values are given for a weight-loss of 5% (T_{d5}). Different scanning calorimetry (DSC) was performed on a Shimadzu DSC-60 apparatus (Shimadzu Co.). Optical microscopy was conducted with Nikon ECLIPSE L150 (Nikon Co.). XRD data for the vacuum-deposited films were collected on a RIGAKU ultraX TTR2-300 X-ray diffractometer. Data was collected at room temperature using Cu K α radiation ($\lambda = 1.54178 \text{ \AA}$).

Computation method.

DFT calculations for optimization and reorganization energies were conducted using the Gaussian 09 program.¹⁶

Synthesis.

1,3-Di(benzo[5,6][1,4]oxazino[2,3,4-*k*]phenoxazin-3-yl)benzene (1).

1,3-Di(Bpin)benzene (1.01 g, 3.06 mmol), **5** (2.47 g, 7.03 mmol), PdCl₂(dppf)·CH₂Cl₂ (74.2 mg, 0.0909 mmol), and cesium carbonate (3.00 g, 9.20 mmol) in THF (120 mL) were charged in a Schlenk tube. After flushed with argon three times, the mixture was stirred at 95 °C for 36 h. The reaction mixture was concentrated under reduced pressure. The obtained solids were extracted with chlorobenzene by using Soxhlet extractor and the resulting solution was concentrated under reduced pressure. The obtained solid was washed with CH₂Cl₂ and purified by sublimation (300–330 °C, 0.05 mmHg) to give 0.630 g (1.01 mmol) of **1** in 33% yields as white solids.

mp: 301.5–302.5 °C; ¹H NMR (500 MHz, CD₂Cl₂/CS₂ = 1/2): δ 7.75 (s, 1H), 7.55–7.47 (m, 3H), 7.07–7.02 (m, 2H), 7.43 (d, ³J(H,H) = 8.0 Hz, 2H), 7.39 (d, ³J(H,H) = 8.0 Hz, 2H), 7.28 (dd, ³J(H,H) = 8.5 Hz, ⁴J(H,H) = 2.5 Hz, 1H), 7.23 (d, ⁴J(H,H) = 2.5 Hz, 2H), 7.00 (dd, ³J(H,H) = 7.5 Hz, ⁴J(H,H) = 1.5 Hz, 2H), 6.96 (m, 4H), 6.80 (t, ³J(H,H) = 8.5 Hz, 2H), 6.54 (³J(H,H) = 8.0 Hz, 4H); HRMS (FAB) (*m/z*): [M]⁺ calcd. for C₄₂H₂₄N₂O₄, 620.1736; found, 620.1739; Elemental analysis calcd (%) for C₄₂H₂₄N₂O₄: C 81.28, H 3.90, N 4.51; found: C 81.33, H 4.00, N 4.54.

3-(4,4,5,5-Tetramethyl-1,3,2-dioxaborolan-2-yl)benzo[5,6][1,4]oxazino[2,3,4-*k*]phenoxazine (7).

Pd₂(dba)₃·CHCl₃ (157 mg, 0.151 mmol) and PCy₃ (171 mg, 0.608 mmol) were dissolved in 1,4-dioxane (100 mL) and the mixture was stirred at room temperature for 30 min. After addition of **5** (3.52 g, 10.0 mmol), bis(pinacolato)diboron (2.25 g, 13.2 mmol), and KOAc (1.47 g, 15.0 mmol), the mixture was further stirred at 80 °C for 16 h. The reaction mixture was poured into water (100 mL). The aqueous phase was extracted with CH₂Cl₂ (40 mL × 3) and the organic phase was washed with brine. The organic phase was dried over Na₂SO₄, filtered off and the filtrate was concentrated under reduced pressure. The obtained crude product was purified by silica gel column chromatography (CH₂Cl₂ : hexane = 1 : 1, *R*_f = 0.42) to give 3.48 g (8.72 mmol) of **7** in 87% yields as white solids.

mp: 139.7–141.4 °C; ¹H NMR (500 MHz, CD₂Cl₂): δ 7.37–7.30 (m, 3H), 7.25 (s, 1H), 6.97 (td, ³J(H,H) = 8.0 Hz, ⁴J(H,H) = 2.0 Hz, 1H), 6.93 (td, ³J(H,H) = 8.0 Hz, ⁴J(H,H) =

1.5 Hz, 1H), 6.90 (dd, $^3J(\text{H},\text{H})$ = 8.0 Hz, $^4J(\text{H},\text{H})$ = 2.0 Hz, 1H), 6.78 (t, $^3J(\text{H},\text{H})$ = 8.0 Hz, 1H), 6.51 (d, $^3J(\text{H},\text{H})$ = 8.0 Hz, 2H), 1.33 (s, 12H); ^{13}C NMR (125 MHz, CD_2Cl_2): δ 147.3, 146.7, 146.0, 145.6, 132.3, 130.9, 128.9, 124.3, 124.1, 124.0, 123.3, 121.0, 117.7, 115.5, 114.2, 111.5, 111.3, 84.2, 25.0 (One signal for the carbon atom bonding to the boron atom was not observed due to the quadrupolar relaxation of the boron atom); HRMS (EI) (m/z): $[\text{M}]^+$ calcd. for $\text{C}_{24}\text{H}_{22}\text{BNO}_4$, 399.1646; found, 399.1645; Elemental analysis calcd (%) for $\text{C}_{24}\text{H}_{22}\text{BNO}_4$: C 72.20, H 5.55, N 3.51; found: C 71.95, H 5.55, N 3.46.

7-(4,4,5,5-Tetramethyl-1,3,2-dioxaborolan-2-yl)benzo[5,6][1,4]oxazino[2,3,4-*k*]phenoxazine (8).

$\text{Pd}_2(\text{dba})_3 \cdot \text{CHCl}_3$ (9.53 mg, 0.00921 mmol) and PCy_3 (6.40 mg, 0.0228 mmol) were dissolved in 1,4-dioxane (6 mL) and the mixture was stirred at room temperature for 30 min. After addition of **6** (213 mg, 0.603 mmol), bis(pinacolato)diboron (169 mg, 0.665 mmol), and KOAc (91.5 mg, 0.932 mmol), the mixture was further stirred at 80 °C for 36 h. The reaction mixture was poured into water (10 mL). The aqueous phase was extracted with CH_2Cl_2 (10 mL × 3). The organic phase was dried over Na_2SO_4 , filtered off and the filtrate was concentrated under reduced pressure. The obtained crude product was purified by silica gel column chromatography (CH_2Cl_2 : hexane = 1 : 1, R_f = 0.42) and further purified by gel permeation chromatography (toluene) to give 170 mg (0.427 mmol) of **8** in 71% yields as white solids.

mp: 171.5–173.2 °C; ^1H NMR (500 MHz, CD_2Cl_2): δ 7.33 (d, $^3J(\text{H},\text{H})$ = 8.0 Hz, 2H), 6.98–6.86 (m, 8H), 1.31 (s, 12H); ^{13}C NMR (125 MHz, CD_2Cl_2): δ 147.5, 145.1, 129.2, 124.2, 124.0, 123.9, 117.7, 117.3, 115.1, 84.3, 25.0 (One signal for the carbon atom bonding to the boron atom was not observed due to the quadrupolar relaxation of the boron atom); HRMS (EI) (m/z): $[\text{M}]^+$ calcd. for $\text{C}_{24}\text{H}_{22}\text{BNO}_4$, 399.1646; found, 399.1646; Elemental analysis calcd (%) for $\text{C}_{24}\text{H}_{22}\text{BNO}_4$: C 72.20, H 5.55, N 3.51; found: C 72.26, H 5.53, N 3.49.

3-(3-(Bromophenyl)benzo[5,6][1,4]oxazino[2,3,4-*k*]phenoxazine (9).

7 (239 mg, 0.599 mmol), 1,3-dibromobenzene (220 μL , 1.82 mmol), $\text{PdCl}_2(\text{dppf}) \cdot \text{CH}_2\text{Cl}_2$ (7.44 mg, 0.00911 mmol), and cesium carbonate (293 mg, 0.899 mmol) in THF (18 mL) were charged in a Schlenk tube. After flushed with argon three times, the mixture was stirred at 95 °C for 45 h. Insoluble materials were filtered off and washed with CH_2Cl_2 (9 mL). The combined organic phase was absorbed on silica gel and

purified by silica gel column chromatography (CH_2Cl_2 : hexane = 1 : 3, R_f = 0.51) to give 186 mg (0.435 mmol) of **9** in 73% yields as yellow solids.

mp: 179.1–180.4 °C; ^1H NMR (500 MHz, CD_2Cl_2) δ 7.73 (s, 1H), 7.52 (d, $^3J(\text{H},\text{H})$ = 8.0 Hz, 1H), 7.46 (d, $^3J(\text{H},\text{H})$ = 8.0 Hz, 1H), 7.41 (d, $^3J(\text{H},\text{H})$ = 8.0 Hz, 1H), 7.37 (d, $^3J(\text{H},\text{H})$ = 8.0 Hz, 1H), 7.31 (t, $^3J(\text{H},\text{H})$ = 8.0 Hz, 1H), 7.20 (dd, $^3J(\text{H},\text{H})$ = 8.0 Hz, $^4J(\text{H},\text{H})$ = 2.0 Hz, 1H), 7.15 (d, $^4J(\text{H},\text{H})$ = 2.5 Hz, 1H), 6.99 (td, $^3J(\text{H},\text{H})$ = 7.5 Hz, $^4J(\text{H},\text{H})$ = 1.5 Hz, 1H), 6.96–6.90 (m, 2H), 6.80 (td, $^3J(\text{H},\text{H})$ = 8.0 Hz, $^4J(\text{H},\text{H})$ = 1.5 Hz, 1H), 6.56–6.52 (m, 2H); ^{13}C NMR (125 MHz, CD_2Cl_2): δ 147.6, 147.3, 145.7, 145.5, 142.1, 135.0, 130.8, 130.4, 129.7, 129.3, 129.2, 125.4, 124.3, 124.1, 124.0, 123.2, 122.5, 121.0, 117.8, 116.0, 115.3, 115.1, 111.5, 111.4; HRMS (FAB) (m/z): $[\text{M}]^+$ calcd. for $\text{C}_{24}\text{H}_{14}\text{BrNO}_2$, 427.0208; found, 427.0210; Elemental analysis calcd (%) for $\text{C}_{24}\text{H}_{14}\text{BrNO}_2$: C 67.31, H 3.29, N 3.27; found: C 67.21, H 3.41, N 3.29.

3-(3-(Benzo[5,6][1,4]oxazino[2,3,4-*k*]phenoxazin-7-yl)phenyl)benzo[5,6][1,4]oxazin-*o*[2,3,4-*k*]phenoxazine (**2**).

9 (229 mg, 0.534 mmol), **8** (213 mg, 0.534 mmol), $\text{PdCl}_2(\text{dppf}) \cdot \text{CH}_2\text{Cl}_2$ (6.86 mg, 0.00840 mmol), and cesium carbonate (273 mg, 0.838 mmol) in THF (15 mL) were charged in a Schlenk tube and the mixture was degassed for 10 min. The mixture was stirred at 95 °C for 65 h. The solution was concentrated under reduced pressure. The obtained solids were extracted with chlorobenzene by using Soxhlet extractor and the resulting solution was concentrated under reduced pressure. The solid was washed with hexane and purified by sublimation (280–310 °C, 0.05 mmHg) to give 171 mg (0.276 mmol) of **2** in 52% yield as white solids.

mp: 295.6–297.1 °C; ^1H NMR (500 MHz, CD_2Cl_2) δ 7.73 (s, 1H), 7.54 (d, $^3J(\text{H},\text{H})$ = 7.0 Hz, 1H), 7.51–7.46 (m, 2H), 7.42 (d, $^3J(\text{H},\text{H})$ = 8.0 Hz, 1H), 7.39 (t, $^3J(\text{H},\text{H})$ = 7.5 Hz, 3H), 7.28 (dd, $^3J(\text{H},\text{H})$ = 8.0 Hz, $^4J(\text{H},\text{H})$ = 2.0 Hz, 1H), 7.23 (d, $^4J(\text{H},\text{H})$ = 2.0 Hz, 1H), 7.02–6.96 (m, 3H), 6.96–6.90 (m, 6H), 6.86 (s, 2H), 6.80 (t, $^3J(\text{H},\text{H})$ = 8.5 Hz, 1H), 6.54 (td, $^3J(\text{H},\text{H})$ = 8.5 Hz, $^4J(\text{H},\text{H})$ = 1.0 Hz, 2H); HRMS (FAB) (m/z): $[\text{M}]^+$ calcd. for $\text{C}_{42}\text{H}_{24}\text{N}_2\text{O}_4$, 620.1736; found, 620.1737; Elemental analysis calcd (%) for $\text{C}_{42}\text{H}_{24}\text{N}_2\text{O}_4$: C 81.28, H 3.90, N 4.51; found: C 81.34, H 3.92, N 4.40.

Space-charge-limited current measurement.

The hole mobilities in the films of materials were measured from the space-charge-limitation of current (SCLC) J – V characteristics obtained in the dark for hole-only devices. Hole mobilities were calculated using the Mott-Gurney law by fitting Equation 1, where J is the current density, ϵ_0 is the permittivity of free space (8.85×10^{-12}

¹² F/m), ϵ is the relative permittivity of the material (approaching 3 for organic semiconductors), μ is the hole mobility, V is the applied voltage, and d is the thickness of the active layer, respectively.

$$J = \frac{9}{8} \epsilon \epsilon_0 \mu \frac{V^2}{d^3} \quad 1$$

All layers were prepared by sublimation at pressures of 10^{-5} Pa at a deposition rate of 0.1 nm/s. A thin layer of MoO₃ (0.8 nm) was prepared onto a platinum substrate by sublimation. Then hole-transporting materials were deposited by sublimation at 65–100 nm. Another thin layer of MoO₃ (3 nm) was deposited onto hole-transporting layer. As a counter electrode, Au was deposited on the film (100 nm). The film thicknesses were measured with TENCOR P-10 (KLA-Tencor). The current density–voltage curves of the devices were taken with an Agilent 4156C Precision Semiconductor Parameter Analyzer.

Reference

1. (a) Shirota, Y.; Kageyama, H. *Chem. Rev.* **2007**, *107*, 953. (b) Xiao, L.; Chen, Z.; Qu, B.; Luo, J.; Kong, S.; Gong, Q.; Kido, J. *Adv. Mater.* **2011**, *23*, 926. (c) Yamamori, A.; Adachi, C.; Koyama, T.; Taniguchi, Y. *J. Appl. Phys.* **1999**, *86*, 4369. (d) Parthasarathy, G.; Adachi, C.; Burrows, P. E.; Forrest, S. R. *Appl. Phys. Lett.* **2000**, *76*, 2128. (e) Zhou, X.; Pfeiffer, M.; Huang, J. S.; Blochwitz-Nimoth, J.; Qin, D. S.; Werner, A.; Drechsel, J.; Maennig, B.; Leo, K. *Appl. Phys. Lett.* **2002**, *81*, 922. (f) Pfeiffer, M.; Forrest, S. R.; Zhou, X.; Leo, K. *Org. Electron.* **2003**, *4*, 21. (g) Ju, S.; Li, J.; Liu, J.; Chen, P.-C.; Ha, Y.-g.; Ishikawa, F.; Chang, H.; Zhou, C.; Facchetti, A.; Janes, D. B.; Marks, T. J. *Nano Lett.* **2008**, *8*, 997.
2. (a) Anthony, J. E. *Angew. Chem., Int. Ed.* **2008**, *47*, 452. (b) Klauk, H. *Chem. Soc. Rev.* **2010**, *39*, 2643. (c) Wang, C.; Dong, H.; Hu, W.; Liu, Y.; Zhu, D. *Chem. Rev.* **2012**, *112*, 2208. (d) Lin, Y.-J.; Li, Y.-C.; Wen, T.-C.; Huang, L.-M.; Chen, Y.-K.; Yeh, H.-J.; Wang, Y.-H. *Appl. Phys. Lett.* **2008**, *93*, 043305. (e) Li, Y.-C.; Lin, Y.-J.; Wei, C.-Y.; Lin, Z.-X.; Wen, T.-C.; Chang, M.-Y.; Tsai, C.-L.; Wang, Y.-H. *Appl. Phys. Lett.* **2009**, *95*, 163303. (f) Yuan, Y.; Giri, G.; Ayzner, A. L.; Zoombelt, A. P.; Mannsfeld, S. C. B.; Chen, J.; Nordlund, D.; Toney, M. F.; Huang, J.; Bao, Z. *Nat. Commun.* **2014**, *5*, 3005.
3. (a) Walker, B.; Kim, C.; Nguyen, T.-Q. *Chem. Mater.* **2011**, *23*, 470. (b) Facchetti, A. *Chem. Mater.* **2011**, *23*, 733. (c) Mishra, A.; Bäuerle, P. *Angew. Chem., Int. Ed.*

- 2012**, *51*, 2020. (d) Kularatne, R. S.; Magurudeniya, H. D.; Sista, P.; Biewer, M. C.; Stefan, M. C. *J. Polym. Sci., Part A: Polym. Chem.* **2013**, *51*, 743.
4. (a) Snaith, H. J. *J. Phys. Chem. Lett.* **2013**, *4*, 3623. (b) Löper, P.; Moon, S.-J.; de Nicolas, S. M.; Niesen, B.; Ledinsky, M.; Nicolay, S.; Bailat, J.; Yum, J.-H.; Wolf, S. D.; Ballif, C. *Phys. Chem. Chem. Phys.* **2015**, *17*, 1619. (c) Bailie, C. D.; Christoforo, M. G.; Malioa, J. P.; Bowring, A. R.; Unger, E. L.; Nguyen, W. H.; Burschka, J.; Pellet, N.; Lee, J. Z.; Grätzel, M.; Noufi, R.; Buonassisi, T.; Salleo, A.; McGehee, M. D. *Energy Environ. Sci.* **2015**, *8*, 956.
5. (a) Gao, P.; Grätzel, M.; Nazeeruddin, M. K. *Energy Environ. Sci.* **2014**, *7*, 2448. (b) Miyasaka, T. *Chem. Lett.* **2015**, *44*, 720. (c) Jung, H. S.; Park, N.-G. *Small* **2015**, *11*, 10. (d) Luo, S.; Daoud, W. A. *J. Mater. Chem. A* **2015**, *3*, 8992.
6. (a) Pattanasattayavong, P.; Yaacobi-Gross, N.; Zhao, K.; Ndjawa, G. O. N.; Li, J.; Yan, F.; O'Regan, B. C.; Amassian, A.; Anthopoulos, T. D. *Adv. Mater.* **2013**, *25*, 1504. (b) Qin, P.; Tanaka, S.; Ito, S.; Tetreault, N.; Manabe, K.; Nishino, H.; Nazeeruddin, M. K.; Grätzel, M. *Nat. Commun.* **2014**, *5*, 3834. (c) Perumal, A.; Faber, H.; Yaacobi-Gross, N.; Pattanasattayavong, P.; Burgess, C.; Jha, S.; McLachlan, M. A.; Stavrinou, P. N.; Anthopoulos, T. D.; Bradley, D. D. C. *Adv. Mater.* **2015**, *27*, 93. (d) Jung, J. W.; Chueh, C.-C.; Jen, A. K.-Y. *Adv. Energy Mater.* **2015**, *5*, 1500486. (e) Wijeyasinghe, N.; Anthopoulos, T. D. *Semicond. Sci. Technol.* **2015**, *30*, 104002.
7. Wang, J.; Ibarra, V.; Barrera, D.; Xu, L.; Lee, Y.-J.; Hsu, J. W. P. *J. Phys. Chem. Lett.* **2015**, *6*, 1071.
8. Liu, M.-L.; Wu, L.-B.; Huang, F.-Q.; Chen, L.-D.; Chen, I.-W. *J. Appl. Phys.* **2007**, *102*, 116108.
9. (a) Battaglia, C.; Yin, X.; Zheng, M.; Sharp, I. D.; Chen, T.; McDonnell, S.; Azcatl, A.; Carraro, C.; Ma, B.; Maboudian, R.; Wallace, R. M.; Javey, A. *Nano Lett.* **2014**, *14*, 967. (b) Du, W.; Takabe, R.; Baba, M.; Takeuchi, H.; Hara, K. O.; Toko, K.; Usami, N.; Suemasu, T. *Appl. Phys. Lett.* **2015**, *106*, 122104.
10. (a) Steirer, K. X.; Ndione, P. F.; Widjonarko, N. E.; Lloyd, M. T.; Meyer, J.; Ratcliff, E. L.; Kahn, A.; Armstrong, N. R.; Curtis, C. J.; Ginley, D. S.; Berry, J. J.; Olson, D. C. *Adv. Energy Mater.* **2011**, *1*, 813. (b) Manders, J. R.; Tsang, S.-W.; Hartel, M. J.; Lai, T.-H.; Chen, S.; Amb, C. M.; Reynolds, J. R.; So, F. *Adv. Funct. Mater.* **2013**, *23*, 2993. (c) Jeng, J.-Y.; Chen, K.-C.; Chiang, T.-Y.; Lin, P.-Y.; Tsai, T.-D.; Chang, Y.-C.; Guo, T.-F.; Chen, P.; Wen, T.-C.; Hsu, Y.-J. *Adv. Mater.* **2014**, *26*, 4107.

11. (a) Paul, G. K.; Mwaura, J.; Argun, A. A.; Taranekar, P.; Reynolds, J. R. *Macromolecules* **2006**, *39*, 7789. (b) Jang, J.; Ha, J.; Kim, K. *Thin Solid Films* **2008**, *516*, 3152. (c) Lin, C. W.; Tai, Y.; Liaw, D. J.; Chen, M. C.; Huang, Y. C.; Lin, C. T.; Huang, C. W.; Yang, Y. J.; Chen, Y. F. *J. Mater. Chem.* **2012**, *22*, 57. (d) Lee, J.-H.; Lee, S.; Kim, J.-B.; Jang, J.; Kim, J.-J. *J. Mater. Chem.* **2012**, *22*, 15262. (e) Shelton, S. W.; Chen, T. L.; Barclay, D. E.; Ma, B. *ACS Appl. Mater. Interfaces* **2012**, *4*, 2534. (f) Blankenburg, L.; Sensfuss, S.; Schache, H.; Marten, J.; Milker, R.; Schrödner, M. *Synth. Met.* **2015**, *199*, 93.
12. Wakamiya, A.; Nishimura, H.; Fukushima, T.; Suzuki, F.; Saeki, A.; Seki, S.; Osaka, I.; Sasamori, T.; Murata, M.; Murata, Y.; Kaji, H. *Angew. Chem., Int. Ed.* **2014**, *53*, 5800.
13. (a) Patterson, A. L. *Phys. Rev.* **1939**, *56*, 978. (b) Ould-Ely, T.; Luger, M.; Kapln-Reinig, L.; Niesz, K.; Doherty, M.; Morse, D. E. *Nat. Photon.* **2011**, *6*, 97. (c) Mai, N. T.; Thuy, T. T.; Mott, D. M.; Maenosono, S. *CrystEngComm* **2013**, *15*, 6606.
14. (a) Blom, P. W. M.; deJong, M. J. M.; Vleggaar, J. J. M. *Appl. Phys. Lett.* **1996**, *68*, 3308. (b) Bozano, L.; Carter, S. A.; Scott, J. C.; Malliaras, G. G.; Brock, P. J. *Appl. Phys. Lett.* **1999**, *74*, 1132.
15. (a) Marcus, R. A. *J. Chem. Phys.* **1956**, *24*, 966. (b) Marcus, R. A.; Sutin, N. *Biochem. Biophys. Acta* **1985**, *811*, 265.
16. Gaussian 09 (Revision A.02), Frisch, M. J.; Trucks, G. W.; Schlegel, H. B.; Scuseria, G. E.; Robb, M. A.; Cheeseman, J. R.; Scalmani, G.; Barone, V.; Mennucci, B.; Petersson, G. A.; Nakatsuji, H.; Caricato, M.; Li, X.; Hratchian, H. P.; Izmaylov, A. F.; Bloino, J.; Zheng, G.; Sonnenberg, J. L.; Hada, M.; Ehara, M.; Toyota, K.; Fukuda, R.; Hasegawa, J.; Ishida, M.; Nakajima, T.; Honda, Y.; Kitao, O.; Nakai, H.; Vreven, T.; Montgomery, Jr., J. A.; Peralta, J. E.; Ogliaro, F.; Bearpark, M.; Heyd, J. J.; Brothers, E.; Kudin, K. N.; Staroverov, V. N.; Keith, T.; Kobayashi, R.; Normand, J.; Raghavachari, K.; Rendell, A.; Burant, J. C.; Iyengar, S. S.; Tomasi, J.; Cossi, M.; Rega, N.; Millam, J. M.; Klene, M.; Knox, J. E.; Cross, J. B.; Bakken, V.; Adamo, C.; Jaramillo, J.; Gomperts, R.; Stratmann, R. E.; Yazyev, O.; Austin, A. J.; Cammi, R.; Pomelli, C.; Ochterski, J. W.; Martin, R. L.; Morokuma, K.; Zakrzewski, V. G.; Voth, G. A.; Salvador, P.; Dannenberg, J. J.; Dapprich, S.; Daniels, A. D.; Farkas, O.; Foresman, J. B.; Ortiz, J. V.; Cioslowski, J.; Fox, D. J., Gaussian, Inc., Wallingford CT, 2009.

Chapter 4

Hole-Transporting Materials with a Two-Dimensionally Expanded π -System around an Azulene Core for Efficient Perovskite Solar Cells

Abstract: As hole-transporting material (HTM) for perovskite solar cells, two-dimensionally expanded π -systems, consisting of partially oxygen-bridged triarylamine skeletons that are connected to an azulene (**1–3**) or biphenyl core (**4**), were synthesized and characterized. When tetra-substituted azulene **1** was used in perovskite solar cells, the observed performance (power conversion efficiency = 16.5%) was found to be superior to that of the standard HTM (Spiro-OMeTAD). A comparison of the hole mobility, the ability to control the HOMO and LUMO levels, as well as the hole-collection efficiency at the perovskite/HTM interface in **1** with reference compounds (**2–4** and Spiro-OMeTAD) led to the elucidation of key factors required for HTMs to act efficiently in perovskite solar cells.

Introduction

Perovskite solar cells represent attractive cost-effective next generation printable photovoltaics.¹ In this type of solar cells, perovskite semiconductors, such as lead halide perovskite $\text{CH}_3\text{NH}_3\text{PbI}_3$, act as photoabsorbers to generate free carriers that can be collected in the electrodes through both p- and n-type buffer layers.² In a relatively short period, power conversion efficiencies (PCEs) in such cells have been substantially increased, mainly due to improvements of the fabrication protocols for the perovskite layer.³

Although tremendous efforts have been devoted to the development of improved hole-transporting materials (HTMs) for buffer layers,^{4,5} the number of high-performance HTMs is still limited.⁵ Hence, 2,2',7,7'-tetrakis(*N,N*-di-*p*-methoxyphenylamine)-9,9'-spirobifluorene (Spiro-OMeTAD), traditionally used for solid-state dye-sensitized solar cells,⁶ remains the standard buffer material even in perovskite solar cells, despite its high cost. For further improvements of the PCE, the development of superior and cost-effective next-generation HTMs based on new molecular design concepts, as well as the elucidation of the key factors that determine the photovoltaic performance in perovskite solar cells, will be crucial.

Conventional HTMs for perovskite solar cells are often based on triarylamine skeletons with propeller-like structures.^{4,5} As mentioned in chapter 1, compounds containing partially oxygen-bridged triarylamines as quasiplanar scaffolds facilitates delocalized π -conjugation and on-top π -stacking in the solid state, which ensures high carrier mobilities in the π -stacking direction.⁷

In this chapter, the author described the development of novel hole-transporting materials and their application for the p-type buffer layer materials in perovskite solar cells. As the materials for perovskite solar cells, the two-dimensionally expanded system **1** with a sheet-shaped structure, in which four oxygen-bridged triarylamines that contain alkoxy groups to enhance the solubility were attached to a core skeleton (Figure 1), were designed and synthesized. For the core skeleton, the author selected azulene, which is a nonbenzenoid aromatic hydrocarbon⁸ that exhibits unique electron-donating and accepting character arising from the five- and seven-membered ring, respectively. Using **1** as a HTM in perovskite solar cells led to high PCEs (16.5%), even when compared to Spiro-OMeTAD. By comparison with reference compounds **2** (1,3-disubstituted azulene), **3** (5,7-disubstituted azulene), **4** (3,3',5,5'-tetra-substituted 1,1'-biphenyl), and Spiro-OMeTAD, the key factors that improve the efficiency of HTMs in perovskite solar cells, which ultimately led to an increase in cell performance,

were determined.

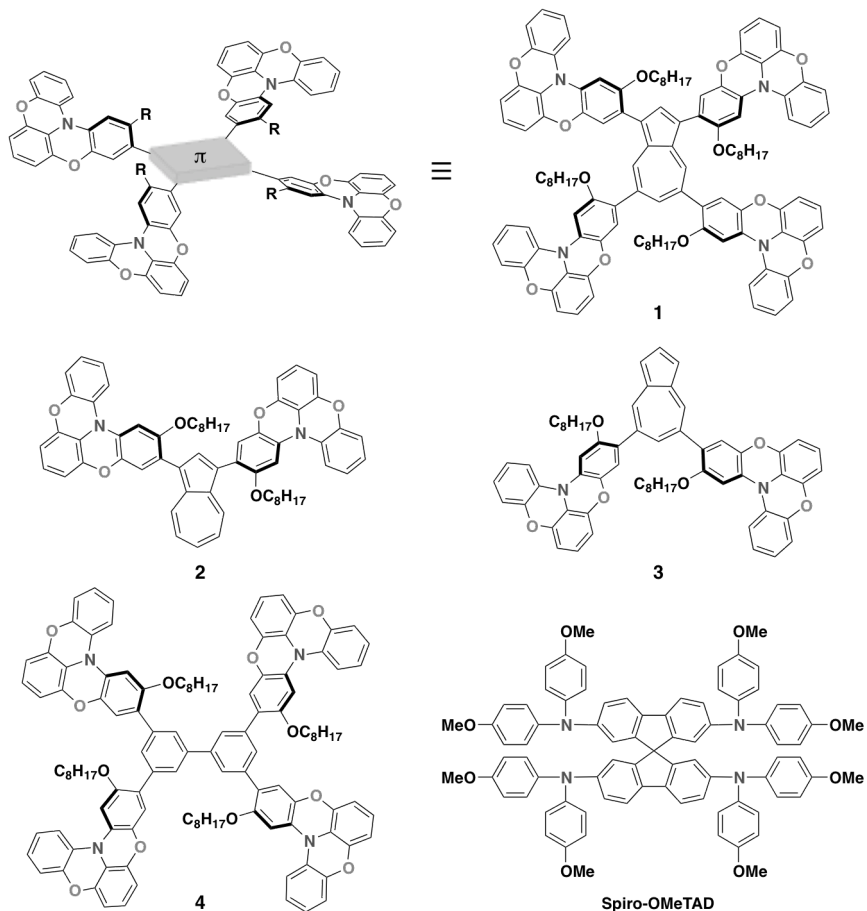


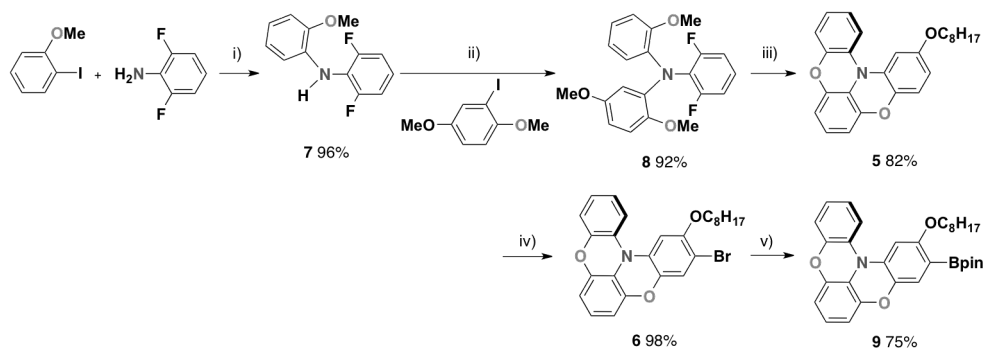
Figure 1. The molecular design for the HTMs in this study together with structures of **1–4** and Spiro-OMeTAD.

Results and Discussion

Synthesis

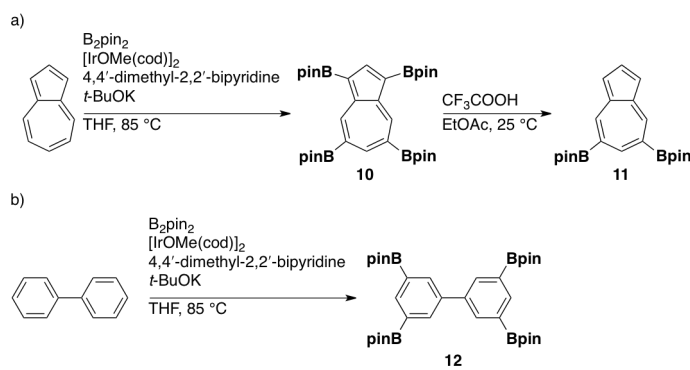
Octyloxy-substituted oxygen-bridged triarylamine derivative **5** was synthesized according to similar synthetic method as shown in Chapter 1 (Scheme 1).⁷ Using *o*-iodoanisole and 2,6-difluoroaniline as starting materials, monoarylated difluoroaniline **7** was selectively synthesized by Buchwald-Hartwig arylation in 96% yield. Subsequently, Ullmann arylation of **7** with 2-iodo-1,4-dimethoxybenzene using Cu and K₂CO₃ gave bisarylated difluoroaniline **8** in 92% yield. After cleavage of methyl groups of **8** by BBr₃, double-cyclization under the condition with K₂CO₃ in DMF at 120 °C, followed by treatment with 1-bromooctane at 80 °C gave **5** in 82% yield. Treatment of

5 with 1 equiv NBS selectively afforded monobrominated derivative **6** in 98% yield. Lithiation of **6** with *n*-BuLi, followed by treatment with *i*PrOBpin afforded monoborylated **9** in 75% yield.



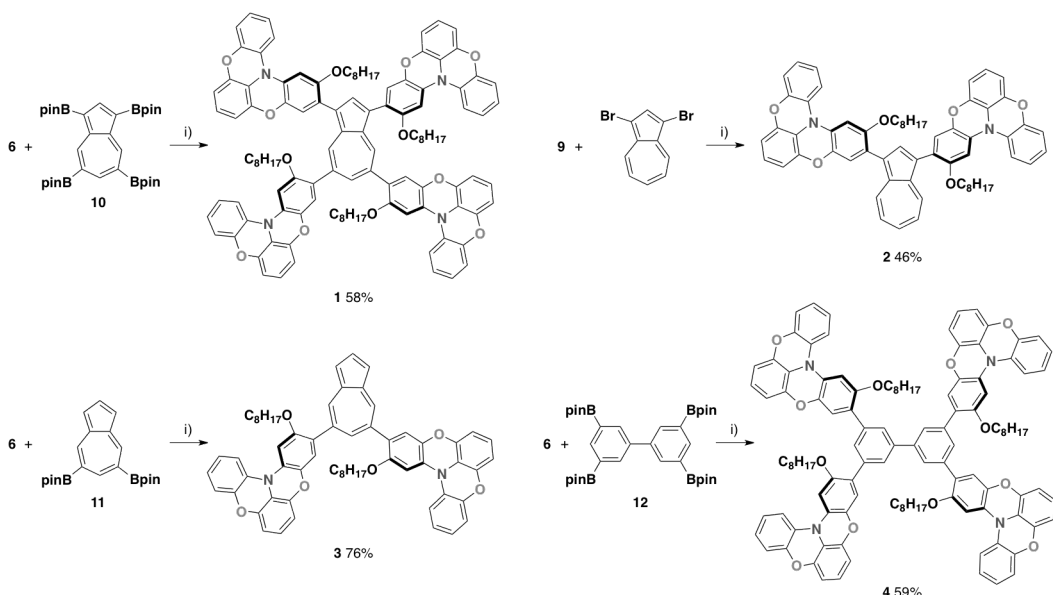
Scheme 1. Reagents/conditions: i) $\text{Pd}_2(\text{dba})_3 \cdot \text{CHCl}_3$, $\text{P}(t\text{-Bu})_3$, $\text{NaOt-}t\text{-Bu}$, toluene, 100°C ; ii) Cu , K_2CO_3 , 18-crown-6, mesitylene, 220°C ; iii) 1. BBr_3 , CH_2Cl_2 , rt, 2. K_2CO_3 , DMF, 120°C , 3. $\text{C}_8\text{H}_{17}\text{Br}$, 80°C ; iv) NBS (1 equiv), CH_2Cl_2 , rt; v) 1. $n\text{-BuLi}$, THF, -78°C , 2. *i*PrOBpin, rt.

Compound **1–4** were afforded by Suzuki-Miyaura cross coupling of corresponding brominated and borylated skeletons. The author found and optimized the reaction condition for selective borylation of azulene using Ir catalyst in the presence of potassium *t*-butoxide, which made the facile preparation of a series of azulene derivatives possible. Thus, 1,3,5,7-tetra(Bpin)azulene **10** was synthesized by direct borylation using Ir catalyst (Scheme 2a).⁹ 5,7-Di(Bpin)azulene **11** was obtained by the selective deborylation of **10** (Scheme 2a).⁹ In a similar manner, 3,3',5,5'-tetra(Bpin)-1,1'-biphenyl **12** was also synthesized by direct borylation using Ir catalyst (Scheme 2b).¹⁰



Scheme 2.

Tetra-substituted azulene derivative **1** was obtained by Suzuki-Miyaura cross coupling of the brominated derivative **6** and tetra-borylated azulene **10** in 58% yield as green solids (Scheme 3). In a similar manner, coupling reaction of **6** and diborylated azulene **11** afforded the derivative **3** in 76% yield as green solids. Coupling reaction of **6** and tetra-borylated biphenyl **12** afforded tetra-substituted biphenyl derivative **4** in 59% yield as pale yellow solids. 1,3-Dibromoazulene was obtained by bromination of azulene with 2 equiv NBS in 79% yield.¹¹ Suzuki-Miyaura cross coupling of 1,3-dibromoazulene and borylated derivative **9** afforded **2** in 46% yield as green solids. Compounds **1–4** were characterized by NMR, HRMS, and elemental analysis.



Scheme 3. Reagents/conditions: i) $\text{PdCl}_2(\text{dppf}) \cdot \text{CH}_2\text{Cl}_2$, Cs_2CO_3 , THF, 95 °C.

Solubility and Thermal Stability

In perovskite solar cells, hole-transporting layers are prepared by spin-coating of solution, thus the solubility of hole transporting materials is important. All of **1–4** exhibit good solubility in common organic solvents (e.g. >100 mg/mL in chlorobenzene) enough for spin-coating.

In order to examine their thermal stabilities, thermogravimetric analysis (TGA) was conducted. All of **1–4** exhibit high decomposition temperatures (T_{d5}) of **1**: 419 °C, **2**: 428 °C, **3**: 428 °C, and **4**: 421 °C, respectively, indicating good thermal stability (Figure 2).

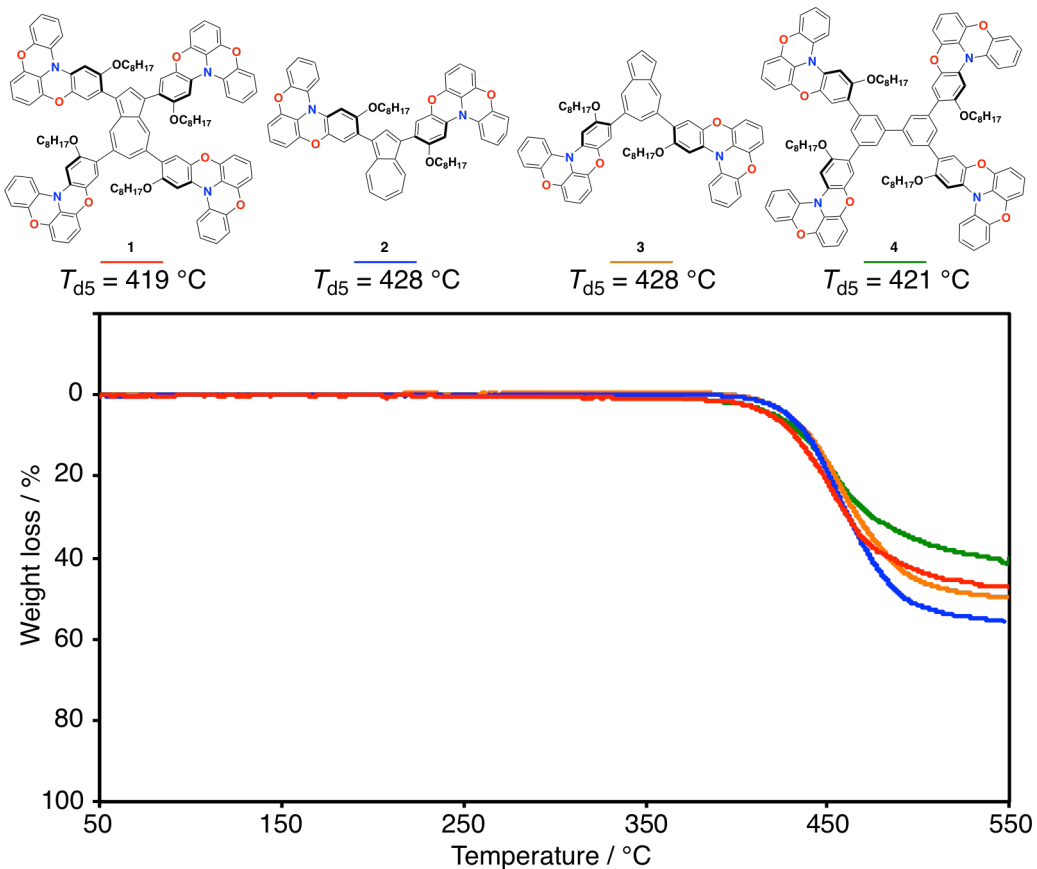


Figure 2. Thermogravimetric analysis of **1–4** heating at 10 °C/min under N₂.

Theoretical Calculations

DFT calculations at the B3LYP/6-31G(d) level of theory showed that the Kohn-Sham (KS)-HOMOs of 1,3,5,7-tetra-substituted **1** (−4.23 eV) and 1,3-disubstituted **2** (−4.42 eV) are delocalized over the entire π-conjugated skeleton, including the azulene core (Figure 3). The calculated KS-HOMO levels reflect the high electron-donating ability of the five-membered ring of azulene. In comparison to **1** and **2**, the KS-HOMO levels in 5,7-disubstituted **3** (−4.60 eV) and biphenyl core compound **4** (−4.61 eV) are lower. The KS-LUMOs of azulene core compounds **1–3** are localized on the azulene skeleton. In contrast, the KS-LUMO of biphenyl core compound **4** is slightly delocalized over triphenylamine skeleton. The calculated KS-LUMO levels of azulene core compounds **1–3** (−1.61 to −1.75 eV) are lower than biphenyl core compound **4** (−0.87 eV).

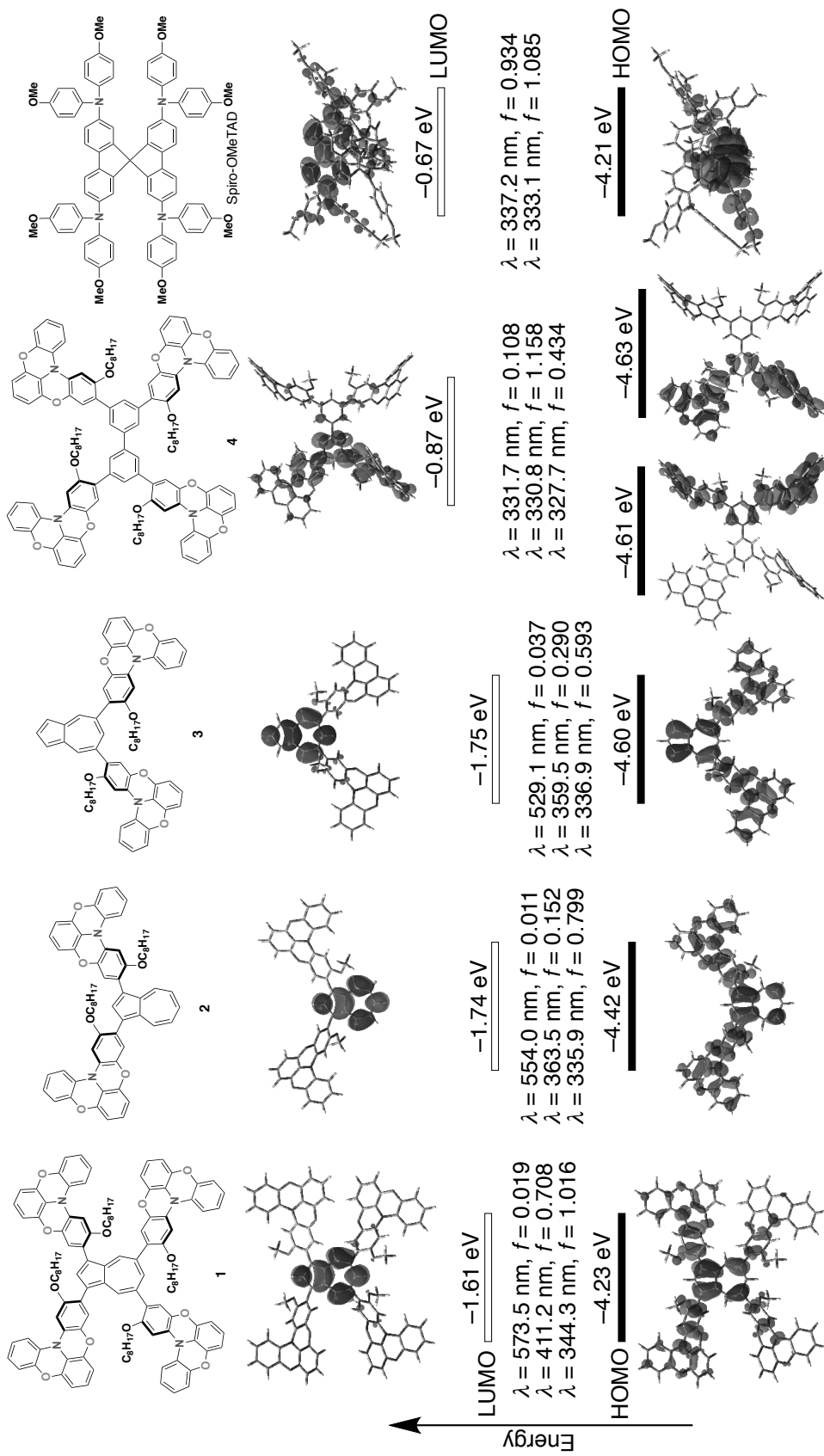


Figure 3. Pictorial presentation of the frontier orbitals, a plot of the Kohn-Sham HOMO and LUMO energy levels for **1–4** and Spiro-OMeTAD (B3LYP/6-31G(d)), and optical transition with oscillator strength (CAM-B3LYP/6-31G(d)/B3LYP/6-31G(d)).

Electrochemical Property

The electrochemical properties of **1–4** were measured by cyclic voltammetry in CH_2Cl_2 (Figure 4). **1** shows four reversible oxidation waves, indicating the stability of the cationic species. As predicted by DFT calculations, the experimentally observed first oxidation potentials of **1** and **2** are lower (**1**: +0.00 V vs. Fc/Fc^+ ; **2**: +0.09 V) than those of **3** (+0.41 V) and **4** (+0.26 V). The HOMO levels of **1–4** estimated according to the equation $\text{HOMO} = -(E_{\text{onset}} + 5.10 \text{ eV})^{12}$ were –5.04 eV, –5.12 eV, –5.42 eV, and –5.27 eV, respectively.

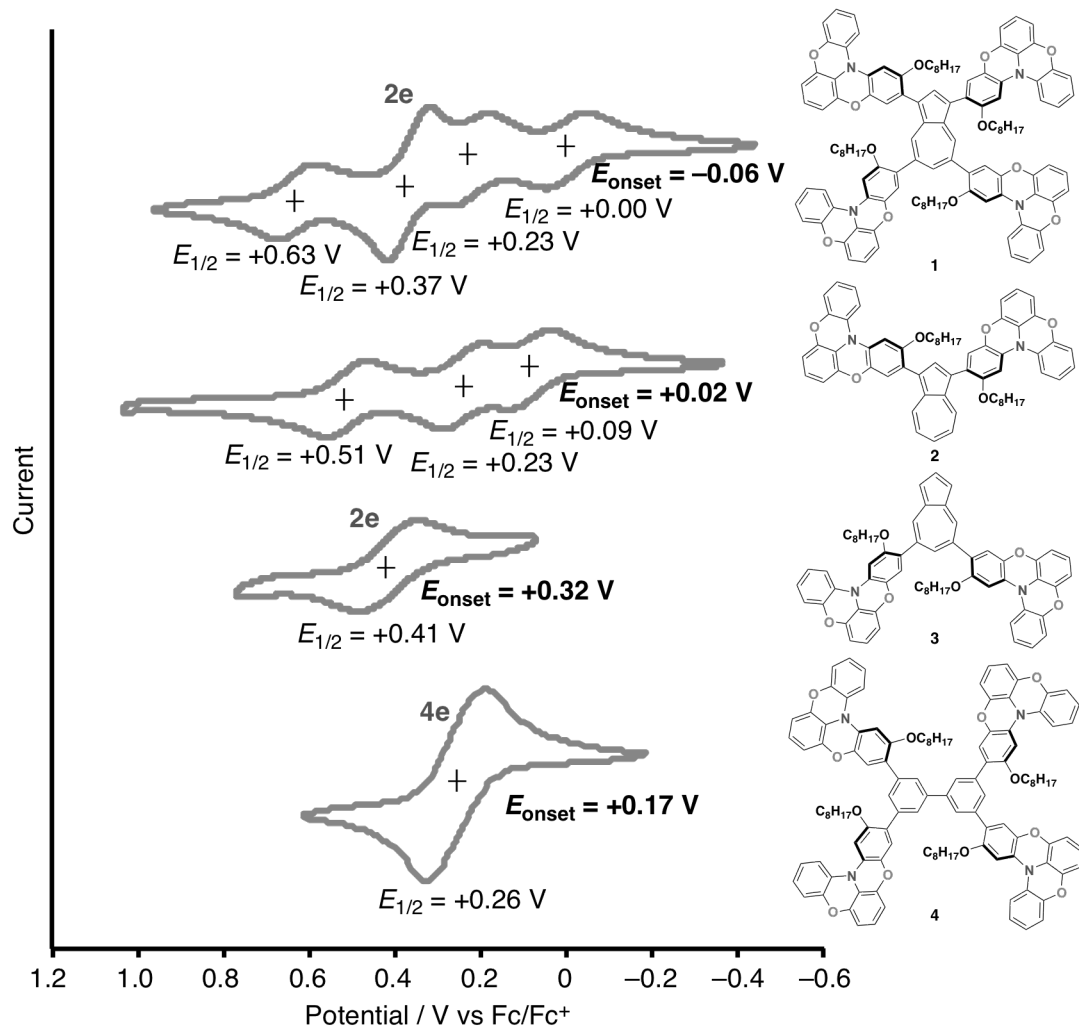


Figure 4. Cyclic voltammograms of **1–4** in CH_2Cl_2 (0.5 mM), measured with $(n\text{-Bu})_4\text{N}^+\text{PF}_6^-$ as a supporting electrolyte at a scan rate of 100 mVs^{–1}.

Photophysical Property

The UV-vis absorption measurements of **1–4** were conducted in CH_2Cl_2 and spin-coated films. All of **1–4** exhibit an intense absorption in the UV and/or short wavelength visible region (≤ 450 nm), associated with a $\pi-\pi^*$ transition in CH_2Cl_2 (Figure 5). In addition, azulene derivatives **1–3** exhibit a very weak and broad peak in the visible region around 500–900 nm, corresponding to the intramolecular charge transfer transition of the azulene moiety. In spin-coated films, **1–4** show similar absorption spectra with those in CH_2Cl_2 (Figure 6).

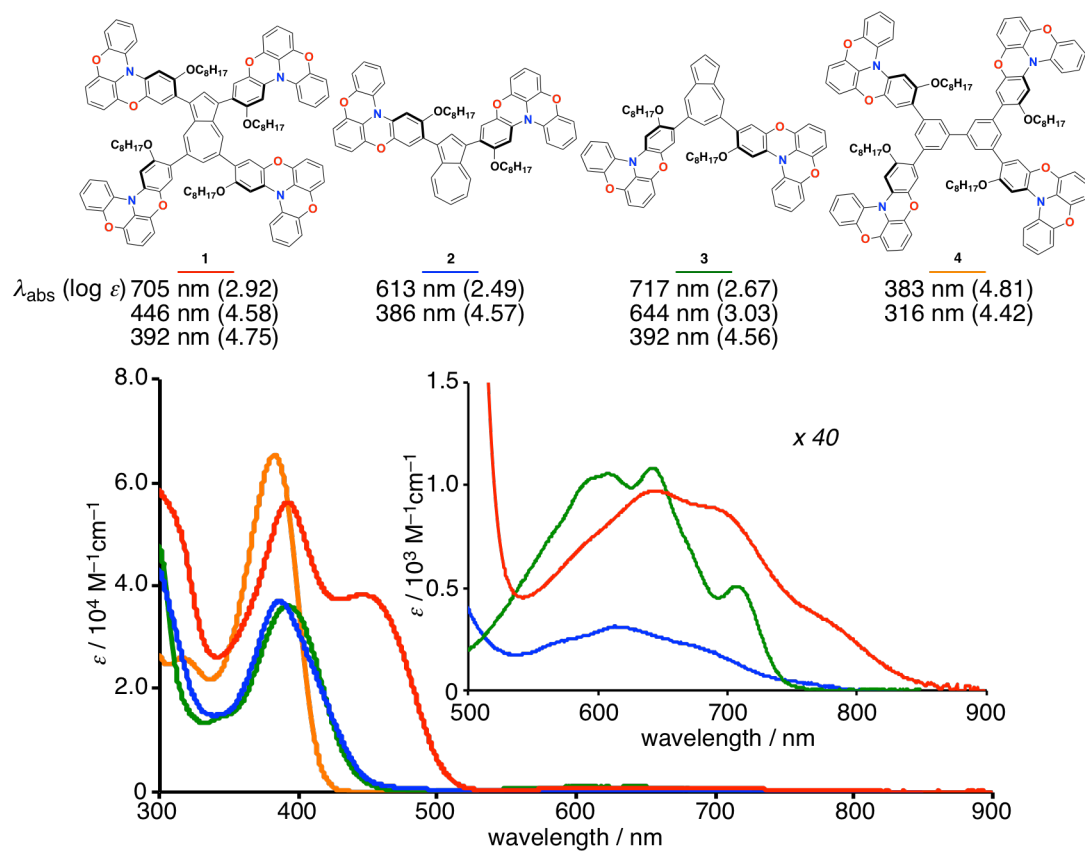


Figure 5. UV-vis absorption spectra of **1–4** in CH_2Cl_2 .

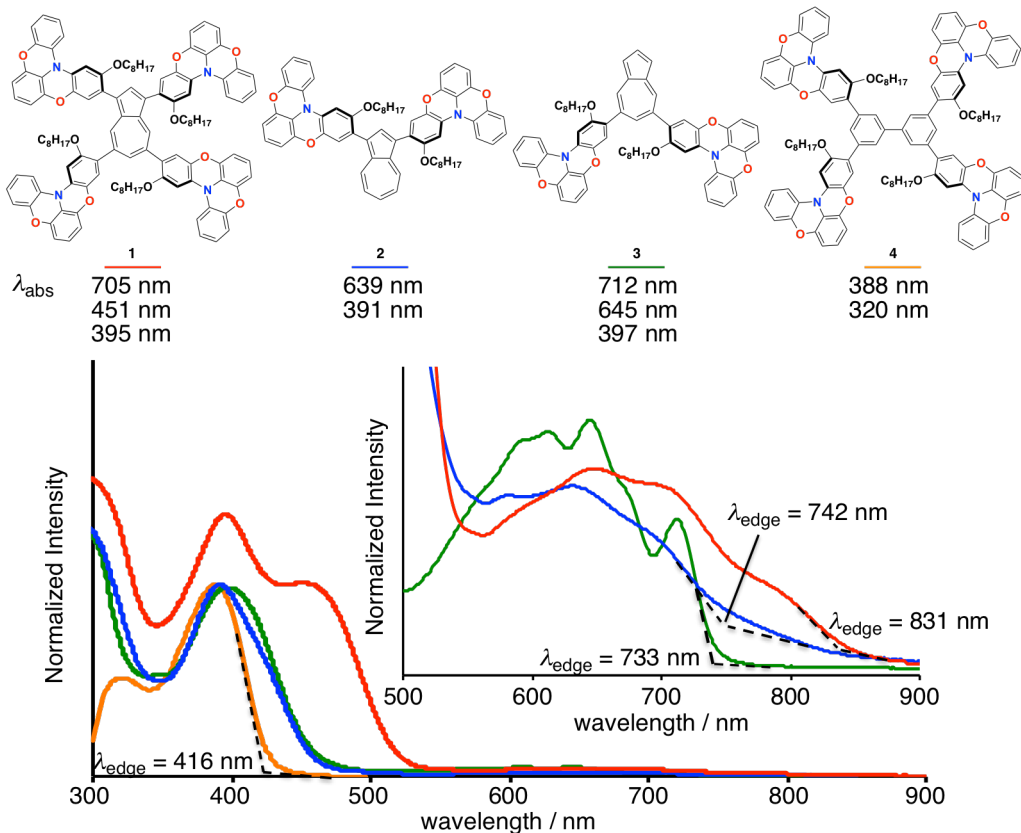


Figure 6. UV-vis absorption spectra of **1–4** in the spin-coated films.

Device Fabrication

In order to investigate the performance of **1–4** in perovskite solar cells, devices using **1–4** as HTMs were fabricated. The standard cells were based on the following structure: FTO/ compact-TiO₂ (30 nm)/ mesoporous-TiO₂ (200 nm)/ perovskite CH₃NH₃PbI₃ (250 nm)/ HTM (250 nm)/ Au (80 nm). The perovskite layers were prepared according to optimized sequential two-step solution method.¹³ Hole-transport layers (HTLs) were deposited under an inert atmosphere (N₂) on the perovskite layer by spin-coating a chlorobenzene solution of the HTM with additives, such as Co(III)-based oxidizing agent (FK209),¹⁴ lithium bis(trifluoromethane)sulfonamide (LiTFSI), and 4-*tert*-butylpyridine. The PCE is defined as the following equation:

$$\text{PCE} = J_{\text{SC}} \cdot V_{\text{OC}}/\text{FF}$$

where J_{SC} is the short-circuit current density (mA/cm²), V_{OC} is the open-circuit voltage (V), and FF is the fill factor, respectively. The use of purified solvents and materials, such as CH₃NH₃I and PbI₂, has proven to be essential in order to achieve good results (PCE = 13.4±0.5%), both in terms of performance and reproducibility (Figure 7).

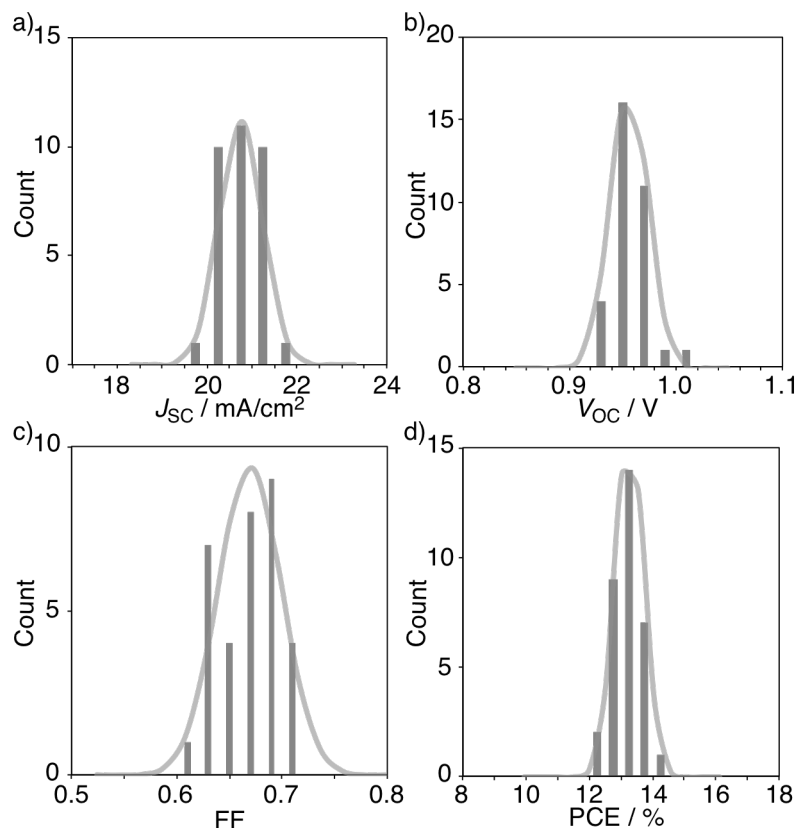


Figure 7. Histograms of each value of (a) J_{SC} , (b) V_{OC} , (c) FF and (d) PCE for 33 samples of perovskite solar cells (0.04 cm^2 mask), which were prepared by optimum two-step solution method for perovskite layer using Spiro-OMeTAD with 0.10 eq. Co (III) dopant as a HTM.

Device Performance

In order to examine the effect of the amount of oxidizing agent on the solar cell performance, the amount of Co(III) dopant in **1** was initially screened (Figure 8, Table 1). Upon gradual increasing of the amount of oxidant from 0.0 eq. (PCE = 4.8%) to 0.20 eq. (PCE = 14.8%), a significant increase in the solar cell performance was observed, exhibiting a maximum for 0.15 eq. (PCE = 15.7%). The observed PCE is significantly higher than that using Spiro-OMeTAD under identical conditions (PCE = 13.6% with 0.10 eq. of Co(III) dopant), and thus demonstrates the superior performance of **1** as a HTM (Figure 9, Table 2). In the cell using **1**, the increases in open-circuit voltage ($V_{OC} = 1.04 \text{ V}$) and fill factor ($FF = 0.73$) were remarkably higher relative to the Spiro-OMeTAD cell ($V_{OC} = 0.96 \text{ V}$, $FF = 0.68$). Cells containing reference compounds **2–4** were also prepared using the same two-step method for the preparation of the

perovskite layer. Even after screening of the amount of Co(III) dopant, only moderate PCEs were obtained for cells using **2** (9.7%, 0.15 eq.) or **3** (8.5%, 0.0eq.), whereas a cell with **4** showed an even lower performance (0.5%, 0.15 eq.).

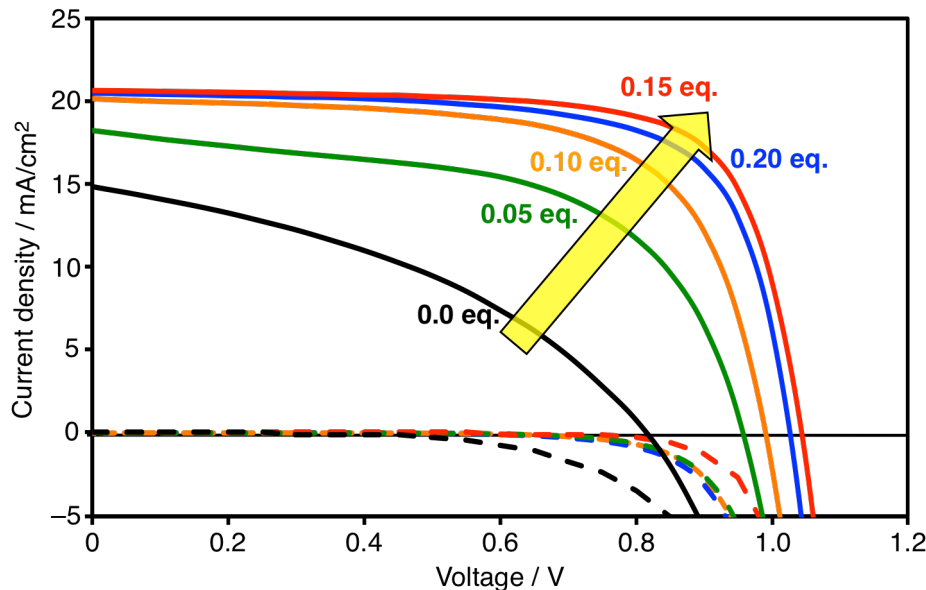


Figure 8. Current density-voltage characteristics for perovskite solar cells using **1** with different amount of Co(III) dopant (0.0 eq.: black, 0.05 eq.: green, 0.10 eq.: orange, 0.15 eq.: red, 0.20 eq.: blue) measured with a mask (0.04 cm^2) under 100 mW/cm^2 photon flux (AM1.5G) (solid line) and dark condition (dashed line).

Table 1. Summary of Photovoltaic Parameters Derived from J-V Measurements of Perovskite Solar Cells using **1 as HTM**

Co(III) Dopant [eq.]	J_{SC} [mA/cm ²]	V_{OC} [V]	FF	PCE [%]	R_s [Ωcm^2]	R_{sh} [Ωcm^2]
0.0	14.9	0.82	0.39	4.8	15	1.2×10^2
0.05	18.2	0.96	0.57	9.9	6.8	2.1×10^2
0.10	20.1	0.99	0.66	13.2	7.0	7.4×10^2
0.15	20.7	1.04	0.73	15.7	8.6	1.6×10^3
0.20	20.5	1.02	0.71	14.8	6.8	1.6×10^3

Components in the solution for the deposition of hole-transporting layer: **1** (0.050 M), FK209 (0.0–0.010 M), TBP (0.165 M), and LiTFSI (0.027 M) in chlorobenzene.

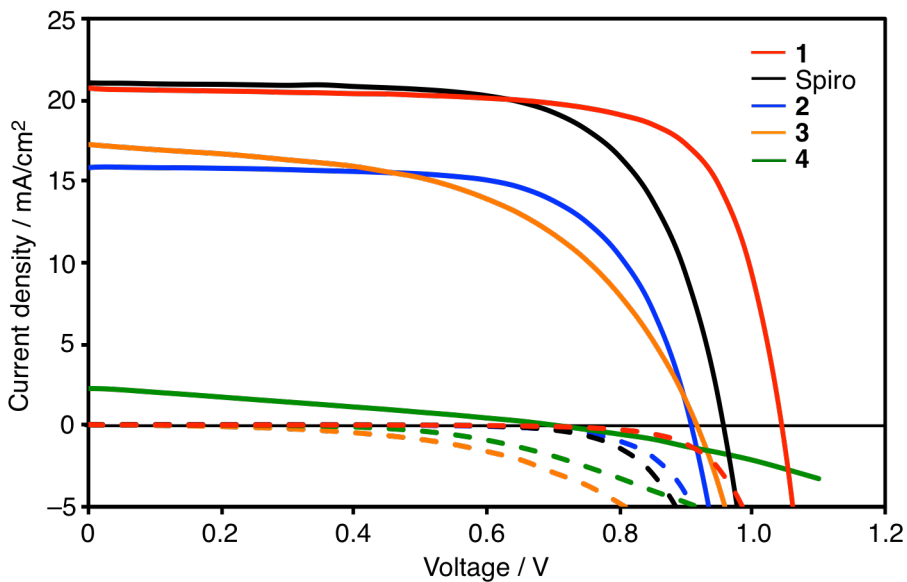


Figure 9. Current density-voltage characteristics of perovskite solar cells using **1** (red), **2** (blue), **3** (orange), **4** (green), and Spiro-OMeTAD (black) as HTMs measured with a mask (0.04 cm^2) under 100 mW/cm^2 photon flux (AM1.5G) (solid line) and dark condition (dashed line).

Table 2. Summary of Photovoltaic Parameters Derived from J - V Measurements of Perovskite Solar Cells using **1–**4** and Spiro-OMeTAD as HTMs**

HTM	J_{SC} [mA/cm ²]	V_{OC} [V]	FF	PCE [%]	R_s [Ωcm^2]	R_{sh} [Ωcm^2]
1	20.7	1.04	0.73	15.7	8.6	1.6×10^3
2	15.9	0.91	0.67	9.7	4.7	8.2×10^2
3	17.3	0.91	0.54	8.5	8.5	2.7×10^2
4	2.31	0.70	0.28	0.45	180	3.4×10^2
Spiro	21.0	0.96	0.68	13.6	4.6	2.6×10^3

Components in the solution for the deposition of hole-transporting layer: HTM (0.050 M), FK209 (0.0–0.0075 M), TBP (0.165 M), and LiTFSI (0.027 M) in chlorobenzene.

Recently, modified one-step solution methods using solvent engineering have been reported as effective methods to prepare flat and dense perovskite layers that provide high PCEs.³ When cells with **1** were prepared in such a one-step manner (toluene dropping), the PCEs further increased to 16.5% (Figure 10a). This result is even more

remarkable, considering that this method has not yet been optimized, which clearly demonstrates the high potential of **1** as a HTM in perovskite solar cells. As shown in Figure 10, the cell using **1** showed moderate hysteresis behavior, in which the forward scan performs better than the reverse scan. This hysteresis behavior is diametrically opposed to that observed in cells using Spiro-OMeTAD (Figure 10b). The origin of this moderate hysteresis remains unclear at present.

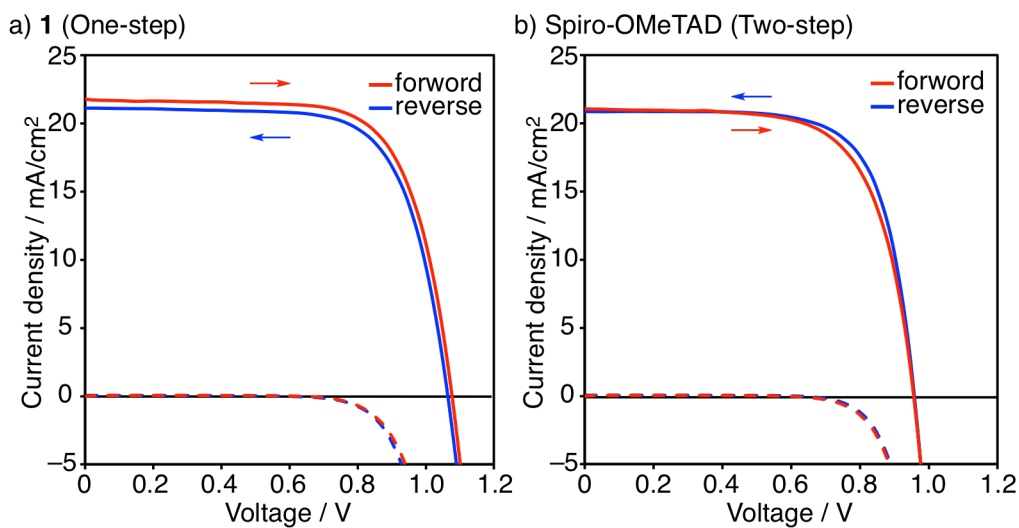


Figure 10. Current density-voltage characteristics of perovskite solar cells using a) **1** in which perovskite layer was fabricated by one-step solution method and b) Spiro-OMeTAD in which perovskite layer was fabricated by two-step solution method, measured by forward (red) and reverse (blue) scans under 100 mW/cm² photon flux (AM1.5G) (solid line) and dark condition (dashed line).

Table 3. Summary of Photovoltaic Parameters Derived from J-V Measurements of Perovskite Solar Cells using **1 and Spiro-OMeTAD as HTMs**

HTM	Scan Direction	J_{SC} [mA/cm ²]	V_{OC} [V]	FF	PCE [%]	R_s [Ωcm ²]	R_{sh} [Ωcm ²]
1	Forward	21.7	1.08	0.71	16.5	6.9	1.9×10^3
1	Reverse	21.1	1.06	0.70	15.8	7.7	2.4×10^3
Spiro	Forward	21.0	0.96	0.68	13.6	4.6	2.7×10^3
Spiro	Reverse	20.9	0.96	0.71	14.2	5.2	3.7×10^4

Components in the solution for the deposition of hole-transporting layer: HTM (0.050 M), FK209 (0.0050–0.0075 M), TBP (0.165 M), and LiTFSI (0.027 M) in chlorobenzene.

SEM Images

The film morphologies of the cells were confirmed by cross-sectional scanning electron microscopy (SEM). SEM images show that the perovskite layer fabricated by one-step method is flattened compared to those fabricated by two-step method (Figure 11). These differences of morphologies would lead higher PCE of cells prepared by one-step method. In the cells fabricated by two-step method, all doped HTM layers is comparable. This result suggests that the morphology of the films does not affect observed difference of photovoltaic performance between the cells using these materials.

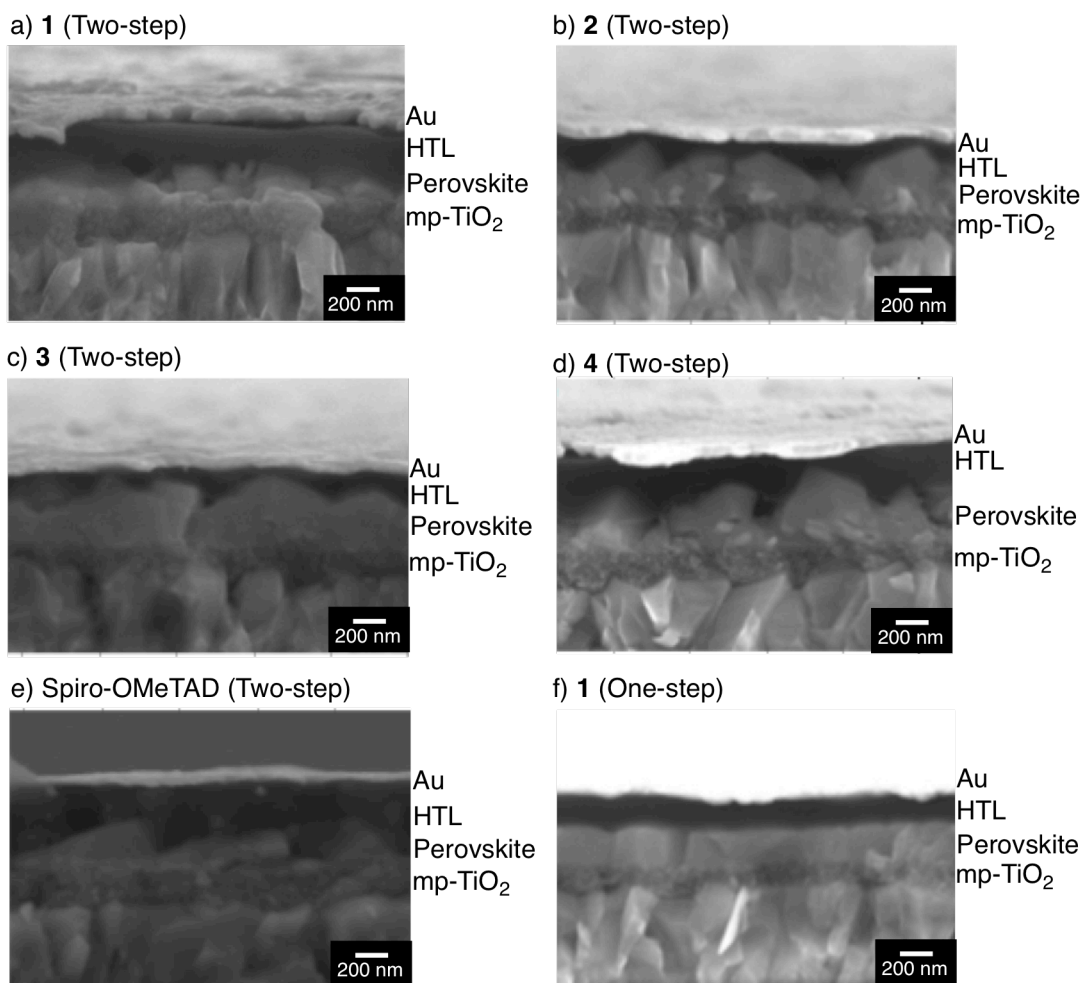


Figure 11. Cross-sectional SEM image for perovskite solar cell using (a) **1** with 0.15 eq. Co (III) dopant, (b) **2** with 0.15 eq. Co (III) dopant, (c) **3**, (d) **4** with 0.15 eq. Co (III) dopant, and (e) Spiro-OMeTAD with 0.10 eq. Co (III) dopant in which perovskite layer was fabricated by two-step solution method, and (f) **1** with 0.15 eq. Co (III) dopant in which perovskite layer was fabricated by one-step solution method.

Elucidation of the Factors to Improve PCEs

To elucidate the factors that enable compounds to act efficient HTMs in perovskite solar cells, **1–4** as well as Spiro-OMeTAD were compared with respect to 1) hole mobility, 2) electronic structure, i.e. HOMO and LUMO levels in bulk films, and 3) charge collection at the HTM/perovskite layer interface.

Hole Mobility

The hole mobility in neat bulk films of **1–4** and Spiro-OMeTAD with a thickness of 200–400 nm, which is comparable to films used in current perovskite solar cells, was examined by the space-charge-limited current (SCLC) method¹⁵ (Figure 12). The hole mobility of **1** ($2.1 \times 10^{-4} \text{ cm}^2/\text{Vs}$) was comparable to that of Spiro-OMeTAD ($2.7 \times 10^{-4} \text{ cm}^2/\text{Vs}$),¹⁶ and both values were higher than those of **2** ($7.6 \times 10^{-5} \text{ cm}^2/\text{Vs}$), **3** ($6.3 \times 10^{-6} \text{ cm}^2/\text{Vs}$), and **4** ($2.4 \times 10^{-5} \text{ cm}^2/\text{Vs}$). The observed correlation between the hole mobility and the PCE of **1–3** and Spiro-OMeTAD indicates a critical importance of a high carrier mobility, which should contribute in particular to high FF values.

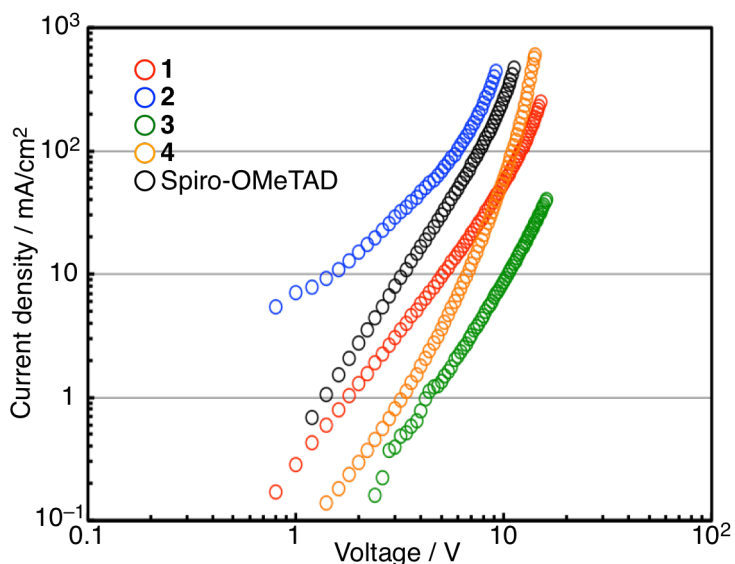


Figure 12. J – V characteristics of space-charge-limited current of non-doped HTMs. Relatively low threshold voltages indicate that these SCLC devices have ohmic contact.

The local charge mobility was measured by time-resolved microwave conductivity (TRMC) method.¹⁷ A spin-coated film of **1** exhibited a local mobility ($\Sigma\mu = 1.8 \text{ cm}^2/\text{Vs}$), which was four times higher than that of Spiro-OMeTAD ($\Sigma\mu = 0.45 \text{ cm}^2/\text{Vs}$), measured under the same conditions (Figure 13a).

Since the p-type buffer layer in the optimized cells contained oxidizing agents, TRMC measurements were also conducted on Co(III)-doped films of **1**. The TRMC signal ($\phi\Sigma\mu$), corresponding to the product of photogeneration efficiency of the charge carrier (ϕ) and $\Sigma\mu$, increased up to 4–5 times upon addition of 0.05–0.20 eq. of the oxidant (Figure 13b). Under the assumption that ϕ remains unchanged in the doped films, this result indicates that Co(III) doping induced a significant increase of the local mobility, which contributes to a reduced series resistance and facilitated ohmic contact with the metal.¹⁸ These tendencies are also shown in other compounds (Figure 14).

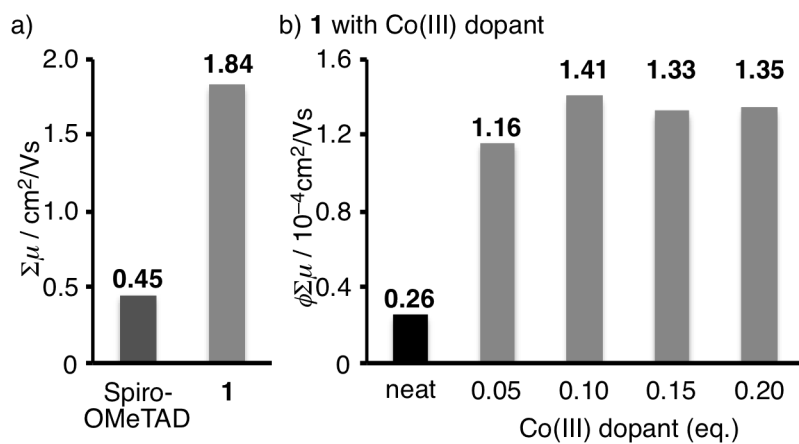


Figure 13. (a) Local mobility ($\Sigma\mu$) in non-doped films of Spiro-OMeTAD (blue) and **1** (red) measured by TRMC. (b) Maximum TRMC signal ($\phi\Sigma\mu$) for the spin-coated neat film (black) and Co(III) doped films (red) of **1**. The films were prepared by deposition of the solution containing additives, LiTFSI (0.54 eq.), TBP (3.3 eq.) and Co(III) dopant (0.0–0.20 eq.).

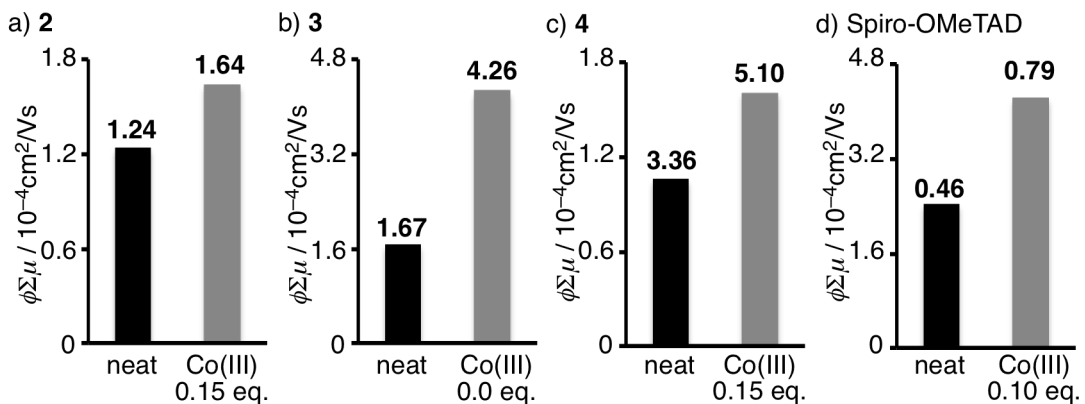


Figure 14. Maximum TRMC signal ($\phi\Sigma\mu$) for the spin-coated film (neat (black) and doped (red) HTMs): (a) **2**, (b) **3**, (c) **4**, and (d) Spiro-OMeTAD. The films were prepared by deposition of the solution containing additives, LiTFSI (0.54 eq.), TBP (3.3 eq.) and Co(III) dopant (0.0–0.15 eq.).

HOMO and LUMO Levels in Bulk Films

Subsequently, taking the effects of the oxidizing agents into account, the HOMO and LUMO levels in bulk films were evaluated (Figure 15). The ionization potentials (IPs, HOMO levels) were obtained from photoelectron spectroscopy measurements in air on the spin-coated films of **1–4** and Spiro-OMeTAD containing the previously determined optimum amount of Co(III) dopant. Compared to neat films without oxidant, the IPs of the doped films were found to decrease by ~0.1 eV due to partial oxidation. The IPs in **1–3** and Spiro-OMeTAD (-5.05 to -5.35 eV, $\Delta E = +0.10$ to $+0.40$ eV) are higher than that of the valence band (VB) in $\text{CH}_3\text{NH}_3\text{PbI}_3$ (-5.45 eV). In contrast, the IP in **4** (-5.44 eV) is comparable to that of the VB, indicating that an effective hole injection from the perovskite to **4** is impossible. This result is consistent with the fact that only very low PCE (0.45%) was observed for the cells using **4**.

Furthermore, the LUMO levels of **1–4** were determined based on these HOMO levels (IPs) and the optical band-gap energies that were determined from the absorption spectra of the spin-coated films. The LUMO levels of **1**, **2**, **4**, and Spiro-OMeTAD (-3.56 to -2.18 eV, $\Delta E = +0.34$ to $+1.72$ eV) are enough higher than the conduction band (CB) of $\text{CH}_3\text{NH}_3\text{PbI}_3$ (-3.90 eV),^{1c} indicating an efficient electron blocking ability of these materials. On the other hand, the LUMO level of **3** (-3.66 eV, $\Delta E = +0.24$ eV) is close to CB of $\text{CH}_3\text{NH}_3\text{PbI}_3$, which probably reflects an inefficient electron blocking ability of **3**, thus leading to a relatively small R_{sh} . These results clearly indicate the importance of being able to control the HOMO and LUMO levels of the HTM relative to the VB and CB levels of the perovskite material.

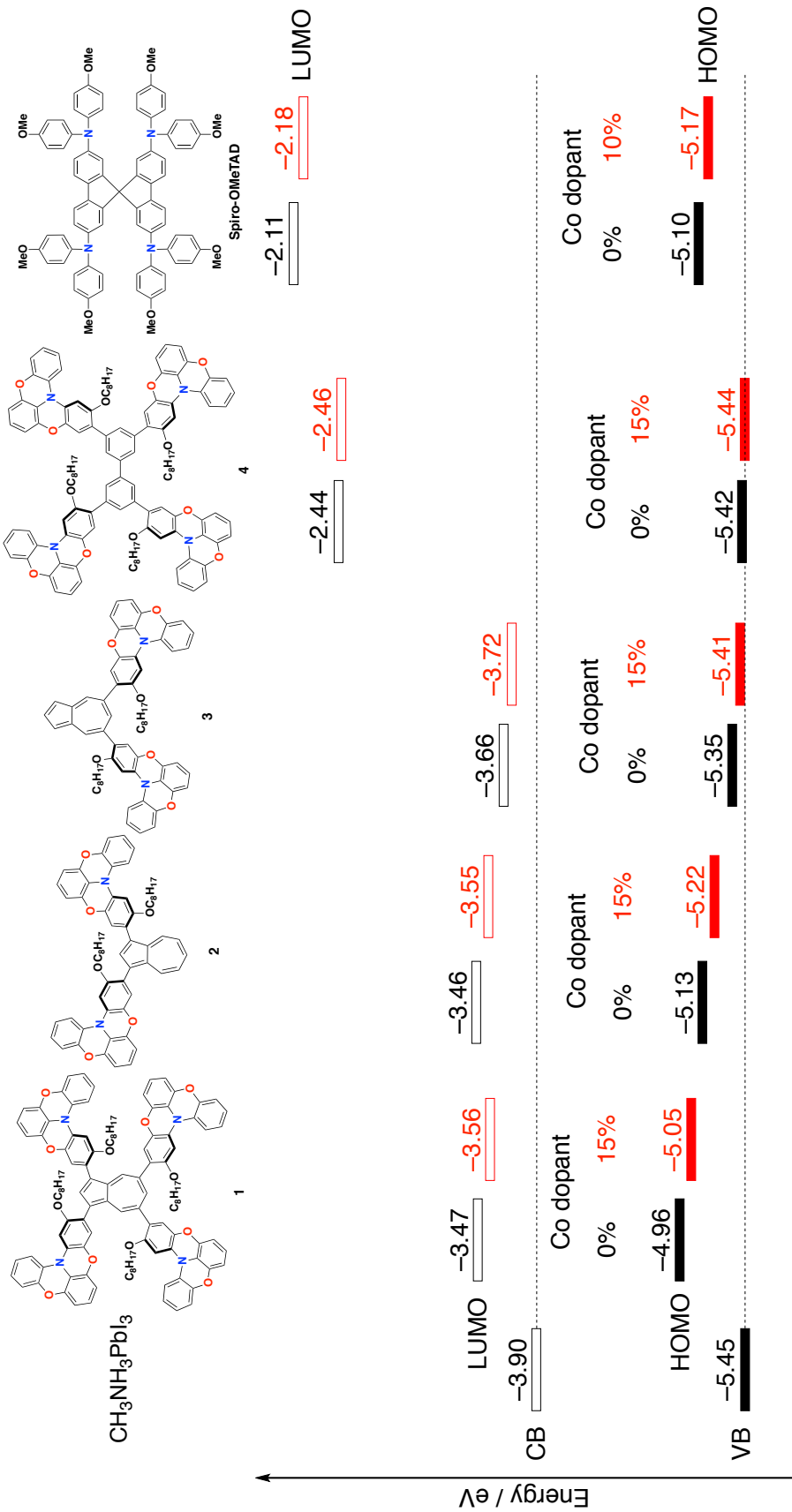


Figure 15. The HOMO and LUMO energy levels for **1–4** and Spiro-OMeTAD in neat films (black) and doped film (red). The HOMO energy levels in spin-coated films were measured by photoelectron spectroscopy in air and the LUMO energy levels were determined from the HOMO and absorption edge measured for the film.

Charge Collection at the HTM/perovskite Layer Interface

The question why tetra-substituted azulene derivative **1** exhibited a better performance than Spiro-OMeTAD and 1,3-disubstituted azulene **2** still remains to be addressed. For this purpose, the author examined the charge collection ability of these HTMs at their interface with the perovskite layer by measuring the transient decay of the TRMC. Recent TRMC studies on perovskite materials revealed that a TRMC signal ($\phi\Sigma\mu$) for perovskite on a mesoporous TiO_2 layer was by two orders of magnitude higher than those of organic HTMs such as Spiro-OMeTAD.^{17b} Accordingly, the charge collection ability of HTMs from the perovskite layer can be evaluated by the intensity decrease of the TRMC transient after deposition of the HTM onto the perovskite layer.

Figure 16 and 17 shows the transient TRMC decay prior and posterior to HTM coating. A significant decrease of peak intensity ($\Delta\phi\Sigma\mu$) and delay time was observed for both **1** (0.15 equiv Co(III) dopant) and Spiro-OMeTAD (0.10 equiv Co(III) dopant) (Figure 16e, 17g). In comparison, only a moderate decline was observed for **2** (0.15 equiv Co(III) dopant) (Figure 17b). This result indicates that the latter HTM coatings

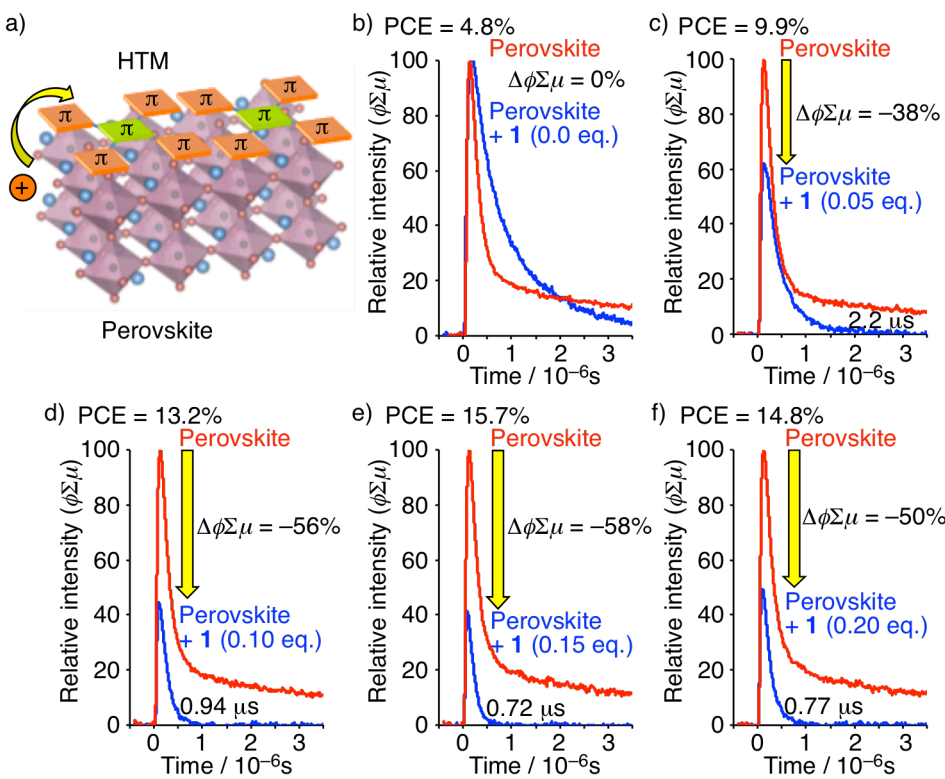


Figure 16. (a) Image of charge collection at the interface between perovskite and hole-transporting layer. (b–f) $\phi\Sigma\mu$ transients of perovskite films prior (red) and posterior (blue) to **1** coating at a photon flux of $I_0 = 1.4 \times 10^{11} \text{ photons/cm}^2$ with different amount of Co(III) dopant ((b) 0.0 eq., (c) 0.05 eq., (d) 0.10 eq., (e) 0.15 eq., and (f) 0.20 eq.).

effectively quench the perovskite conductivity, leading to efficient hole-collection ability of the HTM to yield high J_{SC} , V_{OC} , and FF values. In the profile for **1**, the magnitude of peak suppression was higher ($\Delta\phi\Sigma\mu = -58\%$) and the speed of decay faster ($t = 0.72 \mu\text{s}$) than that of Spiro-OMeTAD ($\Delta\phi\Sigma\mu = -41\%$, $t = 0.97 \mu\text{s}$) or **2** with 0.15 equiv Co(III) dopant. These results suggest the strong contacts between perovskite layer and π -conjugated skeleton in tetra-substituted azulene **1** by its two-dimensionally expanded molecular shape, which could facilitate charge collection. Such strong contacts couldn't be realized in a smaller π -system like disubstituted azulene **2** and a spherical shape like Spiro-OMeTAD. It should also be noted that a good correlation was observed between the PCE values of the solar cells and the extent of transient decay in the TRMC measurements (Table 4). These results thus demonstrate the utility of this method for the evaluation of device performance and optimal doping conditions for newly synthesized semiconductors prior to the laborious fabrication of solar cells.

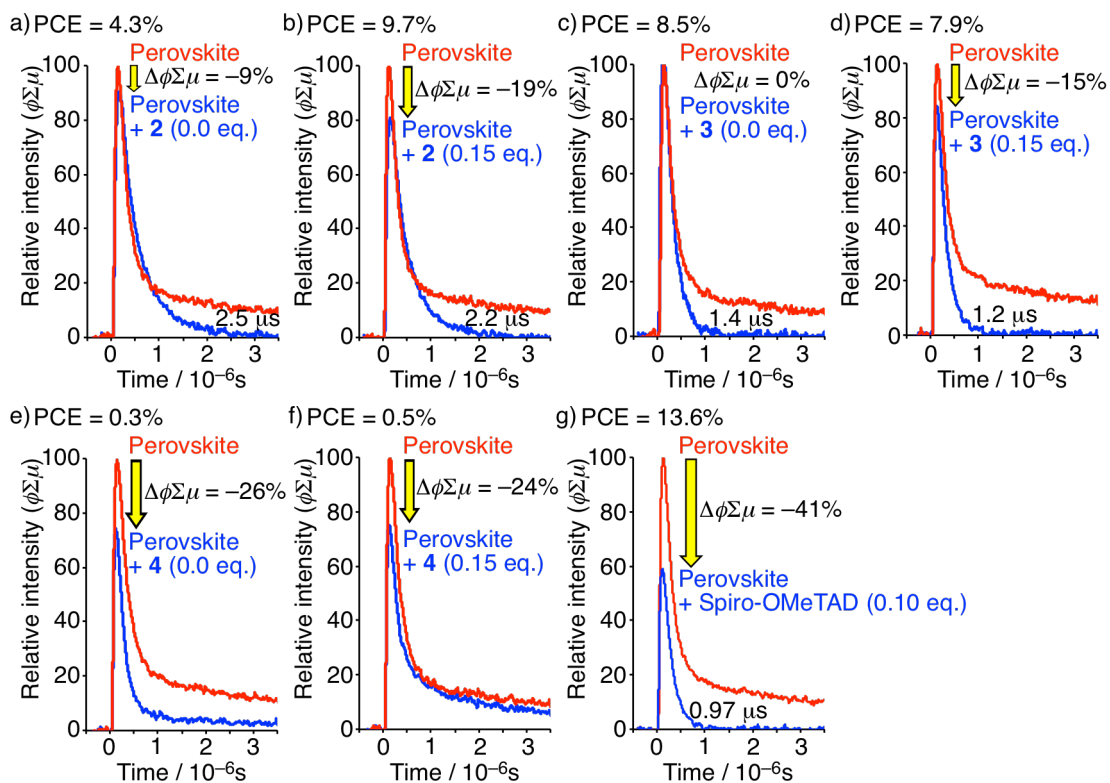


Figure 17. $\phi\Sigma\mu$ transients of perovskite films prior (red) and posterior (blue) to HTM coating of HTM at a photon flux of $I_0 = 1.4 \times 10^{11}$ photons/cm 2 : (a) **2** (Co(III)): 0.0 eq.), (b) **2** (0.15 eq.), (c) **3** (0.0 eq.), (d) **3** (0.15 eq.), (e) **4** (0.0 eq.), (f) **4** (0.15 eq.), and (g) Spiro-OMeTAD (0.10 eq.).

Table 4. Summary for the Parameters in Perovskite Solar Cells and the Transient Decay of TRMC Measurements for 1–4 and Spiro-OMeTAD

HTM	Co(III) Dopant [eq.]	J_{SC} [mA/cm ²]	V_{OC} [V]	FF	PCE [%]	R_s [Ωcm ²]	R_{sh} [Ωcm ²]	$\Delta\phi\Sigma\mu$ [%]	time [μs]
1	0.0	14.9	0.82	0.39	4.8	15	1.2×10^2	0	—
1	0.05	18.2	0.96	0.57	9.9	6.8	2.1×10^2	-38	2.2
1	0.10	20.1	0.99	0.66	13.2	7.0	7.4×10^2	-56	0.94
1	0.15	20.7	1.04	0.73	15.7	8.6	1.6×10^3	-58	0.72
1	0.20	20.5	1.02	0.71	14.8	6.8	1.6×10^3	-50	0.77
2	0.0	14.1	0.84	0.36	4.3	34	1.3×10^2	-9	2.5
2	0.15	15.9	0.91	0.67	9.7	4.7	8.2×10^2	-19	2.2
3	0.0	17.3	0.91	0.54	8.5	8.5	2.7×10^2	0	1.4
3	0.15	17.1	0.87	0.53	7.9	5.2	4.1×10^2	-15	1.2
4	0.0	1.20	0.78	0.35	0.32	350	9.6×10^2	-26	—
4	0.15	2.31	0.70	0.28	0.45	180	3.4×10^2	-24	—
Spiro	0.10	21.0	0.96	0.68	13.6	4.6	2.7×10^3	-41	0.97

Conclusion

In conclusion, the synthesis of **1**, in which the conjugated π-system is two-dimensionally expanded over four quasiplanar skeletons and a central azulene core, have been described. Perovskite solar cells using **1** as a HTM exhibited a superior performance (PCE ≤ 16.5%) relative to those using the current standard Spiro-OMeTAD. Based on the evaluation and a comparison of the optoelectronic and electrochemical properties of **1–4** and Spiro-OMeTAD, the factors that are required for HTMs to act efficiently in perovskite solar cells were able to be elucidated: 1) a good hole mobility that can be partly modified by chemical doping; 2) control over the HTM HOMO and LUMO levels, which should be at least 0.1 eV and 0.25 eV higher than the perovskite VB and CB, respectively; 3) high hole-collecting ability at the HTM/perovskite interface. With respect to 3), the preferred horizontal molecular orientation of two-dimensionally expanded π-systems should be particularly beneficial. In line with these new molecular design principles, the author believes that several more sophisticated HTMs for perovskite solar cells should be easily attainable.

Experimental Section

General.

All reactions were carried out under an argon atmosphere. Thin layer chromatography (TLC) was performed on plates coated with 0.25 mm thick silica gel 60F-254 (Merck). Column chromatography was performed using PSQ 60B (Fuji Silysia). Preparative gel permeation chromatography (GPC) was performed with a JAI LC-918 system equipped with RI-50 detector, JAIGEL-2H column (20 mm ID × 600 mm) and 1H column (20 mm ID × 600 mm) using toluene as eluent (flow rate: 3.8 mL/min). Melting points (mp) were measured on a Yanaco Micro Melting Point Apparatus. ¹H and ¹³C NMR spectra were recorded with a JEOL ECA 500 (500 MHz for ¹H and 125 MHz for ¹³C) spectrometers. The NMR chemical shifts are reported in ppm with reference to residual protons and carbons of CDCl₃ (δ 7.26 ppm in ¹H NMR, δ 77.0 ppm in ¹³C NMR) and CD₂Cl₂ (δ 5.32 ppm in ¹H NMR, δ 53.8 ppm in ¹³C NMR). UV-vis absorption measurement was performed with a Shimadzu UV-3150 spectrometer (Shimadzu Co.,), in degassed spectral grade solvents. Cyclic voltammetry (CV) was performed on an ALS/chi-620C electrochemical analyzer with the CV cell consisting of a glassy carbon electrode, a Pt wire counter electrode, and an Ag/AgNO₃ reference electrode. The measurement was carried out under an argon atmosphere using CH₂Cl₂ solutions of samples (0.5 mM) with 0.1 M tetrabutylammonium hexafluorophosphate (Bu₄N⁺PF₆⁻) as a supporting electrolyte. The redox potentials were calibrated with ferrocene as an internal standard. The HOMO energy levels in the solid state were determined from the onset of photoelectron spectra measured with a photoelectron spectrometer in air, model AC-3 (Riken Keiki Co., Ltd.). Thermogravimetric analysis (TGA) was performed on a Shimadzu TGA-50 apparatus (Shimadzu Co.,). The values are given for a weight-loss of 5% (T_{d5}). Photocurrent-voltage measurements ($J-V$ curves) for perovskite solar cells were measured in air with an OTENTO-SUNIII (BUNKOUKEIKI Co., Ltd.) and a Keithley 2400. External quantum efficiency (EQE) spectra were recorded on a SMO-250III system. The light intensity of the illumination source was adjusted by using standard silicon photodiodes: BS520 for $J-V$ characteristics and SiPD S1337-1010BQ for EQE measurements, respectively.

Synthesis.

2,6-Difluoro-N-(2-methoxyphenyl)aniline (7).

o-Iodoanisole (21.7 g, 92.5 mmol), 2,6-difluoroaniline (10.7 g, 82.7 mmol),

$\text{Pd}_2(\text{dba})_3 \cdot \text{CHCl}_3$ (1.60 g, 1.59 mmol), sodium *tert*-butoxide (9.22 g, 95.9 mmol), and tri-*tert*-butylphosphine (2.58 g, 12.7 mmol) were dissolved in dry toluene (200 mL) and the mixture was stirred at 100 °C for 16 h. The insoluble materials were filtered off, and the solids were washed with toluene (150 mL). After addition of water to the filtrate, the aqueous phase was extracted with toluene (50 mL × 3). The combined organic phase was dried over Na_2SO_4 , filtered off, and concentrated under reduced pressure. The obtained crude product was passed through a short pad of silica gel with the eluent of a mixture of CH_2Cl_2 and hexane (CH_2Cl_2 : hexane = 1 : 2, R_f = 0.45), and then purified by silica gel column chromatography (CH_2Cl_2 : hexane = 1 : 4, R_f = 0.25) to give 18.7 g (79.4 mmol) of **7** in 96% yields as orange oil.

^1H NMR (500 MHz, CDCl_3): δ 7.18–7.01 (m, 1H), 7.18–6.93 (m, 2H), 6.91–6.81 (m, 3H), 6.60 (ddd, $^3J(\text{H},\text{H})$ = 9.0 Hz, $^3J(\text{H},\text{H})$ = 7.0 Hz, $^4J(\text{H},\text{H})$ = 2.5 Hz, 1H), 5.88 (s, 1H), 3.93 (s, 3H); ^{13}C NMR (125 MHz, CDCl_3): δ 157.1 (dd, $^1J(\text{C},\text{F})$ = 246.1 Hz, $^3J(\text{C},\text{F})$ = 5.7 Hz), 147.6, 133.2, 123.6 (t, $^3J(\text{C},\text{F})$ = 9.8 Hz), 120.7, 119.7, 119.0 (t, $^2J(\text{C},\text{F})$ = 15.5 Hz), 112.9 (t, $^4J(\text{C},\text{F})$ = 2.3 Hz), 111.8 (dd, $^2J(\text{C},\text{F})$ = 16.6 Hz, $^4J(\text{C},\text{F})$ = 6.8 Hz), 110.0, 55.5; HRMS(FAB) (*m/z*): [M]⁺ calcd. for $\text{C}_{13}\text{H}_{11}\text{F}_2\text{NO}$: 235.0809; found, 235.0811; Elemental analysis calcd (%) for $\text{C}_{13}\text{H}_{11}\text{F}_2\text{NO}$: C 66.38, H 4.71, N 5.95; found: C 66.27, H 4.53, N 6.06.

2,6-Difluoro-N-(2,5-dimethoxyphenyl)-N-(2-methoxyphenyl)aniline (8).

The mixture of **7** (23.3 g, 99.0 mmol), 2-iodo-1,4-dimethoxylbenzene (28.8 g, 109 mmol), K_2CO_3 (34.6 g, 250 mmol), copper powder (12.7 g, 200 mmol), and 18-crown-6 (1.28 g, 4.86 mmol) was dissolved in mesitylene (150 mL). The mixture was stirred at 220 °C for 30 h. The resulting insoluble materials were filtered off, and the solids were washed with CH_2Cl_2 (250 mL). The combined filtrate was concentrated under reduced pressure. The obtained crude product was washed with hexane (250 mL) and methanol (100 mL) to give 33.9 g (91.3 mmol) of **8** in 92% yield as white solids.

mp: 152.6–153.6 °C; ^1H NMR (500 MHz, CDCl_3): δ 7.07 (td, $^3J(\text{H},\text{H})$ = 7.5 Hz, $^4J(\text{H},\text{H})$ = 1.5 Hz, 1H), 7.01 (tt, $^3J(\text{H},\text{H})$ = 8.0 Hz, $^3J(\text{H},\text{F})$ = 6.0 Hz, 1H), 6.97 (dd, $^3J(\text{H},\text{H})$ = 7.5 Hz, $^4J(\text{H},\text{H})$ = 1.5 Hz, 1H), 6.90 (dd, $^3J(\text{H},\text{H})$ = 8.0 Hz, $^4J(\text{H},\text{H})$ = 1.0 Hz, 1H), 6.87 (td, $^3J(\text{H},\text{H})$ = 7.5 Hz, $^4J(\text{H},\text{H})$ = 1.5 Hz, 1H), 6.84 (d, $^3J(\text{H},\text{H})$ = 6.0 Hz, 1H), 6.83–6.81 (m, 2H), 3.68 (s, 3H), 3.60 (s, 3H), 3.52 (s, 3H); ^{13}C NMR (125 MHz, CD_2Cl_2): δ 159.1 (dd, $^1J(\text{C},\text{F})$ = 249 Hz, $^3J(\text{C},\text{F})$ = 6.0 Hz), 154.4, 153.5, 147.4, 138.2, 136.3, 125.0, 124.8 (t, $^2J(\text{C},\text{F})$ = 13.1 Hz), 124.7, 124.1 (t, $^3J(\text{C},\text{F})$ = 9.6 Hz), 121.1, 115.3, 113.1, 111.5 (dd, $^2J(\text{C},\text{F})$ = 18.4 Hz, $^4J(\text{C},\text{F})$ = 5.4 Hz), 110.5, 107.8, 57.3, 56.1, 55.5; HRMS (FAB) (*m/z*): [M]⁺ calcd. for $\text{C}_{21}\text{H}_{19}\text{F}_2\text{NO}_3$, 371.1333; found, 371.1336;

Elemental analysis calcd (%) for C₂₁H₁₉F₂NO₃: C 67.92, H 5.16, N 3.77; found: C 67.93, H 5.16, N 3.92.

2-(Octyloxy)benzo[5,6][1,4]oxazino[2,3,4-*k*]phenoxazine (5).

8 (6.10 g, 16.4 mmol) was dissolved in CH₂Cl₂ (180 mL). BBr₃ (5.10 mL, 53.8 mmol) was added to the solution at -78 °C. The mixture was slowly warmed up to room temperature and further stirred for 3 h. The reaction mixture was poured into water and extracted with ethyl acetate (30 mL × 3). The combined organic phase was dried over Na₂SO₄, filtered off, and concentrated under reduced pressure to give 6.37 g of the crude product as white solids, which was used without further purification.

These solids were dissolved in DMF (150 mL). After addition of K₂CO₃ (9.13 g, 66.1 mmol), the mixture was stirred at 120 °C for 14 h. After the solution was cooled to room temperature, 1-bromooctane (5.30 mL, 24.7 mmol) was added. The solution was further stirred at 80 °C for 8 h. The resulting insoluble materials were filtered off, and the filtrate was concentrated under reduced pressure. The obtained solids were dissolved in CH₂Cl₂ (30 mL). After addition of water, the mixture was extracted with CH₂Cl₂ (20 mL × 3). The organic phase was dried over Na₂SO₄, filtered off, and concentrated under reduced pressure. The obtained crude product was dissolved in CH₂Cl₂. After passed through a short pad of silica gel, the crude product was purified by silica gel column chromatography (CH₂Cl₂ : hexane = 1 : 10, R_f = 0.40) to give 5.42 g (13.5 mmol) of **5** in 82% yield as colorless oil.

¹H NMR (500 MHz, CD₂Cl₂): δ 7.36 (d, ³J(H,H) = 8.0 Hz, 1H), 6.97 (td, ³J(H,H) = 8.0 Hz, ⁴J(H,H) = 2.0 Hz, 1H), 6.94–6.88 (m, 3H), 6.81 (d, ³J(H,H) = 9.0 Hz, 1H), 6.77 (t, ³J(H,H) = 8.0 Hz, 1H), 6.49 (d, ³J(H,H) = 9.0 Hz, 2H), 6.42 (dd, ³J(H,H) = 9.0 Hz, ⁴J(H,H) = 2.5 Hz, 1H), 3.88 (t, ³J(H,H) = 7.0 Hz, 2H), 1.73 (quin, ³J(H,H) = 7.5 Hz, 2H), 1.43 (quin, ³J(H,H) = 7.5 Hz, 2H), 1.37–1.23 (m, 8H), 0.88 (t, ³J(H,H) = 7.0 Hz, 3H); ¹³C NMR (125 MHz, CD₂Cl₂): δ 155.9, 147.4, 146.1, 145.7, 141.0, 130.0, 129.3, 124.06, 124.02, 123.8, 120.9, 117.73, 117.69, 115.4, 111.3, 111.1, 108.3, 102.3, 69.0, 32.2, 29.8, 29.68, 29.66, 26.4, 23.1, 14.3; HRMS (FAB) (*m/z*): [M]⁺ calcd. for C₂₆H₂₇NO₃, 401.1991; found, 401.1990; Elemental analysis calcd (%) for C₂₆H₂₇NO₃: C 77.78, H 6.78, N 3.49; found: C 77.57, H 6.68, N 3.75.

3-Bromo-2-(octyloxy)benzo[5,6][1,4]oxazino[2,3,4-*k*]phenoxazine (6).

5 (4.28 g, 10.7 mmol) was dissolved in CH₂Cl₂ (160 mL). *N*-Bromosuccinimide (1.90 g, 10.7 mmol) was added to the solution and the solution was stirred at room temperature for 14 h. The reaction mixture was passed through a short pad of silica gel with an

eluent of CH_2Cl_2 to give 5.00 g (10.4 mmol) of **6** in 98% yield as white solids.
mp: 65.6–66.6 °C; ^1H NMR (500 MHz, CD_2Cl_2): δ 7.29 (d, $^3J(\text{H},\text{H})$ = 8.0 Hz, 1H), 7.06 (s, 1H), 6.98 (dd, $^3J(\text{H},\text{H})$ = 7.5 Hz, $^4J(\text{H},\text{H})$ = 1.5 Hz, 1H), 6.97–6.88 (m, 3H), 6.77 (t, $^3J(\text{H},\text{H})$ = 8.0 Hz, 1H), 6.50 (d, $^3J(\text{H},\text{H})$ = 8.5 Hz, 1H), 6.48 (d, $^3J(\text{H},\text{H})$ = 8.5 Hz, 1H), 3.89 (t, $^3J(\text{H},\text{H})$ = 6.5 Hz, 2H), 1.78 (quin, $^3J(\text{H},\text{H})$ = 7.0 Hz, 2H), 1.47 (quin, $^3J(\text{H},\text{H})$ = 6.5 Hz, 2H), 1.40–1.23 (m, 8H), 0.90 (t, $^3J(\text{H},\text{H})$ = 7.5 Hz, 3H); ^{13}C NMR (125 MHz, CD_2Cl_2): δ 152.1, 147.4, 145.8, 145.7, 141.2, 129.3, 129.0, 124.3, 124.13, 124.05, 121.6, 120.6, 117.9, 115.0, 111.46, 111.42, 104.1, 101.0, 70.5, 32.2, 29.7, 29.6, 29.5, 26.3, 23.0, 14.3; HRMS (FAB) (m/z): [M]⁺ calcd. for $\text{C}_{26}\text{H}_{26}\text{BrNO}_3$, 481.1079; found, 481.1083; Elemental analysis calcd (%) for $\text{C}_{26}\text{H}_{26}\text{BrNO}_3$: C 65.00, H 5.46, N 2.92; found: C 64.89, H 5.44, N 2.94.

2-(Octyloxy)-3-(4,4,5,5-tetramethyl-1,3,2-dioxaborolan-2-yl)benzo[5,6][1,4]oxazino[2,3,4-*k*]phenoxazine (9).

6 (961 mg, 2.00 mmol) was dissolved in THF (40 mL) and the solution was cooled to –78 °C. *n*-BuLi in hexane (850 μL , 2.21 mmol) was added dropwise to the solution and the mixture was stirred at –78 °C for 1 h. After addition of *i*PrOBpin (450 μL , 2.21 mmol), the mixture was slowly warmed up to room temperature and further stirred for 2 h. The reaction mixture was concentrated under reduced pressure. The obtained solids were dissolved in CH_2Cl_2 (30 mL). After addition of water (30 mL), organic phase was extracted with CH_2Cl_2 (20 mL \times 3). The organic phase was dried over Na_2SO_4 , filtered off, and concentrated under reduced pressure. The obtained crude products were purified by gel permeation chromatography (eluent: toluene) to give 797 mg (1.51 mmol) of **9** in 75% yield as colorless oil.

^1H NMR (500 MHz, CD_2Cl_2): δ 7.35 (dd, $^3J(\text{H},\text{H})$ = 8.5 Hz, $^4J(\text{H},\text{H})$ = 1.5 Hz, 1H), 7.15 (s, 1H), 6.99 (td, $^3J(\text{H},\text{H})$ = 7.5 Hz, $^4J(\text{H},\text{H})$ = 1.5 Hz, 1H), 6.96–6.90 (m, 2H), 6.86 (s, 1H), 6.78 (t, $^3J(\text{H},\text{H})$ = 8.5 Hz, 1H), 6.50 (dd, $^3J(\text{H},\text{H})$ = 8.5 Hz, $^4J(\text{H},\text{H})$ = 1.5 Hz, 2H), 3.85 (t, $^3J(\text{H},\text{H})$ = 6.5 Hz, 2H), 1.74 (quin, $^3J(\text{H},\text{H})$ = 6.0 Hz, 2H), 1.51 (quin, $^3J(\text{H},\text{H})$ = 7.5 Hz, 2H), 1.37–1.26 (m, 20H), 0.89 (t, $^3J(\text{H},\text{H})$ = 7.0 Hz, 3H); ^{13}C NMR (125 MHz, CD_2Cl_2): δ 161.2, 147.5, 146.3, 145.6, 140.5, 132.7, 129.0, 124.5, 124.3, 124.1, 120.7, 117.8, 115.6, 111.4, 111.1, 100.0, 83.6, 70.0, 32.3, 29.8, 29.7, 26.4, 25.0, 23.1, 14.2 (One signal for the carbon atom bonding to the boron atom was not observed due to the quadrupolar relaxation of the boron atom and one sp^3 -carbon signal was overlapped); HRMS (EI) (m/z): [M]⁺ calcd. for $\text{C}_{32}\text{H}_{38}\text{BNO}_5$, 527.2849; found, 527.2852; Elemental analysis calcd (%) for $\text{C}_{32}\text{H}_{38}\text{BNO}_5$: C 72.87, H 7.26, N 2.66; found: C 72.78, H 7.17, N 2.71.

1,3,5,7-Tetrakis(4,4,5,5-tetramethyl-1,3,2-dioxaborolan-2-yl)azulene (10).

B_2Pin_2 (16.8 g, 66.0 mmol), $[IrOMe(cod)]_2$ (1.99 g, 3.01 mmol), 4,4'-dimethyl-2,2'-bipyridyl (1.11 g, 6.01 mmol), and potassium *t*-butoxide (168 mg, 1.50 mmol) were charged in the Schlenk flask and flushed with Ar. THF (13 mL) was added to the flask and the mixture was heated at 50 °C for 10 min. Azulene (1.93 g, 15.0 mmol) was added to the solution and the mixture was stirred at 85 °C for 6 d. The mixture was diluted with CH_2Cl_2 (100 mL). The solution was quenched with water (100 mL). The aqueous phase was extracted with CH_2Cl_2 (50 mL × 3), and the combined organic layer was washed with water and brine, successively. The organic phase was dried over Na_2SO_4 , filtered off, and concentrated under reduced pressure. The obtained crude product was washed with MeOH (200 mL) by sonication for 30 min, until purple solids formed. The solids were filtered and further washed with MeOH (100 mL) to give 3.62 g (5.73 mmol) of **10** in 38% yields as purple solids.

mp (decomp.): 289.0 °C; 1H NMR (500 MHz, $CDCl_3$): δ 9.72 (s, 2H), 8.69 (s, 1H), 8.62 (s, 1H), 1.41 (s, 48H); ^{13}C NMR (125 MHz, $CDCl_3$): δ 153.3, 149.8, 149.4, 146.0, 84.2, 82.9, 25.1, 25.0 (Two signals for the carbon atoms bonding to the boron atom were not observed due to the quadrupolar relaxation of the boron atom); HRMS (FAB) (*m/z*): $[M]^+$ calcd. for $C_{34}H_{52}B_4O_8$, 632.4056; found, 632.4071. Elemental analysis calcd (%) for $C_{34}H_{52}B_4O_8$: C 64.61, H 8.29; found: C 64.53, H 8.10.

5,7-Bis(4,4,5,5-tetramethyl-1,3,2-dioxaborolan-2-yl)azulene (11).

10 (127 mg, 0.201 mmol) was dissolved in ethyl acetate (24 mL). A mixture of CF_3COOH and ethyl acetate (1/1, 24 mL) was added to the solution by syringe over 1 h, and the reaction mixture was stirred for an additional 1.5 h. CH_2Cl_2 (30 mL) was added to the solution, and the obtained organic solution was poured into water (100 mL). The organic phase was washed with water (100 mL × 3), dried over Na_2SO_4 , filtered off, and concentrated under reduced pressure. The obtained crude products were purified by GPC (toluene) to give 55.2 mg (0.145 mmol) of **11** in 72% yield as blue solids.

mp: 176.7–177.9 °C; 1H NMR (500 MHz, $CDCl_3$): δ 8.87 (s, 2H), 8.60 (s, 1H), 7.84 (t, $^3J(H,H) = 4.0$ Hz, 1H), 7.53 (d, $^3J(H,H) = 4.0$ Hz, 2H), 1.40 (s, 24H); ^{13}C NMR (125 MHz, $CDCl_3$): δ 150.1, 144.5, 139.3, 136.1, 122.4, 84.2, 24.9 (One signal for the carbon atoms bonding to the boron atoms was not observed due to the quadrupolar relaxation of the boron atom); HRMS (FAB) (*m/z*): $[M]^+$ calcd. for $C_{22}H_{30}B_2O_4$, 380.2338; found, 380.2339. Elemental analysis calcd (%) for $C_{22}H_{30}B_2O_4$: C 69.52, H 7.96; found: C 69.62, H 8.16.

1,3,5,7-Tetrakis(2-(octyloxy)benzo[5,6][1,4]oxazino[2,3,4-*k*]phenoxazin-3-yl)azulene (1).

10 (639 mg, 1.01 mmol), **6** (2.33 g, 4.84 mmol), $\text{PdCl}_2(\text{dppf}) \cdot \text{CH}_2\text{Cl}_2$ (50.5 mg, 61.8 μmol), and cesium carbonate (3.29 g, 10.1 mmol) in THF (90 mL) were charged in a Schlenk tube. After flushed with argon three times, the mixture was stirred at 95 °C for 2 d. After passed through a short pad of silica gel with an eluent of CH_2Cl_2 , the obtained crude product was further purified by silica gel column chromatography (hexane : $\text{CH}_2\text{Cl}_2 = 3 : 1$, $R_f = 0.20$) to give 1.01 g (0.583 mmol) of **1** in 58% yield as green solids.

mp: 114.9–116.7 °C; ^1H NMR (500 MHz, CD_2Cl_2): δ 8.48 (s, 2H), 8.12 (s, 1H), 7.89 (s, 1H), 7.45 (d, $^3J(\text{H},\text{H}) = 8.0$ Hz, 2H), 7.41 (d, $^3J(\text{H},\text{H}) = 8.0$ Hz, 2H), 7.08 (s, 4H), 7.04–6.97 (m, 8H), 6.95–6.91 (m, 8H), 6.79 (t, $^3J(\text{H},\text{H}) = 8.0$ Hz, 2H), 6.78 (t, $^3J(\text{H},\text{H}) = 8.0$ Hz, 2H), 6.54–6.49 (m, 8H), 3.89 (t, $^3J(\text{H},\text{H}) = 7.0$ Hz, 4H), 3.83 (t, $^3J(\text{H},\text{H}) = 7.0$ Hz, 4H), 1.65 (quin, $^3J(\text{H},\text{H}) = 7.5$ Hz, 4H), 1.60 (quin, $^3J(\text{H},\text{H}) = 7.5$ Hz, 4H), 1.28–1.09 (m, 40H), 0.79 (t, $^3J(\text{H},\text{H}) = 7.0$ Hz, 6H), 0.78 (t, $^3J(\text{H},\text{H}) = 7.0$ Hz, 6H); ^{13}C NMR (125 MHz, CD_2Cl_2): δ 153.1, 152.3, 147.4, 146.0, 145.9, 145.8, 145.7, 142.4, 140.9, 140.7, 138.0, 135.8, 131.8, 129.6, 129.5, 129.3, 128.6, 127.9, 126.5, 124.15, 124.07, 123.7, 123.6, 121.6, 121.0, 120.8, 120.0, 117.78, 117.75, 115.0, 111.4, 111.2, 111.1, 101.2, 100.8, 69.94, 69.91, 32.3, 29.8, 29.74, 29.69, 29.66, 29.60, 29.5, 26.5, 26.3, 23.05, 23.03, 14.3 (seven sp^2 and two sp^3 -carbon signals were overlapped); HRMS (FAB) (m/z): $[\text{M}]^+$ calcd. for $\text{C}_{114}\text{H}_{108}\text{N}_4\text{O}_{12}$, 1724.7964; found, 1724.7959; Elemental analysis calcd (%) for $\text{C}_{114}\text{H}_{108}\text{N}_4\text{O}_{12}$: C 79.32, H 6.31, N 3.25; found: C 79.25, H 6.26, N 3.27.

1,3-Bis(2-(octyloxy)benzo[5,6][1,4]oxazino[2,3,4-*k*]phenoxazin-3-yl)azulene (2).

1,3-Dibromoazulene (129 mg, 0.453 mmol), **9** (518 mg, 0.982 mmol), $\text{PdCl}_2(\text{dppf}) \cdot \text{CH}_2\text{Cl}_2$ (12.9 mg, 15.8 μmol), and cesium carbonate (739 mg, 2.27 mmol) in THF (20 mL) were charged in a Schlenk tube. After flushed with argon three times, the mixture was stirred at 95 °C for 24 h. The mixture was passed through a short pad of silica gel with an eluent of CH_2Cl_2 . The obtained crude product was purified by gel permeation chromatography (eluent: toluene) and further purified by silica gel column chromatography (hexane : $\text{CH}_2\text{Cl}_2 = 3 : 1$, $R_f = 0.30$) to give 191 mg (0.206 mmol) of **2** in 46% yield as green solids.

mp: 73.8–75.7 °C; ^1H NMR (500 MHz, CD_2Cl_2): δ 8.32 (d, $^3J(\text{H},\text{H}) = 9.5$ Hz, 2H), 8.11 (s, 1H), 7.58 (t, $^3J(\text{H},\text{H}) = 9.5$ Hz, 1H), 7.48 (d, $^3J(\text{H},\text{H}) = 8.0$ Hz, 2H), 7.13 (t, $^3J(\text{H},\text{H}) = 9.5$ Hz, 2H), 7.10 (s, 2H), 7.06–7.02 (m, 4H), 6.97–6.92 (m, 4H), 6.80 (t, $^3J(\text{H},\text{H}) =$

8.0 Hz, 2H), 6.54 (t, $^3J(H,H) = 8.5$ Hz, 4H), 3.83 (t, $^3J(H,H) = 7.0$ Hz, 4H), 1.58 (quin, $^3J(H,H) = 7.0$ Hz, 4H), 1.21 (quin, $^3J(H,H) = 7.0$ Hz, 4H), 1.18–1.09 (m, 16H), 0.82 (t, $^3J(H,H) = 7.0$ Hz, 6H); ^{13}C NMR (125 MHz, CD_2Cl_2): δ 153.2, 147.5, 146.1, 145.8, 140.8, 140.4, 138.6, 137.2, 136.3, 129.7, 128.2, 125.7, 124.2, 123.7, 123.3, 121.6, 121.0, 120.8, 117.8, 115.1, 111.5, 111.2, 101.2, 100.8, 69.9, 32.2, 29.65, 29.63, 29.57, 26.5, 23.0, 14.2 (one sp^2 -carbon signal was overlapped); HRMS (FAB) (m/z): $[\text{M}]^+$ calcd. for $\text{C}_{62}\text{H}_{58}\text{N}_2\text{O}_6$, 926.4295; found, 926.4301; Elemental analysis calcd (%) for $\text{C}_{62}\text{H}_{58}\text{N}_2\text{O}_6$: C 80.32, H 6.31, N 3.02; found: C 80.35, H 6.40, N 3.07.

5,7-Bis(2-(octyloxy)benzo[5,6][1,4]oxazino[2,3,4-*k*]phenoxyazin-3-yl)azulene (3).

11 (237 mg, 0.624 mmol), **6** (663 mg, 1.38 mmol), $\text{PdCl}_2(\text{dppf}) \cdot \text{CH}_2\text{Cl}_2$ (15.0 mg, 18.4 μmol), and cesium carbonate (1.04 g, 3.19 mmol) in THF (30 mL) were charged in a Schlenk tube. After flushed with argon three times, the mixture was stirred at 95 °C for 48 h. The mixture was passed through a short pad of silica gel with an eluent of CH_2Cl_2 . The obtained crude product was purified by silica gel column chromatography (hexane : $\text{CH}_2\text{Cl}_2 = 2 : 1$, $R_f = 0.38$) to give 439 mg (0.473 mmol) of **3** in 76% yield as green solids.

mp: 73.5–74.7 °C; ^1H NMR (500 MHz, CD_2Cl_2): δ 8.54 (d, $^4J(H,H) = 1.5$ Hz, 2H), 7.92 (t, $^4J(H,H) = 1.5$ Hz, 1H), 7.88 (t, $^3J(H,H) = 3.5$ Hz, 1H), 7.43 (d, $^3J(H,H) = 7.5$ Hz, 2H), 7.37 (d, $^3J(H,H) = 3.5$ Hz, 2H), 7.04 (s, 2H), 7.05–7.00 (m, 4H), 6.96–6.92 (m, 4H), 6.79 (t, $^3J(H,H) = 8.0$ Hz, 2H), 6.53 (d, $^3J(H,H) = 8.0$ Hz, 2H), 6.52 (d, $^3J(H,H) = 8.0$ Hz, 2H), 3.89 (t, $^3J(H,H) = 6.5$ Hz, 4H), 1.65 (quin, $^3J(H,H) = 7.5$ Hz, 4H), 1.31 (quin, $^3J(H,H) = 7.5$ Hz, 4H), 1.25–1.12 (m, 16H), 0.82 (t, $^3J(H,H) = 7.0$ Hz, 6H); ^{13}C NMR (125 MHz, CD_2Cl_2): δ 152.4, 147.5, 146.0, 145.8, 141.5, 141.0, 139.0, 138.8, 137.3, 131.5, 129.6, 129.5, 128.8, 124.24, 124.16, 123.8, 120.9, 119.9, 119.1, 117.8, 115.1, 111.4, 111.3, 100.9, 69.9, 32.2, 29.63, 29.60, 29.5, 26.4, 23.0, 14.2; HRMS (FAB) (m/z): $[\text{M}]^+$ calcd. for $\text{C}_{62}\text{H}_{58}\text{N}_2\text{O}_6$, 926.4295; found, 926.4300; Elemental analysis calcd (%) for $\text{C}_{62}\text{H}_{58}\text{N}_2\text{O}_6$: C 80.32, H 6.31, N 3.02; found: C 80.29, H 6.29, N 3.00.

3,3',5,5'-Tetrakis(2-(octyloxy)benzo[5,6][1,4]oxazino[2,3,4-*k*]phenoxyazin-3-yl)-1,1'-biphenyl (4).

12 (39.5 mg, 0.601 mmol), **8** (173 mg, 0.360 mmol), $\text{PdCl}_2(\text{dppf}) \cdot \text{CH}_2\text{Cl}_2$ (10.1 mg, 12.3 μmol), and cesium carbonate (196 mg, 0.601 mmol) in THF (5 mL) were charged in a pressure vessel. After degassed for 10 min, the solution was stirred at 95 °C for 27 h. After diluted with CH_2Cl_2 (20 mL), the reaction mixture was quenched with 1 M HCl aq. The organic phase was extracted with CH_2Cl_2 (5 mL \times 3), followed by washing with

water and brine. The combined organic phase was dried over MgSO₄, filtered off, and concentrated under reduced pressure. The obtained crude product was purified by silica gel column chromatography (hexane : CH₂Cl₂ = 4 : 1, *R*_f = 0.17) to give 62.3 mg (0.0355 mmol) of **4** in 59% yield as pale yellow solids.

mp: 99.8–101.6°C; ¹H NMR (500 MHz, CD₂Cl₂): δ 7.87 (s, 4H), 7.75 (s, 2H), 7.43 (d, ³J(H,H) = 8.0 Hz, 4H), 7.09 (s, 4H), 7.04 (s, 4H), 7.03–6.98 (m, 4H), 6.97–6.92 (m, 8H), 6.79 (t, ³J(H,H) = 8.0 Hz, 4H), 6.53 (d, ³J(H,H) = 8.0 Hz, 4H), 6.52 (d, ³J(H,H) = 8.0 Hz, 4H), 3.91 (t, ³J(H,H) = 6.5 Hz, 8H), 1.74 (quin, ³J(H,H) = 7.5 Hz, 8H), 1.34 (quin, ³J(H,H) = 7.5 Hz, 8H), 1.20–1.06 (m, 32H), 0.75 (t, ³J(H,H) = 7.0 Hz, 12H); ¹³C NMR (125 MHz, CD₂Cl₂): δ 152.7, 147.5, 146.0, 145.8, 141.1, 140.9, 138.1, 129.54, 129.48, 128.8, 127.1, 125.7, 124.2, 124.1, 123.8, 120.9, 119.3, 117.8, 115.1, 111.5, 111.2, 100.8, 69.9, 32.3, 29.78, 29.71, 29.5, 26.6, 23.0, 14.2; HRMS (FAB) (*m/z*): [M]⁺ calcd. for C₁₁₆H₁₁₀N₄O₁₂, 1750.8120; found, 1750.8118; Elemental analysis calcd (%) for C₁₁₆H₁₁₀N₄O₁₂: C 79.52, H 6.33, N 3.20; found: C 79.15, H 6.63, N 3.05.

Computation Method.

DFT calculations for optimization of the geometries were conducted using the Gaussian 09 program.¹⁹

Peovskite Solar cells: Device Fabrication.

1) Preparation of mesoporous TiO₂ layer

Patterned transparent conducting oxide substrate (FTO, 25 mm × 25 mm, Asahi Glass Co., Ltd., Japan) was treated with ultrasonic cleaning for 10 min with a 1wt% neutral aqueous detergent solution, acetone, 2-propanol, and distilled water, respectively, and then subjected to an O₃/ultraviolet treatment for 15 min.

FTO substrate was covered with a compact TiO₂ layer by spray pyrolysis of a ethanol solution (0.05 M) of titanium di-isopropoxide bis(acetylacetone) (75wt% in 2-propanol, Tokyo Chemical Industry Co., Ltd., Japan) at 450 °C. The resulting compact TiO₂ layer was treated with an aqueous solution (100 mL) of TiCl₄ (440 μL, special grade, Wako Pure Chemical Industries Ltd., Japan) at 70 °C for 30 min, followed by rinsing twice with distilled water. The substrate was sintered at 500 °C for 20 min.

Subsequently, mesoporous-TiO₂ layer (thickness: 200 nm; average particle size: ca. 20 nm) was deposited on the plate by spin-coating (slope 5 s, 5000 rpm, 30 s, slope 5 s) of a suspension of TiO₂ paste (PST-18NR, JGC Catalysts and Chemicals Ltd.) in ethanol (paste : ethanol = 1 : 5 wt ratio), followed by sintering at 500 °C for 30 min.

The obtained substrate was treated with ultraviolet-ozone cleaning for 15 min before used for perovskite layer fabrication.

2-A) Two-step solution method for perovskite layer

In a glove box filled with an inert gas, a 1.0 M solution of PbI₂ (L0279 for perovskite precursor, Tokyo Chemical Industry Co., Ltd., Japan) in dehydrated DMF at 70 °C was deposited on the mesoporous TiO₂ films by spin-coating (slope 5 s, 6500 rpm, 5 s, slope 5 s). The resulting yellow film was annealed on a hot plate at 70 °C for 1 h. The film was dipped in a 0.06 M 2-propanol solution of CH₃NH₃I (Tokyo Chemical Industry Co., Ltd., Japan) for 40 s. The formed perovskite film was then annealed on a hot plate at 70 °C for 1 h.

2-B) One-step solution method using toluene dropping for perovskite layer

In a glove box filled with an inert gas, a 1.1 M solution of PbI₂ and CH₃NH₃I in DMSO (room temperature) was deposited on the mesoporous TiO₂ films by spin-coating (slope 1 s, 1000 rpm 40 s, slope 1 s, 0 rpm. 30 s, slope 5 s, 5000 rpm 20 s, slope 5 s: At the last 5 s of spin-coating, 0.5 mL of toluene was slowly dropped on the rotating substrate.). The resulting transparent film was annealed on a hot plate at 100 °C for 10 min to form perovskite layer (250 nm).

3) Preparation of hole-transporting layer and Au electrode

A mixture of hole-transporting material (HTM, 0.050 M) and [tris(2-(1*H*-pyrazol-1-yl)-4-*tert*-butylpyridine)cobalt(III) tris(bis(trifluoromethylsulfonyl)imide)]⁶ (FK209, 0–15.0 mg, 0–0.010 M (for 0.0 eq. – 0.20 eq.)) as an oxidizing agent was dissolved with a solution containing chlorobenzene (1 mL), 4-*tert*-butylpyridine (TBP, 24.4 μL, 0.165 M, Aldrich), and lithium bis(trifluoromethylsulfonyl)imide (LiTFSI, 7.6 mg, 0.027 M, Wako Pure Chemical Industries Co., Ltd.). After 30 min, the resulting suspension was filtered with a membrane filter (Cosmonice filter S, Nacarai Tesque, Inc.) in order to remove the formed insoluble Co(II) complex. The hole-transporting layer was deposited on the perovskite layer by spin-coating (slope 5 s, 4000 rpm, 30 s, slope 5 s) of the obtained filtrate. The resulting film was dried on a hot plate (at 40 °C for 1–4, and at 70 °C for Spiro-OMeTAD, respectively) for 30 min. Finally, a gold layer (80 nm) was thermally deposited on the hole-transporting layer.

Space-Charge-Limitation of Current (SCLC) Method.¹⁵

The hole mobilities in the films of materials were measured from the space-charge-limitation of current (SCLC) J - V characteristics obtained in the dark for hole-only devices. Hole mobilities were calculated using the Mott-Gurney law by fitting Equation 1, where J is the current density, ϵ_0 is the permittivity of free space (8.85×10^{-12} F/m), ϵ is the relative permittivity of the material (approaching 3 for organic semiconductors), μ is the hole mobility, V is the applied voltage, and d is the thickness of the active layer, respectively.

$$J = \frac{9}{8} \epsilon \epsilon_0 \mu \frac{V^2}{d^3} \quad 1$$

The ITO-coated glass substrate ($5 \Omega/\text{sq}$, 2.5 cm \times 2.5 cm, GEOMATEC) was washed carefully under ultrasonic irradiation using acetone (15 min), and ethanol (15 min). The substrate was further cleaned with a Filgen UV230 UV/ozone cleaner. A thin layer of PEDOT:PSS (Nagase ChemteX, Denatron PT-100) was prepared onto the ITO surface by the spin-coating (5000 rpm, 60 s). The resulting substrate was heated at 200 °C for 10 min under ambient conditions. Then, hole transporting layer was prepared onto PEDOT:PSS layer by spin-coating (slope 5 s, 2000 rpm, 40 s, slope 5 s) of chlorobenzene solution of hole transporting material with a concentration of 60 mmol/L. The film thicknesses were measured with Alpha-Step IQ (KLA-Tencor Co.). As a counter electrode, Au was deposited on the film by vacuum evaporation. The current density–voltage curves of the devices were taken with a Keithley 2400 source.

Time-Resolved Microwave Conductivity (TRMC) Method.¹⁷

1) Treatment of quartz substrate

Quartz substrate (Daiko MFG Co. Ltd.) was treated with ultrasonic cleaning for 10 min with acetone and 2-propanol, respectively, and then subjected to an O₃/ultraviolet treatment for 30 min.

2) Preparation of HTM solution

A mixture of HTM (0.040 M) and FK209 (0–12.0 mg, 0–0.0080 M) as an oxidizing agent was dissolved in a solution containing chlorobenzene (1 mL), TBP (19.5 µL, 0.132 M, Aldrich), and LiTFSI (6.2 mg, 0.022 M, Wako Pure Chemical Industries Co., Ltd.). After 30 min, the resulting suspension was filtered with a membrane filter (Cosmonice filter S, Nacarai Tesque, Inc.) to remove the formed insoluble Co(II) complex.

3) Fabrication of HTM sample

In a glove box filled with an inert gas, the hole-transporting layer was deposited on the quartz substrate by spin-coating (slope 5 s, 2000 rpm, 40 s, slope 5 s) of the solution of each **HTM**. The resulting film was dried on a hot plate (at 40 °C for **1–4** and at 70 °C for Spiro-OMeTAD, respectively) for 30 min.

4) Fabrication of perovskite (mesoporous-TiO₂/CH₃NH₃PbI₃) sample

Quartz substrate was covered with the mesoporous TiO₂ layer by spin-coating (slope 5 s, 5000 rpm, 30 s, slope 5 s) of a suspension of TiO₂ paste (PST-18NR, TiO₂) in ethanol (paste : ethanol = 1 : 5 wt ratio), followed by sintering at 500 °C for 20 min. The obtained substrate was treated with ultraviolet-ozone cleaning for 15 min before used for perovskite layer fabrication. In a glove box filled with an inert gas, a 0.75 M solution of PbI₂ in dehydrated DMF (70 °C) was deposited on the mesoporous TiO₂ films by spin-coating (slope 5 s, 4000 rpm, 20 s, slope 5 s). The resulting yellow film was annealed on a hot plate at 70 °C for 1 h. The film was dipped for 40 s in a 0.06 M solution of CH₃NH₃I in 2-propanol. The formed perovskite film was then annealed on a hot plate at 70 °C for 1 h. The hole-transporting layer was deposited on the perovskite layer by spin-coating (slope 5 s, 2000 rpm, 40 s, slope 5 s) of the solution of **HTM**. The resulting film was dried on a hot plate (at 40 °C for **1–4** and at 70 °C for Spiro-OMeTAD, respectively) for 30 min.

5) TRMC measurement

Transient photoconductivity was measured by flash-photolysis time-resolved microwave conductivity (FP-TRMC). A resonant cavity was used to obtain a high degree of sensitivity in the measurement of conductivity. The resonant frequency was set at ~9.1 GHz and the microwave power was set at 3 mW, so that the electric field of the microwave was sufficiently small not to disturb the motion of charge carriers. The value of conductivity is converted to the product of the quantum yield ϕ and the sum of charge carrier mobilities $\Sigma\mu$, by $\phi\Sigma\mu = \Delta\sigma(eI_0F_{\text{light}})^{-1}$, where e , I_0 , F_{light} , and $\Delta\sigma$ are the unit charge of a single electron, incident photon density of excitation laser (photons/m²), a correction (or filling) factor (/m), and a transient photoconductivity, respectively. The change of conductivity is equivalent with $\Delta P_r/(AP_r)$, where ΔP_r , P_r , and A are change of reflected microwave power, a power of reflected microwave, and a sensitivity factor [(S/m)⁻¹], respectively. Third harmonic generation (355 nm for HTM-only samples and 550 nm for perovskite samples w/wo HTL) from an Optical Parametric Oscillator (OPO) of a Nd:YAG laser (Continuum Surelite II, 5–8 ns pulse duration) was used as an excitation source. The incident photon density of HTM-only sample and perovskite

sample were set at 4.6×10^{15} photons/cm² and 1.4×10^{11} photons/cm², respectively. The sample was set at the highest electric field in a resonant cavity. FP-TRMC experiments were performed at room temperature.

The values of ϕ in the compounds were determined by conventional photo-current measurement^{9b} in a vacuum chamber (10^{-4} Pa) using an inter-digited Au electrodes on a glass substrate with 5 μm gap under excitation at 355 nm with the photon density of 4.6×10^{15} photons/cm². Transient current was predominantly observed on the film sample under the applied bias of 0–10 V (0– 2.0×10^4 V/cm), and monitored by a Tektronix TDS3032B digital oscilloscope.

Reference

1. For reviews, see: (a) Gao, P.; Grätzel, M.; Nazeeruddin, M. K. *Energy Environ. Sci.* **2014**, *7*, 2448. (b) Miyasaka, T. *Chem. Lett.* **2015**, *44*, 720. (c) Jung, H. S.; Park, N.-G. *Small* **2015**, *11*, 10. (d) Luo, S.; Daoud, W. A. *J. Mater. Chem. A* **2015**, *3*, 8992.
2. (a) Yamada, Y.; Nakamura, T.; Endo, M.; Wakamiya, A.; Kanemitsu, Y. *J. Am. Chem. Soc.* **2014**, *136*, 11610. (b) Manser, J. S.; Kamat, P. J. *Nat. Photonics* **2014**, *8*, 737. (c) La-o-vorakiat, C.; Salim, T.; Kadro, J.; Khuc, M.-T.; Haselsberger, R.; Cheng, L.; Xia, H.; Gurzadyan, G. G.; Su, H.; Lam, Y. M.; Marcus, R. A.; Michel-Beyerle, M.-E.; Chia, E. E. M. *Nat. Commun.* **2015**, *6*, 7903.
3. For examples, see: (a) Jeon, N. J.; Noh, J. H.; Kim, Y. C.; Yang, W. S.; Ryu, S.; Seok, S. I. *Nat. Mater.* **2014**, *6*, 897. (b) Xiao, M.; Huang, F.; Huang, W.; Dkhissi, Y.; Zhu, Y.; Etheridge, J.; Gray-Weale, A.; Bach, U.; Cheng, Y.-B.; Spiccia, L. *Angew. Chem. Int. Ed.* **2014**, *53*, 9898. (c) Yang, W. S.; Noh, J. H.; Jeon, N. J.; Kim, Y. C.; Ryu, S.; Seo, J.; Seok, S. I. *Science* **2015**, *348*, 1234. (d) Ahn, N.; Son, D.-Y.; Jang, I.-H.; Kang, S. M.; Choi, M.; Park, N.-G. *J. Am. Chem. Soc.* **2015**, *137*, 8696.
4. Yu, Z.; Sun, L. *Adv. Energy Mater.* **2015**, *5*, 1500213.
5. (a) Heo, J. H.; Im, S. H.; Noh, J. H.; Mandal, T. N.; Lim, C.-S.; Chang, J. A.; Lee, Y. H.; Kim, H.; Sarkar, A.; Nazeeruddin, M. K.; Grätzel, M.; Seok, S. I. *Nat. Photonics* **2013**, *7*, 486. (b) Jeon, N. J.; Lee, H. G.; Kim, Y. C.; Seo, J.; Noh, J. H.; Lee, J.; Seok, S. I. *J. Am. Chem. Soc.* **2014**, *136*, 7837. (c) Li, H.; Fu, K.; Hagfeldt, A.; Grätzel, M.; Mhaisalkar, S. G.; Grimsdale, A. C. *Angew. Chem. Int. Ed.* **2014**, *53*, 4085. (d) Li, H.; Fu, K.; Boix, P. P.; Wong, L. H.; Hagfeldt, A.; Grätzel, M.; Mhaisalkar, S. G.; Grimsdale, A. C. *ChemSusChem* **2014**, *7*, 3420. (e) Qin, P.; Paek, S.; Dar, M. I.; Pellet, N.; Ko, J.; Grätzel, M.; Nazeeruddin, M. K. *J. Am.*

- Chem. Soc.* **2014**, *136*, 8516. (f) Gratia, P.; Magomedov, A.; Malinauskas, T.; Daskeviciene, M.; Abate, A.; Ahmad, S.; Grätzel, M.; Getautis, V.; Nazeeruddin, M. K. *Angew. Chem. Int. Ed.* **2015**, *54*, 11409. (g) Rakstys, K.; Abate, A.; Dar, M. I.; Gao, P.; Jankauskas, V.; Jacopin, G.; Kamarauskas, E.; Kazim, S.; Ahmad, S.; Grätzel, M.; Nazeeruddin, M. K. *J. Am. Chem. Soc.* **2015**, *137*, 16172.
6. Bach, U.; Lupo, D.; Comte, P.; Moser, J. E.; Weissörtel, F.; Salbeck, J.; Spreitzer, H.; Grätzel, M. *Nature* **1998**, *395*, 583.
 7. Wakamiya, A.; Nishimura, H.; Fukushima, T.; Suzuki, F.; Saeki, A.; Seki, S.; Osaka, I.; Sasamori, T.; Murata, M.; Murata, Y.; Kaji, H. *Angew. Chem. Int. Ed.* **2014**, *53*, 5800.
 8. Plattner, P. A.; St. Pfau, A. *Helv. Chim. Acta* **1937**, *20*, 224.
 9. Nishimura, H.; Eliseeva, M. N.; Wakamiya, A.; Scott, L. T. *Synlett* **2015**, *26*, 1578.
 10. Eliseeva, M. N.; Scott, L. T. *J. Am. Chem. Soc.* **2012**, *134*, 15169.
 11. Salman, H.; Abraham, Y.; Tal, S.; Meltzman, S.; Kapon, M.; Tessler, N.; Speiser, S.; Eichen, Y. *Eur. J. Org. Chem.* **2005**, 2207.
 12. Cardona, C. M.; Li, W.; Kaifer, A. E.; Stockdale, D.; Bazan, G. C. *Adv. Mater.* **2011**, *23*, 2367.
 13. Wakamiya, A.; Endo, M.; Sasamori, T.; Tokitoh, N.; Ogomi, Y.; Hayase, S.; Murata, Y. *Chem. Lett.* **2014**, *5*, 711.
 14. Burschka, J.; Kessler, F.; Nazeeruddin, M. K.; Grätzel, M. *Chem. Mater.* **2013**, *25*, 2986.
 15. (a) Choi, H.; Cho, J. W.; Kang, M.-S.; Ko, J. *Chem. Commun.* **2015**, *51*, 9305. (b) Steck, C.; Franckevič, M.; Zakeeruddin, S. M.; Mishra, A.; Bäuerle, P.; Grätzel, M. *J. Mater. Chem. A* **2015**, *3*, 17738.
 16. This value is in good agreement with that obtained from time-of-flight measurement ($2 \times 10^{-4} \text{ cm}^2/\text{Vs}$). See: Poplavskyy, D.; Nelson, J. *J. Appl. Phys.* **2003**, *93*, 341.
 17. (a) Saeki, A.; Koizumi, Y.; Aida, T.; Seki, S. *Acc. Chem. Res.* **2012**, *45*, 1193. (b) Oga, H.; Saeki, A.; Ogomi, Y.; Hayase, S.; Seki, S. *J. Am. Chem. Soc.* **2014**, *136*, 13818.
 18. Shen, Y.; Hosseini, A. R.; Wong, M. H.; Malliaras, G. G. *ChemPhysChem* **2004**, *5*, 16.
 19. Gaussian 09 (Revision A.02), Frisch, M. J.; Trucks, G. W.; Schlegel, H. B.; Scuseria, G. E.; Robb, M. A.; Cheeseman, J. R.; Scalmani, G.; Barone, V.; Mennucci, B.; Petersson, G. A.; Nakatsuji, H.; Caricato, M.; Li, X.; Hratchian, H. P.; Izmaylov, A. F.; Bloino, J.; Zheng, G.; Sonnenberg, J. L.; Hada, M.; Ehara, M.;

Toyota, K.; Fukuda, R.; Hasegawa, J.; Ishida, M.; Nakajima, T.; Honda, Y.; Kitao, O.; Nakai, H.; Vreven, T.; Montgomery, Jr., J. A.; Peralta, J. E.; Ogliaro, F.; Bearpark, M.; Heyd, J. J.; Brothers, E.; Kudin, K. N.; Staroverov, V. N.; Keith, T.; Kobayashi, R.; Normand, J.; Raghavachari, K.; Rendell, A.; Burant, J. C.; Iyengar, S. S.; Tomasi, J.; Cossi, M.; Rega, N.; Millam, J. M.; Klene, M.; Knox, J. E.; Cross, J. B.; Bakken, V.; Adamo, C.; Jaramillo, J.; Gomperts, R.; Stratmann, R. E.; Yazyev, O.; Austin, A. J.; Cammi, R.; Pomelli, C.; Ochterski, J. W.; Martin, R. L.; Morokuma, K.; Zakrzewski, V. G.; Voth, G. A.; Salvador, P.; Dannenberg, J. J.; Dapprich, S.; Daniels, A. D.; Farkas, O.; Foresman, J. B.; Ortiz, J. V.; Cioslowski, J.; Fox, D. J., Gaussian, Inc., Wallingford CT, 2009.

Chapter 5

Oxygen-Bridged Diphenylnaphthylamine as a Scaffold for Full-Color Circularly Polarized Luminescent Materials

Abstract: Oxygen-bridged diphenylnaphthylamine with a helical shape was designed and synthesized as a key scaffold for circularly polarized luminescent materials. The introduction of the electron-withdrawing group, such as formyl and 2,2-dicyanovinyl groups, at the naphthyl moiety in this skeleton effectively decreases the LUMO level to tune the band-gap. The prepared model compounds exhibited circularly polarized luminescence (CPL) signals with dissymmetry factor (*g* value) of 10^{-3} both in CH_2Cl_2 and in the solid states. Furthermore, the emission colors from these derivatives were found to be changed by the substituents as well as solvent effects, covering the whole visible region from blue to deep-red.

Introduction

Circularly polarized luminescence (CPL), which is the differential emission of right- and left-handed circularly polarized light by chiral molecular systems,¹ has attracted attention due to their potential applications, such as 3D optical display,² CPL lasers,³ chiral recognition,⁴ and asymmetric photosynthesis.⁵ Several kinds of organic molecules emitting CPL have been developed so far, which are classified into small organic molecules,⁶ polymers,⁷ transition metal complexes,⁸ and lanthanide complexes.^{4c,9} Among them, small organic molecules have an advantage of being tunable of their photophysical properties owing to their accessible structural variations. Nevertheless, examples for developments of the materials with tunability of their CPL wavelengths have been still limited.^{6w,y,7j,m}

As shown in previous chapters, the author developed partially oxygen-bridged triarylamine as a key skeleton for hole-transporting materials, in which three phenyl rings were constrained in a quasiplanar structure by two oxygen-tethers.¹⁰ Besides hole-transporting ability, all of these compounds having this skeleton show intense fluorescence, offering the potential use as emissive materials. Regarding the structural feature in this skeleton, the inversion barrier for the flipping of the non-tethered phenyl rings was estimated to be only 9.1 kcal/mol by DFT calculations (B3LYP/6-31G(d)), indicating that two phenyl rings are easily flipping in the gas phase or in solution at ambient conditions. Upon increasing steric hindrance in this moiety by expansion of the skeleton, the ring flipping can be suppressed to form the isolable helical-shaped structure. For example, the DFT calculations suggested that replacement of one phenyl ring to a naphthyl ring in oxygen-bridged triphenylamine skeleton increases the inversion barrier to 29.3 kcal/mol, indicating the possibility of optical resolution for this skeleton (Figure 1a). Considering intense fluorescence of oxygen-bridged triarylaminates, this skeleton is expected to be used as a scaffold for CPL materials. Based on this idea, the author designed and synthesized oxygen-bridged diphenylnaphthylamine **1** and its derivatives **2–3** that have electron-withdrawing groups at the naphthyl ring (Figure 1b). In this asymmetric system, the author anticipated that introduction of the naphthyl ring and substituents attached thereto would induce the deflection in the HOMO and the LUMO to enhance intramolecular charge transfer character, which enables developments of emission-color-tunable CPL systems.

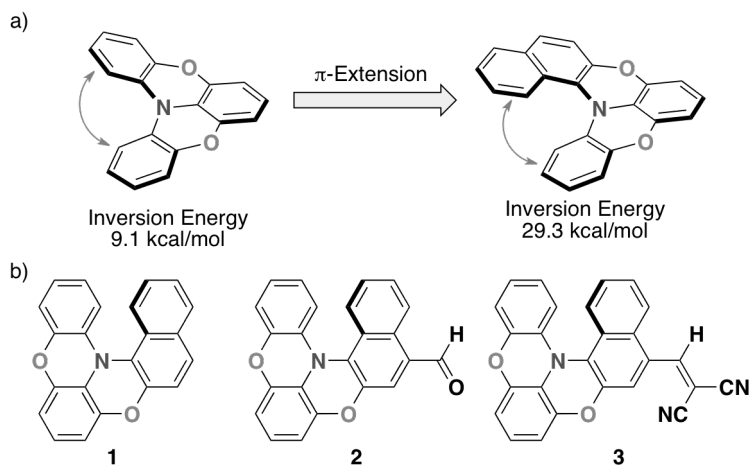
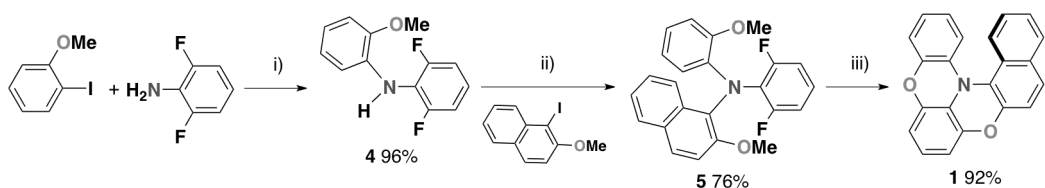


Figure 1. (a) Molecular design for CPL material in this study and calculated ring-inversion energies, and (b) molecular structures of **1–3**.

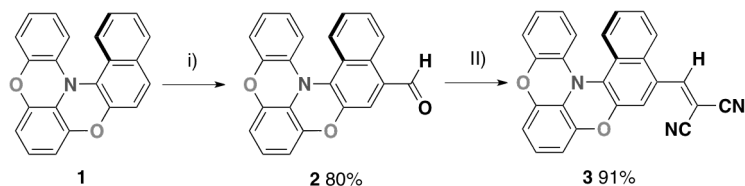
Results and Discussion

Synthesis

Oxygen-bridged diphenylnaphthylamine **1** was synthesized by the similar method described in Chapter 1 and Chapter 4.¹⁰ As shown in Scheme 1, Buchwald-Hartwig arylation of 2,6-difluoroaniline with *o*-iodoanisole selectively gave monoarylated difluoroaniline **4** in 96% yield. Subsequently, Ullmann arylation of **4** with 1-*ido*-2-methoxynaphthalene¹¹ afforded bisarylated difluoroaniline **5** in 76% yield. After removal of the protecting methyl groups in **5** by BBr_3 , treatment with K_2CO_3 in DMF at 120 °C afforded oxygen-bridged diphenylnaphthylamine **1** in 92% yield as yellow solids.



The selective Vilsmeier-Haack reaction of **1** at the 4-position in the naphthyl moiety allowed facile preparation of functionalized derivatives **2** and **3** (Scheme 2). Thus, treatment of **1** with POCl_3 in DMF selectively afforded monoformyl derivative **2** in 80% yield as orange solids. The reaction of **2** with malononitrile in the presence of triethylamine gave mono-2,2-dicyanovinyl derivative **3** in 91% yield as purple solids. Compounds **1–3** were characterized by NMR, HRMS, and elemental analysis.



Scheme 2. Reagents/conditions: i) POCl_3 , DMF, $\text{C}_2\text{H}_4\text{Cl}_2$, 80 °C; ii) malononitrile, NEt_3 , CHCl_3 , rt.

Photophysical Property

Photophysical properties of **1–3** were measured in CH_2Cl_2 (Figure 2). In UV-vis absorption spectra, diphenylnaphthylamine **1** shows a relatively weak absorption band at $\lambda_{\text{abs}} = 395$ nm ($\log \epsilon = 3.60$), which is red-shifted by 40 nm compared with triphenylamine **6** ($\lambda_{\text{abs}} = 355$ nm ($\log \epsilon = 3.81$)). In contrast, formyl derivative **2** ($\lambda_{\text{abs}} = 461$ nm ($\log \epsilon = 4.00$)) and 2,2-dicyanovinyl derivative **3** ($\lambda_{\text{abs}} = 552$ nm ($\log \epsilon = 4.24$))) show significantly intense absorption bands with bathochromic shifts. The observed increase in the molar absorption coefficients and their red-shifts are due to the introduction of the electron-withdrawing groups.

In the fluorescence spectra obtained for CH_2Cl_2 solution, whereas triphenylamine **6** shows moderate emission at $\lambda_{\text{em}} = 399$ nm ($\Phi = 0.19$, $\tau = 3.43$ ns), diphenylnaphthylamine **1** exhibits intense bluish green emission at $\lambda_{\text{em}} = 488$ nm ($\Phi = 0.86$) with large Stokes shift (4825 cm^{-1}). It is noteworthy that the emission was found to have a lifetime of $\tau = 25.4$ ns which is rather long among π -conjugated systems. For formyl derivative **2** and 2,2-dicyanovinyl derivative **3**, the introduction of electron-withdrawing groups caused significant red-shift on their emission bands; orange ($\lambda_{\text{em}} = 580$ nm, $\Phi = 0.44$, $\tau = 6.76$ ns) and deep-red emission ($\lambda_{\text{em}} = 685$ nm, $\Phi = 0.09$, $\tau = 1.16$ ns), respectively. These are red-shifted by 92 nm and 197 nm compared to **1**, corresponding to the large Stokes shifts (**2**: 4451 cm^{-1} , **3**: 3517 cm^{-1}) from that of **1**. The radiative rate constants (k_r) and non-radiative rate constants (k_{nr}) for **1–3** under these conditions were determined as follows: $k_r = 3.4 \times 10^7 \text{ s}^{-1}$, $k_{\text{nr}} = 5.5 \times 10^6 \text{ s}^{-1}$ for **1**, k_r

$= 6.5 \times 10^7 \text{ s}^{-1}$, $k_{\text{nr}} = 8.3 \times 10^7 \text{ s}^{-1}$ for **2**, and $k_r = 7.8 \times 10^7 \text{ s}^{-1}$, $k_{\text{nr}} = 7.8 \times 10^8 \text{ s}^{-1}$ for **3**, respectively.

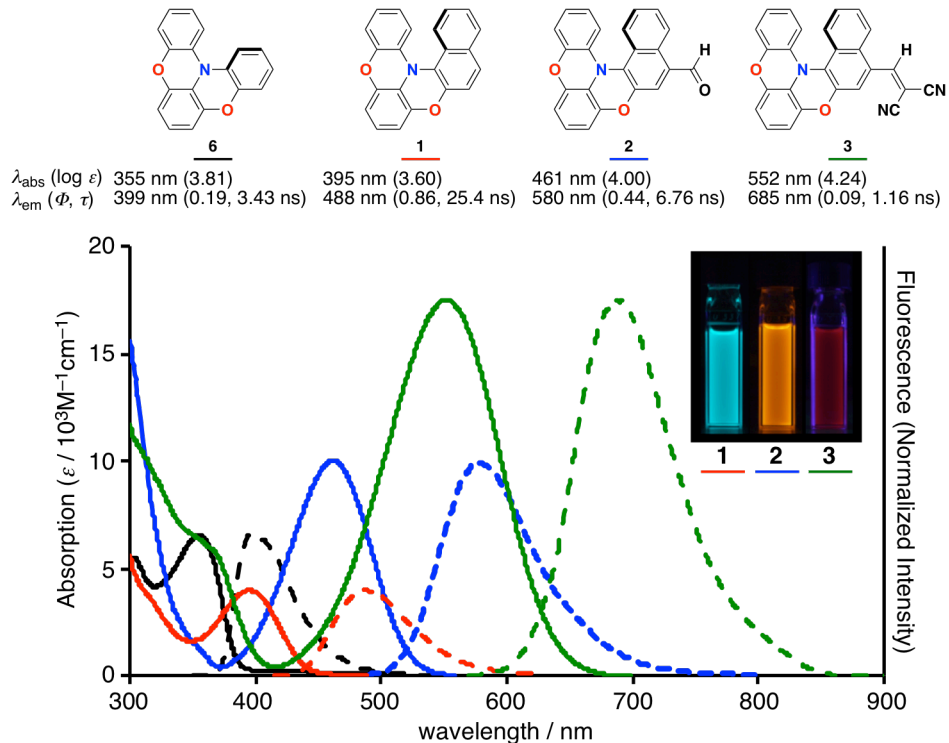


Figure 2. UV-vis absorption spectra (solid line) and fluorescence spectra (dash line) of **1–3** and **6** in CH_2Cl_2 . The photograph shows the emission of **1–3** showing distinguished color for each compound depending on the substituents.

Optical Resolution

To examine chiroptical properties of **1–3**, which should arise from their helical structure, isolation of each of the pure enantiomers was needed. The optical resolution for **1–3** was achieved by preparative chiral HPLC using the CHIRALPAK-IF to give each of enantiomers in pure form (Figure 3).

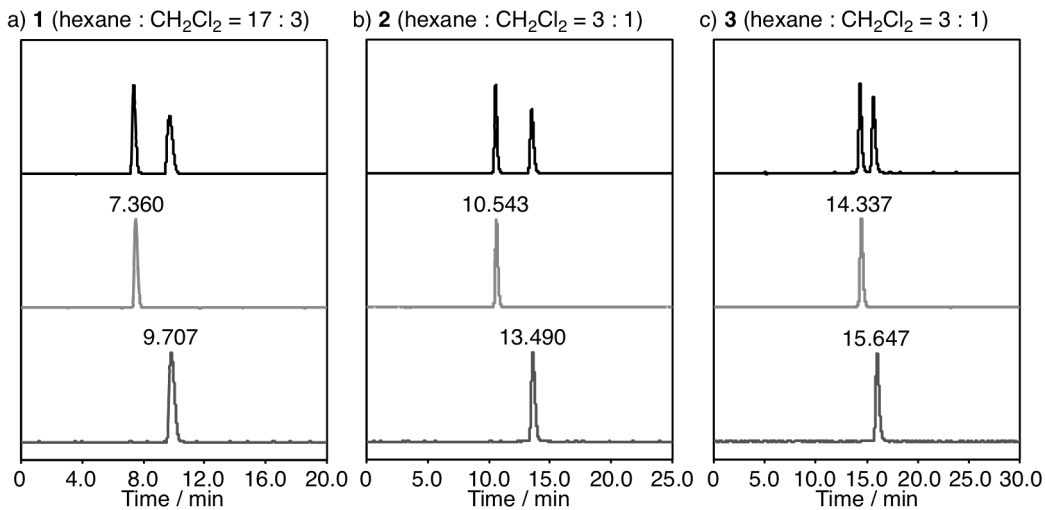


Figure 3. Optical resolution of (a) **1**, (b) **2**, and (c) **3** on HPLC using the CHIRALPAK-IF with mixed solvents of hexane and CH_2Cl_2 as eluent. The ratios of hexane : CH_2Cl_2 are 17 : 3 for **1**, 3 : 1 for **2**, and 3 : 1 for **3**, respectively. The top, middle, and bottom lines show the traces before resolution, those of the separated fraction 1, and those of the separated fraction 2, respectively.

Chiral Stability

As predicted by the DFT calculations shown above, all enantiomers of **1–3** were stable under ambient conditions so that no racemization was observed at room temperature. However, racemization would be possible at higher temperature. Thus, chiral stabilities of **1–3** were studied by tracing the racemization in toluene at 100 °C for **1** and 80 °C for **2** and **3**. The changes of the ratio of each fraction were monitored using HPLC with the CHIRALPAK-IF every 1 hour (Figure 4). The rate constants (k) for racemization, that is an inversion of the naphthyl ring, are estimated by the following equation:

$$\Delta C/C = A \ln(-kt)$$

where C is total concentration of fraction 1 ($C_{\text{fr}1}$) and fraction 2 ($C_{\text{fr}2}$), ΔC is the difference between $C_{\text{fr}1}$ and $C_{\text{fr}2}$, A is a constant, and t is the heating time, respectively. According to this equation, rate constants k for the racemization were determined to be $7.31 \times 10^{-5} \text{ s}^{-1}$ for **1**, $5.86 \times 10^{-5} \text{ s}^{-1}$ for **2**, and $1.20 \times 10^{-4} \text{ s}^{-1}$ for **3**, respectively, reflecting electron densities of the naphthyl moiety; *i.e.*, the electron deficient naphthyl ring flips faster. The ring inversion energies (ΔG^\ddagger) are estimated by the following equation:

$$\Delta G^\ddagger = RT \ln \left(\frac{k_B T}{h k} \right)$$

where R is the gas constant (1.987×10^{-3} kcal/Kmol), T is the heating temperature (K), k_B is the Boltzmann constant (1.381×10^{-23} J/K), and h is the Planck constant (6.626×10^{-34} Js), respectively. Thus, the ring inversion energies were obtained as 29.0 kcal/mol for **1**, 27.6 kcal/mol for **2**, and 27.1 kcal/mol for **3**, respectively. These are quantitatively in good agreement with the values predicted by the DFT calculations (B3LYP/6-31G(d)) as shown in Figure 1.

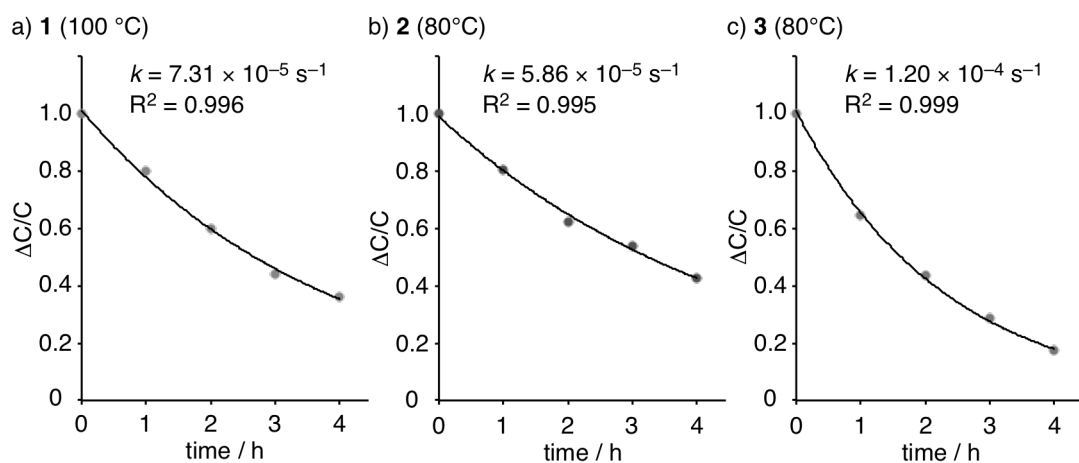


Figure 4. Changes of the enantiomer ratio of a) **1** at 100 °C, b) **2** at 80 °C, and c) **3** at 80 °C in toluene. ΔC is the difference in the concentration of the fraction 1 and the fraction 2 ($\Delta C = C_{\text{fr1}} - C_{\text{fr2}}$) and C is the total concentration of the fraction 1 and the fraction 2 ($C = C_{\text{fr1}} + C_{\text{fr2}}$).

Chiroptical Property

Since each enantiomer was obtained in a pure form, the chiroptical properties of **1–3** were investigated by circular dichroism (CD) and CPL spectroscopy for CH₂Cl₂ solutions. CD spectroscopy of (*P*)- and (*M*)-helix of **1–3** showed clear Cotton effects as the mirror images, in which the first eluted fractions of **1–3** (fraction 1) exhibited (–) Cotton effects and the second eluted fractions (fraction 2) exhibited (+) Cotton effects at around 400–600 nm (Figure 5). The absolute structures of enantiomerically pure **1–3** in each fraction were assigned to be (*P*)-helix for the first fraction and (*M*)-helix for the second fraction, on the basis of comparison with the results of the TD-DFT calculations. In CPL spectra, **1–3** exhibited significant signals as shown in Figure 5, owing to their helicity in addition to the strong emissive properties. In general, degrees of CD and CPL

intensity are given by the dissymmetry factors (g), which are defined as $g_{\text{abs}} = 2(\varepsilon_L - \varepsilon_R)/(\varepsilon_L + \varepsilon_R)$ for CD and $g_{\text{em}} = 2(I_L - I_R)/(I_L + I_R)$ for CPL, where ε_L , ε_R , I_L and I_R are the absorption and emission intensities for left- and right-handed light, respectively. By measuring the CD signals for each of the pure enantiomers of **1–3** in CH_2Cl_2 , the g_{abs} values were determined to be 5.6×10^{-3} for **1**, 2.1×10^{-3} for **2**, 0.9×10^{-3} for **3**, respectively. In addition, by observing the CPL signals, the g_{em} values were obtained for all of the oxygen-bridged diphenylnaphthylamine derivatives; 4.7×10^{-3} for **1**, 1.4×10^{-3} for **2**, and 0.9×10^{-3} for **3**, respectively. These values are relatively high among small organic molecules reported so far.⁶

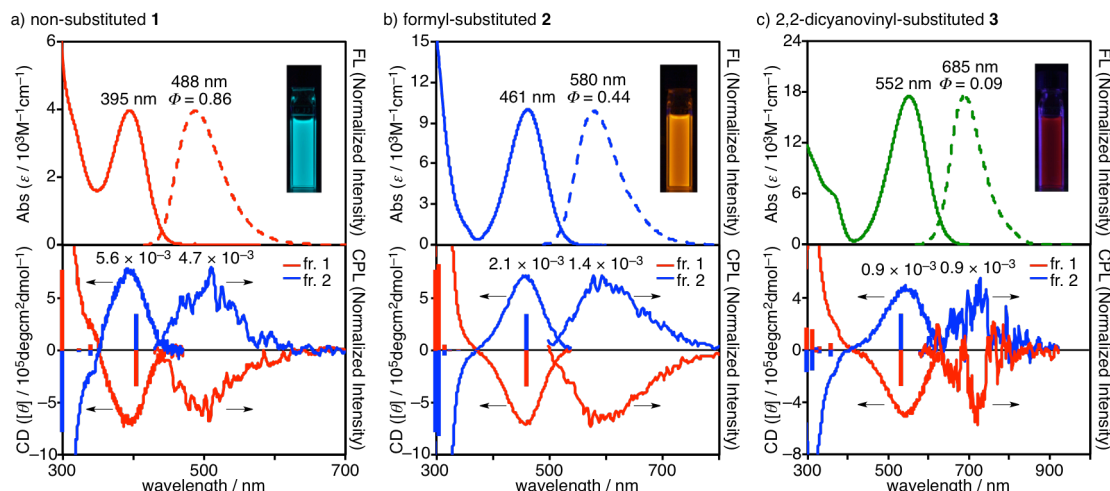


Figure 5. UV-vis absorption (solid) and fluorescence (dashed) spectra (top), and CD and CPL spectra (bottom) for a) **1**, b) **2**, and c) **3** in CH_2Cl_2 . The red and blue bars show the calculated CD bands (CAM-B3LYP/6-31G(d)) for (*P*)- and (*M*)-helix, respectively. Transition energies are calibrated by using a factor of 0.88. Photographs show the emission of **1–3**.

X-ray Crystal Structure

Single crystal X-ray structural analysis was conducted on racemic crystals (*rac-1* and *rac-2*) as well as enantiomerically pure crystals (*ena-1* and *ena-2*) in order to see if there are differences in molecular structures and packing motif that would affect solid-state properties (Figure 6). As for crystals of **3**, unfortunately, suitable single crystals for X-ray analysis could not be obtained from neither racemic mixture nor enantiomerically pure fraction. In this study, the absolute structures for enantiomerically pure crystals could not be determined because the lack of heavy elements for these

compounds did not give any meaningful information for the absolute structures, which are usually obtained by a Flack parameter with anomalous X-ray scattering. Thus, the absolute structures for each of the enantiomers of **1–3** had been determined according to the comparison with the TD-DFT calculations and the CD spectra in solution as shown previously. The crystal structure analyses confirmed that all molecules of **1** and **2** in both racemic and enantiomerically pure crystals have helical structures with dihedral angles ($\angle\text{C2–C1–C14–C15}$) of 72.6° and 73.1° for *rac*-**1**, 75.7° for *ena*-**1**, 72.8° for *rac*-**2**, and 76.5° for *ena*-**2**, respectively, which are in good agreement with those in the optimized structures by the DFT calculations (**1**: 72.3° , **2**: 73.4°). The small differences in the dihedral angles would be attributed to the packing force. In the packing structures, one-dimensional columnar like structure with slipped π -stacking was observed as a general tendency for both racemic and enantiomerically pure crystals. In a racemic crystal of **1** (*rac*-**1**), two independent molecules exist and they form a pair in a columnar stacking structure. In the case of racemic crystal of **2** (*rac*-**2**), (*P*)- and (*M*)-helix of **2** form independent columnar structures, which are aligned alternately. It should be mentioned that the short co-facial distances for the central benzene rings are observed in the packing structure of enantiomerically pure crystals (*ena*-**1** and *ena*-**2**): 3.44 \AA for *ena*-**1** and 3.33 \AA for *ena*-**2**, respectively, adopting a slipped π -stacking in the columnar-like structures.

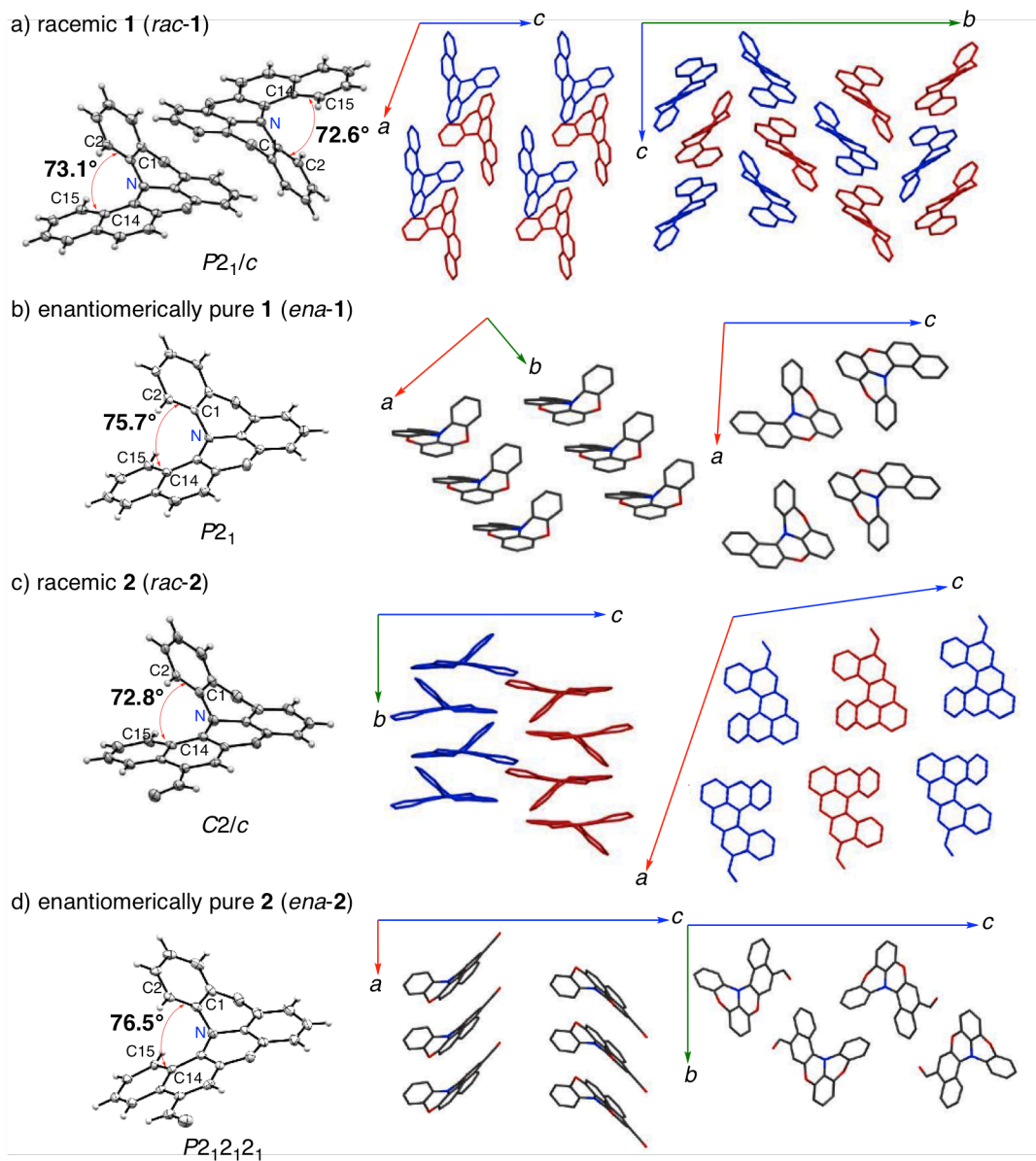


Figure 6. X-ray crystal structures: ORTEP drawings (50% probability for thermal ellipsoids) and packing structures for (a) *rac*-**1**, (b) *ena*-**1**, (c) *rac*-**2**, and (d) *ena*-**2**. The *P*- and *M*-helix in racemic crystals are shown in red and blue, respectively.

Fluorescence in the Solid State

Then, the author moved his attention to the fluorescence properties of **1–3** in the solid state for both the racemic and enantiomerically pure crystals. Arising from the differences in the packing motifs, **1–3** exhibited different emission behaviors between racemic mixture and enantiomerically pure compounds (Figure 7). Interestingly, whereas both crystals of *rac*-**1** and *ena*-**1** show similar bluish green emissions (*rac*-**1**: $\lambda_{\text{em}} = 480 \text{ nm}$, *ena*-**1**: 482 nm), the quantum yield of *ena*-**1** ($\Phi = 0.55$) is higher than that of *rac*-**1** ($\Phi = 0.35$). In the case of **2** and **3**, fluorescence wavelengths as well as quantum yields are varied. Thus, crystals of *rac*-**2** and *ena*-**2** exhibited different colors with different quantum efficiencies: yellowish orange emission ($\lambda_{\text{em}} = 572 \text{ nm}$, $\Phi = 0.09$) and orange emission ($\lambda_{\text{em}} = 585 \text{ nm}$, $\Phi = 0.14$), respectively. The microcrystalline powder of *rac*-**3** and *ena*-**3** also exhibited different emissions that appeared in near-IR region ($\lambda_{\text{em}} = 735 \text{ nm}$, $\Phi = 0.02$) and deep-red region ($\lambda_{\text{em}} = 706 \text{ nm}$, $\Phi = 0.08$), respectively. Since these differences are supposed to be due to the differences in the packing structures, the author conducted quantitative analyses for the solid samples as shown below.

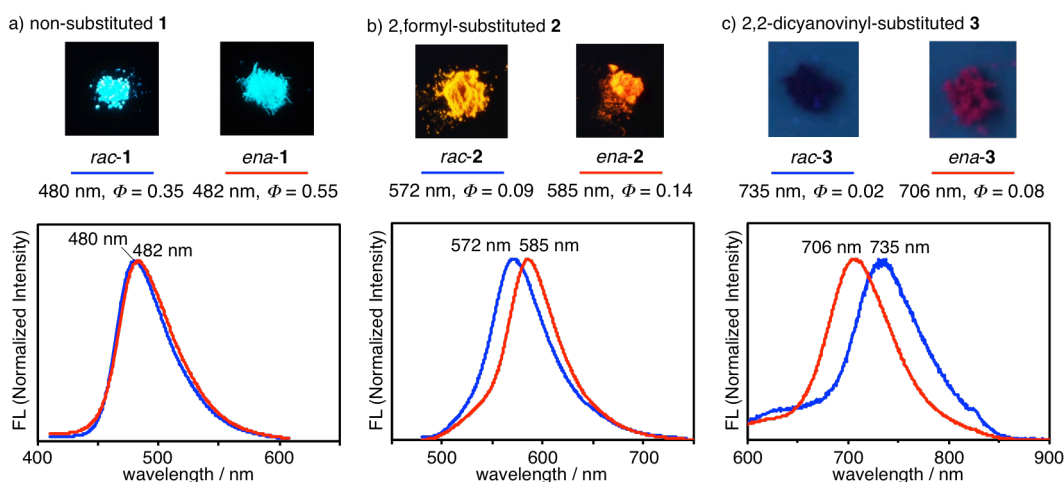


Figure 7. Photographs of emission (top) and fluorescence spectra for racemic mixture (red) and enantiomerically pure solids of **1–3** (bottom).

Photophysical and Chiroptical Properties of Dispersion

The solid-state chiroptical properties were examined quantitatively using the dispersions of the enantiomerically pure compounds in addition to the racemic mixture in water prepared by rapid reprecipitation method.¹² The absorption and fluorescence spectra, and CD and CPL spectra of the dispersions of *ena*-**1–3** in water are shown in

Figure 8. As to the absorption and the emission, the dispersions of *ena-1–3* show similar bands to those for the CH₂Cl₂ solutions. The quantum yields for emission from the dispersion are very close to those from crystals, confirming that the dispersions are composed of fine crystals. Table 1 summarizes absorption and emission bands of solution and crystals for racemic compounds, and of crystals and dispersion in water for enantiomerically pure compounds.

In CD spectra, the Cotton effects in the solid state were observed as the mirror image similar to that for the solution. It should be noted that these compounds also exhibit the CPL activities even in the solid states. The *g*_{em} values determined for the dispersions of *ena-1–3* are 4.5×10^{-3} , 1.5×10^{-3} , and 2.5×10^{-3} , respectively, which are comparable with those in CH₂Cl₂ solutions. These results suggest the potential use of these compounds as CPL materials even in the solid-state.

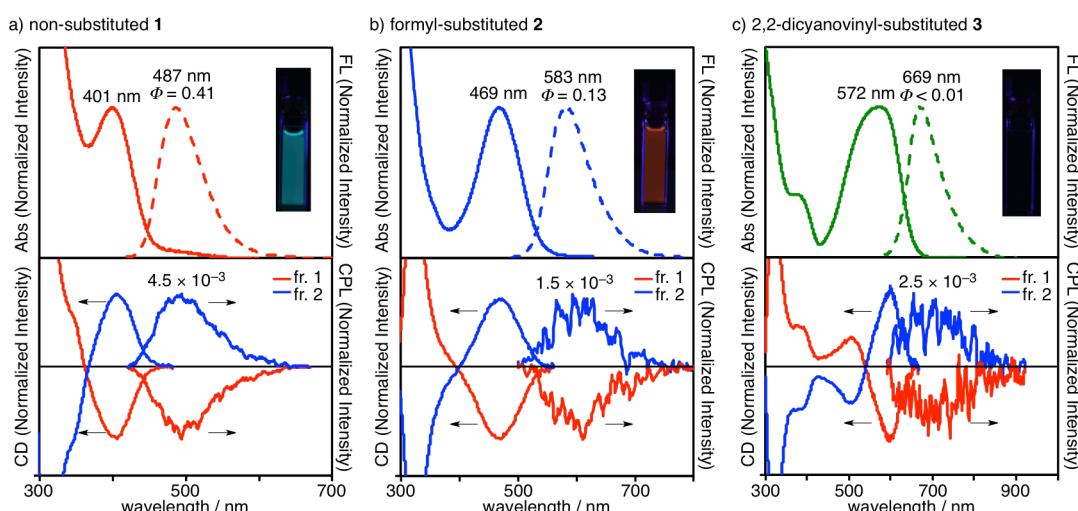


Figure 8. UV-vis absorption (solid) and fluorescence (dashed) spectra for a) *ena-1*, b) *ena-2*, and c) *ena-3* (top). CD and CPL spectra for a) *ena-1*, b) *ena-2*, and c) *ena-3* as dispersions in water (bottom). Photographs show the emission of the dispersions of *ena-1–3*.

Table 1. Photophysical Properties of 1–3 in Various States

compd.	states	λ_{abs} [nm]	λ_{em} [nm]	Φ [%]	τ [ns]	λ_{CD} [nm]	g_{abs} $[10^{-3}]$	g_{em} $[10^{-3}]$
1	CH ₂ Cl ₂ ^a	395	488	0.86	25.4	393	5.6	4.7
	Crystal ^a	—	480	0.35	—	—	—	—
	Crystal ^b	—	482	0.55	—	—	—	—
	Dispersion ^b	401	487	0.41	15.9	405	3.6	4.5
2	CH ₂ Cl ₂ ^a	461	580	0.44	6.76	458	2.1	1.4
	Crystal ^a	—	572	0.09	—	—	—	—
	Crystal ^b	—	585	0.14	—	—	—	—
	Dispersion ^b	469	583	0.13	4.99	471	2.1	1.5
3	CH ₂ Cl ₂ ^a	552	685	0.09	1.16	551	0.9	0.9
	Crystal ^a	—	735	0.02	—	—	—	—
	Crystal ^b	—	706	0.08	—	—	—	—
	Dispersion ^b	572	669	<0.01	1.28	600	4.3	2.5

^a Prepared from racemic mixture. ^b Prepared from enantiomer.

DFT Calculations

To gain deeper insights into the electronic structures as well as photophysical and chiroptical properties of oxygen-bridged diphenylnaphthylamines, DFT calculations (B3LYP/6-31G(d)) were conducted to obtain the optimized structures at the ground states (S_0), and the single-point TD-DFT calculations (TD-CAM-B3LYP/6-31G(d)) were done to evaluate absorption properties (Figure 9). The Kohn-Sham (KS)-HOMO of **1** (−4.79 eV) delocalizes over the whole skeleton, whereas the KS-LUMO (−1.25 eV) of **1** mainly locates on naphthalene ring. Accordingly, the electron-withdrawing groups introduced at the naphthyl moiety effectively decreases the LUMO levels in formyl derivative **2** (KS-LUMO: −2.10 eV) and 2,2-dicyanovinyl derivative **3** (KS-LUMO: −2.88 eV). In contrast, the HOMO levels (**2**: −5.09 eV and **3**: −5.34 eV) decreased moderately, which leads to the narrower HOMO-LUMO gaps for **2** and **3** compared with that of **1**.

The results of the TD-DFT calculations on the S_0 ground states in addition to the energy levels and the coefficients of the HOMO and the LUMO are shown in Figure 9. The longest absorptions for **1–3** are assignable to the $\pi-\pi^*$ transitions from the HOMO to the LUMO. Reflecting the narrow HOMO-LUMO gaps arising from the π -expansion and the electron-withdrawing effects by the substituent at the naphthyl ring in **2** and **3**, the transition energies for the longest absorption for **2** (407 nm, $f = 0.1994$) and **3** (472 nm, $f = 0.4444$) are red-shifted compared with that of **1** (358 nm, $f = 0.0837$), accompanied with the larger oscillator strength. These results are in good agreement with the observed absorption spectra for **1–3**. The increasing of oscillator strength would be due to non-negligible contribution of charge transfer character induced by the deflection in the HOMO and the LUMO.

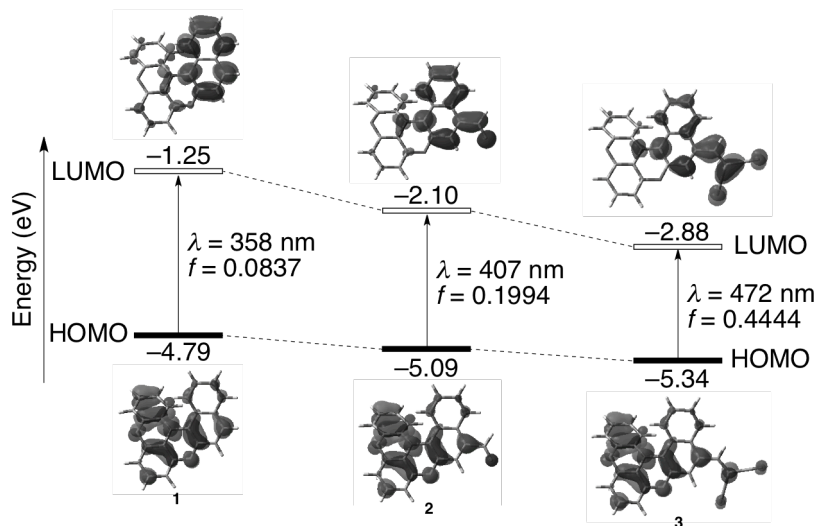


Figure 9. Pictorial presentation of the frontier orbitals, a plot of the Kohn-Sham HOMO and LUMO energy levels for **1–3** (B3LYP/6-31G(d)), and optical transition with oscillator strength (TD-CAM-B3LYP/6-31G(d)//B3LYP/6-31G(d)) for the ground (S_0) state.

Next, in order to discuss the emission properties, theoretical calculations on the S_1 excited states for **1–3** were conducted. The structures of the S_1 excited states were optimized at the TD-B3LYP/6-31G(d) level of theory, and the emission properties were evaluated by the single-point calculations at the TD-CAM-B3LYP/6-31G(d) for the optimized structures of the S_1 states (Figure 10).^{6z,13} Similarly to the DFT calculations on the S_0 states, the deflection in the KS-HOMO and KS-LUMO on the S_1 excited states are also observed for all of **1–3**, suggesting again that intramolecular charge

transfer (ICT) character was induced in the excited states. It was shown that the deflection in the KS-HOMO and KS-LUMO leads to smaller oscillator strengths of the emissions compared with the absorptions: **1** (440 nm, $f = 0.0585$), **2** (495 nm, $f = 0.1149$), and **3** (545 nm, $f = 0.2488$). Such small oscillator strength for the S_1 state rationales the long lifetime with rather small radiative rate constant as was observed in the emission of **1**. Nevertheless, the present compound **1** exhibit an intense emission band with a good quantum yield ($\lambda_{\text{em}} = 488$ nm, $\Phi = 0.86$, $\tau = 25.4$ ns), although the reason is not clear at the present stage.

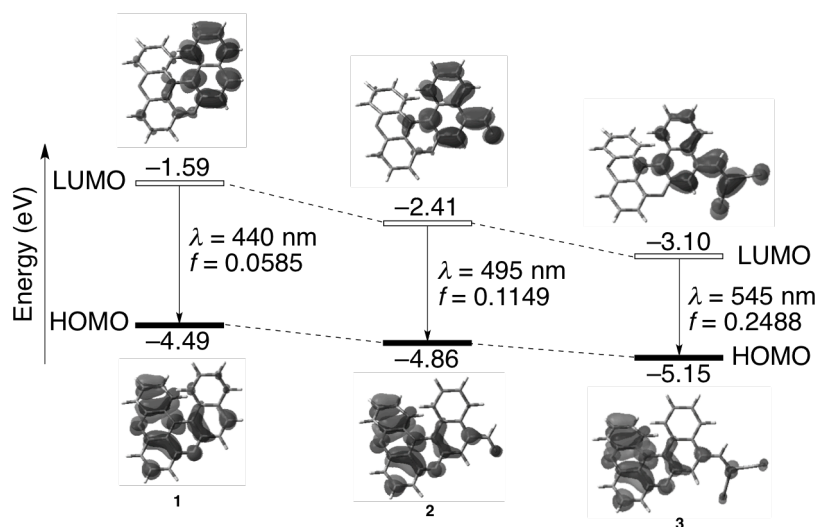


Figure 10. Pictorial presentation of the frontier orbitals, a plot of the Kohn-Sham HOMO and LUMO energy levels, and optical transition with oscillator strength for the optimized structures of the excited (S_1) states for **1–3** (TD-CAM-B3LYP/6-31G(d)//TD-B3LYP/6-31G(d)).

The chiroptical g values for CD and CPL are also known to be estimated by TD-DFT calculations (TD-CAM-B3LYP/6-31G(d)) for both of the S_0 and S_1 states optimized at the B3LYP/6-31G(d) level and TD-B3LYP/6-31G(d) level, respectively. The calculated g values are evaluated according to the equation as follows: $g = 4R/D$, where D and R are dipole strengths and rotatory strengths, respectively.¹⁴ D is defined from the oscillator strength (f) and the corresponding excitation energy (ν / cm^{-1}) as following equation:

$$D = \frac{3he^2}{8\pi^2\nu m_e c} f$$

where h is the Planck constant (6.626×10^{-34} J/s), e is the charge on the electron ($4.80 \times$

10^{-10} esu), m_e is the electron mass (9.11×10^{-31} kg), and c is the speed of light (3.00×10^{10} cm/s), respectively. R could be directly evaluated by TD-DFT calculations. The obtained g_{abs} and g_{em} for **1–3** by the TD-DFT calculations are shown in Table 2, which are in good agreement with the experimental values.

Table 2. Theoretical Chiroptical Parameters for **1–3^a**

Compd.	State	λ [nm]	D [10^{-36} esu 2 cm 2]	R [10^{-40} esu 2 cm 2]	$ g $ [10^{-3}]
1	S_0	358	6.37	105	6.6 (5.6) ^b
	S_1	440	5.47	72.9	5.3 (4.7) ^b
2	S_0	407	17.3	117	2.7 (2.1) ^b
	S_1	495	12.1	80.2	2.7 (1.4) ^b
3	S_0	472	44.6	130	1.2 (0.9) ^b
	S_1	545	28.9	90.8	1.3 (0.9) ^b

^aThe structure of the S_0 states were optimized at the B3LYP/6-31G(d) level and the optical transition was calculated at the TD-CAM-B3LYP/6-31G(d). The structures of the S_1 states were optimized at the TD-B3LYP/6-31G(d) level and the optical transition was calculated at the TD-CAM-B3LYP/6-31G(d). ^bExperimental g values.

Full Color Fluorescence

As discussed above, the theoretical calculations suggested that intramolecular charge transfer (ICT) character are induced in the excited states. Actually, the Lippert-Mataga plots¹⁵ demonstrate that **1–3** have intramolecular charge transfer character especially in the excited state. Reflecting such ICT characters, all of **1–3** show significant red-shifts of the emission bands in the solvent with higher polarity. Interestingly, these emissions cover the whole visible region, displaying full-color emission (Figure 11).

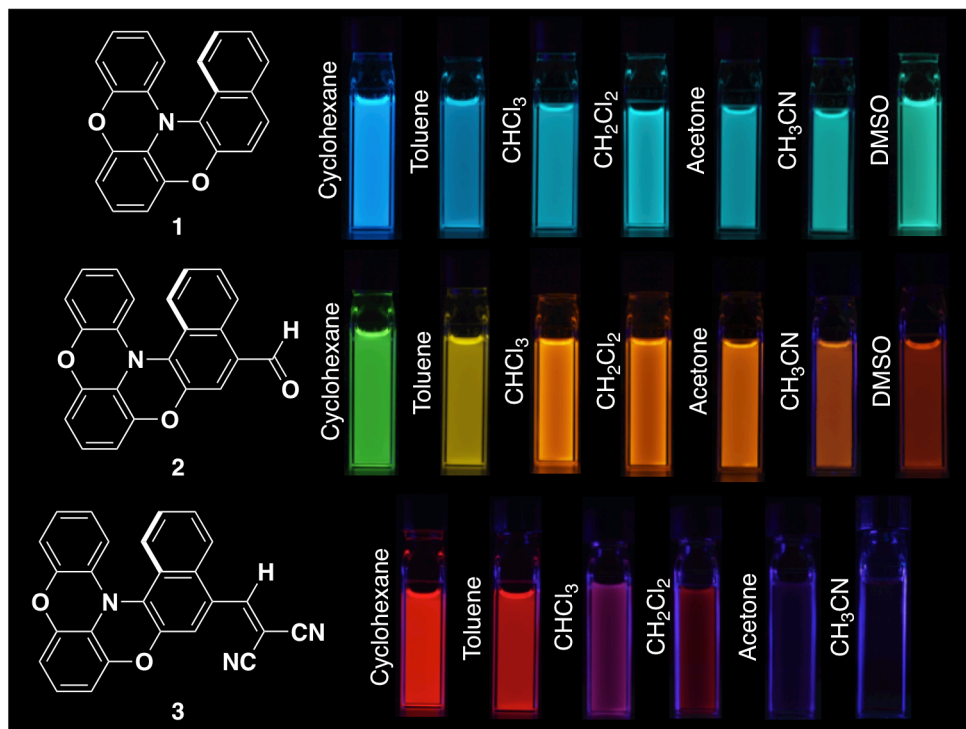


Figure 10. Full color emission from **1–3** in a variety of the solvent.

Conclusion

In conclusion, oxygen-bridged diphenylnaphthylamine derivatives **1–3** having a helical shape were designed and synthesized. All of **1–3** exhibited fluorescence both in solution and in the solid states, and also exhibited CPL signals with good g_{em} values of $\sim 10^{-3}$. Furthermore, due to their intramolecular charge transfer characters in the excited states, their emission colors could be tunable from blue to deep-red by the selection of solvents.

Experimental Section

General.

All reactions were carried out under an argon atmosphere. Thin layer chromatography (TLC) was performed on plates coated with 0.25 mm thick silica gel 60F-254 (Merck). Column chromatography was performed using PSQ 60B (Fuji Silysys). Preparative gel permeation chromatography (GPC) was performed with a JAI LC-918 system equipped with RI-50 detector, JAIGEL-2H column (20 mm ID \times 600 mm) and 1H column (20 mm ID \times 600 mm) using toluene as eluent (flow rate: 3.8 mL/min). Melting points (m.p.) were measured on a Yanaco Micro Melting Point

Apparatus. ^1H and ^{13}C NMR spectra were recorded with a JEOL ECA 500 (500 MHz for ^1H and 125 MHz for ^{13}C) spectrometer. The NMR chemical shifts are reported in ppm with reference to residual protons and carbons of CDCl_3 (δ 7.26 ppm in ^1H NMR, and δ 77.00 ppm in ^{13}C NMR). FAB and EI mass spectra were performed with a JEOL JMS-MS700V by the Joint Usage/Research Center (JURC) at the ICR, Kyoto Univ. Elemental analyses were performed by the JURC at the ICR, Kyoto Univ. UV-vis absorption measurement was performed with a Shimadzu UV-3150 spectrometer, in degassed spectral grade solvents. Fluorescence measurement was performed with a HORIBA FluoroMax 4P-NIR. Quantum yields were determined with a Hamamatsu Photonics Quantaurus QY C11347 with calibrated integrating sphere system. Circular dichromism (CD) measurement was performed with a JASCO J-820 spectropolarimeter at room temperature. Circularly polarized luminescence (CPL) measurement was performed with a JASCO CPL-200S spectropolarimeter at room temperature. Dynamic light scattering (DLS) measurement was performed at room temperature on an ELS-ZA2 (Otsuka Electronics Co., Ltd.) with a semiconductor laser (50 nW) as a light source. The particle size distribution was derived using the CONTIN algorithm.

Synthesis.

2,6-Difluoro-N-(2-methoxyphenyl)-N-(2-methoxynaphthalenyl)aniline (5).

The mixture of **4** (1.16 g, 4.93 mmol), 1-iodo-2-methoxynaphthalene (1.69 g, 5.93 mmol), K_2CO_3 (1.61 g, 11.7 mmol), copper powder (0.562 g, 8.85 mmol), and 18-crown-6 (0.138 g, 0.524 mmol) was dissolved in mesitylene (8.0 mL). The mixture was stirred at 220 °C for 46 h. The insoluble materials were filtered off, and the solids were washed with CH_2Cl_2 (50 mL). After addition of 1M NH_4Cl aq. to the filtrate, the aqueous phase was extracted with CH_2Cl_2 (10 mL × 3). The organic phase was washed with water and brine, dried over Na_2SO_4 , filtered off, and concentrated under reduced pressure. The obtained crude product was purified by silica gel column chromatography (CH_2Cl_2 : hexane = 1 : 3, R_f = 0.18) to give 1.47 g (3.77 mmol) of **5** in 76% yield as white solids.

mp: 156.1–157.1 °C; ^1H NMR (500 MHz, CD_2Cl_2): δ 7.88 (d, $^3J(\text{H},\text{H})$ = 8.0 Hz, 1H), 7.82 (d, $^3J(\text{H},\text{H})$ = 9.0 Hz, 1H), 7.80 (dd, $^3J(\text{H},\text{H})$ = 7.5 Hz, $^4J(\text{H},\text{H})$ = 1.5 Hz, 1H), 7.33 (d, $^3J(\text{H},\text{H})$ = 8.5 Hz, 1H), 7.36–7.29 (m, 2H), 6.97–6.92 (m, 2H), 6.93 (td, $^3J(\text{H},\text{H})$ = 8.0 Hz, $^4J(\text{H},\text{H})$ = 1.5 Hz, 1H), 6.80 (t, $^3J(\text{H},\text{H})$ = 10.0 Hz, 1H), 6.77 (t, $^3J(\text{H},\text{H})$ = 10.0 Hz, 1H), 6.68 (ddd, $^3J(\text{H},\text{H})$ = 7.5 Hz, $^3J(\text{H},\text{H})$ = 6.5 Hz, $^4J(\text{H},\text{H})$ = 2.0 Hz, 1H), 6.57 (dd, $^3J(\text{H},\text{H})$ = 7.5 Hz, $^4J(\text{H},\text{H})$ = 1.5 Hz, 1H), 3.71 (s, 3H), 3.63 (s, 3H); ^{13}C NMR (125 MHz, CD_2Cl_2): δ 158.9 (dd, $^1J(\text{C},\text{F})$ = 248 Hz, $^3J(\text{C},\text{F})$ = 106 Hz), 154.9, 152.4, 137.7,

132.4, 130.2, 128.9, 128.4, 128.3, 126.9, 126.3 (t , $^2J(C,F) = 12.5$ Hz), 124.2, 123.6, 123.2, 123.0 (t , $^3J(C,F) = 9.5$ Hz), 122.3, 121.3, 120.5, 115.4, 112.9, 111.5 (d , $^2J(C,F) = 22.0$ Hz), 57.0, 56.2; HRMS (EI) (m/z): $[M]^+$ calcd. for $C_{24}H_{19}F_2NO_2$, 391.1384; found, 391.1393; Elemental analysis calcd (%) for $C_{24}H_{19}F_2NO_2$: C 73.65, H 4.89, N 3.58; found: C 73.74, H 4.94, N 3.72.

Naphtho[2,1-*b*][1,4]oxazino[2,3-*k*]phenoxazine (1).

5 (1.12 g, 2.87 mmol) was dissolved in dry CH_2Cl_2 (45 mL). BBr_3 (0.600 mL, 6.33 mmol) was added to the solution at -78 °C. The mixture was slowly warmed up to room temperature and further stirred for 12 h. The reaction mixture was poured into water and extracted with ethyl acetate (15 mL \times 3). The combined organic phase was washed with brine, dried over Na_2SO_4 , filtered off, and concentrated under reduced pressure to give 1.30 g of the crude product as white solids, which was used without further purification. These solids were dissolved in DMF (85 mL). After addition of K_2CO_3 (1.21 g, 8.75 mmol), the mixture was stirred at 120 °C for 24 h. The resulting insoluble materials were filtered off and washed with CH_2Cl_2 (25 mL), and the filtrate was concentrated under reduced pressure. The obtained solids were dissolved in CH_2Cl_2 (30 mL). After addition of 1M HCl aq. (30 mL), the mixture was extracted with CH_2Cl_2 (10 mL \times 3) and washed with brine. The organic phase was dried over Na_2SO_4 , filtered off, and concentrated under reduced pressure. The obtained crude product was dissolved in CH_2Cl_2 . After passed through a short pad of silica gel, the crude product was purified by silica gel column chromatography (CH_2Cl_2 : hexane = 1 : 3, $R_f = 0.64$) to give 855 mg (2.64 mmol) of **1** in 92% yield as yellow solids.

mp: 182.1–183.1 °C; 1H NMR (500 MHz, $CDCl_3$): δ 7.78 (d, $^3J(H,H) = 8.0$ Hz, 1H), 7.57 (d, $^3J(H,H) = 9.0$ Hz, 1H), 7.44 (d, $^3J(H,H) = 8.1$ Hz, 1H), 7.37 (td, $^3J(H,H) = 7.0$ Hz, $^4J(H,H) = 1.0$ Hz, 1H), 7.29 (td, $^3J(H,H) = 7.0$ Hz, $^4J(H,H) = 1.0$ Hz, 1H), 7.15 (d, $^3J(H,H) = 9.0$ Hz, 1H), 7.06 (dd, $^3J(H,H) = 8.0$ Hz, $^4J(H,H) = 1.5$ Hz, 1H), 6.95 (td, $^3J(H,H) = 7.5$ Hz, $^4J(H,H) = 1.0$ Hz, 1H), 6.86 (t, $^3J(H,H) = 8.0$ Hz, 1H), 6.85 (td, $^3J(H,H) = 7.5$ Hz, $^4J(H,H) = 1.0$ Hz, 2H), 6.68 (dd, $^3J(H,H) = 8.0$ Hz, $^4J(H,H) = 1.0$ Hz, 1H), 6.60 (dd, $^3J(H,H) = 8.0$ Hz, $^4J(H,H) = 1.5$ Hz, 1H), 6.42 (dd, $^3J(H,H) = 8.0$ Hz, $^4J(H,H) = 1.5$ Hz, 1H); ^{13}C NMR (125 MHz, $CDCl_3$): δ 148.6, 148.1, 146.3, 145.4, 134.4, 131.4, 128.5, 125.7, 125.3, 124.8, 124.6, 124.0, 123.9, 123.7, 123.1, 122.7, 119.9, 117.7, 117.0, 115.9, 111.5, 111.0; HRMS (EI) (m/z): $[M]^+$ calcd. for $C_{22}H_{13}NO_2$, 323.0946; found, 323.0943; Elemental analysis calcd (%) for $C_{22}H_{13}NO_2$: C 81.72, H 4.05, N 4.33; found: C 81.45, H 4.06, N 4.24.

4-Formylnaphtho[2,1-*b*][1,4]oxazino[2,3,4-*k*l]phenoxazine (2).

Phosphoryl chloride (940 μ L, 10.1 mmol) was added to dry DMF (2 mL) at 0 °C and the solution was stirred for 15 min. **1** (163 mg, 0.505 mmol) was dissolved in dry C₂H₄Cl₂ (2 mL). The DMF solution was added to the C₂H₄Cl₂ solution. The mixture was heated at 75 °C for 6 h. The reaction mixture was neutralized by sat. Na₂CO₃aq. (40 mL), and extracted with CH₂Cl₂ (20 mL \times 3). The organic phase was washed with brine, dried over Na₂SO₄, filtered off, and concentrated under reduced pressure. The obtained crude product was purified by silica gel column chromatography (CH₂Cl₂ : hexane = 1 : 2, *R*_f = 0.10) to give 142 mg (0.405 mmol) of **2** in 80% yield as orange solids.

mp: 177.7–178.7 °C; ¹H NMR (500 MHz, CD₂Cl₂): δ 10.27 (s, 1H), 9.17 (d, ³J(H,H) = 8.0 Hz, 1H), 7.65 (s, 1H), 7.57 (td, ³J(H,H) = 8.0 Hz, ⁴J(H,H) = 1.5 Hz, 1H), 7.56 (dd, ³J(H,H) = 8.5 Hz, ⁴J(H,H) = 1.5 Hz, 1H), 7.36 (td, ³J(H,H) = 8.0 Hz, ⁴J(H,H) = 1.5 Hz, 1H), 7.10 (dd, ³J(H,H) = 8.0 Hz, ⁴J(H,H) = 1.0 Hz, 1H), 7.03 (td, ³J(H,H) = 8.0 Hz, ⁴J(H,H) = 1.5 Hz, 1H), 6.94 (t, ³J(H,H) = 8.0 Hz, 1H), 6.87 (td, ³J(H,H) = 8.0 Hz, ⁴J(H,H) = 1.0 Hz, 1H), 6.72 (d, ³J(H,H) = 8.0 Hz, 1H), 6.65 (d, ³J(H,H) = 8.5 Hz, 1H), 6.46 (d, ³J(H,H) = 8.0 Hz, 1H); ¹³C NMR (125 MHz, CD₂Cl₂): δ 191.2, 149.0, 148.1, 145.7, 145.6, 133.3, 129.9, 128.5, 128.1, 127.5, 126.6, 126.2, 125.5, 125.4, 124.9, 124.4, 124.3, 123.6, 123.0, 117.7, 116.9, 112.2, 111.5; HRMS (FAB) (*m/z*): [M]⁺ calcd. for C₂₃H₁₃NO₃, 351.0895; found, 351.0895; Elemental analysis calcd (%) for C₂₃H₁₃NO₃: C 78.62, H 3.73, N 3.99; found: C 78.44, H 3.91 N 3.97.

4-(2,2-Dicyanovinyl)naphtho[2,1-*b*][1,4]oxazino[2,3,4-*k*l]phenoxazine (3).

2 (26.9 mg, 0.0766 mmol) and malononitrile (14.1 mg, 0.213 mmol) were dissolved in dry CHCl₃ (7.5 mL). NEt₃ (24 μ L) was added to the solution and the mixture was stirred at room temperature for 5 h. The obtained crude products were absorbed on silica gel and purified by silica gel column chromatography (CH₂Cl₂ : hexane = 1 : 1, *R*_f = 0.25) to give 27.9 mg (0.0699 mmol) of **3** in 91% yield as purple solids.

mp: 290.4–291.4 °C; ¹H NMR (500 MHz, CD₂Cl₂): δ 8.54 (s, 1H), 8.09 (s, 1H), 7.99 (d, ³J(H,H) = 8.5 Hz, 1H), 7.59 (d, ³J(H,H) = 8.5 Hz, 1H), 7.58 (td, ³J(H,H) = 8.0 Hz, ⁴J(H,H) = 1.5 Hz, 1H), 7.37 (td, ³J(H,H) = 8.0 Hz, ⁴J(H,H) = 1.0 Hz, 1H), 7.11 (dd, ³J(H,H) = 8.0 Hz, ⁴J(H,H) = 2.0 Hz, 1H), 7.06 (td, ³J(H,H) = 8.0 Hz, ⁴J(H,H) = 2.0 Hz, 1H), 6.96 (t, ³J(H,H) = 8.5 Hz, 1H), 6.89 (td, ³J(H,H) = 8.0 Hz, ⁴J(H,H) = 2.0 Hz, 1H), 6.74 (dd, ³J(H,H) = 8.5 Hz, ⁴J(H,H) = 1.0 Hz, 1H), 6.68 (dd, ³J(H,H) = 8.0 Hz, ⁴J(H,H) = 1.0 Hz, 1H), 6.46 (dd, ³J(H,H) = 8.0 Hz, ⁴J(H,H) = 2.0 Hz, 1H); ¹³C NMR (125 MHz, CDCl₃): δ 153.9, 148.6, 147.5, 145.4, 145.0, 132.2, 130.5, 128.2, 127.6, 126.0, 125.4, 125.0, 124.5, 124.0, 123.34, 123.30, 122.7, 122.0, 118.9, 117.7, 116.7, 114.4, 113.1,

112.1, 111.4, 81.6; HRMS (FAB) (*m/z*): [M]⁺ calcd. for C₂₆H₁₃N₃O₂, 399.1008; found, 399.1008; Elemental analysis calcd (%) for C₂₆H₁₃N₃O₂: C 78.19, H 3.28, N 10.52; found: C 77.91, H 3.58, N 10.15.

Computation Method.

DFT calculations for optimization of the geometries and estimation of inversion barrier as well as TD-DFT calculations for transitions and optimization of the excited states were conducted using the Gaussian 09 program.¹⁶

X-Ray Crystal Structure Analysis.

Crystallographic data have been deposited with the Cambridge Crystallographic Data Center as supplementary publication no. CCDC-1451626 (racemic **1** (*rac-1*)), CCDC-1451627 (enantiomerically pure **1** (*ena-1*)), CCDC-1451628 (racemic **2** (*rac-2*)), and CCDC-1451629 (enantiomerically pure **2** (*ena-2*)). These data can be obtained free of charge from The Cambridge Crystallographic Data Centre via www.ccdc.cam.ac.uk/data_request/cif.

Racemic 1. Single crystals suitable for X-ray analysis were obtained by diffusion of hexane into a solution of racemic mixture *rac-1* in CH₂Cl₂. Intensity data were collected at 103 K using a diffractometer equipped with an ADSC Quantun315 CCD detector with synchrotron radiation at a wavelength of 0.85 Å at the SPring-8 beamline BL38B1. The collected diffraction data were processed with the HKL2000 software program. A total of 27055 reflections were measured with a maximum 2θ angle of 62.0°, of which 5383 were independent reflections ($R_{\text{int}} = 0.0346$). The structure was solved by direct methods (SHELXS-97¹⁷) and refined by the full-matrix least-squares on F^2 (SHELXL-97¹⁷). All non-hydrogen atoms were refined anisotropically. All hydrogen atoms were placed using AFIX instructions. The crystal data are as follows: C₂₂H₁₃NO₂; FW = 323.33, crystal size 0.03 × 0.02 × 0.02 mm³, Monoclinic, *P*2₁/*c*, *a* = 9.95060(10) Å, *b* = 28.1717(2) Å, *c* = 11.23010(10) Å, β = 111.0381(3)°, *V* = 2938.24(4) Å³, *Z* = 8, *D*_c = 1.462 g cm⁻³. The refinement converged to $R_1 = 0.0407$, wR₂ = 0.1072 (*I* > 2σ(*I*)), GOF = 1.018.

Enantiomerically pure 1. Single crystal suitable for X-ray analysis were obtained by diffusion of hexane into a solution of enantiomerically pure *ena-1* in CH₂Cl₂. Intensity data were collected at 100 K on a Bruker Single Crystal CCD X-ray Diffractometer (SMART APEX) with Mo Kα radiation (λ = 0.71073 Å) and graphite monochromater.

A total of 5388 reflections were measured with a maximum 2θ angle of 50.1° , of which 2614 were independent reflections ($R_{\text{int}} = 0.0417$). The structure was solved by direct methods (SHELXS-97¹⁷) and refined by the full-matrix least-squares on F^2 (SHELXL-97¹⁷). All non-hydrogen atoms were refined anisotropically. All hydrogen atoms were placed using AFIX instructions. The crystal data are as follows: $\text{C}_{22}\text{H}_{13}\text{NO}_2$; FW = 323.33, crystal size $0.30 \times 0.10 \times 0.10 \text{ mm}^3$, Monoclinic, $P2_1$, $a = 9.5876(12) \text{ \AA}$, $b = 4.9235(6) \text{ \AA}$, $c = 15.7998(19) \text{ \AA}$, $\beta = 93.660(2)^\circ$, $V = 744.30(16) \text{ \AA}^3$, $Z = 2$, $D_c = 1.443 \text{ g cm}^{-3}$. The refinement converged to $R_1 = 0.0512$, $wR_2 = 0.0881$ ($I > 2\sigma(I)$), GOF = 1.031.

Because of the presence of only light atoms in the crystal structure, the absolute structure of *ena-1* could not be determined unequivocally. Therefore the author estimated the absolute structures of *ena-1* in each fraction to be (*P*)-helix obtained from the first fraction and (*M*)-helix from the second fraction on the basis of CD spectra and results of TD-DFT calculations.

Racemic 2. Single crystals suitable for X-ray analysis were obtained by slow evaporation of racemic mixture *rac-2* in hexane. Intensity data were collected at 100 K on a Bruker Single Crystal CCD X-ray Diffractometer (SMART APEXII) with Mo K α radiation ($\lambda = 0.71073 \text{ \AA}$) and graphite monochromater. A total of 7711 reflections were measured with a maximum 2θ angle of 51.0° , of which 2983 were independent reflections ($R_{\text{int}} = 0.0549$). The structure was solved by direct methods (SHELXS-97¹⁷) and refined by the full-matrix least-squares on F^2 (SHELXL-97¹⁷). All non-hydrogen atoms were refined anisotropically. All hydrogen atoms were placed using AFIX instructions. The crystal data are as follows: $\text{C}_{23}\text{H}_{13}\text{NO}_3$; FW = 351.34, crystal size $0.16 \times 0.06 \times 0.04 \text{ mm}^3$, Monoclinic, $C2/c$, $a = 25.150(6) \text{ \AA}$, $b = 7.0195(17) \text{ \AA}$, $c = 20.374(5) \text{ \AA}$, $\beta = 116.883(3)^\circ$, $V = 3208.1(13) \text{ \AA}^3$, $Z = 8$, $D_c = 1.455 \text{ g cm}^{-3}$. The refinement converged to $R_1 = 0.0651$, $wR_2 = 0.1361$ ($I > 2\sigma(I)$), GOF = 1.060.

Enantiomerically pure 2. Single crystals suitable for X-ray analysis were obtained by diffusion of hexane into a solution of *ena-2* in CH_2Cl_2 . Intensity data were collected at 100 K on a Bruker Single Crystal CCD X-ray Diffractometer (SMART APEXII) with Mo K α radiation ($\lambda = 0.71073 \text{ \AA}$) and graphite monochromater. A total of 7702 reflections were measured with a maximum 2θ angle of 51.0° , of which 2871 were independent reflections ($R_{\text{int}} = 0.0423$). The structure was solved by direct methods (SHELXS-97¹⁷) and refined by the full-matrix least-squares on F^2 (SHELXL-97¹⁷). All non-hydrogen atoms were refined anisotropically. All hydrogen atoms were placed

using AFIX instructions. The crystal data are as follows: C₂₃H₁₃NO₃; FW = 351.34, crystal size 0.40 × 0.08 × 0.04 mm³, Orthorhombic, P2₁2₁2₁, $a = 4.8751(11)$ Å, $b = 12.299(3)$ Å, $c = 26.050(6)$ Å, $V = 1560.8(6)$ Å³, $Z = 4$, $D_c = 1.495$ g cm⁻³. The refinement converged to $R_1 = 0.0370$, $wR_2 = 0.0605$ ($I > 2\sigma(I)$), GOF = 1.054.

Because of the presence of only light atoms in the crystal structure, the absolute structure of *ena*-**2** could not be determined unequivocally. Therefore the author estimated the absolute structures of *ena*-**2** in each fraction to be (*P*)-helix obtained from first fraction and (*M*)-helix from the second fraction on the basis of CD spectra and results of TD-DFT calculations.

Preparation of Dispersion in Water

The solid-state chiroptical properties were measured using the dispersions of enantiomerically pure compounds **1–3** in water that could be prepared by rapid reprecipitation method.¹² This method is effective for preparing the particles of organic compounds, and the obtained suspension can be used for the measurement of the solid-state properties with keeping relative concentrations, which enables quantitative analysis similarly to a solution sample. By injection of enantiomerically pure compounds **1–3** in THF (10⁻³ M, 100 µL) into vigorously stirred degassed water (10 mL), nanoparticles of **1–3** were prepared as dispersions in water. The sizes of the nanoparticles of **1–3** were determined by dynamic light scattering (DLS) measurements. The averaged particle sizes of **1–3** were determined to be 138 nm, 104 nm, and 69 nm, respectively (Figure 12).

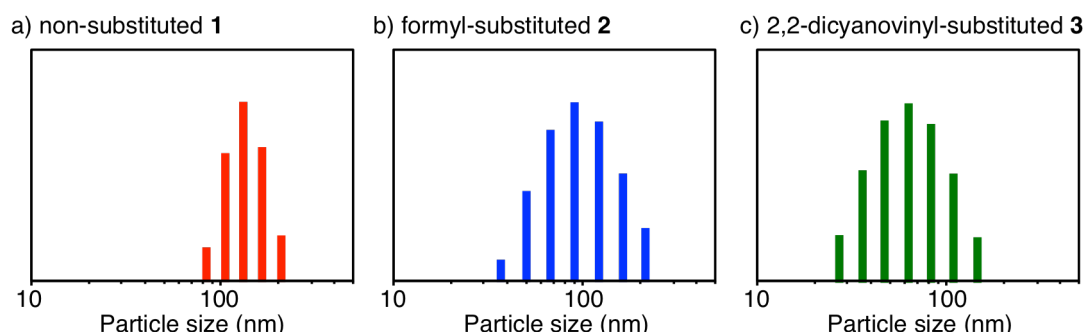


Figure 12. Particle size distributions of dispersion of a) **1**, b) **2**, and c) **3** in water determined by dynamic light scattering measurements.

Solvent Dependency in Fluorescence

In order to examine the ICT character of **1–3** experimentally, their absorption and fluorescence were examined in a variety of solvents (Figure 12–14, Table 3–5). In the absorption spectra, although compounds **1** and **2** show solvent dependences in some degree, they are very small compared to those for **3**. In the case of **3**, red-shifts for the absorption bands were observed with increasing of solvent polarity from cyclohexane (dielectric constant ϵ : 2.017) to chloroform (ϵ : 4.711). In contrast, the absorption bands are blue-shifted in the solvent with polarities higher than chloroform. These phenomena may be rationalized in terms of the back electron transfer in polar solvents.¹⁸

In fluorescence spectra, however, all of **1–3** show significant red-shifts of the emission bands in the solvent with higher polarity (Figure 13–15, Table 3–5). In cyclohexane, emission colors of **1–3** are blue ($\lambda_{\text{em}} = 459$ nm), light green (520 nm), and red (608 nm), respectively. In polar solvents, such as CH₃CN or DMSO, emission colors of **1–3** are green ($\lambda_{\text{em}} = 500$ nm in DMSO), red (600 nm in DMSO) and deep-red (706 nm in CH₃CN), respectively.

The solvent dependency of the absorption and the emission shows that the solvent effects are very strong at the excited S₁ states, clearly indicating the ICT characters at the S₁ states. Such ICT characters are observed distinctly in the emission spectra rather than the absorption spectra. An excited species, i.e., the Frank-Condon state, generated just after absorption of light would undergo structural relaxation to the most stable S₁ excited state, which would interact with polar solvent strongly, resulting in emission with solvent dependency accompanied by a large Stokes shift.

Fluorescence quantum yields and fluorescence lifetimes of **1–3** are also summarized in Table 3–5. Non-substituted **1** exhibits high or good fluorescence quantum yields ($\Phi = 0.86$ –0.57) with long lifetimes ($\tau = 17.9$ –31.2 ns) in all solvents. In contrast, formyl derivative **2** and 2,2-dicyanovinyl derivative **3** show solvent dependency on the quantum yields of emission. In cyclohexane, **2** and **3** exhibited high quantum yields of $\Phi = 0.96$ and 0.63, respectively, whereas the quantum yields were decreased with increasing solvent polarities (**2**: $\Phi = 0.11$ (DMSO), **3**: $\Phi = 0.02$ (CH₃CN)), accompanied with shortened fluorescence lifetime. The non-radiative rate constants of k_{nr} of **2** and **3** significantly increase as emission wavelengths red-shift, which is mainly attributed to decreasing fluorescence quantum yields in the polar solvents. These phenomena are usually seen for other small organic molecules.¹⁹

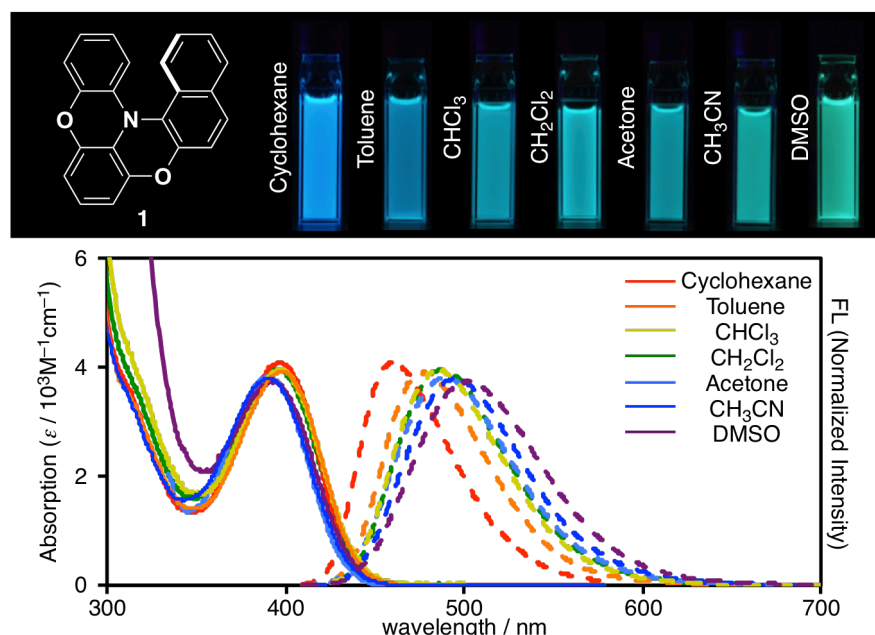


Figure 13. Photographs of emission (top) and UV-vis absorption (solid) and fluorescence (dashed) spectra (bottom) for **1** in various solvents.

Table 3. Photophysical Properties of **1 in Various Solvents**

Solvent	λ_{abs} [nm] (log ϵ)	λ_{em} [nm]	Stokes Shift [cm ⁻¹]	Φ	τ [ns]	k_r [10 ⁷ s ⁻¹]	k_{nr} [10 ⁷ s ⁻¹]
Cyclohexane	396 (3.61)	459	3466	0.68	19.2	3.5	1.7
Toluene	398 (3.59)	478	4205	0.80	21.3	3.8	0.94
CHCl ₃	396 (3.60)	485	4634	0.57	17.9	3.2	2.4
CH ₂ Cl ₂	395 (3.60)	488	4825	0.86	25.4	3.4	0.55
Acetone	392 (3.58)	490	5102	0.79	27.5	2.9	0.76
CH ₃ CN	392 (3.58)	496	5349	0.81	31.2	2.6	0.61
DMSO	394 (3.57)	500	5381	0.81	27.0	3.0	0.70

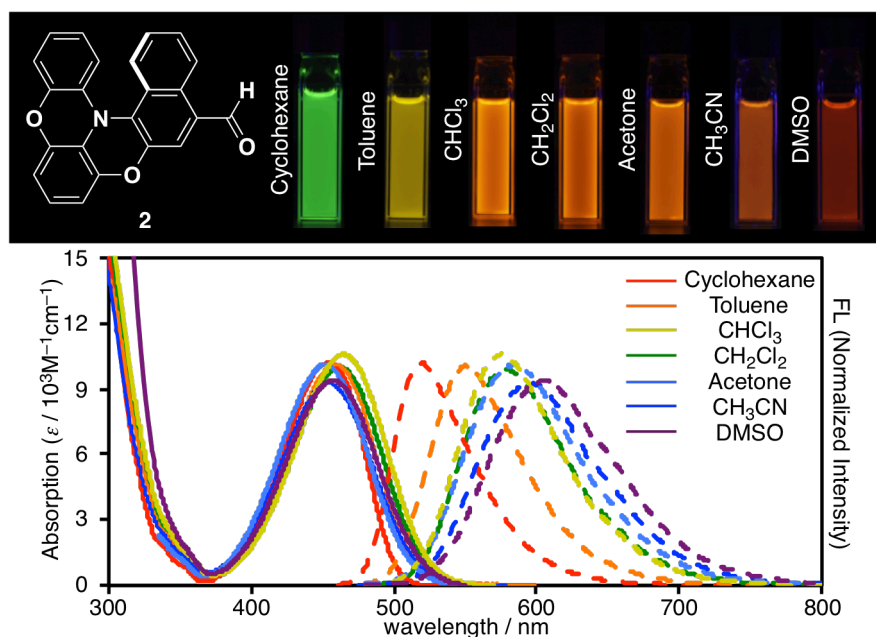


Figure 14. Photographs of emission (top) and UV-vis absorption (solid) and fluorescence (dashed) spectra (bottom) for **2** in various solvents.

Table 4. Photophysical Properties of **2 in Various Solvents**

Solvent	λ_{abs} [nm] (log ε)	λ_{em} [nm]	Stokes Shift [cm ⁻¹]	Φ	τ [ns]	k_r [10 ⁷ s ⁻¹]	k_{nr} [10 ⁷ s ⁻¹]
Cyclohexane	453 (4.01)	520	2444	0.96	12.7	7.6	0.32
Toluene	459 (4.01)	550	3605	0.75	11.9	6.3	2.1
CHCl ₃	464 (4.02)	575	4160	0.45	7.26	6.2	7.6
CH ₂ Cl ₂	461 (4.00)	580	4451	0.44	6.76	6.5	8.3
Acetone	452 (4.00)	584	5001	0.20	4.15	4.8	19
CH ₃ CN	455 (3.97)	595	5171	0.14	2.78	5.0	31
DMSO	457 (3.97)	603	5298	0.11	1.95	5.6	46

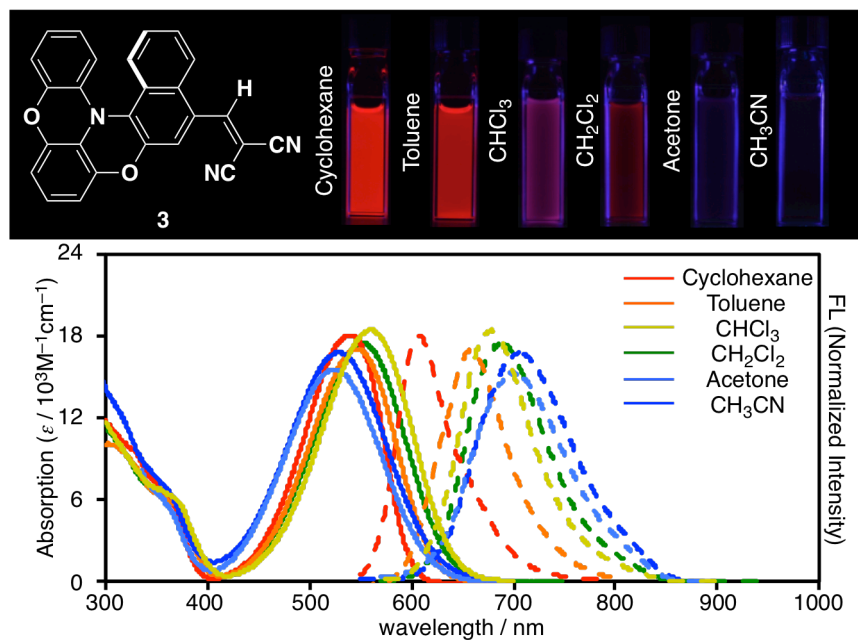


Figure 15. Photographs of emission (top) and UV-vis absorption (solid) and fluorescence (dashed) spectra (bottom) for **3** in various solvents.

Table 5. Photophysical Properties of 3 in Various Solvents

Solvent	λ_{abs} [nm] ($\log \varepsilon$)	λ_{em} [nm]	Stokes Shift [cm^{-1}]	Φ	τ [ns]	k_r [10^7s^{-1}]	k_{nr} [10^7s^{-1}]
Cyclohexane	539 (4.26)	608	2106	0.63	6.66	9.5	5.6
Toluene	548 (4.23)	657	3027	0.29	3.37	8.6	21
CHCl_3	559 (4.27)	678	3140	0.15	1.77	8.5	48
CH_2Cl_2	552 (4.24)	685	3517	0.09	1.16	7.8	78
Acetone	525 (4.19)	701	4782	0.03	0.42	7.1	230
CH_3CN	530 (4.22)	706	4701	0.02	0.36	5.6	270

The change in dipole moments from the ground state to the excited state ($\mu_e - \mu_g = \Delta\mu$) for **1–3** were estimated by the Lippert-Mataga plot [Eq. (1)],¹⁵ in which C is a constant, ϵ_0 ($= 8.854 \times 10^{-12}$ F/m) is the permittivity of vacuum, h ($= 6.626 \times 10^{-34}$ J/s) is the Planck's constant, c (2.9979×10^{10} cm/s) is the speed of light, a is the radius of the cavity, μ_e and μ_g are the dipole moments in the excited state and ground state, respectively, and $\Delta\nu$ is the Stokes shift. In the Eq. (2), the function of orientation polarizability is defined as Δf , in which ϵ is the dielectric constant of the solvent and n is the optional refractive constant of the solvent. The values for the radius of the cavity (a) were determined by DFT calculations (B3LYP/6-31G(d)) as 5.36 Å for **1**, 5.30 Å for **2**, and 5.65 Å for **3**, respectively. All of **1–3** show good linear correlations between the Stokes shifts and Δf values depending on the solvents (Figure 16). Accordingly, $\Delta\mu$ values of **1–3** are determined to be 8.8, 10.0 and 11.4 D, respectively. These results suggest that **1–3** have intramolecular charge transfer character especially in the excited state, facilitating significant red-shift of emission to realize large variation in emission colors covering the whole visible region.

$$\Delta\nu = \nu_{abs} - \nu_{FL} = \Delta f(\mu_e - \mu_g)/2\epsilon_0 h c a^3 + C \quad (1)$$

$$\Delta f = (\epsilon - 1)/(2\epsilon + 1) - (n^2 - 1)/(2n^2 + 1) \quad (2)$$

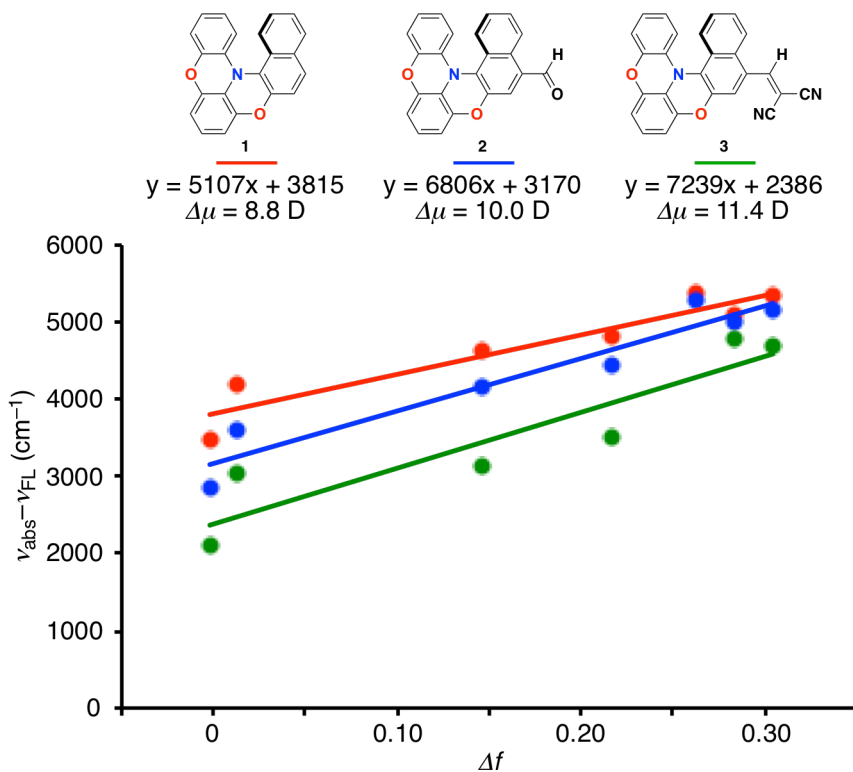


Figure 16. The Lippert-Mataga plots for **1–3**.

Reference

1. (a) Riehl, J. P.; Richardson, F. S.; *J. Chem. Phys.* **1976**, *65*, 1011. (b) Richardson, F. S.; Riehl, J. P. *Chem. Rev.* **1977**, *77*, 773. (c) Riehl, J. P. *Chem. Rev.* **1986**, *86*, 1.
2. (a) Dyreklev, P.; Berggren, M.; Inganäs, O.; Andersson, M. R.; Wennerström, O.; Hjertberg, T. *Adv. Mater.* **1995**, *7*, 43. (b) Schadt, M. *Annu. Rev. Mater. Sci.* **1997**, *27*, 305. (c) Peeters, E.; Christiaans, M. P. T.; Janssen, R. A. J.; Schoo, H. F. M.; Dekkers, H. P. J. M.; Meijer, E. W. *J. Am. Chem. Soc.* **1997**, *119*, 9909. (d) Montali, A.; Bastiaansen, C.; Smith, P.; Weder, C. *Nature* **1998**, *392*, 261. (e) Chen, S. H.; Katsis, D.; Schmid, A. W.; Mastrangelo, J. C.; Tsutsui, T.; Blanton, T. N. *Nature* **1999**, *397*, 506. (f) Grell, M.; Oda, M.; Whitehead, K. S.; Asimakis, A.; Neher, D.; Bradley, D. D. C. *Adv. Mater.* **2001**, *13*, 577.
3. (a) Furumi, S. *Chem. Rec.* **2010**, *10*, 394. (b) Topf, R. D. M.; McCall, M. W. *Phys. Rev. A* **2014**, *90*, 053824.
4. (a) Li, Z.-B.; Sabat, M.; Hyacinth, M.; Pu, L. *J. Org. Chem.* **2007**, *72*, 4905. (b) Muller, G. *Dalton Trans.* **2009**, 9692. (c) Liu, N.-N.; Song, S.; Li, D.-M.; Zheng, Y.-S. *Chem. Commun.* **2012**, *48*, 4908. (d) Yuasa, J.; Ohno, T.; Tsumatori, H.; Shiba, R.; Kamikubo, H.; Kataoka, M.; Hasegawa, Y.; Kawai, T. *Chem. Commun.* **2013**, *49*, 4604.
5. (a) Feringa, B. L.; van Delden, R. A. *Angew. Chem., Int. Ed.* **1999**, *38*, 3418. (b) Sato, I.; Yamashita, R.; Kadowaki, K.; Yamamoto, J.; Shibata, T.; Soai, K. *Angew. Chem., Int. Ed.* **2001**, *40*, 1096. (c) Podlech, J.; Gehring, T. *Angew. Chem., Int. Ed.* **2005**, *44*, 5776. (d) Kawasaki, T.; Soai, K. *Bull. Chem. Soc. Jpn.* **2011**, *84*, 879.
6. (a) Emeis, C. A.; Oosterhoff, L. J. *Chem. Phys. Lett.* **1967**, *1*, 129. (b) Steinberg, N.; Gafni, A.; Steinberg, I. Z. *J. Am. Chem. Soc.* **1981**, *103*, 1636. (c) Schippers, P. H.; van der Pleog, J. P. M.; Dekkers, H. P. J. M. *J. Am. Chem. Soc.* **1983**, *105*, 84. (d) Gossauer, A.; Fehr, F.; Nydegger, F.; Stöckli-Evans, H. *J. Am. Chem. Soc.* **1997**, *119*, 1599. (e) Field, J. E.; Muller, G.; Riehl, J. P.; Venkataraman, D. *J. Am. Chem. Soc.* **2003**, *125*, 11808. (f) Tsumatori, H.; Nakanishi, T.; Kawai, T. *Org. Lett.* **2010**, *12*, 2362. (g) Ikeda, T.; Masuda, T.; Hirao, T.; Yuasa, J.; Tsumatori, H.; Kawai, T.; Haino, T. *Chem. Commun.* **2012**, *48*, 6025. (h) Liu, J.; Su, H.; Meng, L.; Zhao, Y.; Deng, C.; Ng, J. C. Y.; Lu, P.; Faisal, M.; Lam, J. W. Y.; Huang, X.; Wu, H.; Wong, K. S.; Tang, B. Z. *Chem. Sci.* **2012**, *3*, 2737. (i) Kinuta, T.; Tajima, N.; Fujiki, M.; Miyazawa, M.; Imai, Y. *Tetrahedron* **2012**, *68*, 4791. (j) Sawada, Y.; Furumi, S.; Takai, A.; Takeuchi, M.; Noguchi, K.; Tanaka, K. *J. Am. Chem. Soc.* **2012**, *134*, 4080. (k) Goto, K.; Yamaguchi, R.; Hiroto, S.; Ueno, H.; Kawai, T.; Shinokubo, H. *Angew. Chem., Int. Ed.* **2012**, *51*, 10333. (l) Kimoto, T.; Amako,

- T.; Tajima, N.; Kuroda, R.; Fujiki, M.; Imai, Y. *Asian J. Org. Chem.* **2013**, *2*, 404. (m) Oyama, H.; Nakano, K.; Harada, T.; Kuroda, R.; Naito, M.; Nobusawa, K.; Nozaki, K. *Org. Lett.* **2013**, *15*, 2104. (n) Amako, T.; Kimoto, T.; Tajima, N.; Fujiki, M.; Imai, Y. *Tetrahedron* **2013**, *69*, 2753. (o) Sánchez-Carnerero, E. M.; Moreno, F.; Maroto, B. L.; Agarrabeitia, A. R.; Ortiz, M. J.; Bo, B. G.; Muller, G.; de la Moya, S. *J. Am. Chem. Soc.* **2014**, *136*, 3346. (p) Morisaki, Y.; Gon, M.; Sasamori, T.; Tokitoh, N.; Chujo, Y. *J. Am. Chem. Soc.* **2014**, *136*, 3350. (q) Nakamura, K.; Furumi, S.; Takeuchi, M.; Shibuya, T.; Tanaka, K. *J. Am. Chem. Soc.* **2014**, *136*, 5555. (r) Sundar, M. S. Talele, H. R.; Mande, H. M.; Bedekar, A. V.; Tovar, R. C.; Muller, G. *Tetrahedron Lett.* **2014**, *55*, 1760. (s) Kitayama, Y.; Amako, T.; Suzuki, N.; Fujiki, M.; Imai, Y. *Org. Biomol. Chem.* **2014**, *12*, 4342. (t) Amako, T.; Nakabayashi, K.; Mori, T.; Inoue, Y.; Fujiki, M.; Imai, Y. *Chem. Commun.* **2014**, *50*, 12836. (u) Kitayama, Y.; Nakabayashi, K.; Wakabayashi, T.; Tajima, N.; Fujiki, M.; Imai, Y. *RSC Adv.* **2015**, *5*, 410. (v) Gon, M.; Morisaki, Y.; Chujo, Y. *J. Mater. Chem. C* **2015**, *3*, 521. (w) Sakai, H.; Shinto, S.; Kumar, J.; Araki, Y.; Sakanoue, T.; Takenobu, T.; Wada, T.; Kawai, T.; Hasobe, T. *J. Phys. Chem. C* **2015**, *119*, 13937. (x) Matsuno, T.; Koyama, Y.; Hiroto, S.; Kumar, J.; Kawai, T.; Shinokubo, H. *Chem. Commun.* **2015**, *51*, 4607. (y) Zhang, S.; Wang, Y.; Meng, F.; Dai, C.; Cheng, Y.; Zhu, C. *Chem. Commun.* **2015**, *51*, 9014. (z) Imagawa, T.; Hirata, S.; Totani, K.; Watanabe, T.; Vacha, M. *Chem. Commun.* **2015**, *51*, 13268.
7. (a) Langeveld-Voss, B. M. W.; Janssen, R. A.; Christiaans, M. P. T.; Meskers, S. C. J.; Dekkers, H. P. J. M.; Meijer, E. W. *J. Am. Chem. Soc.* **1996**, *118*, 4908. (b) Oda, M.; Nothofer, H.-G.; Lieser, G.; Scherf, U.; Meskers, S. C. J.; Neher, D. *Adv. Mater.* **2000**, *12*, 362. (c) Wilson, J. N.; Steffen, W.; McKenzie, T. G.; Lieser, G.; Oda, M.; Neher D.; Bunz, U. H. F. *J. Am. Chem. Soc.* **2002**, *124*, 6830. (d) Goto, H.; Akagi, K. *Angew. Chem., Int. Ed.* **2005**, *44*, 4322. (e) Satrijio, A.; Meskers, S. C. J.; Swager, T. M. *J. Am. Chem. Soc.* **2006**, *128*, 9030. (f) Fukao, S.; Fujiki, M. *Macromolecules* **2009**, *42*, 8062. (g) Nakano, Y.; Liu, Y.; Fujiki, M. *Polym. Chem.* **2010**, *1*, 460. (h) Watanabe, K.; Sakamoto, T.; Taguchi, M.; Fujiki, M.; Nakano, T. *Chem. Commun.* **2011**, *47*, 10996. (i) Morisaki, Y.; Hifumi, R.; Lin, L.; Inoshita, K.; Chujo, Y. *Polym. Chem.* **2012**, *3*, 2727. (j) Watanabe, K.; Osaka, I.; Yorozuya, S.; Akagi, K. *Chem. Mater.* **2012**, *24*, 1011. (k) Ma, X.; Azeem, E. A.; Liu, X.; Cheng, Y.; Zhu, C. *J. Mater. Chem. C* **2014**, *2*, 1076. (l) Zhang, S.; Sheng, Y.; Wei, G.; Quan, Y.; Cheng, Y.; Zhu, C. *Polym. Chem.* **2015**, *6*, 2416. (m) Li, F.; Wang, Y.; Wang, Z.; Cheng, Y.; Zhu, C. *Polym. Chem.* **2015**, *6*, 6802.

8. (a) Meskers, S. C. J.; Dekkers, H. P. J. M.; Rapenne, G.; Sauvage, J.-P. *Chem.–Eur. J.* **2000**, *6*, 2129. (b) Schaffner-Hamann, C.; von Zelewsky, A.; Barbieri, A.; Barigelli, F.; Muller, G.; Riehl, J. P.; Neels, A. *J. Am. Chem. Soc.* **2004**, *126*, 9339. (c) Oyler, K. D.; Coughlin, F. J.; Bernhard, S. *J. Am. Chem. Soc.* **2006**, *128*, 210.
9. (a) de Bettencourt-Dias, A. *J. Am. Chem. Soc.* **2007**, *129*, 15436. (b) Lunkley, J. L.; Shirotani, D.; Yamanari, K.; Kaizaki, S.; Muller, G. *J. Am. Chem. Soc.* **2008**, *130*, 13814. (c) Seitz, M.; Do, K.; Ingram, A. J.; Moore, E. G.; Muller, G.; Raymond, K. N. *Inorg. Chem.* **2009**, *48*, 8469. (d) Harada, T.; Nakano, Y.; Fujiki, M.; Naito, M.; Kawai, T.; Hasegawa, Y. *Inorg. Chem.* **2009**, *48*, 11242. (e) Samuel, A. P. S.; Lunkley, J. L.; Muller, G.; Raymond, K. N. *Eur. J. Inorg. Chem.* **2010**, 3343. (f) Bozoklu, G.; Marchal, C.; Gateau, C.; Pécaut, J.; Imbert, D.; Mazzanti, M. *Chem.–Eur. J.* **2010**, *16*, 6159. (g) Yuasa, J.; Ohno, T.; Miyata, K.; Tsumatori, H.; Hasegawa, Y.; Kawai, T. *J. Am. Chem. Soc.* **2011**, *133*, 9892. (h) Kitchen, J. A.; Barry, D. E.; Mercs, L.; Albrecht, M.; Peacock, R. D.; Gunnlaugsson, T. *Angew. Chem., Int. Ed.* **2012**, *51*, 704. (i) Yuasa, J.; Ohno, T.; Tsumatori, H.; Shiba, R.; Kamikubo, H.; Kataoka, M.; Hasegawa, Y.; Kawai, T. *Chem. Commun.* **2013**, *49*, 4604. (j) Yuasa, J.; Ueno, H.; Kawai, T. *Chem.–Eur. J.* **2014**, *20*, 8621.
10. Wakamiya, A.; Nishimura, H.; Fukushima, T.; Suzuki, F.; Saeki, A.; Seki, S.; Osaka, I.; Sasamori, T.; Murata, M.; Murata, Y.; Kaji, H. *Angew. Chem. Int. Ed.* **2014**, *53*, 5800.
11. Yamamoto, T.; Toyota, K.; Morita, N. *Tetrahedron Lett.* **2010**, *51*, 1364.
12. (a) Kasai, H.; Nalwa, H. S.; Oikawa, H.; Okada, S.; Matsuda, H.; Minami, N.; Kakuta, A.; Ono, K.; Mukoh, A.; Nakanishi, H. *Jpn. J. Appl. Phys.* **1992**, *31*, L1132. (b) Kasai, H.; Kamatani, H.; Okada, S.; Oikawa, H.; Matsuda, H.; Nakanishi, H. *Jpn. J. Appl. Phys.* **1996**, *35*, L221. (c) Kasai, H.; Oikawa, H.; Okada, S.; Nakanishi, H. *Bull. Chem. Soc. Jpn.* **1998**, *71*, 2597.
13. (a) Affeldt, R. F.; Iglesias, R. S.; Rodembusch, F. S.; Russowsky, D. *J. Phys. Org. Chem.* **2012**, *25*, 769. (b) Cui, X.; Charaf-Eddin, A.; Wang, J.; Guennic, B. L.; Zhao, J.; Jacquemin, D. *J. Org. Chem.* **2014**, *79*, 2038. (c) Yamaguchi, E.; Fukazawa, A.; Kosaka, Y.; Yokogawa, D.; Irle, S.; Yamaguchi, S. *Bull. Chem. Soc. Jpn.* **2015**, *88*, 1545.
14. (a) Bing, Y.; Selassie, D.; Paradise, R. H.; Isborn, C.; Kramer, N.; Sadilek, M.; Kaminsky, W.; Kahr, B. *J. Am. Chem. Soc.* **2010**, *132*, 7454. (b) Longhi, G.; Castiglioni, E.; Abbate, S.; Lebon, F.; Lightner, D. A. *Chirality* **2013**, *25*, 589.

15. (a) Mataga, N.; Kaifu, Y.; Koizumi, M. *Bull. Chem. Soc. Jpn.* **1955**, *28*, 690. (b) Mataga, N.; Kaifu, Y.; Koizumi, M. *Bull. Chem. Soc. Jpn.* **1956**, *29*, 465. (c) Lippert, E. *Z. Elektrochem.* **1957**, *61*, 962.
16. Gaussian 09 (Revision A.02), Frisch, M. J.; Trucks, G. W.; Schlegel, H. B.; Scuseria, G. E.; Robb, M. A.; Cheeseman, J. R.; Scalmani, G.; Barone, V.; Mennucci, B.; Petersson, G. A.; Nakatsuji, H.; Caricato, M.; Li, X.; Hratchian, H. P.; Izmaylov, A. F.; Bloino, J.; Zheng, G.; Sonnenberg, J. L.; Hada, M.; Ehara, M.; Toyota, K.; Fukuda, R.; Hasegawa, J.; Ishida, M.; Nakajima, T.; Honda, Y.; Kitao, O.; Nakai, H.; Vreven, T.; Montgomery, Jr., J. A.; Peralta, J. E.; Ogliaro, F.; Bearpark, M.; Heyd, J. J.; Brothers, E.; Kudin, K. N.; Staroverov, V. N.; Keith, T.; Kobayashi, R.; Normand, J.; Raghavachari, K.; Rendell, A.; Burant, J. C.; Iyengar, S. S.; Tomasi, J.; Cossi, M.; Rega, N.; Millam, J. M.; Klene, M.; Knox, J. E.; Cross, J. B.; Bakken, V.; Adamo, C.; Jaramillo, J.; Gomperts, R.; Stratmann, R. E.; Yazyev, O.; Austin, A. J.; Cammi, R.; Pomelli, C.; Ochterski, J. W.; Martin, R. L.; Morokuma, K.; Zakrzewski, V. G.; Voth, G. A.; Salvador, P.; Dannenberg, J. J.; Dapprich, S.; Daniels, A. D.; Farkas, O.; Foresman, J. B.; Ortiz, J. V.; Cioslowski, J.; Fox, D. J., Gaussian, Inc., Wallingford CT, 2009.
17. Sheldrick, G. M. SHELX-97, Program for the Refinement of Crystal Structures; University of Göttingen: Göttingen, Germany, 1997.
18. (a) Davies, J. A.; Elangovan, A.; Sullivan, P. A.; Olbricht, B. C.; Bale, D. H.; Ewy, T. R.; Isborn, C. M.; Eichinger, B. E.; Robinson, B. H.; Reid, P. J.; Li, X.; Dalton, L. R. *J. Am. Chem. Soc.* **2008**, *130*, 10565. (b) Dallos, T.; Hamburger, M.; Baumgarten, M. *Org. Lett.* **2011**, *13*, 1936.
19. (a) Caspar, J. V.; Kober, E. M.; Sullivan, B. P.; Meyer, T. J. *J. Am. Chem. Soc.* **1982**, *104*, 630. (b) Kucherak, O. A.; Didier, P.; Mély Y.; Klymchenko, A. S. *J. Phys. Chem. Lett.* **2010**, *1*, 616. (c) Yamaguchi, E.; Wang, C.; Fukazawa, A.; Taki, M.; Sato, Y.; Sakai, T.; Ueda, M.; Sasaki, N.; Higashiyama, T.; Yamaguchi, S. *Angew. Chem., Int. Ed.* **2015**, *54*, 4539.

List of Publications

Publications included in this thesis

Chapter 1

Wakamiya, A.; Nishimura, H.; Fukushima, T.; Suzuki, F.; Saeki, A.; Seki, S.; Osaka, I.; Sasamori, T.; Murata, M.; Murata, Y.; Kaji, H.
“On-top π -Stacking of Quasiplanar Molecules in Hole-Transporting Materials: Inducing Anisotropic Carrier Mobility in Amorphous Films”
Angew. Chem., Int. Ed. **2014**, *53*, 5800–5804.

Chapter 2

Nishimura, H.; Fukushima, T.; Wakamiya, A.; Murata, Y.; Kaji, H.
“The Influence of Quasiplanar Structures of Partially Oxygen-Bridged Triphenylamine Dimers on the Properties of their Bulk Films”
Bull. Chem. Soc. Jpn. **2016**, under revised.

Chapter 3

Nishimura, H.; Hasegawa, Y.; Wakamiya, A.; Murata, Y.
“Development of Transparent Organic Hole-Transporting Materials Using Partially Oxygen-Bridged Triphenylamine Skeletons”
In preparation.

Chapter 4

Nishimura, H.; Ishida, N.; Shimazaki, A.; Wakamiya, A.; Saeki, A.; Scott, L. T.; Murata, Y.
“Hole-Transporting Materials with a Two-Dimensionally Expanded π -System around an Azulene Core for Efficient Perovskite Solar Cells”
J. Am. Chem. Soc. **2015**, *137*, 15656–15659.

Chapter 5

Nishimura, H.; Tanaka, K.; Morisaki, Y.; Chujo, Y.; Wakamiya, A.; Murata, Y.
“Oxygen-Bridged Diphenylnaphthylamine as a Scaffold for Full-Color Circularly Polarized Luminescent Materials”
In preparation.

Publications not included in this thesis

- (1) Lee, J.; Kim, B.; Kwon, J. E.; Kim, J.; Yokoyama, D.; Suzuki, K.; Nishimura, H.; Wakamiya, A.; Park, S. Y.; Park, J.
“Excimer Formation in Organic Emitter Films Associated with a Molecular Orientation Promoted by Steric Hindrance”
Chem. Commun. **2014**, *50*, 14145–14148.
- (2) Nishimura, H.; Eliseeva, M. N.; Wakamiya, A.; Scott, L. T.
“1,3,5,7-Tetra(Bpin)azulene by Exhaustive Direct Borylation of Azulene and 5,7-Di(Bpin)azulene by Selective Subsequent Deborylation”
Synlett **2015**, *26*, 1578–1580.
- (3) Yamada, Y.; Yamada, T.; Phuong, L. Q.; Maruyama, N.; Nishimura, H.; Wakamiya, A.; Murata, Y.; Kanemitsu, Y.
“Dynamic Optical Properties of CH₃NH₃PbI₃ Single Crystals As Revealed by One- and Two-photon Excited Photoluminescence Measurements”
J. Am. Chem. Soc. **2015**, *137*, 10456–10459.
- (4) Makuta, S.; Liu, M.; Endo, M.; Nishimura, H.; Wakamiya, A.; Tachibana, Y.
“Photo-excitation Intensity Dependent Electron and Hole Injections from Lead Iodide Perovskite to Nanocrystalline TiO₂ and Spiro-OMeTAD”
Chem. Commun. **2016**, *52*, 673–676.
- (5) Yamada, T.; Yamada, Y.; Nishimura, H.; Nakaike, Y.; Wakamiya, A.; Murata, Y.; Kanemitsu, Y.
“Fast Free-Carrier Diffusion in CH₃NH₃PbBr₃ Single Crystals Revealed by Time-Resolved One- and Two-Photon Excitation Photoluminescence Spectroscopy”
Adv. Electron. Mater. **2016**, DOI: 10.1002/aelm.201500290.
- (6) Lee, J.; Jung, H.; Shin, H.; Kim, J.; Yokoyama, D.; Nishimura, H.; Wakamiya, A.; Park, J.
“Excimer Emission Based on the Control of Molecular Structure and Intermolecular Interactions”
J. Mater. Chem. C **2016**, DOI: 10.1039/c5tc03289j.

Acknowledgement

The study presented in this thesis has been carried out under the direction of Professor Yasujiro Murata and Associate Professor Atsushi Wakamiya at Institute for Chemical Research, Kyoto University during the period of April 2010 to March 2016.

The author would like to express his sincerest gratitude to Professor Yasujiro Murata for his kind guidance, suggestions, and hearty encouragement throughout this study. The author wishes to express his deep gratitude to Associate Professor Atsushi Wakamiya for his precise guidance, technical assistance, and kind encouragement. The author is grateful to Assistant Professor Michihisa Murata for helpful discussion and kind advice.

The author would like to give heartfelt thanks to Professor Lawrence T. Scott for giving him a precious opportunity to join the exciting research group at Boston College from September to December, 2013. He is also grateful to all members of Professor Scott's group for their kind assistance and warm friendship during his stay in Boston. The Mazume scholarship was indispensable, and the author wishes to acknowledge the founder, Dr. Akira Mazume.

The author is grateful to Professor Hironori Kaji, Assistant Professor Tatsuya Fukushima and Dr. Furitsu Suzuki at Institute for Chemical Research, Kyoto University for theoretical calculations, TOF measurement, and fabrication and measurement of OLED devices.

The author is grateful to Professor Shuhei Seki at Graduate School of Engineering, Kyoto University, Associate Professor Akinori Saeki and Mr. Naoki Ishida at Graduate School of Engineering, Osaka University for TRMC measurement.

The author is grateful to Dr. Itaru Osaka at RIKEN Center for Emergent Matter Science and Dr. Tomoyuki Koganezawa at Japan Advanced Institute of Science and Technology for 2D-GIXD measurement.

The author is grateful to Associate Professor Takahiro Sasamori at Institute for Chemical Research, Kyoto University for his support of single-crystal X-ray analysis.

The author is grateful to Dr. Yuta Hasegawa at Sony Corporation for X-ray diffraction measurement and SCLC measurement.

The author is grateful to Professor Yoshihiko Kanemitsu at Institute for Chemical

Research, Kyoto University and Associate Professor Yasuhiro Yamada at Graduate School of Science and Technology, Chiba University for advice and important discussion on the perovskite solar cells.

The author is grateful to Professor Kazunari Matsuda and Mr. Feiji Wang at Institute of Advanced Energy, Kyoto University for advice on the measurement of SEM images.

The author is grateful to Professor Yasuhiro Morisaki at School of Science and Technology, Kwansei Gakuin University, Professor Yoshiki Chujo, Associate Professor Kazuo Tanaka, Mr. Masayuki Gon and Ms. Risa Sawada at Graduate School of Engineering, Kyoto University for the support of CPL measurement.

The author is grateful to Professor Takeo Kawabata and Associate Professor Takumi Furuta at Institute for Chemical Research, Kyoto University for advice on the measurement of CD spectra.

The author is grateful to Professor Yoshinobu Tsujii and Assistant Professor Keita Sakakibara for advice on the measurement of DLS measurement.

The author appreciates to Professor Yasuhiro Tachibana at Royal Melbourne Institute of Technology University and Professor Jongwook Park at The Catholic University of Korea for their joint researches.

The author appreciates to Ms. Toshiko Hirano, Ms. Akiko Fujihashi and Ms. Kyoko Ohmine at Institute for Chemical Research, Kyoto University for their work of elemental analysis, mass spectrometry, and NMR analysis, respectively. Single-crystal X-ray analysis and 2D-GIXD measurements were measured at the SPring-8 beamlines BL38B1 and BL19B2. The author would like to appreciate to the beamline staffs.

The author is grateful to the experimental contribution of Dr. Masaru Endo and Ms. Ai Shimazaki for their helpful experiments in this study. The author also thanks all present members and alumni of Professor Murata's laboratory for their kind supports and encouragement.

The author would like to appreciate Professor Kouichi Ohe and Professor Fumiyuki Ozawa for careful reviewing of this thesis and fruitful comments.

The author is thankful to all members of Professor Kaji's lab., Professor Ozawa's lab., Professor Nakamura's lab., Professor Tokitoh's lab., Professor Kanemitsu's lab.,

and Professor Kawabata's lab.

The author thanks to the Japan Society for the Promotion of Science (JSPS) for the Research Fellowship for Young Scientists (DC2).

Finally, the author would like to express his sincerest appreciation to his family: Mr. Shigeru Nishimura, Ms. Yoshiko Nishimura, and Ms. Miki Nishimura for their constant assistance, warm support, and encouragement.

Hidetaka Nishimura

Department of Energy and Hydrocarbon Chemistry
Kyoto University
2016